A Study of Flow Boiling Phenomena Using Real Time Neutron Radiography

by

David Raymond Novog, B.Sc. Eng., M.Eng.

A Thesis
Submitted to the School of Graduate Studies
in Partial Fulfillment
of the Requirements for the Degree
Doctor of Philosophy.

McMaster University

A STUDY OF FLOW BOILING PHENOMENA USING REAL TIME NEUTRON RADIOGRAPHY

DOCTOR OF PHILOSOPHY (2000) MCMASTER UNIVERSITY

(Engineering Physics) Hamilton, Ontario, Canada

Title: **A Study of Flow Boiling Phenomena Using Real Time Neutron Radiography**

Author: David Raymond Novog, B.Sc. Eng., M.Eng.

Supervisor: Dr. J.S. Chang

Number of Pages: xix, 206, A-31

Summary

The operation and safety of both fossil-fuel and nuclear power stations depend on adequate cooling of the thermal source involved. This is usually accomplished using liquid coolants that are forced through the high temperature regions by a pumping system; this fluid then transports the thermal energy to another section of the power station. However, fluids that undergo boiling during this process create vapor that can be detrimental, and influence safe operation of other system components. The behavior of this vapor, or void, as it is generated and transported through the system is critical in predicting the operational and safety performance. This study uses two advanced penetrating radiation techniques, Real Time Neutron Radiography (RTNR), and High Speed X-Ray Tomography (HS-XCT), to examine void generation and transport behavior in a flow boiling system.

The geometries studied were tube side flow boiling in a cylindrical configuration, and a similar flow channel with an internal twisted tape swirl flow generator. The heat transfer performance and pressure drop characteristics were monitored in addition to void distribution measurements, so that the impact of void distribution could be determined. The RTNR and heat transfer pipe flow studies were conducted using boiling Refrigerant 134a at pressures from 500 to 700 kPa, inlet subcooling from 3 to 12 °C and mass fluxes from 55 to 170 kg/m^2-s with heat fluxes up to 40 kW/m^2.

RTNR and HS-XCT were used to measure the distribution and size of the vapor phases in the channel for cylindrical tube-side flow boiling and swirl-flow boiling geometries. The results clearly show that the averaged void is similar for both geometries, but that there is a significant difference in the void distribution, velocity and transport behavior from one configuration to the next. Specifically, the void distribution during flow boiling in a cylindrical-tube test section showed that the void fraction was largest near the tube center and decreased with increasing radial distance. For swirling flow, the void concentration was highest in the center of each subchannel formed by the twisted tape insert, producing two local void maxima at each axial position. Furthermore, the instantaneous RTNR results show that the effects of bubble agglomeration change from one geometry to the next. To further examine the application of RTNR for void distribution measurement, both vertical and horizontal orientations were examined. These experimental results show similar cross sectional averaged axial distributions of the void fraction but significant differences in the local void behavior.

The HS-XCT experiments were conducted on swirl-flow boiling of Refrigerant 123 at similar conditions as the RTNR experiments. These tests were conducted to qualitatively compare and verify the void distribution and behavior obtained using RTNR techniques. The HS-XCT results verify that during smooth flow boiling in a vertical tube the void tends to concentrate in the center of the channel and decrease outward to the channel walls. For swirl flow, the void tends to concentrate near the center of each subchannel formed by the twisted tape. Furthermore, wall region void fraction for smooth-flow boiling was significantly higher than swirling flow conditions due to the significant centrifugal forces present in swirl-flow. These centrifugal forces may improve the heat transfer and dryout behavior during swirl-flow conditions.

This work contributes to the development of two-phase flow diagnostics based on penetrating radiative techniques, i.e., RTNR and HS-XCT for void distribution measurement, and enhances the knowledge of flow boiling systems. The application of HS-XCT and RTNR for the study of flow boiling phenomena using smooth and swirl-flow geometries has clearly demonstrated that differences in local void distribution result in differences in heat transfer behavior.

ACKNOWLEDGMENTS

I wish to acknowledge my supervisor Dr. Jen-Shih Chang for his research guidance, knowledge and supervision throughout my graduate studies. I would also like to thank my Ph.D. supervisory committee, Dr. R.L. Judd, Dr. K. Krishnan and Dr. D.P. Jackson for their invaluable input and supervision during this endeavor. I also acknowledge the contributions of Dr. K. Hori for his involvement and supervision during the X-Ray experiments in Japan.

This research work was completed with contributions from several industrial sponsors and individuals. The Real Time Neutron Radiography experiments were conducted at McMaster University Nuclear Reactor and ultra-high speed X-Ray Computed Tomography was conducted at Mitsubishi Heavy Industries in Japan. This work has been sponsored in part by Mitsubishi Heavy Industries Ltd. of Japan and the Canadian Fusion Fuels Technology Program. Additionally, the loan of equipment from Atomic Energy of Canada Limited is also appreciated.

I would like to thank my colleagues in the Nuclear Research Building for their discussions and friendship. Mr . Paul Looy provided excellent technical assistance throughout this work; but more importantly he is a great friend. I also wish to thank Dr. G.D. Harvel, Mr. Fukuhara, Dr. I.C. Lim, Mr. O. Kelly, Mr. M. Butler, and Dr. K. Urashima for their technical input and involvement in this work. Mr. H. Sugimoto and Mr. S. Mirukami also contributed a large amount of time and effort in completing the X-Ray experiments. Thanks to the 10 am coffee club: Joey, Mike, Bryan, Kelly, Dwayne, Collin, Dennis, Craig, Stu and Andrew.

This work I really owe to my parents; they have taught me the greatest lessons in life through their own words and deeds since June 8, 1971. Karen, Annette, Tom and Darryl, your love has always meant a great deal to me. I want to thank my entire fammily for their support in every aspect of my life.

C.J.. I could never thank you enough for your love, sacrifice, commitment and friendship.

TABLE OF CONTENTS

Summary ii

Acknowledgments iv

Table of Contents v

List of Figures x

List of Tables xvi

Nomenclature xvii

1 Introduction 1
  1.1 Heat Transfer 3
  1.2 Introduction to Single Phase Flow and Heat Transfer 5
  1.3 Introduction to Two Phase Flow and Heat Transfer 6
  1.4 Void Fraction and Distribution 7
  1.5 Void Distribution in Two-phase Flow Analysis 12
  1.6 Interactions Between Radiation and Matter 17
  1.7 Overview 19

2 Literature Review of Flow Boiling and Void Distribution Measurement 27
  2.1 Single Phase Flow 27
    2.1.1 Single Phase Flow 27

2.1.2 Single Phase Pressure Drop 29

2.2 Two-phase Flow 30

2.2.1 Two Phase Flow-Regime 31

2.2.2 Two-phase Flow Boiling Heat Transfer 32

2.2.3 Onset of Nucleate Boiling / Onset of Significant Void 32

2.2.4 Nucleate Boiling Heat Transfer 34

2.2.5 Swirl Flow Effects 37

2.3 Void Distribution Measurement Techniques 40

2.3.1 Electrostatic/Impedance Devices 40

2.3.2 X-Ray Tomography 41

2.3.3 Other Techniques 42

2.3.4 Real Time Neutron Radiography Void Distribution Measurement . 44

2.4 Void Fraction Correlations 47

3 Experimental Details 59

3.1 Refrigerant 134a Boiling Experiments 60

3.1.1 Refrigerant 134a Flow Loop 60

3.1.2 Secondary Side Water Heating Loop 61

3.1.3 Direct Electrical Heating 62

3.1.4 Surface Temperature Correction 63

3.1.5 Flow Diagnostics 65

3.2 McMaster Nuclear Reactor 67

3.2.1 Beam Port Facilities 67

3.3 Real Time Neutron Radiography 68

3.4 Refrigerant 123 Flow Boiling Facility 69

3.4.1 Refrigerant 123 Flow Loop 69

3.4.2 Ultra-High Speed X-Ray Computed Tomography System 70

3.5 Test Sections 71

3.5.1 Horizontal Flow Test Section 71

3.5.2 Vertical Flow Test Section 71

3.6 Twisted-Tape Inserts 72

4 RTNR Void Distribution Measurement Theory 88

4.1 Radiographic Principles 88

4.2 Real Time Neutron Radiography 91

4.2.1 Vertical RTNR Radial Void Distribution Reconstruction 93

4.2.2 RTNR Image Processing 95

4.2.3 RTNR Void Distribution Dependencies 97

4.3 Accuracy of Void Reconstruction Methodology 97

5 Heat Transfer and Pressure Drop Characteristics 105

5.1 Smooth Flow 106

5.1.1 Effect of Mass Flux 107

5.1.2 Effect of Inlet Subcooling 107

5.1.3 Effect of System Pressure 108

5.2 Swirl Flow 108

5.2.1 Effect of Twist Ratio 109

5.2.2 Effect of Mass Flux 110

5.2.3 Effect of Inlet Subcooling 110

5.2.4 Effect of System Pressure 110

5.3 Pressure Drop Results 111

6 Smooth Flow-Boiling Void Distribution Measurement 123

6.1 Time and Cross Sectional Averaged Void Fraction 123

6.1.1 Effect of Inlet Subcooling 124

6.1.2 Effect of Mass Flux 124

6.1.3 Effect of System Pressure 125

6.1.4 Effect of Test Section Orientation 126

6.2 Void Quality Relationships 126

6.3 Instantaneous Cross Sectional Averaged Void Fraction 127

6.4 Time Averaged Local Void Distribution 128

6.4.1 Effect of Mass Flux 129

6.4.2 Effect of Inlet Subcooling 130

6.4.3 Effect of System Pressure 130

6.4.4 Effect of Orientation 130

6. 5 Instantaneous Local Void Distribution 131

7 Swirl Flow Void Distribution Measurement 153

7.1 Time and Cross Sectional Averaged Results 154

7.1.1 Inlet Subcooling Effects 155

7.1.2 Mass Flux Effects 155

7.1.3 System Pressure Effects 156

7.1.4 Effect of Test Section Orientation 156

7.2 Instantaneous Cross Sectional Averaged Void Fraction 156

7.3 Time Averaged Local Void Distribution 157

7.4 Instantaneous Swirl Flow Local Void Distribution 159

7.5 Advanced XCT Results 159

7.5.1 XCT Cross Sectional Averaged Void Distribution 160

7.5.2 XCT Instantaneous Void Distribution 160

8 Conclusions 185

8.1 Smooth Flow Time and Cross Sectional Averaged Results 185

8.2 Instantaneous Area Averaged Void Fraction Measurement 187

8.3 Local Time Averaged Void Distribution Results 188

8.4 Instantaneous Local Void Fraction Distribution 188
8.5 Swirl Flow Void Distribution Measurement 189

9 Recommendations for Future Work 191

References 195

Appendix A. Fluid Properties A-1

Appendix B. APWR Fuel RTNR Void Measurements A-6

Appendix C. Calibration Information A-11

Appendix D. RTNR Uncertainty Determination A-17

Appendix E. HP VEE Data Acquisition Program A-21

Appendix F. Contributions to Knowledge A-27

Appendix G. Copyright Exceptions A-31

LIST OF FIGURES

Figure 1.1 The Effect of Turbulence on Typical Velocity Waveforms

Figure 1.2 Typical Two Phase Flow Distributions for Vertical Co-Current Flow

Figure 1.3 Typical Two-phase Flow Distributions for Horizontal Co-Current Flow.

Figure 1.4 Schematic Representation of Flow Boiling Phenomena for a) Vertical and b) Horizontal Configurations.

Figure 1.5 Typical Flow Boiling Curve

Figure 2.1 Moody Diagram for Predicting Single-Phase Friction Factor (Fox and McDonald)

Figure 2.2 Flow Regime Maps for a) Vertical and b) Horizontal Two-phase Flow.

Figure 2.3 Schematic of Basic Tomographic Principles.

Figure 2.4 Advancements in XCT Scanning Time.

Figure 3.1 Schematic of Refrigerant 134a Flow Loop Used For RTNR Experiments.

Figure 3.2 Schematic of the McMaster University Secondary Side Water Heating Loop.

Figure 3.3 Schematic of the Bulk Fluid Thermocouple Measurement Assembly.

Figure 3.4 Refrigerant Side Venturi Flow Meter.

Figure 3.5 Schematic of the Multi-Ring Capacitance Flow Meter.

Figure 3.6 Schematic of the McMaster Nuclear Reactor Arrangement.

Figure 3.7 McMaster University Beam Port #2 Layout.

Figure 3.8 RTNR Void Distribution Measurement System.

Figure 3.9 Schematic of Refrigerant 123 Flow Loop Used for Ultra-High Speed XCT Experiments.

Figure 3.10 High Speed XCT Void Distribution Measurement System.

Figure 3.11 Timing Control Circuit for High Speed XCT .

Figure 3.12 Schematic Horizontal Flow Boiling Test Section.

Figure 3.13 Schematic of Vertical Flow Boiling Test Section.

Figure 3.14 Twisted Tape Swirl-Flow Generating Inserts.

Figure 4.1 Schematic of Basic Radiographic Principals

Figure 4.2 Unprocessed RTNR Images for a) an Empty Channel, b) Full Channel, c) Time Averaged Smooth-flow Boiling, d) Time Averaged Swirl-flow Boiling and e) Instantanious Swirl-flow Boiling.

Figure 4.3 Radial RTNR Void Distribution Reconstruction Theory.

Figure 4.4 Image Processing Flow Chart.

Figure 4.5 Effect of Flow Distribution on RTNR Void Measurement.

Figure 5.1 Horizontal Smooth-Flow Boiling Curve at 100 kg/m^2-s, 630 kPa and 9 °C Subcooling.

Figure 5.2 Effect of Mass Flux on Smooth-Flow Boiling of Refrigerant 134a at 630 kPa and 6 °C Subcooling.

Figure 5.3 Effect of Inlet Subcooling on Smooth-Flow Boiling of Refrigerant 134a at 100 kg/m^2-s and 630 kPa.

Figure 5.4 Effect of System Pressure on Smooth-Flow Boiling of Refrigerant 134a at 100 kg/m^2-s and 6 °C Subcooling.

Figure 5.5 Effect of Twist Ratio on Swirl-Flow Boiling of Refrigerant 134a at 100 kg/m^2-s and 630 kPa.

Figure 5.6 Effect of Mass Flux on Swirl-Flow Boiling of Refrigerant 134a at 630 kPa and 6 °C Subcooling.

Figure 5.7 Effect of Inlet Subcooling on Horizontal Swirl-Flow Boiling of Refrigerant 134a at 100 kg/m^2-s, 9 °C Subcooling and 630 kPa.

Figure 5.8 Effect of System Pressure on Horizontal Swirl-Flow Boiling of Refrigerant 134a at 100 kg/m^2-s and 6 °C Subcooling.

Figure 5.9 Effect of Twisted Tapes on CHF for Flow Boiling [Celata].

Figure 5.10 Effect of Mass Flux on Subcooled Boiling Pressure Drop Waveforms for

Smooth-Flow.
Figure 5.11 Effect of Mass Flux on Subcooled Boiling Pressure Drop Waveforms for Swirl-Flow.
Figure 6.1 Refrigerant 134a Smooth-Flow Cross Sectional and Time Averaged Void Fraction Distribution and Comparison with Correlations from Wallis, Thom et al. and the Homogeneous Equilibrium Model
Figure 6.2 Effect of Inlet Subcooling on Cross Sectional and Time Averaged Void Distribution for Refrigerant 134a Smooth-Flow Boiling at 55 kg/m^2-s and 630 kPa.
Figure 6.3 Effect of Mass Flux on Refrigerant 134a Cross Sectional and Time Averaged Void Distribution for Refrigerant 134a Smooth-Flow Boiling at 6 °C Inlet Subcooling and 630 kPa.
Figure 6.4 Effect of System Pressure on Cross Sectional and Time Averaged Void Distribution for Refrigerant 134a Smooth-Flow Boiling at 6 °C Subcooling and 55 kg/m^2-s.
Figure 6.5 Effect of Test Section Orientation of Cross Sectional and Time Averaged Void Distribution for Refrigerant 134a Smooth-Flow Boiling at 630 kPa and 55 kg/m^2-s.
Figure 6.6 Smooth Flow Void to Quality Relationship at 630 kPa and Comparison to Wallis Correlation.
Figure 6.7 Instantaneous Cross Sectional Void Fraction Distribution.
Figure 6.8 Effect of Mass Flux on the Vapor Slug Slip Ratio at 630 kPa.
Figure 6.9 Effect of Inlet Subcooling on Vapor Slug Slip Ratio at 630 kPa.
Figure 6.10 RTNR Processed Image of Flow Boiling at 55 kg/m^2-s, 6 °C Inlet Subcooling and 630 kPa.
Figure 6.11 Time Averaged Local Void Fraction Distribution for Refrigerant 134a Smooth-Flow Boiling at 55 kg/m^2-s, 6 °C Inlet Subcooling and 630 kPa.

Figure 6.12 Effect of Mass Flux on the Time Averaged Local Void Fraction Distribution for Refrigerant 134a Smooth-Flow Boiling at 6 °C Inlet Subcooling, 630 kPa and a)55 kg/m^2-s, b) 100 kg/m^2-s and c) 140 kg/m^2-s.

Figure 6.13 Effect of Inlet Subcooling on the Time Averaged Local Void Distribution at 100 kg/m^2-s and 630 kPa for a) 12 °C, b) 9 °C, and c) 6 °C Inlet Subcooling.

Figure 6.14 Effect of System Pressure on the Time Averaged Local Void distribution at 1000 kg/m^2-s and 9 °C Inlet Subcooling at a) 500 kPa, b) 630 kPa, and c) 700 kPa.

Figure 6.15 Effect of Orientation on Void Distribution at 100 kg/m^2-s, 630 kPa and 6 °C Subcooling for a Horizontal Orientation.

Figure 6.16 Instantaneous Local Void Distribution for Smooth-Flow Boiling of Refrigerant 134a at 55 kg/m^2-s and 630 kPa.

Figure 6.17 Effect of Mass Flux on the Instantaneous Local Void Distribution for Smooth-Flow Boiling of Refrigerant 134a at 630 kPa and 6 °C Inlet Subcooling for a) 100 kg/m^2-s and b) 140 kg/m^2-s.

Figure 6.18 Effect of System Pressure on Instantaneous Local Void Distribution at 55 kg/m^2-s and 6 °C Inlet Subcooling for a) 500 kPa and b) 630 kPa.

Figure 6.19 Effect of Inlet Subcooling on Instantaneous Local Void Distribution at 100 kg/m^2-s and 630 kPa for a) 9 °C and b) 12 °C Inlet Subcooling.

Figure 7.1 Effect of Swirl Flow on the Time and Cross Sectional Averaged Void Distribution at 55 kg/m^2-s, 6 °C Inlet Subcooling and 630 kPa.

Figure 7.2 Effect of Swirl Flow on the Time and Cross Sectional Averaged Void Distribution 55 kg/m^2-s, 12 °C Inlet Subcooling and 630 kPa.

Figure 7.3 Effect of Swirl-Flow on the Time and Cross Sectional Averaged Void Fraction Distribution at 100 kg/m^2-s, 6 °C Inlet Subcooling and 630 kPa.

Figure 7.4 Effect of Inlet Subcooling on Cross Sectional and Time Averaged Void Distribution for Refrigerant 134a Smooth-Flow Boiling at 100 kg/m^2-s and

630 kPa.

Figure 7.5 Effect of Mass Flux on Refrigerant 134a Cross Sectional and Time Averaged Void Distribution for Refrigerant 134a Swirl-Flow Boiling at 6 °C Inlet Subcooling and 630 kPa.

Figure 7.6 Effect of System Pressure on Cross Sectional and Time Averaged Void Distribution for Refrigerant 134a Swirl-Flow Boiling at 55 kg/m^2-s and 6 °C Inlet Subcooling.

Figure 7.7 Effect of Test Section Orientation of Cross Sectional and Time Averaged Void Distribution for Refrigerant 134a Swirl-Flow Boiling at a twist ratio of 3, 630 kPa and 55 kg/m^2-s.

Figure 7.8 Instantaneous Cross Sectional Void Fraction Distribution for Swirl Flow at 55 kg/m^2-s, 9 °C Inlet Subcooling and 630 kPa.

Figure 7.9 Effect of Mass Flux on the Vapor Slug Slip Ratio at 630 kPa for Swirl Flow.

Figure 7.10 Effect of Swirl-Flow on the Vapor Slug Slip Ratio at 630 kPa.

Figure 7.11 Time Averaged Local Void Fraction Distribution for Refrigerant 134a Swirl-Flow Boiling at 55 kg/m^2-s.

Figure 7.12 Time Averaged Local Void Fraction Distribution for Refrigerant 134a a) Smooth-Flow and b) Swirl-Flow Boiling at 55 kg/m^2-s, 9 °C Inlet Subcooling and 630 kPa.

Figure 7.13 Effect of Mass Flux on Swirl Flow Boiling Time Averaged Local Void Distribution for a) 55 kg/m^2-s, b) 110 kg/m^2-s and c) 140 kg/m^2-s at 630 kPa and 6 °C Subcooling.

Figure 7.14 Effect of Inlet Subcooling on Swirl Flow Boiling Time Averaged Void Distribution for a) 12 °C, b) 9 °C and c) 6 °C Inlet Subcooling at 110 kg/m^2-s and 630 kPa.

Figure 7.15 Effect of System Pressure on Swirl Flow Boiling Time Averaged Void Distribution for a) 500 kPa, b) 630 kPa and c) 700 kPa at 55 kg/m^2-s and 9

°C Inlet Subcooling.
Figure 7.16 Orientation on Swirl-Flow Boiling Time Averaged Void Fraction Distribution at 100 kg/m^2-s and 6 °C Inlet Subcooling.
Figure 7.17 Instantaneous Local Void Distribution for Swirl-Flow Boiling of Refrigerant 134a at 55 kg/m^2-s, 6 °C Inlet Subcooling and 630 kPa.
Figure 7.18 Effect of Mass Flux on the Instantaneous Local Void Distribution for Swirl-Flow Boiling of Refrigerant 134a for a) 100 kg/m^2-s and b) 140 kg/m^2-s at 9 °C Inlet Subcooling and 630 kPa.
Figure 7.19 Effect of Inlet Subcooling on Instantaneous Local Void Distribution at 55 kg/m^2-s and 630 kPa at a) 9 °C and b) 12 °C Subcooling.
Figure 7.20 Effect of System Pressure on Instantaneous Local Void Distribution at 55 kg/m^2-s and 6 °C Inlet Subcooling for a) 500 kPa and b) 630 kPa.
Figure 7.21 Time Averaged XCT Measurement of Swirl Flow Boiling of Refrigerant 123 at 750 kg/m^2-s and 630 kPa.
Figure 7.22 Instantaneous Void Distribution Measurement (0.9 ms per slice) of Swirl Flow Boiling of Refrigerant 123 at 750 kg/m^2-s and 630 kPa Using High Speed XCT.
Figure 7.23 Instantaneous 3-Dimensional Reconstruction of Refrigerant 123 Flow Boiling at 750 kg/m^2-s and 630 kPa Based on 300 High Speed XCT Slices (shown in Figure 7.22).

LIST OF TABLES

Table 1.1 Typical Values of the Convection Heat Transfer Coefficient.

Table 1.2 Radiation Attenuation of Common Materials

Table 2.1 Single-Phase Heat Transfer Correlations.

Table 2.2 Single Phase Pressure Drop Correlations.

Table 2.3 ONB Correlations.

Table 2.4 Subcooled Flow Boiling Correlations.

Table 2.5 Void Quality Relationships.

NOMENCLATURE

ΔT_{sub}	liquid subcooling, $T_{sat} - T_{liquid}$
ΔT_{wall}	wall superheat, $T_{wall} - T_{sat}$
ΔT	temperature difference
h	heat transfer coefficient
k	thermal conductivity
q	heat transfer rate
q''	heat flux
$\dot{m}$	mass flow rate
G	mass flux
P	pressure
ΔP	pressure drop
I	radiation intensity
Io	un-attenuated radiation intensity
A	chordal total attenuation
B	radiation back scatter build-up factor
d	diameter
f	friction factor
G_w	wall material neutron interaction factor
I_{tp}	two-phase neutron beam intensity
I_{full}	single-phase liquid neutron beam intensity
I_{empty}	empty test section neutron beam intensity
y_{tp}	two-phase measured liquid thickness
y_{full}	single-phase liquid measure thickness
y_{empty}	empty test section liquid thickness

j	slip velocity
u	local velocity
$\overline{u}$	superficial velocity
V	velocity
x	quality
Re	Reynold number $[VD/\nu]$
Pr	Prandtl number $[\nu/\kappa]$
Nu	Nusselt number $[hD/k]$
Ra	Rayleigh number $[g\beta L^3(\Delta T)/(\nu\kappa)]$
$\tilde{\alpha}$	chordal void fraction
α	cross sectional averaged void fraction
α_{local}	local void fraction
α_{volume}	volume averaged void fraction
β	neutron camera calibration constant
Π	RTNR system coefficient
ξ	discretized path length
λ	attenuation coefficient
κ	thermal diffusivity
μ	viscosity
ν	dynamic viscosity (μ / ρ)
Σ	neutron attenuation coefficient
ϕ	heat flux
ρ	density

Subscripts

b	bulk

gen	internal heat generation
i	interfacial
l	liquid
nb	nucleate boiling
o	original
pb	pool boiling
t	total
tp	two-phase
tt	turbulent liquid - turbulent vapor flow
v	vapor
vd	viscous dissipation
w	wall

CHAPTER 1 INTRODUCTION

Application of convective heat transfer principles and boiling phenomena in modern society has led to numerous improvements in the quality of human life. The understanding of this thermal energy transport is critical in many energy conversion technologies including fossil fuel and nuclear based electrical power production. Liquid coolants exposed to excessive thermal energy undergo a phase change that alters the energy transfer mechanisms. Operation and safety of these power production systems depends on thorough understanding of the complex heat transport and vapor generation behavior during flow boiling. The generation, distribution and dynamics of vapor transportation are integral parts of the formulation used to predict the overall behavior of a boiling heat transport system. These mechanisms for vapor behavior are complex, and can not be accurately modeled based on first principles. Instead vapor dynamics are often empirically or semi-empirically represented based on local vapor distribution measurements. Many conventional measurement techniques such as hot wire or optical void measurement probes require that instruments must be inserted into the flow field and hence may cause a redistribution of the flow as a result of the measurement. The focus of this thesis is developing and applying Real Time Neutron Radiography and High Speed X-Ray Computed Tomography for the experimental determination of the dynamic void distribution during tube-side flow boiling. These systems measure both the time averaged and instantaneous void distribution inside metal-walled channels undergoing flow boiling. Through the use of cylindrical-pipe flow geometries and enhanced swirling flow boiling channels the significant advantages of these systems are demonstrated over a range of boiling conditions.

The void distribution and its effect on system behavior and governing equations can be illustrated using thermodynamic and heat transfer principles. Classical thermodynamics defines the transport of energy in terms of heat, work, internal, kinetic, and potential energy. The first law of thermodynamics for a closed system at steady state is often written as follows;

$$w + \Delta u + \Delta pe + \Delta ke = q \qquad 1.1$$

where q and w are the energy transport from the system in the forms of heat and work and Δu, Δpe, Δke are the changes in the internal, the potential and the kinetic energies respectively. If Equation 1.1 is applied to a heated channel with insignificant potential and kinetic energy effects, then the result for a system with constant physical properties and no phase change is;

$$q = \dot{m}\, C_p \Delta T \qquad 1.2$$

where m is the mass flow rate, C_p is the specific heat at constant pressure and ΔT is the mean temperature difference of the fluid entering and leaving the channel. This equation is of fundamental importance in predicting force convective heat transfer because it relates the change in temperature of a cooling medium to its thermodynamic properties, mass flow rate and the total heat supplied.

In some cases, the initiation of flow boiling can lead to changes in heat transfer and pressure drop. Since the pressure drop has a significant effect on the system flow rate, this can lead to changes in the bulk coolant velocity, or alternately changes in heat transfer may alter the fluid state (temperature, pressure, thermodynamic mass quality) from predicted values. These changes in flow rate and state variables can lead to further excursions from normal operation and hence may lead to an undesirable and/or an unstable system. The first law of thermodynamics describes the total energy transport through a system but does not address the mechanisms of thermal energy transport across system boundaries that may limit the application of this law [Incopera and DeWitt[1]].

This work focuses on the importance of vapor (void) distribution on the system behavior; and specifically on the accurate measurement of this distribution using Real Time Neutron Radiography and Ultra-High Speed Computed Tomography.

1.1 HEAT TRANSFER

The mechanisms for thermal energy transport are of primary concern in many electrical power production applications because these mechanisms are responsible for transferring energy to electrical generators and for cooling high temperature equipment. Heat transport capability is a function of the physical design, composition and environment of the system and is significantly affected by the presence and distribution of multiple phases. The transport of heat is accomplished through the mechanisms of conduction, convection and radiation, and the study of these mechanisms is known as heat transfer. Radiation is the mechanism for heat transport resulting from the exchange of electromagnetic radiation from one object to another. Conduction arises from thermal diffusion (in liquids and gases) and through free electron transport in metals with no bulk motion of the substance. Convection is the heat transfer mechanism from a surface to a fluid resulting from mean molecular motion due to advection or diffusion in the fluid. Newtons law of cooling describes convective cooling using;

$$q = h(\Delta T) \tag{1.3}$$

where q is the heat flux through a surface, h is the convective heat transfer coefficient and ΔT is the temperature difference between the heat transfer surface and the cooling medium. The heat transfer coefficient is dependent on a number of physical parameters including the fluid viscosity, velocity, density, specific heat and conductivity with these fluid properties are a function of temperature, as well as the surface geometry and wall roughness. Furthermore, if there is a change of state in the fluid medium such as boiling, the surface tension, latent heat, saturation pressure, liquid to vapor density ratio, mass quality, vapor fraction and distribution may also affect the heat transfer [Leppert and Pitts[2]]. The study of convection problems ultimately relies on the ability to assess the convective heat transfer coefficient accurately.

In many cases convection can be further classified into forced and natural cooling modes. Under natural convection, property gradients (such as density/buoyancy driven flow) give rise to fluid motion. Forced convection involves motion imposed by a secondary mechanical component (such as a pump) to increase the cooling medium flow rate and hence the heat transfer. Table 1.1 shows some typical values of the heat transfer coefficient for various modes of convective heat transfer.

Table 1.1 Typical magnitude for the convective heat transfer coefficient.

System	h [W/m^{2}K]
Natural Convection	< 500 -1000
Forced Single Phase Convection	300 - 5000
Nucleate Flow Boiling	3000 - 30000

1.2 INTRODUCTION TO SINGLE PHASE FLOW AND HEAT TRANSFER

The most common form of forced convective cooling uses a substance in either its liquid or gaseous state forced over a heated surface. Dimensionless numbers are often used in thermalhydraulics because they can be used to scale results from one physical situation or material to another. Dimensionless numbers are also used to correlate experimental results involving the interaction of many variables because a dimensionless group usually contains many physical parameters thus simplifying the design and analysis by reducing the number of independent parameters. Single phase flow is characterized by the non dimensional Reynolds number:

$$Re = \frac{V\,D}{\nu} \qquad 1.4$$

where V is the velocity, D is the characteristic length and ν is the kinematic viscosity. The Reynolds number effectively gives the ratio of inertial to viscous forces in a flowing system. It is also used to catagorize the flow into turbulent and laminar regimes. Turbulent flow is characterized by strong inertial forces which give rise to random fluctuations in the local velocity. Laminar flow does not have these local fluctuations and the velocity waveform is more stable. Figure 1.1 shows typical local velocity waveforms for laminar and turbulent flow. There is no absolute Reynolds number corresponding to transition between these regimes, as it is dependent on many characteristics such as the flow geometry and surface properties and complete transition from laminar to turbulent flow can take place over a range of Reynolds numbers.

The ratio of the thermal to momentum diffusivity is another common dimensionless group in heat transfer and is defined as the Prandtl number;

$$\Pr = \frac{\mu C_p}{k} = \frac{\nu}{\kappa} \tag{1.5}$$

where k is the thermal conductivity, κ is the thermal diffusivity, ρ is the density and C_p is the specific heat at constant pressure. The physical interpretation of the Prandtl number for laminar flow is the relative thickness of the thermal to momentum boundary layers.

The non-dimensional heat transfer coefficient, Nusselt number, is also often used to scale heat transfer coefficients;

$$Nu = \frac{hD}{k} \tag{1.6}$$

where h is the convective heat transfer coefficient, D is the channel diameter and k is the thermal conductivity of the heat transfer fluid.

1.3 INTRODUCTION TO TWO PHASE FLOW AND HEAT TRANSFER

In many systems where energy is transferred from a boundary to a liquid, there may be a change in the thermodynamic phase of the fluid. If the energy is transferred in the form of heat, the result may be boiling or evaporation or if the transfer is from mechanical work (such as a pump) the result may be cavitation. These vapor generation phenomena cause changes in the heat transfer, pressure drop, flow rate and performance of the system. The thermodynamic mass quality, x, of a system is defined as;

$$x = \frac{m_v}{m_v + m_l} \tag{1.7}$$

where m_v and m_l are the masses of the vapor and liquid components respectively. The creation and presence of a second phase can lead to either an increase or decrease in the thermal performance of a system. The predictive methods used in flow boiling are complex and rely upon numerous experimentally based constitutive relationships to model the transfer of mass, momentum, and energy.

Ishii[3] and Boure[4] have presented three-dimensional differential equations to describe two-phase flow under transient conditions. The computational solution of these equations for a given system is often prohibited by cost and computer limitations. In many situations, some form of averaging is employed that reduces the number of variables needed to describe the system. Typically some type of spatial or time averaging is used to reduce the local flow properties to area or volume averaged quantities; or time averaging is used to remove temporal fluctuations, however during this process information may be lost. For example, using spatial averaging reduces the information provided on the flow distribution or the velocity components of the separate phases. Using an area or volume averaging technique reduces the number of unknown velocities in computational schemes from three to two or one. In the case of time averaging, information on the instantaneous fluctuations in the velocity and temperature are not predicted.

1.4 VOID FRACTION AND DISTRIBUTION

A quantity used extensively in the study of two-phase flow is the cross sectional averaged void fraction, α, defined as;

$$\alpha = \frac{A_v}{A} \qquad 1.8$$

where A_v is the cross sectional area occupied by vapor, and A is the total cross sectional area of the channel. Thus, the void fraction represents the percentage of the flow area occupied by vapor. Furthermore, the volume averaged void fraction, α_{volume}, can be expressed as the ratio of the volumes of gas to the total volume considered. At the local level, the point void fraction (i.e. the local void fraction, α_{local}) in the flow field discretely varies between 1 (i.e. gas is present at that point in the flow field) or 0 (i.e. liquid is present at that point in the flow field). For this study, the term local void fraction is used to describe the percentage of gas present in the smallest measurement volume possible for a given diagnostic technique, which in fact represents a small volume averaged quantity. Additionally, the void fractions discussed above can be considered on a time averaged, or instantaneous basis.

The difficulty in analytically evaluating the void distribution for a system undergoing phase change is complicated by the lack of thermodynamic equilibrium between the phases (both the internal energy and momentum of each phase can be different). In general experimentally based correlations are used to evaluate the void fraction in terms of the mass quality, flow, fluid temperature and pressure. These correlations will be discussed in Chapter 2.

The distribution of vapor in two-phase systems is known as the local void distribution and is qualitatively described using flow patterns, or flow regimes. The flow patterns observed in vertical and horizontal flow are shown in Figure 1.2 and 1.3 respectively. In vertical flow, the pattern is quasi-symmetric about the centerline of the flow channel with deviations resulting from surface waves or droplet transport. For low qualities, the flow distribution is bubbly, with small vapor bubbles dispersed throughout the liquid phase. At higher qualities, small bubbles may coalesce and form vapor slugs with a size almost equal to the channel diameter. For higher quality flow the vapor velocity is high and tends to force the remaining liquid to the walls, resulting in an annular type flow pattern. During annular flow, the liquid-vapor interface may become unstable and interfacial waves are produced. These waves can break to form liquid droplets which become entrained in the gas core. At lower flow rates and moderate qualities, two subtypes of the annular regime can result. Wispy-annular is characterized by heavy liquid entrainment in the gas core of annular flow. Churn flow occurs where the time averaged liquid velocity remains positive, but the instantaneous value oscillates so that at some positions the liquid flow periodically reverses. Under some very high heat flux conditions and low flow rates, a vapor film may form on the liquid surface while the core of the flow remains liquid. This flow regime is referred to as inverted annular flow.

The horizontal void distribution patterns are also shown in Figure 1.3, but due to gravitational forces the flow patterns tend to stratify with heavier liquid on the bottom of the channel. At low qualities, the flow pattern is bubbly but due to buoyancy effects, the bubbles tend to flow mainly in the top portion of the tube. As the quality increases, the bubbles tend to coalesce into vapor plugs. At low flow rates and large qualities, the flow tends to completely stratify into a liquid and vapor layer which is know as stratified flow. For increased velocities the gas-liquid interface may become unstable and wavy flow results. At higher velocities these waves may completely span the width of the channel forming liquid slugs traveling at velocities that can damage system components. Similar to the vertical flow case, at high qualities the vapor inertia tends to force the liquid toward the wall forming annular flow.

Figure 1.4a shows a typical vertical channel undergoing boiling heat transfer with subcooled liquid entering the bottom of the heated channel. For distances z, from the heated section inlet less than z_{ONB}, the heat transferred from the walls to the liquid is not sufficient to initiate boiling and the flow is single phase. At z_{ONB}, nucleate boiling is initiated and subcooled boiling occurs in the wall region. The bubbles produced are very small and collapse back into liquid as they are cooled by bulk subcooled liquid. The void fraction in this regime is small, and primarily in the wall region. As more thermal energy is transferred, the bulk fluid temperature increases and more vapor is generated near the wall. For increased fluid temperatures the amount of vapor in the main flow increases and bubble agglomeration may begin. As more vapor is generated and bubbles begin to coalesce, intermittent slug or churn flow develops. The vapor velocity increases until annular flow results where the liquid is forced to the wall by the faster moving vapor. During this phase, heat is not transferred from the wall through nucleate boiling, but through direct evaporation at the liquid vapor interface. Furthermore, liquid droplets entrained in the gas core also can significantly contribute to the heat transfer. Eventually all the liquid in the wall region is evaporated resulting in wall dryout. Under sufficiently high heat fluxes, bubbles in the wall region may be of sufficient size for the wall to dryout and the flow regime may pass directly from nucleate boiling to film boiling at the wall for both vertical or horizontal orientations. At these high heat fluxes, the flow regime would be inverted annular and such a transition involves large increases in the wall temperature leading to a burnout condition. Severe damage to system components can result during this heat transfer mode.

A similar system is shown in Figure 1.4b for horizontal flow boiling in a channel. Due to gravitational effects, the void distribution is no longer symmetric and void tends to concentrate at the top of the pipe. Under horizontal flow conditions, gravitational effects may cause premature dryout at the top of the pipe due to vapor-liquid stratification.

Heat transfer results are often expressed as boiling curves showing the relationship between the wall temperature, liquid saturation temperature, and wall heat flux. Figure 1.5 shows a typical boiling curve schematic. Under single phase flow conditions, the convective heat transfer coefficient changes only slightly with temperature so that the heat flux approximately increases linearly with increasing wall temperature. Eventually the liquid temperature or wall heat flux increases sufficiently so that boiling may initiate at the heated wall; a phenomena that is know as the onset of nucleate boiling (ONB). During nucleate boiling, the increased flow mixing along with the vaporization process cause a substantial increase in the heat transfer coefficient at a given wall temperature. This is represented in Figure 1.4 as an increase in the slope of the heat flux versus wall temperature curve. If the bulk flow remains subcooled, the intense turbulence caused by bubble creation and collapse is the most significant heat transfer mechanism. The fluid inlet temperature and flow rate do not significantly affect the heat transfer performance compared to the enhanced boiling turbulence effect, so that the slope of the boiling curves are similar during the initial stages of subcooled boiling. As the heat flux is increased further, the bulk liquid subcooling decreases until vapor bubbles no longer collapse and the system begins to again show mass flow and fluid temperature effects. At high heat flux levels, the wall temperature may greatly increase with only a small change in the operating heat flux, a condition know as the critical heat flux (CHF). The large increases in wall temperature associated with CHF can often exceed the channel material thermal limits, and lead to local melting of the test section known as burn-out.

It is possible to predict the equilibrium thermodynamic quality for saturated flow entering a channel using;

$$x = \frac{q''A}{\dot{m}\ \lambda_{fg}} \tag{1.9}$$

where A is the heat transfer area, q" is the heat flux, m is the mass flow rate, and λ_{fg} is the latent heat of vaporization. For a subcooled system, the equilibrium quality can be established using a modified form of the above;

$$x = \frac{\left(q''A - \dot{m}C_p\Delta T_{sub}\right)}{\dot{m}\lambda_{fg}} \tag{1.10}$$

where ΔT_{sub} is the liquid subcooling. However, the void fraction for this system cannot be predicted accurately from the quality shown in equation 1.10, because the vapor-liquid mixture is not in thermodynamic equilibrium. Therefore, correlations are required that relate the thermodynamic quality to the void fraction. Typical void-quality relationships are provided in

Chapter 2.

As the complexity of the two-phase modeling increases, the techniques require detailed void distribution measurements. The void distribution can have direct consequences on the heat transfer, pressure drops and in some cases the safety of a system. For example, excessive quantities of vapor near a surface can suppress heat transfer and cause significant increases in the local surface temperature and reduce the CHF. Accurate measurements of the void fraction are important so that void/quality relationships are established which adequately represent the two-phase phenomena. There are many void fraction measurement techniques available including optical, conductivity, capacitance, and ultrasonic probes, along with penetrating radiation techniques such as gamma attenuation, neutron radiography and X-Ray tomography. These methods will be further described in Chapter 2.

1.5 VOID DISTRIBUTION IN TWO-PHASE FLOW ANALYSIS

Until the recent advances in computational power, the solution of the full set of conservation equations for each phase in a flow system was not practical. These conservation laws were often simplified using spatial and/or time averaging.

One typical two-phase averaging technique involves treating the flow as an equivalent single phase system know as a homogenous formulation. For this formulation, the spatial and time dimensions are averaged so that the result is a one-dimensional steady-flow approximation. The liquid and vapor phase velocities are assumed equal and the distribution of flow is well mixed. The fluid properties are based on averages of the liquid and gas phases, for example the mixture viscosity from Dukler et al.[5] is;

$$\frac{\mu}{\rho} = x\frac{\mu_v}{\rho_v} + (1-x)\frac{\mu_l}{\rho_l} \tag{1.11}$$

where ρ represents the average density, given as;

$$\frac{1}{\rho} = \frac{x}{\rho_v} + \frac{1-x}{\rho_l} \tag{1.12}$$

Using this formulation, the cross-sectional averaged void fraction can be calculated as;

$$\alpha = \frac{x/\rho_v}{x/\rho_v + (1-x)/\rho_l} \tag{1.13}$$

where x is the thermodynamic mass quality.

An accurate, but more complex, representation of the two-phase flow can be achieved using a separated flow model such as the drift flux[6] formulation that allows unequal phase velocities. This method assumes that the velocity of the vapor and liquid phases can be related through some slip relationship between the phases. For example, the drift velocity between vapor and liquid phases can be expressed as;

$$j = \frac{\overline{u}_v}{\alpha} - \frac{\overline{u}_l}{(1-\alpha)} \tag{1.14}$$

where $\overline{u_v}$ and $\overline{u_l}$ are the vapor and liquid superficial velocities (defined as the liquid or vapor phase flow rate divided by the total flow area) respectively and α is the cross sectional averaged void fraction. With this definition the cross sectional average void fraction can be calculated as;

$$\alpha = \frac{\overline{u}_v - \overline{j}}{C_0 u_t} \tag{1.15}$$

where C_o is an experimentally determined constant that depends on the void distribution, velocity and acceleration, and u_t is the total flow rate . Until recently, accurate local void distribution measurements were not available and C_o was determined through experimental correlation for a given geometry based on system variables such as the flow rate, pressure and temperature. This semi-complex formulation demonstrates the need for flow distribution measurements to support the predictive techniques.

With the speed and accuracy of numerical computations, it has recently become possible to solve a separated flow model based on the individual mass, momentum and energy conservation equations for each phase. Ishii[3] has shown the cross-sectional averaged mass, momentum and energy equations for the vapor phase to be;

Mass

$$\frac{\partial}{\partial t}\langle \alpha\rho_v \rangle + \frac{\partial}{\partial z}\langle \alpha\rho_v u_v \rangle = \Gamma \qquad 1.16$$

where Γ is the interfacial mass transfer.

Momentum

$$\frac{\partial}{\partial t}\langle \alpha\rho_v u_v \rangle + \frac{\partial}{\partial z}\langle \alpha\rho_v u_v^2 \rangle + \alpha\frac{\partial P}{\partial z} = F_i + F_w \qquad 1.17$$

where F_i and F_w are the interfacial and wall momentum transfer respectively.

Energy

$$\frac{\partial}{\partial t}\langle\alpha\rho_v i_v\rangle+\frac{\partial}{\partial z}\langle\alpha\rho_v u_v i_v\rangle+\left\langle\alpha u_z\frac{\partial P}{\partial z}\right\rangle=q_i+q_w+q_{vd}+q_{gen} \qquad 1.18$$

where i is the internal energy and q_i, q_w, q_{vd} and q_{gen} are the interfacial energy transfer, wall energy transfer, viscous dissipation and internal energy generation terms respectively.

A similar set of equations can be written for the liquid phase producing a system of six equations in seven unknowns (α, u_l, u_v, i_l, i_v, P_l, P_v). In its full form, these partial differential equations are highly nonlinear, coupled, time dependent and three-dimensional. As previously mentioned, time and space averaging is used to simplify the computational complexity. This process of averaging requires introduction of flow distribution parameters based on experimental results[3]. For example, during volume averaging of the momentum conservation equation, an averaged term may be approximated as;

$$\langle\alpha u\rangle\equiv C_o\langle\alpha\rangle\langle u\rangle \qquad 1.19$$

where C_o is a distribution parameter used to convert the average of a product into a product of averages. This type of volume averaging of the conservation equations has simplified the governing equations but introduced a parameter that has to be modeled based on the distribution of vapor in the system. To determine C_o experimentally, detailed information is required on the liquid-vapor distribution and velocities.

Additionally these equations require approximations for the interfacial transfer of mass, momentum and energy as well as properties and boundary conditions at the interfaces(jump conditions). To model the interfacial transfer of these parameters, a typical approach is to use;

$$\text{Interfacial Transfer}\propto F_d\times\left[A_i\right] \qquad 1.20$$

where F_d is the interfacial driving force (depending on the mechanism involved) and A_i is the interfacial area concentration; a direct function of the void distribution, velocity and acceleration. Experimental information is required for numerical closure in the form of three-dimensional knowledge of the void behavior as a function of time. For example, Donevski et al.[7] have reviewed the interfacial transfer predictive methods for inverted annular flow for incorporation into Equation 1.20.

In summary, the above predictive techniques all require a-priori knowledge of the void distribution, velocity and acceleration.

The focus of this thesis is the use of advanced penetrating radiation techniques to obtain the void distribution in a flow boiling channel and to demonstrate its importance in the understanding of flow boiling phenomena. The application of RTNR and advanced HS-XCT as complementary devices for understanding flow boiling phenomena has not been systematically investigated in the past. The present RTNR system can provide detailed axial and cross sectional information on the void distribution at a rate of 33ms per frame. Incident neutrons on the test section penetrate the tube and are attenuated by the liquid more than the gas phases. The radiation that is not attenuated by the two-phase flow, projects on a neutron-to-photon convertor and the resultant image is captured on a low-light level video recorder. HS-XCT uses a concentric ring of X-Ray sources and detectors to measure the local void fraction in a cross-section at a specified axial location. The present study was capable of capturing local void fractions at a speed of 0.5 ms per slice. These systems were used on two separate flow boiling geometries, smooth and twisted tape generated swirl flow, in order to demonstrate the techniques and their effectiveness for void distribution measurement. Using these methods in combination with heat transfer and pressure drop information, the importance of local void distribution information is also examined.

1.6 INTERACTIONS BETWEEN RADIATION AND MATTER

Neutron radiography is the process of using the radiation attenuation characteristics to determine an objects structure or composition. The radiation beam can interact with matter in several ways;

- Scattering - the interaction with matter that can result in a change of direction and momentum of the radiation. Initial scattering events tend to reduce the intensity of the radiation beam but as multiple collisions take place, some radiation can be scattered back into the beam. This scattering back into the beam is known as build-up.
- Absorption - the process where radiation is absorbed into the matter and usually excites the material on an atomic level or can transmute individual atoms into different isotopes which may or may not be stable.
- Transmission - the radiation beam passes through the object without interaction.

Radiography is a non-intrusive technique for measuring the density distribution by inserting a recording device on the opposite side of the incident radiation beam. Most medical and industrial radiography uses photographic film that is exposed by an attenuated beam (such as in dental X-Ray radiographs). The transmitted and build-up portions of the beam strike the recording device that can later be used to reconstruct the density distribution of the object. Radiation transmission can be approximated as;

$$\frac{I}{I_o} = B\, e^{-\Sigma_w^t y_w}\, e^{-\Sigma_l^t y_l}\, e^{-\Sigma_v^t y_v} \qquad 1.21$$

where B is the build-up factor to account for back-scatter into the detector, Σ is the thermal neutron cross section, y is the path length and the subscripts w, l, and v correspond to the wall, liquid and vapor regions respectively. Table 1.2 shows typical magnitudes for the attenuation constant of some materials. The neutron cross section is typically very small for most vapor phases; so the last exponential term can be removed for most neutron radiographic measurements. An advantage of Neutron radiography over X-Rays is that Neutrons are attenuated less by metallic materials, making it a valuable measurement technique for high temperature and pressure flows, or for reacting or toxic flows, where metal-walled tubes are often required.

In typical medical radiographs, incident X-Ray radiation is passed through the object of interest and transmitted radiation is used to expose X-Ray film that is then developed using conventional techniques. Typical single exposure radiographic images provide two-dimensional distribution information in a plane orthogonal to the object that are based on total attenuation along the path of the beam.

Neutron radiography uses a neutron beam incident on an object. Unlike X-Rays that are approximately attenuated by the electron content in a substance, neutrons are efficiently attenuated by the hydrogen atoms in a substance[8]. Hence, neutron radiography is an excellent technique for imaging objects located inside metal containers such as aluminum and steel because these materials are virtually transparent to neutrons, and for looking at phase distributions due to the changes in density from the liquid to vapor phases. However, the weak interactions of neutrons with film require special considerations. A large amount of industrial neutron radiographic techniques usually use;

a) Direct methods - a convertor screen is used near traditional X-Ray film[9]. This screen converts neutrons into X-Rays or electrons that are used for film exposure. In some cases, the low neutron to photon conversion rates can be offset by using image intensifier screens that increase the film exposure per generated photon.

b) Indirect or transfer methods - a transfer screen is used in place of the X-Ray film. The transfer screen consists of materials which absorb neutrons to produce radioactive isotopes. The screen is exposed for a period of time then transferred separately to a photographic plate. The decay of the activated isotopes produces photons that expose the film.

1.7 OVERVIEW

This thesis presents the application and results of two insitu methods for void distribution measurement applied to flow-boiling of refrigerant under normal (smooth-flow) and enhanced(swirl-flow) heat-transfer configurations. An extensive literature review of flow-boiling phenomena and void measurement techniques is presented in Chapter 2; with relevant correlations and equations summarized in tabular form at the end of the chapter. Chapter 3 describes Real Time Neutron Radiography and high speed X-Ray Computed Tomography void measurement facilities as well as the flow boiling test apparatus, diagnostics and test sections used. The theoretical aspects and analysis used to measure the void distribution are discussed in Chapter 4. Heat Transfer and pressure drop characteristics are presented in Chapter 5 for smooth and swirl-flow boiling conditions. The cross sectional and time averaged void fraction measurement using RTNR are shown in Chapter 6 for smooth-flow boiling. Chapter 6 also shows the instantaneous and local void distribution results and discusses their impact on the heat transfer performance. The comparison of smooth and swirl-flow boiling void distribution measurements is presented in Chapter 7. This Chapter shows the effects of internal twisted tape generated swirl-flow on the averaged and local void distribution and also discusses the effects of mass flux, inlet subcooling and system pressure on the results. Chapter 8 and 9 present the conclusions of this work and recommendations for future work respectively. Appendix A shows the fluid properties used in the analysis of the experimental results while

Appendix B shows the RTNR void distribution measurements of a simulated APWR fuel bundle assembly. The instrument calibration information is contained in Appendix C while the uncertainty in cross sectional averaged void and local void distribution RTNR measurements is discussed in Appendix D. The computer data acquisition system used to monitor flow loop diagnostics is shown in Appendix E. Appendix F contains a summary of the contributions to knowledge resulting from this work.

Table 1.2 Typical Radiation Attenuation Coefficients for Common Materials

Material	Total Neutron Cross Section (Σ^n) [cm^{-1}]	Total X-Ray Cross Section (Σ^x) [cm^{-1}]
H	0.002	0.000
Be	0.865	0.242
F	20	0.000
Cl	0.003	0.000
C	0.385	0.340
Na	0.115	0.152
Al	0.099	0.459
Fe	1.150	2.930
Ni	2.020	3.960
Cu	0.937	4.100
Water - H_2O	3.450	0.171
Heavy Water - D_2O	0.449	0.170
Refrigerant 134a (CF_3CH_2F)	0.732	Not applicable
Refrigerant 123 (CF_3-$CHCl_2$)	Not applicable	0.114

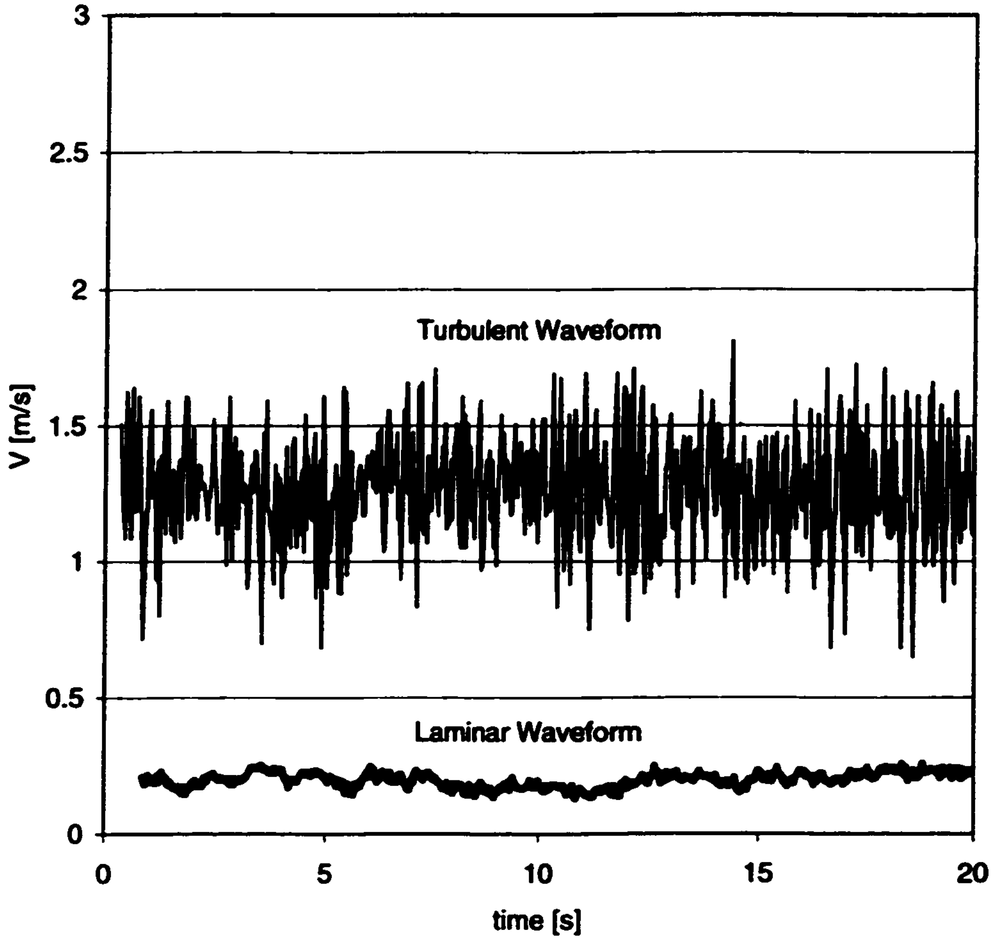

Figure 1.1 The Effect of Turbulence on Typical Velocity Waveforms

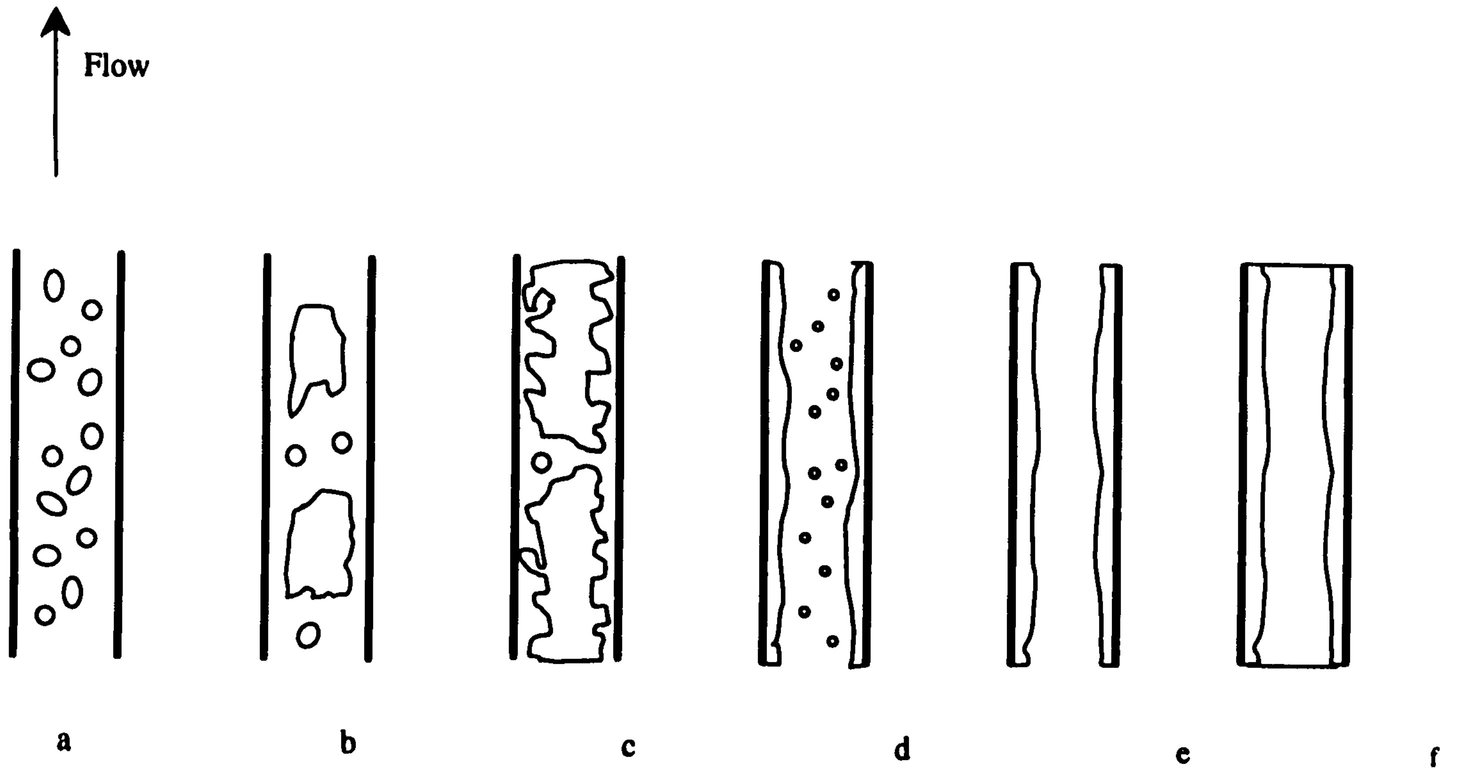

Figure 1.2 Schematic of Flow Regimes Observed in Vertical Co-current Flow (a. *Bubbly Flow*, b. *Slug Flow*, c. *Churn Flow*, d. *Wispy Annular (Mist-Annular)*, e. *Annular*, f. *Inverted Annular*).

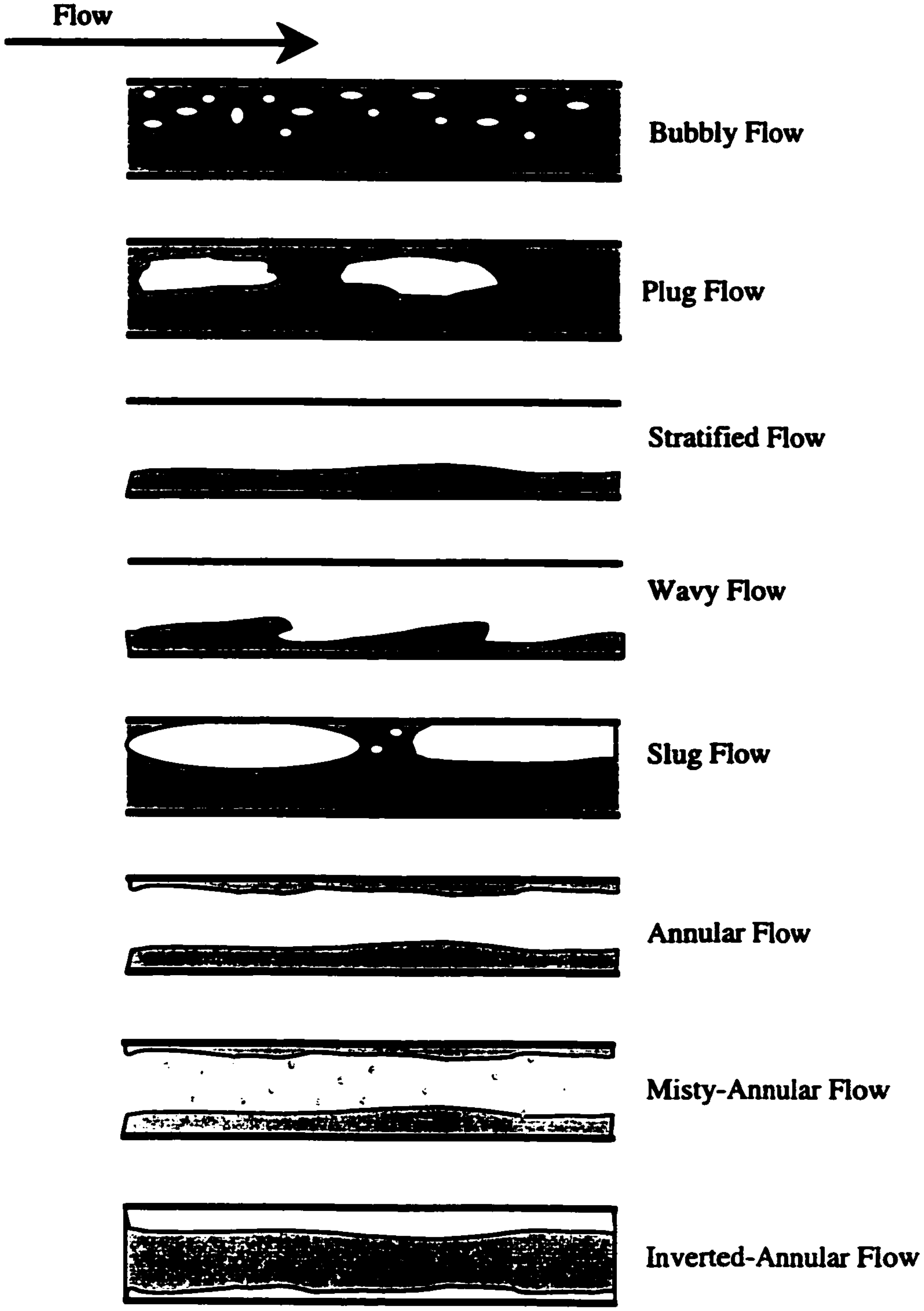

Figure 1.3 Typical Two-phase Flow Distributions for Horizontal Co-Current Flow.

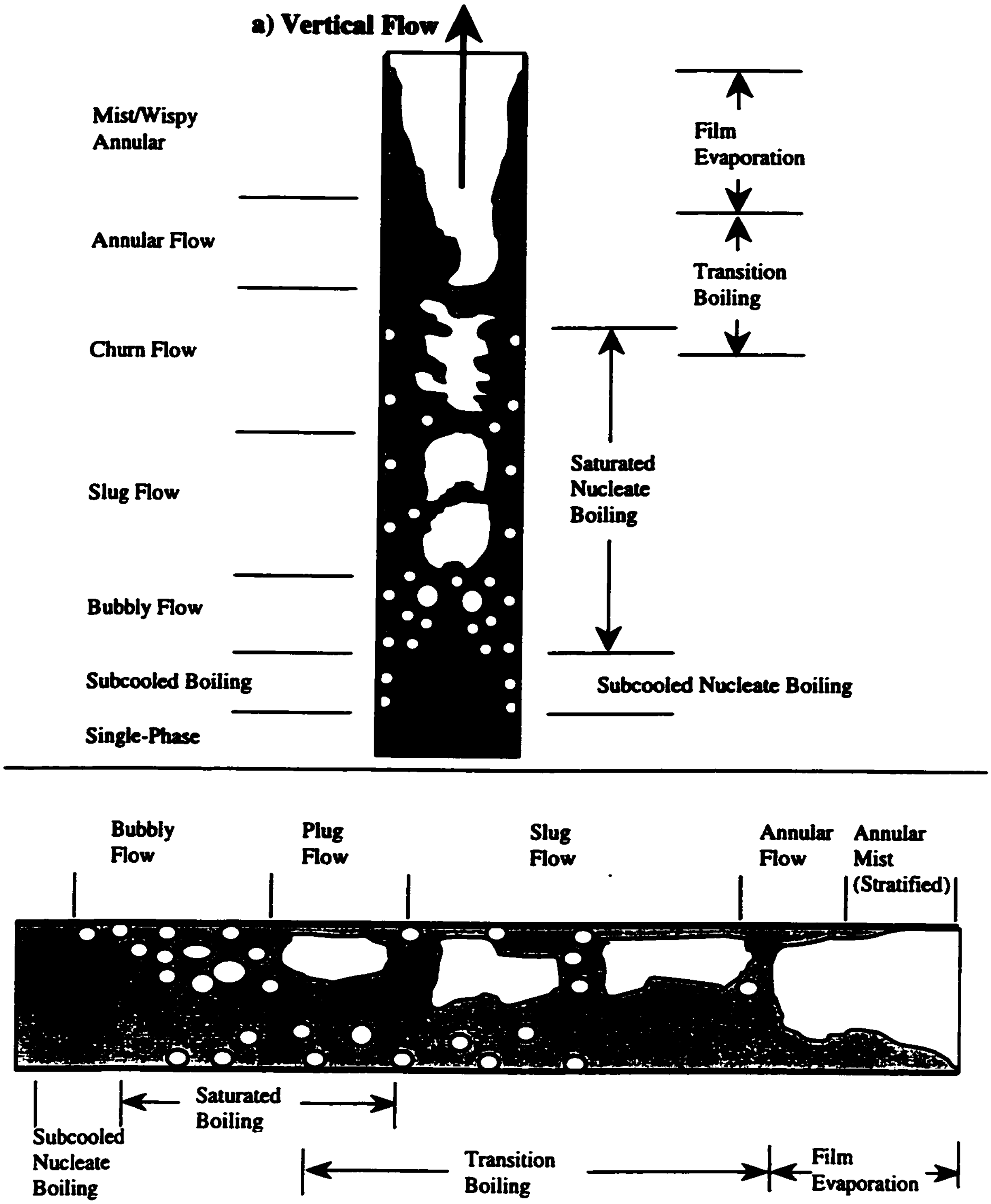

Figure 1.4 Schematic Representation of Flow Boiling Phenomena for a) Vertical and b) Horizontal Configurations.

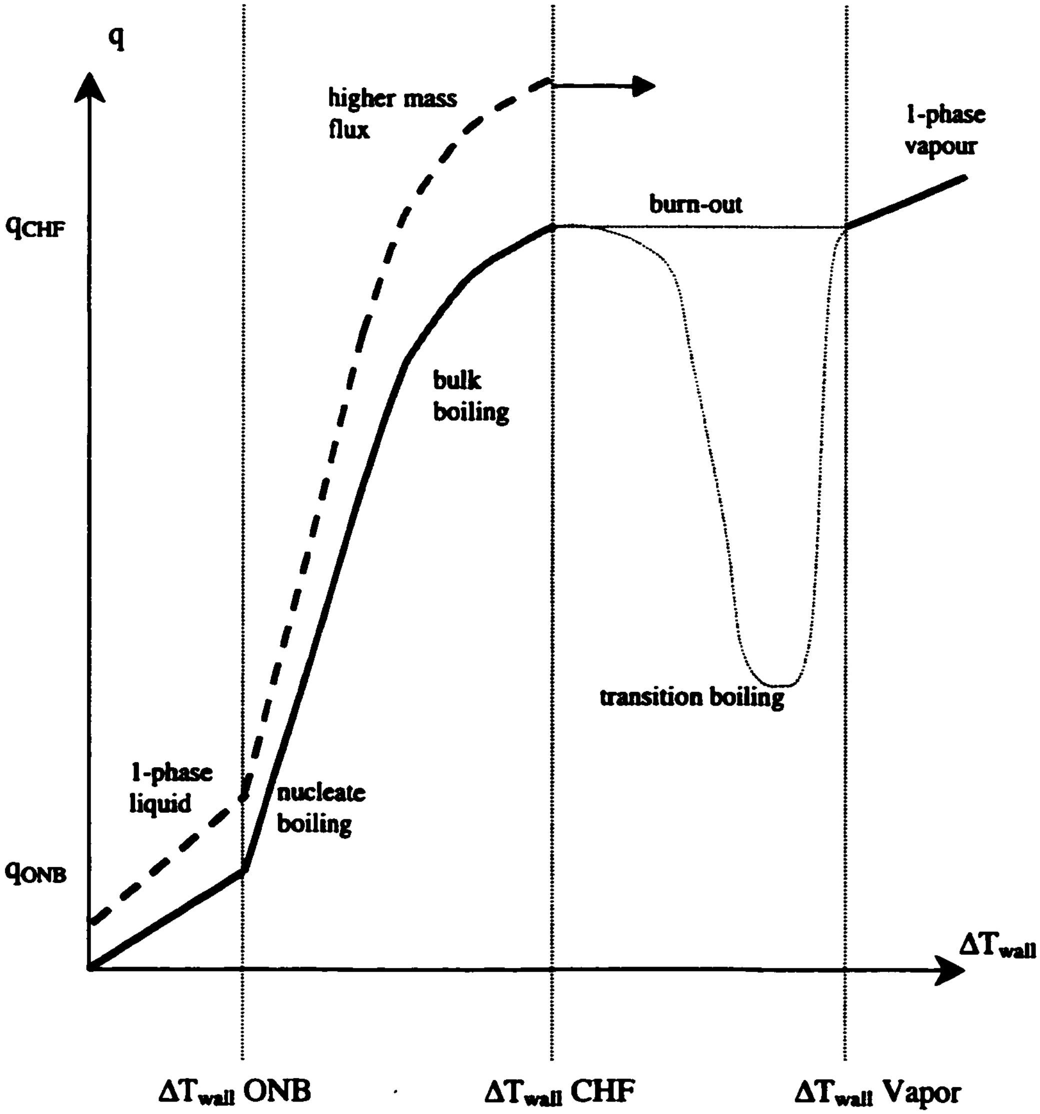

Figure 1.5 Typical Flow Boiling Curve

CHAPTER 2 LITERATURE REVIEW OF FLOW BOILING AND VOID DISTRIBUTION MEASUREMENT

2.1 SINGLE PHASE FLOW

2.1.1 Single Phase Flow

The topic of single phase heat transfer has been studied both experimentally and theoretically for a long period of time. A common method for correlating turbulent pipe flow heat transfer is;

$$\mathrm{Nu} = c\,\mathrm{Re}^{m}\,\mathrm{Pr}^{n} \qquad 2.1$$

where Nu, Re and Pr are the Nusselt, Reynolds and Prandtl numbers respectively. One of most widely used correlations was from Dittus and Boelter[10];

$$Nu = 0.027 Re^{0.8} Pr^{n} \tag*{2.2}$$

where n is 0.3 or 0.4 for cooling and heating respectively. However, Allen and Eckert[11] have shown that this type of correlation is only accurate provided c, m and n do not change significantly over the range of Reynolds and Prandtl numbers. They have shown that the exponent m may vary from 0.79 to 0.92 over the range $10^4 < Re < 5\times10^6$.

Simultaneous solution of the momentum and energy equations based on constant heat flux and wall shear stress assumptions was first proposed by Deissler[12]. Petukhov[13] summarized both semi-theoretical and empirical correlations for turbulent heat transfer to liquids and gases in pipes. This study also integrated the momentum and energy conservation equations and produced the correlation for Reynolds numbers between 10^4 and 5×10^5 with Prandtl numbers between 0.5 and 2000 given as;

$$Nu = \frac{\left(f/8\right) Re\, Pr}{K_1 + K_2 \left(f/8\right)^{0.5} \left(Pr^{0.66} - 1\right)} \tag*{2.3}$$

where f is the friction factor and K_1 and K_2 are linear functions of the friction factor and Prandtl number respectively. This correlation was based on constant wall heat flux assumptions but can be applied to many constant wall temperature systems if the Prandtl and Reynolds numbers are greater than 0.7 and 10^4 respectively. Gnielinski[14] modified this correlation to account for transition between laminar and transition flow to;

$$Nu = \frac{\left(\frac{f}{8}\right)\left(Re - 1000\right) Pr}{1 + 12.7\left(\frac{f}{8}\right)^{0.5} \left(Pr^{0.66} - 1\right)} \tag*{2.4}$$

The effect of large temperature and property gradients on heat transfer to a fluid was examined by Karman[15]. Sieder and Tate[16] attempted to account for the variation in viscosity using the ratio;

$$\frac{Nu}{Nu_0} = \left(\frac{\mu_b}{\mu_w}\right)^n \qquad 2.5$$

where Nu_0 is the Nusselt number calculated using constant viscosity correlations, n is the viscosity exponent, and μ_b and μ_w are the fluid viscosities evaluated at the bulk liquid and wall temperatures respectively. Kreith and Summerfield[17] have shown that the viscosity exponent of 0.14 given by Sieder and Tate is too large. Their study recommends 0.11 and 0.25 for heating and cooling of liquids respectively. The study by Petukhov[13] also included the thermal effects on viscosity and its contribution to the pressure drop and heat transfer.

Table 2.1 summarizes the correlations and range of conditions for single-phase heat transfer prediction.

2.1.2 Single Phase Pressure Drop

The pressure drop due to shear forces generated at the tube wall to liquid interface for a single phase system is critical in assessing the pumping requirements. The prediction of single phase pressure drop based on first principles is limited to only a few special flow systems and geometries. The most common method for predicting the single-phase pressure drop, ΔP, through internal passages is the use of the Darcy friction factor correlation scheme as follows;

$$\frac{\Delta P}{\rho} = f\left(\frac{L}{D}\right)\left(\frac{V^2}{2}\right) \qquad 2.6$$

where L is the channel length, D is the diameter, V is the velocity and f is the friction factor which is a function of the Reynolds number and channel surface conditions. Moody[18] correlated a large number of experimental results in graphical form as shown in Figure 2.1, where e is the characteristic roughness height of the wall and D is the tube hydraulic diameter. Blausius[18] proposed a correlation for turbulent pipe flow pressure drop covering Reynolds numbers up to 10^5. A widely quoted correlation for an adiabatic internal flow pressure drop is the iteratively based Colebrook[18] correlation. Petukhov[13] proposed a similar correlation which does not need to be solved iteratively.

For heated systems, the effect of temperature gradients on fluid properties such as viscosity can be significant. For example, the viscosity of saturated water can change by a factor of 10 between 20 and 120 °C. Sieder and Tate[16] have also proposed a correlation similar to their heat transfer multiplier. However, Petukhov[13] found the exponent provided by Sieder and Tate overestimated the single phase pressure drop. Under high heat flux conditions Novog et al.[19] observed that the correlations from Colebrook predicted high heat flux single-phase pressure drop to within 25%.

Table 2.2 summarizes the available correlations for single phase pressure drop along with the applicable range for each.

2.2 TWO-PHASE FLOW

The basic concepts of flow-boiling prediction were outlined in Chapter 1 and indicated a need for constitutive relationships that can be used to estimate void behavior and two-phase system performance. The Martinelli[6] parameter is often used to characterize two phase flows and is defined as;

$$X = \left(\frac{ \left. {}^{dP}\!/\!_{dz} \right|_l }{ \left. {}^{dP}\!/\!_{dz} \right|_v } \right)^{0.5} \qquad 2.7$$

where the subscripts l and v represent the pressure drop from the liquid and vapor phases respectively. It provides the ratio of the liquid to vapor pressure drop in a two-phase flowing system. If the flow in both phases is turbulent, using the Blausius correlation for each phase gives;

$$X_{tt} = \left(\frac{\rho_v}{\rho_l} \right)^{0.5} \left(\frac{\mu_l}{\mu_v} \right)^{1.25} \left(\frac{1-x}{x} \right)^{0.875} \qquad 2.8$$

where x is the quality, μ is the viscosity and ρ is the density. The Martinelli parameter is often used to establish experimental correlations for void fraction, distribution, heat transfer and pressure drop because it is a non-dimensional quantity[20].

2.2.1 Two Phase Flow-Regime

Flow regime maps, based on experimental observations, are used to predict the phasic distribution in two-phase flow through vertical and horizontal channels. Taitel and Dukler[21] used mechanistic models for flow regime transitions and produced a map which compares favorably to a wide range of conditions[22]. This flow regime map is shown in Figure 2.2a[23] and 2.2b[24] for vertical and horizontal configurations respectively in terms of the liquid superficial (defined as the velocity if the flow in the pipe was only the liquid phase) and gas superficial velocities. Several authors including Baker[25] and Mandhane et al.[26] have produced horizontal flow regime maps based on large amounts of visual observations. A more thorough correlation method was adopted by Taitel and Dukler[27] using semi-empirical models for predicting the flow regime transitions along with the Martinelli parameter. An extension of these mechanistic-based transition maps was produced by Harvel et al.[28] to include the effect of a hexagonal array of tubes on vertical flow regime transitions.

2.2.2 Two-phase Flow Boiling Heat Transfer

The difficulty in predicting two-phase heat transfer and pressure drop have been outlined by Westwater[29] and Tong[30]. The inherent coupling of mass, momentum and energy transfer, as well as the presence of large property variations makes the evaluation of two-phase systems very difficult, and often prohibitive. The mixture and separated flow models shown in Chapter 1 are often employed to numerically predict the flow-boiling behavior over a range of conditions, but require constitutive relationships describing the mass, momentum, and energy transfer between the phases, and to/from the wall. Furthermore, macro-scale quantities such as ONB, OSV and CHF are often modeled empirically based on experimental results. Recently, the excellent review paper by Spindler[31] covers the correlations recommended for empirically predicting ONB, heat transfer, pressure drop and CHF under tube-side flow boiling.

2.2.3 Onset of Nucleate Boiling / Onset of Significant Void

The prediction of ONB or OSV in heat transport systems is critical for determining other system variables such as heat transfer, void fraction and two-phase pressure drop. Many investigations have shown that boiling initiates at small micro-cavities on a heated surface that contain small pockets of vapour. These vapour pockets allow nucleation to take place at much lower temperatures than is possible on a completely smooth surface with no micro-cavities[21]. Harvey et al.[32] and Knapp[33] have shown that eliminating any trapped gas through the use of high pressure liquid pretreatment, increases the required ONB superheat. These studies show the ONB heat flux increases significantly as the pretest static liquid pressure treatment (for trapped vapour removal) was increased. Further support of the micro-cavity mechanism for nucleation is apparent from the investigation by Corty and Foust[34] which showed that the heat required to initiate ONB decreased as a surface was roughened using emery paper. Cole[35] provided a summary of analytical methods for predicting homogenous and heterogeneous boiling in fluids, as well as further evidence that nucleation begins at existing gas-liquid interfaces located in small micro-cavities on a surface. Cole's review also predicted analytically that poorly wetting liquid to metal combinations should have lower ONB conditions than well-wet surfaces. A Refrigerant 134a test on an Inconel surface by Novog et al.[36] have provided experimental evidence that highly wetting fluids require larger heat fluxes to initiate ONB.

The semi-theoretical model proposed by Hsu[37] provides quantitative information on the range of nucleation site sizes that can be thermodynamically active at a prescribed certain wall superheat. Using a linear temperature profile, this model also shows that there is some minimum wall superheat below which no nucleation can occur. Hsu established the ONB condition based on thermodynamic relations and assumptions on the near wall temperature and bubble profiles. Sato and Matsumura[38] have also studied a similar mechanism for ONB in water.

Bergles and Rohsenow[41] modified Hsu[37] formulation to account for forced convective effects for predicting the ONB in water. They solved the resulting equations using a graphical technique and correlated their results for the ONB heat flux in terms of the wall superheat and system pressure. Bergles and Rohsenow also argued that most commercial surfaces have a wide range of cavity sizes that are potential nucleation sites. Davis and Anderson[39] solved these equations analytically for the same range of conditions and developed a correlation for water based on fluid properties, wall superheat and system pressure. This correlation reduces to that of Bergles and Rohsenow or Sato and Matsumura using appropriate simplifications to account for their assumptions. These results were extended by Frost and Dzakowic[40] for other fluids by including the Prandtl number effects on nucleation phenomena. ONB and subcooled boiling heat transfer have been studied by Bergles and Rohsenow[41] for low to moderate heat fluxes and by Yin et al.[42] and Novog et al.[19] for high heat flux conditions. These results show that under low to moderate heat fluxes and low subcooling, the Davis and Anderson[39] correlations most accurately predicts ONB, but under high heat flux and subcooling, it can significantly under predict the required superheat.

Table 2.3 summarizes selected major ONB correlations presented above.

2.2.4 Nucleate Boiling Heat Transfer

The mechanism for flow boiling heat transfer was originally attributed to the following;

- Latent Heat Transport - the energy required to vaporize a unit mass of a liquid. The energy removal is through heat energy being used to convert liquid into vapor.
- Bubble departure - as a vapor bubble is created, eventually the flow or buoyancy effects cause the bubble to depart from the surface. Colder liquid replaces the area originally occupied by the vapor bubble.
- Turbulent creation/collapse - as bubbles are created at the wall and collapsing in the subcooled bulk fluid, large wall turbulence is created, increasing the heat transfer.

The complexity of these forces and their interaction with the main flow field makes the study of nucleate boiling heat transfer very complicated. In most cases, predictive methods rely on experimentally based correlations.

Shah`s[43] correlation for subcooled boiling heat transfer divides the total heat transfer, q into two components;

$$q = q_c + q_{nb} \tag{2.9}$$

where q_c and q_{nb} are the single phase convective and nucleate boiling contributions to the total heat transfer. Kutateladze[44] has proposed a correlation where the effects of nucleate boiling do not contribute linearly to the overall heat transfer. The forced convective flow may partially suppress nucleate pool boiling according to;

$$\frac{h_{tp}}{h_c} = \left[1 + \left(\frac{h_{pb}}{h_c}\right)^2\right]^{1/2} \qquad 2.10$$

where h_{tp}, h_c and h_{pb} are the two-phase, single phase forced convective and pool boiling heat transfer coefficients respectively.

Many empirical correlations have been developed based on specific fluid systems. A widely quoted nucleate boiling correlation was proposed by Jens and Lottes[45] for subcooled boiling of water. High heat flux experiments using different wall materials were investigated by DelValle and Kenning[46]. They studied boiling water at atmospheric conditions and their results showed a strong liquid quenching effect immediately after bubble departure. However, the authors also state that the flow-regime has no effect on heat transfer and that wall material thickness strongly affects heat transfer, which is contrary to most other experimental evidence.

More recently, correlations for high heat flux subcooled boiling heat transfer to water have been developed by Yin et al.[41] and Novog[47] . These correlations cover highly subcooled boiling conditions under vertical and horizontal flow conditions respectively. Percupile et al.[48] have produced a similar correlation for refrigerant 11, 12, and 113 subcooled flow boiling. The application of two-phase cooling, pressure drop and CHF to nuclear fusion reactors has been reviewed by Yin et al.[49] and Celata[50].

Both the studies of Rohsenow and Clark[51] and Kolev[52] show that the effect of latent heat transport on the total heat transfer coefficient is typically small, and that most heat transfer enhancements result from bubble induced turbulence. Kolev has also shown that the variation in nucleate boiling heat transfer data obtained by different authors may be due to surface wetting phenomena. Forster and Zuber[53] have determined that the number of activate nucleation site cavities is highly dependent on the heat flux. Further evidence that the nucleate boiling heat transfer mechanism is predominantly a turbulence promotion phenomena (due to bubble creation and collapse) was provided by Gunther[54]. The semi-empirical correlation developed by Nishikawa and Fujita[55] also demonstrates that the stirring force caused by bubble creation has a much stronger effect than latent heat transport. However, the complexity of their correlation and the number of empirical constants required in many cases does not justify its use. Contrary to the above, Bankoff and Miksel[56] have concluded that latent heat transport through vaporization at the heated surface and condensation at the surface of the bubble projecting out of the laminar sublayer may contribute significantly to the overall heat transfer for lower flow rates and high subcooling levels.

Bubble boundary layer measurements were used to develop a correlation by Jiji and Clark[57] in terms of subcooling, mass flux, heat flux and distance from the location of ONB. This work concludes that the increase in a bubble boundary layer thickness is primarily the result of an increase in bubble size.

The presence and distribution of vapor in a liquid flow field can either enhance or hinder the heat transfer performance. Depending on its distribution, vapor may increase the flow turbulence and hence increase the heat transfer or it may hinder liquid movement near the heat transfer surface or even cover the surface entirely. As a secondary effect, two-phase pressure drop may cause changes in the system flow rate which impact on the system's ability to remove heat. A summary of the common predictive techniques for subcooled boiling is located in Table 2.4. These correlations rely on purely empirical formulations and do not consider void or void distribution information, because this type of information was unavailable until recent advancements in void measurement. Because of this the applicability of these correlations beyond their basis conditions and geometries is not recommended.

2.2.5 Swirl Flow Effects

For forced convective systems, heat transfer enhancement devices are often utilized to increase the total heat transfer per unit area of equipment. In most cases, heat transfer enhancement devices will also cause an increase in system pressure drop. Bhatia et al.[58] investigated this relationship using both coiled wires and twisted tapes and showed that both turbulence promoters caused significant increases in pressure drop. Further investigation by Kumar and Judd[59] further developed coiled wire turbulence promoters and examined their effect on heat transfer and pressure drop.

Under single-phase conditions, internal twisted tape inserts are often used to enhance heat transfer performance. The effect of the twisted tape is to cause the flow to move in a helical, or swirl pattern as it travels through the tube. This flow swirling causes the following effects[60];

- Increased bulk-flow turbulence, as the presence of the twisted tape disturbs the flow and increases bulk fluid mixing.
- Increased effective heat transfer area, as fluid traveling in a helical pattern must travel a farther distance than non-swirling flow.
- Increase in the wall tangential component, as the flow velocity now has an additional component which disturbs the boundary layer near the wall and enhances heat transfer[61].

Furthermore, the twisted tape may act as a fin, conducting heat from the tube walls to the center of the flow channel.

Lopina and Bergles[62] have studied heat transfer and pressure drop under a wide range of single-phase conditions for water. Their correlation is commonly used in the design and analysis of many single-phase swirl-flow systems. The effect of high viscosity fluids was examined by Marmer and Bergles[63], and Wantanabe et al.[64] have examined the optimization of twisted tape generated swirl-flow under single-phase conditions.

Two-phase flow through channels with internal twisted tapes is affected by mechanisms similar to those described for smooth-flow. However, centrifugal acceleration may cause cooler (heavy) fluid to flow to the wall while vapor is forced to the center of the tube[59]. This can potentially affect the phase distribution in the channel and thus can change the heat transfer and pressure drop characteristics.

The heat transfer enhancement under swirl-flow for single-phase liquid with moderate heat fluxes has been investigated by Gambill et al.[65] and Lopina and Bergles[62]. The former showed a significant mass flux effect during boiling swirl-flow which may be due to flow distribution effects. Gambill[66] has also investigated the effect of heat generation inside the twisted tape, not in the tube wall as in most other studies. These results imply that centrifugal forces tend to concentrate the vapor near the twisted tape and hinder heat transfer in this region. Correlations for heat transfer and pressure drop have also been developed based on semi-analytical techniques by Smithberg and Landis[67]. Lopina and Bergles[68] and Cumo et al.[69] have shown that during low quality subcooled boiling, the heat transfer augmentation is not significant compared to the nucleation heat transfer enhancement. Recently Novog et al.[19] have studied highly subcooled water heat transfer under high heat flux conditions and have also shown the contributions of swirl-flow are negligible during nucleate boiling at low qualities.

For swirl-flow boiling at higher qualities, Gambill[70] has shown that vapor tends to be transported to the tube center. This behavior increases CHF margins and results in larger heat transfer coefficients due to liquid flow toward the tube wall. Jensen and Bensler[71] have studied the effect of swirl-flow on the heat transfer coefficient for high quality, saturated flow conditions. Their results show that the heat transfer increases with decreasing twist ratio and increasing quality and pressure. They also recommend the use of the Chen correlation for saturated boiling using the hydraulic diameter and modifications to account for the increase in wall velocity. However, the void distribution and the effect of centrifugal forces caused by rotation of the two-phase mixture have not been studied sufficiently. The void distribution during swirl-flow is important in understanding this effect and this work examines this behavior for both horizontal and vertical flows. High quality heat transfer and pressure drop behavior of two-phase swirl flow has also been studied by Agrawal et al.[72, 73]. They propose that the heat transfer enhancement caused by swirl-flow during high quality boiling is a function of the twist ratio, the Boiling and Reynolds numbers, where the Boiling number is defined as:

$$Bo = \frac{q}{G\,h_{fg}} \qquad 2.11$$

where q is the heat flux, G is the mass flux and h_{fg} is the latent heat of vaporization. Their results agree well with published data at lower exit qualities but deviate significantly at higher qualities.

Swirl-effects on steam condensation have been investigated by Royal and Bergles[74], but much less data is available compared to the boiling case. Their results indicate an increase in the heat transfer coefficient of up to 130% compared to smooth-tubes. They have also correlated their results in terms of the additional tangential, fin and surface area effects.

Laminar heat transfer under swirl-flow conditions has also been studied by Manglik and Bergles[75] and Plessis and Kroger[76]. These studies provide numerical analysis of swirl-flow using boundary layer formulations and show that the transition to turbulent flow takes place at much lower Reynolds numbers compared to the smooth flow case.

2.3 VOID DISTRIBUTION MEASUREMENT TECHNIQUES

As described in Chapter 1, a critical parameter in any flow-boiling system is the distribution of void in the channel. For example, the averaging techniques used to solve the conservation equations introduce the need for a-priori knowledge of the flow distribution in a channel. The size, velocity, and area of the void produced significantly affects the boundary and interfacial transfer of mass, momentum and energy. Measurement techniques must be further developed that can measure both the instantaneous and time-averaged distribution of the void in multiple spatial dimensions.

2.3.1 Electrostatic/Impedance Devices

Fluid and vapor thermodynamic property differences such as the dielectric strength, make it possible to measure void fractions based on electronic measurement of capacitance or impedance. An external ring-type capacitance transducer was developed by Chang et al.[77] who found that the capacitance response in stratified and annular flow was not significantly affected over a 80 °C temperature range. Cimorelli and Evangelisti[78] used a shell and tube heat exchanger configuration with the shell and tube as electrodes. Auracher and Daubert[79] have developed specialized capacitance probes based on numerical techniques which provide linear response of the device over the entire range of void fractions in air-water two-phase flow. Their experiments showed excellent agreement with theoretical predictions and an almost linear void fraction to capacitance response. The application of many capacitance probes can be used to construct tomographic cross sections as demonstrated by Huang et al.[80] and Chang et al.[81] although Huang et al. suggested that a limit to the number of probes prevented fine spatial resolution. Thorough reviews of reconstruction techniques using this method were published by Oyvind[82] and Barber[83].

Huahun and Chuanjing[84] have studied DC conductance probes and given qualitative methods for predicting the flow regime based on output voltage waveforms. This method was accurately used to predict the flow pattern in horizontal and helical flow, but it was intrusive and did not provide quantitative information on the void fraction or distribution. Andreussi et al.[85] have studied volume averaged void fraction measurement using conductance probes while Ishii and Revankar[86] have studied the application of this technique to local void distribution measurement. A tomographic system was developed by Klug and Mayinger[87] using an array of probes placed circumferentially around the test section.

2.3.2 X-Ray Tomography

Tomographic images are mathematical reconstructions based on 360° X-Ray attenuation data that provide cross-sectional information on the density distribution in a given object. The basic principle of tomography is shown in Figure 2.4. By measuring the attenuation of X-Rays through an object at various angular positions the density distribution can be calculated using an appropriate algorithm. A columnated or fan-shaped beam of radiation is passed through an object and the transmitted radiation is measured on the opposite side. The process is repeated at several angular locations around the object providing an array of transmission data for each angular location. The cross-sectional density distribution is calculated using this information and computed tomography routines outlined by Brooks and DiChiro[88]. For Figure 2.4, detectors D and C would detect zero void thickness, while detector B would measure a longer void path length than detector A.

Conventional X-Ray Computed Tomography (XCT) devices use a series of rotating sources and detectors to obtain detailed cross sectional (slice) information. These machines use low powered X-Ray tubes and semiconductor detectors to achieve scanning times on the order of one second per slice. For two-phase flow applications, higher powered X-Ray tubes are required to penetrate metal test sections and the time scales involved require scanning times of less than 1 ms per slice. The historical development of high speed X-Ray computed tomography is shown in Figure 2.5. An early summary of high speed computed tomography visualization of two-phase flow was conducted by Narabayashi et al.[89] and application to high temperature and pressure flow-systems was studied by Narabayashi et al.[90].

The development of high speed tomography for two-phase diagnostics has been reported by Hori et al.[91]. This system is based on stationary detector and X-Ray arrays arranged 360° around the test section to reduce the scanning time. An advanced ultra high speed XCT scanner has been developed for two-phase flow by Hori et al. [92, 93] for void distribution measurement and medical imaging using Cadmium Telluride detectors[94]. These next generation XCT scanners are capable of 0.5 ms per cross section that make them ideal for void distribution measurement. Validation of XCT and RTNR experimental results for two-component two-phase flow in an annulus channel has been performed by Harvel et al.[113] on a system capable of 4.5 ms per cross sectional slice, and good agreement was obtained for both the local and cross sectional averaged void fraction. One disadvantage of the XCT systems is that they only provide information at one axial location, preventing the measurement of void velocity and bubble length and the application to thick or heavily attenuating metal channels is difficult.

2.3.3 Other Techniques

The propagation, transmission and reflection of ultrasonic waves have also been used extensively to measure void fraction distribution in two-phase flow. Chang and Morala[95] have used ultrasonic methods to measure the void fraction, distribution and interfacial area concentration using ultrasonic techniques on air-water two-component flows. The application of pulse-echo for transient interfacial characteristics measurement has been examined by

Matikainen et al.[96]. Whitehouse et. al.[97] have used the Doppler shift to measure the fluid velocity while a separate transducer was used in conjunction with the first to obtain vapor fraction and bubble velocities.

Differential attenuation of radiation based on density and material differences by counting total transmitted radiation has also been applied to void fraction measurement and is known as densitometry. Annunziato et al.[98] have studied the streaming and dynamic errors involved in the application of single beam densitometers to two-phase flow systems. The critical parameters in gamma-densitometry were discussed by Chan and Banerjee[99] for small diameter pipes with air-water flow. Measurement of nucleate boiling void fraction using X-Rays and gamma-rays was conducted by Edelman and Elias[100], and predicted their measurement error as 5%. Results from these experiments showed agreement with empirical correlations to ±25%. Fung and Groeneveld[101] showed the linear response of a 3-beam gamma-ray void detector for plastic flow-regime simulators and measured subcooled and film boiling cross sectional averaged void fractions. The use of several gamma beams and multi-spectrum energy sources has been applied by Pan and Hewitt[102] for three-phase flow distribution measurement. Oyedele[103] has examined the effect of radiation beam transients on densitometry methods and found that this can significantly affect the void measurement error. Lynch and Segal have applied Nuclear Magnetic Resonance techniques for void measurements up to a pipe diameter of 16mm with an accuracy of 1%. This system was also capable of simultaneously measuring liquid and gas phase velocities along with void distribution details.

The techniques of hot thermocouples, optical probes, hot film anemometers and acoustic noise monitoring were compared by Palazzi and Savelli[104] for low pressure air-water systems. For low-pressure systems, Augousti et al.[105] have developed an inexpensive optical fiber technique capable of measuring liquid levels with an accuracy of 3.5%. The effect of surface tension, wettability and probe puncturing bubbles in optical fiber measurement techniques has been studied by Cartellier[106]. More recently, Bakshi et al.[107] have presented advanced signal processing techniques that allow more information to be extracted from probe measurements using wavelet signal processing. These optical techniques show reasonable void fraction measurement accuracy, but the intrusive nature has many undesirable effects.

2.3.4 Real Time Neutron Radiography Void Distribution Measurement

The principle of Neutron Radiography for two-phase flow parameter measurements relies on the differential absorption and scattering of thermal neutrons between liquid and gaseous phases. Advancements in neutron to photon convertors and low light-level video have led to the development of Real Time Neutron Radiography[108, 109]. The application of Real Time Neutron Radiography for two-phase flow diagnostics has been demonstrated by Carlisle et al.[110], Dance and Corollo[111], and Takanaka et al.[112].

Harvel[113] has compared air/water (two-component and two-phase flow) RTNR results to high speed X-Ray tomography experiments for several geometries using an air injection apparatus and a water column, and the same RTNR facilities as those described in Chapter 3. The void reconstruction technique used a single calibration factor β to account for system responses and requires input on the geometry of the test section in the form of the maximum neutron path length. The void reconstruction techniques provided in Chapter 4 were developed to remove the dependency of the measurements on the calibration constant and the need for specific geometry information. The geometries studied included:

- pipe flow,
- annular,
- MAPLE and CANDU type simulated fuel elements.

The void reconstruction for each geometry required separate calibration factors and geometry information. The pipe flow results used a static liquid column with air injection from the bottom of the test section. Harvel et al. compared the void fraction calculated based on liquid column level change, and ultra-sonic measurements, to RTNR void fractions and showed excellent agreement up to void fractions of 20%. The annular flow RTNR measurements were compared to high-speed XCT and optical observations. The flow regime map presented shows that all three methods show good agreement, but the transition regimes show small deviations, which may have resulted from changes in the experimental apparatus as each test was performed in a different facility. The comparison of annular experiments shows that the cross sectional averaged void fraction measured using RTNR and XCT experiments agreed within 20% over the range of void fractions tested (0 to 20%). The simulated nuclear fuel channels studied included a vertical (MAPLE type) and horizontal (37-element CANDU type) test sections. Flow regimes based on RTNR measurements were presented along with the axial void distribution. The majority of nuclear fuel simulations in this work covered only intermittent flow regimes. These two-component two-phase air-water flows under isothermal conditions provided excellent results on RTNR applications. A comparison of optical or radiographic-based flow imaging systems was presented by Beck et al.[114] for air water and showed similar agreement to the above.

The measurement of two-phase flow interfacial area using RTNR has been demonstrated by Chang and Harvel[115]. The effect of flow distribution on the measurement of two-phase properties using RTNR have been investigated by Harvel et al. for bubbly[116] and annular[117] flow regimes. The studies used a bubble column with air-water, two-phase flows and the RTNR camera and beam port as described in Chapter 3. The bubbly-flow results showed that the cross sectional averaged void fraction varied by approximately 2% over a 250 ms period, which is characteristic of a bubbly flow pattern.

High speed RTNR imaging of two-phase flow has also been studied by Hibiki et al. [118,119]. They showed the analytical limits for neutron radiography resolution as a function of neutron flux at the detector. For a system with neutron flux of the order 10^6 and frame rate of

250 frames per second, the maximum resolvable object size is 1mm. To resolve the same object size at 1000 frames per second, a neutron flux of approximately 10^7 neutrons/cm^2-s is required.

Hibiki et al.[120] have presented state-of-the-art RTNR techniques using optimized scintillators, image intensifiers and high speed camera with a neutron flux of 10^8 n/cm^{2}s for measurement of bubble rise velocities. The L/D (length from aperture to object divided by the aperture diameter) of this system was approximately 153. The intermittent slug velocities were calculated by inspection using the relative distance traveled by the bubble leading edge. This technique is used in Chapters 6 and 7 to measure bubble velocities as a function of flow rates and inlet subcoolings. The imaging speed of this system also allowed the study of interfacial waves during annular liquid film flow. The void fraction of these annular films varied by up to 20% over a 66 ms sampling time. The authors goal was to demonstrate as many flow regimes as possible, and hence no detailed phasic flows or experimental conditions are provided. Further demonstration of high frame rate RTNR techniques using a pulsed neutron beam have been presented for air-water flows by Robinson and Wang[121].

Uchimura et al [122] have shown that advanced image processing techniques can reduce the cross sectional averaged void measurement uncertainty to ±4%, using the same equipment described in Chapter 3. Their technique used a variety of image processing filters to reduce noise and equalize image intensities before void calculation. This equalization of the intensities was necessary to account for differences in RTNR camera sensitivities from the camera center to the outside edge.

The theoretical aspects of neutron radiography have been investigated by Osuwa[123]. This work used non-dimensional analysis to predict the reduction in sharpness at physical discontinuities of an object. These prediction techniques were extended by Wyman[124] to model neutronic behavior during radiographic processes using Monte Carlo methods and showed that neutron scattering tends to decrease the overall image sharpness in a nonlinear fashion. The scatter also resulted in some build-up effect which decreases contrast with the increasing material in the neutron beam.

Mishima and Hibiki[125] have performed a detailed qualification of static, real time, and high speed RTNR. This work quantifies the frame speed limitations resulting from the convertor time constant, video recording system and the statistical behavior of neutron to material interactions. In addition to this, Mishima and Hibiki quantify the errors involved in the transformation of image intensity to void fraction; including the effect of geometry. They present the effect of imaging speed and neutron interaction on error. For a 3 mm channel where the neutron to liquid interaction is small (i.e. low neutron cross section liquids), the error in high-speed transient void measurements may be as large as 50%. For strongly interacting liquids the error in transient void measurement when the imaging frame rate is slower than the void velocity is a maximum of 14% and 10% for rectangular ducts and round channels respectively. Mishima and Hibiki also show that the error in the time averaged void fraction decreases with an increasing number of averaged frames. For example, the error can be reduced from 8% to 4% by increasing the number of averaging frames from 10 to 100, but further averaging does not reduce the error significantly.

2.4 VOID FRACTION CORRELATIONS

The void fraction is of primary importance in determining both the heat transfer and pressure drop in a two-phase system. The mass quality can be calculated based on the conservation of energy in the channel. However, during flow boiling the void fraction cannot be derived from the mass quality because thermodynamic equilibrium between the phases does not exist in the system (i.e the phases may have differing momentum and/or internal energy).

The homogeneous model described in Chapter 1 uses single velocities and properties to represent both phases. Clearly if the phases are at unequal temperatures or velocities, then this method is not applicable. Wallis[126] developed a model based on separated cylinders, similar to annular flow, which has been applied to many non-annular flow situations[6]. The interaction of these phases in this model is limited but it in general provides more accurate results than the homogenous model. The correlation developed by Zivi [127] is often used for simple pipe flow boiling of water.

Lockhart and Martinelli[128] developed a method that was used to correlate two-phase pressure drop and void fraction data based on graphical representation. For turbulent liquid and vapor flow Martinelli and Nelson[129] adapted the above method into analytical form and applied it over a range of pressures for water and steam flow. Thom[130] published a correlation based on the water data for a wide range of temperatures. The results of an extensive study on two-phase pressure drop and quality by Baroczy[131], produced a graphical solution method based on complex curves. These works have been summarized by Butterworth[132] and shown to have the form;

$$\alpha = \left[1 + B\left(\frac{1-x}{x}\right)^{n1}\left(\frac{\rho_v}{\rho_l}\right)^{n2}\left(\frac{\mu_l}{\mu_v}\right)^{n3}\right] \qquad 2.12$$

where the constants B, n1, n2 and n3 are given in Table 2.5 for some common correlations. These correlations relate the void fraction to the thermodynamic quality which can be computed based on a system heat balance. The void fraction can then be used to predict the flow regime in the system and hence the two-phase performance can be assessed. Furthermore, the void fraction is a critical parameter in the conservation equations shown in Equations 1.17

to 1.19, and hence must be known a priori. Additionally, most two-phase pressure drop calculations require the void fraction to assess the two-phase contribution to the overall pressure drop.

The effect of large subcooling on the void fraction has not been sufficiently studied. During this type of boiling, only a very small amount of vapor is generated at a heated wall. This vapor collapses as it departs the wall region due to the large subcooling of the bulk liquid. Under highly subcooled flow boiling, Griffith et al.[133] have proposed a correlation based on the assumption that the bubbles are confined to a thin layer near the wall region. For moderate subcooling, Kroger and Zuber[134] proposed a model for average void fractions similar to Equation 2.12 but modified to account for void condensation in the bulk fluid.

The prediction of Refrigerant 134a void fractions has been presented by Abdul-Razzak et al.[135]. This work also presented a correlation for the drift flux and flow regime map. An extensive study on the measurement of two-phase mass flow rate using turbine and orifice-meters in conjunction with void measurements has been presented by Abdul-Razzak et al.[136] [137] [138]. These works also compared ring-type capacitance-meters to gamma-densitometer measurements and show good agreement across the range of test conditions.

Table 2.1 Single -Phase Heat Transfer Correlations

Author	Correlation	Notes
Dittus and Boelter[10]	$\mathrm{Nu} = 0.027\,\mathrm{Re}^{0.8}\,\mathrm{Pr}^{0.4}$	Turbulent heat transfer
Sieder and Tate[16]	$\frac{\mathrm{Nu}}{\mathrm{Nu}_o} = \left(\frac{\mu_b}{\mu_w}\right)^{0.14}$	Thermal Property Gradient Effects
Kreith and Summerfield[17]	$\frac{\mathrm{Nu}}{\mathrm{Nu}_o} = \left(\frac{\mu_b}{\mu_w}\right)^{n}$	$n = 0.11$ heating $n = 0.25$ cooling
Petukhov[13]	$\mathrm{Nu} = \frac{(f/8)\mathrm{Re}\,\mathrm{Pr}}{K_1 + K_2 (f/8)^{0.5}(\mathrm{Pr}^{0.66} - 1)}$ $f = (1.82\log(\mathrm{Re}) - 1.64)^{-2}$ $K_1 = 1 + 3.4f$ $K_2 = 11.7 + 1.8\mathrm{Pr}^{-0.33}$	$1\times10^4 < \mathrm{Re} < 5\times10^6$ $0.5 < \mathrm{Pr} < 2000$
Gnielinski[14]	$\mathrm{Nu} = \frac{\left(\frac{f}{8}\right)(\mathrm{Re} - 1000)\mathrm{Pr}}{1 + 12.7\left(\frac{f}{8}\right)^{0.5}(\mathrm{Pr}^{0.66} - 1)}$	$2300 < \mathrm{Re} < 5\times10^6$ $0.5 < \mathrm{Pr} < 2000$

Table 2.2 Single-Phase Pressure Drop Correlations.

Author	Correlation	Notes
Moody[18]	Figure 2.1	graphical method
Blausius[18]	$f = \dfrac{0.3164}{\mathrm{Re}^{0.25}}$	$\mathrm{Re} < 10^5$
Colebrook[18]	$\dfrac{1}{f^{0.5}} = -2\log\left(\dfrac{1}{3.7}\dfrac{\varepsilon}{D} + \dfrac{2.51}{\mathrm{Re}\, f^{0.5}}\right)$	$\mathrm{Re} < 10^8$
Sieder and Tate[16]	$\dfrac{f}{f_o} = \left(\dfrac{\mu_b}{\mu_w}\right)^{0.14}$	Heated Section
Petukhov[13]	$\dfrac{f}{f_0} = \dfrac{1}{6}\left(7 - \dfrac{\mu_b}{\mu_w}\right)$ *heating* $\dfrac{f}{f_0} = \left(\dfrac{\mu_b}{\mu_w}\right)^{0.24}$ *cooling*	Heated Section

Table 2.3 ONB Correlations.

Author	Correlation	Notes
Bergles and Rohsenow[41]	$q_{onb} = 15.6\left(\Delta T_{sat}\right)^{2.3/0.0234P}$	Water 101 < P < 13800 kPa
Davis and Anderson[39]	$q_{onb} = \frac{k_l \lambda_{fg} \rho_g}{8 \sigma T_{sat}} \left(\Delta T_{sat}\right)^2$	Water 101 < P < 13800 kPa
Frost and Dzakowic[40]	$q_{onb} = \frac{k_l \lambda_{fg}}{8 \sigma T_{sat}} \left(\frac{1}{\rho_g} - \frac{1}{\rho_l}\right) \left(\frac{\Delta T_{sat}}{\mathrm{Pr}_l}\right)$	Includes Pr effect.

Table 2.4 Nucleate Flow Boiling Heat Transfer Correlations

Author	Correlation	Application
Nishikawa and Fujita[55]	$\frac{hL}{k_l} = fnc\left(d_b, Re_b, L_{stir}, Gr, P, ...\right)$	Nucleate Boiling, Graphical
Shah[43]	$\psi = \frac{h_{TP}}{h_c} = \psi_o + \frac{\Delta T_{sub}}{\Delta T_{wall}}$; $Bo = q/G\lambda_g$ $\psi_0 = 230\,Bo^{1/2} \quad \psi_o > 1$ $\psi_o = 1 \quad \psi_o < 1$	Subcooled Boiling $Re > 2300$ $200 < G < 87000$ kg/m²s $0.01 < q < 22.9$ MW/m²
Kutateladze[44]	$\frac{h_{tp}}{h_c} = \left[1 + \left(\frac{h_{pb}}{h_c}\right)^2\right]^{1/2}$	Forced convection partially suppresses pool boiling
Jens and Lottes[45]	$\Delta T_{sat} = 25\,q^{0.25} e^{-P/62}$	Water; $q < 12.5$ MW/m² $11 < G < 10400$ kg/m²s $0.7 < P < 17.2$ MPa
Novog[18, 19]	$\Delta T_{sat} = 21.5\,\phi^{0.6}\,e^{-\frac{P}{8.7}}$	Water; $0 < q < 11$ MW/m² $50 < \Delta T_{sub} < 150$ °C
Yin et al.[41]	$\Delta T_{sat} = 7.195\phi\left(\frac{1}{L}\right)^{1.82} P^{-0.072}$	Water; $5 < q < 16$ MW/m² $30 < \Delta T_{sub} < 150$ °C
Percupile et al.[48]	$\Delta T_{sat} = 2.28\left(\rho_l/\rho_g\right)^{-0.25} q^{0.3} D^{0.6}$	R-11,12; $143 < P < 960$ kPa $14.7 < q < 102$ kW/m²
Thom[130]	$\Delta T_{sat} = 25.0\,\phi^{0.25}\,e^{-\frac{P}{62}}$	Water; $q < 1.6$ MW/m² $20 < \Delta T_{sub} < 200$ °C

Table 2.5 Void Quality Constants for Equation 1.12. (Compiled from Reference 132)

Correlation or Model	B	n1	n2	n3
Homogeneous Model	1	1	1	0
Zivi model	1	1	0.67	0
Wallis Model	1	0.72	0.4	0.08
Lockhart and Martinelli correlation	0.28	0.64	0.36	0.07
Thom correlation	1	1	0.89	0.18
Baroczy correlation	1	0.74	0.65	0.13

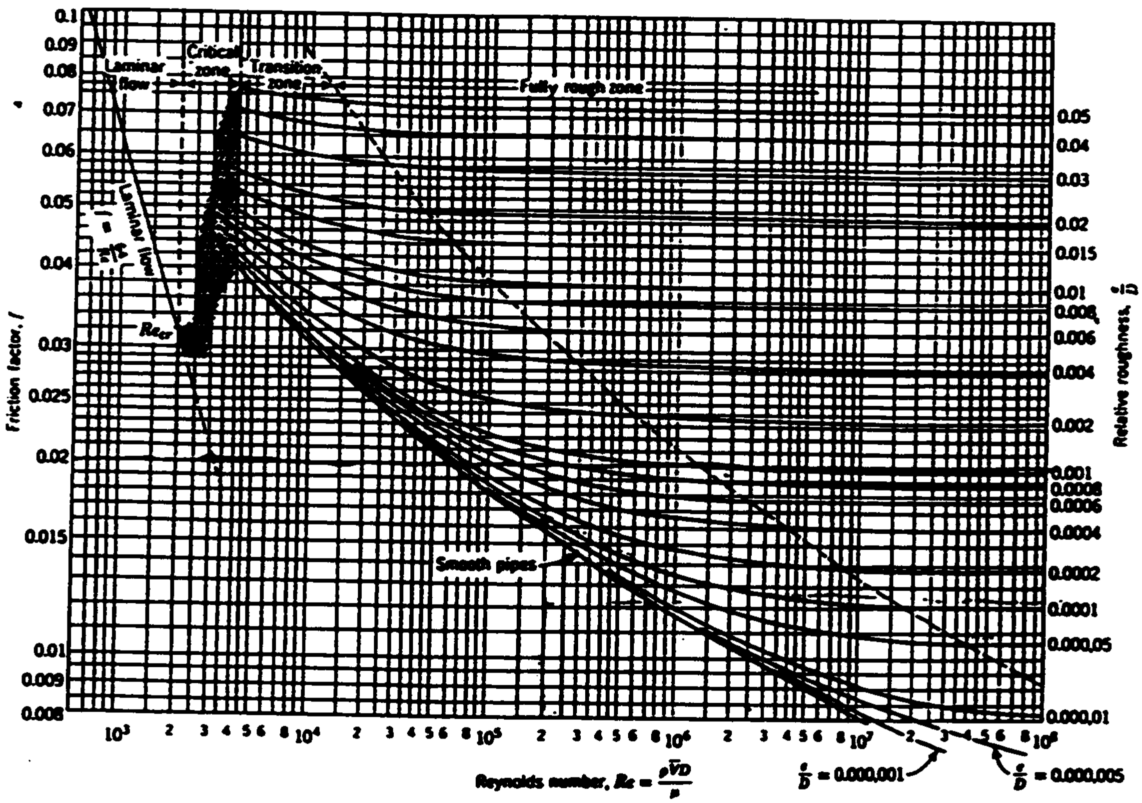

Figure 2.1 Moody Diagram for Predicting Single-Phase Friction Factor (Fox and McDonald)

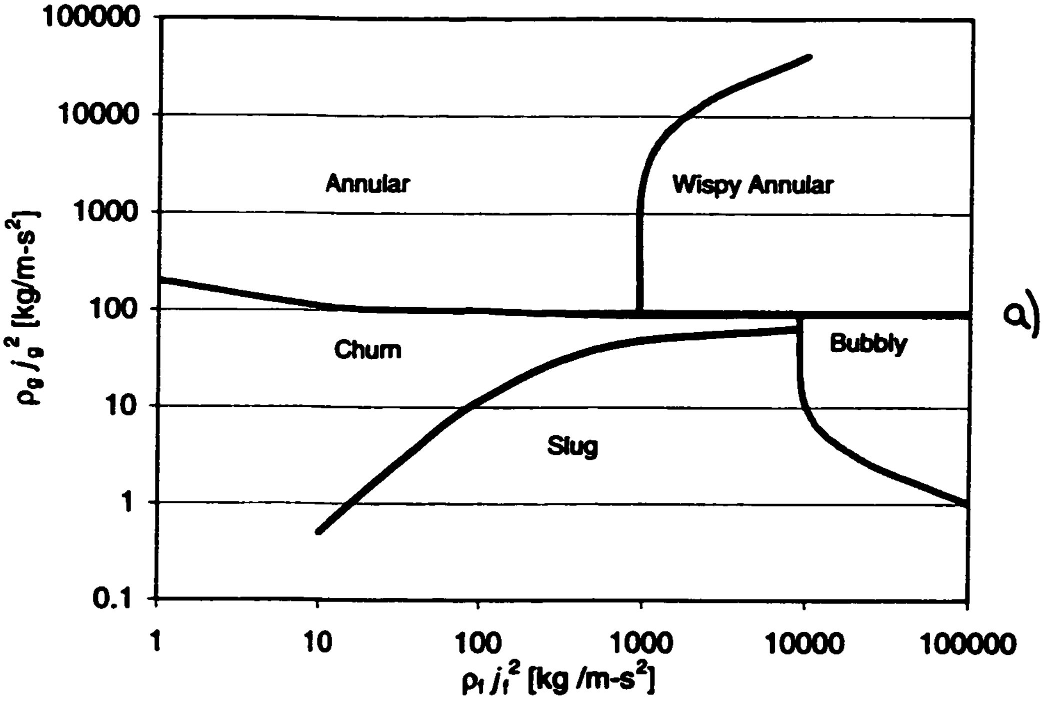

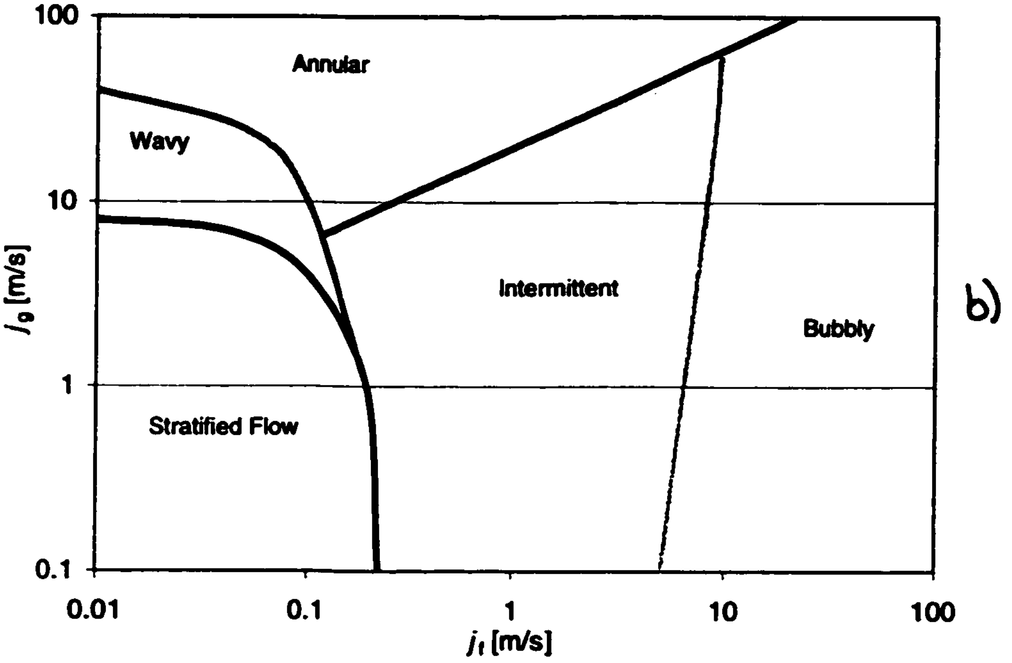

Figure 2.2 Flow Regime Maps for a) Vertical and b) Horizontal Two-Phase Flow.

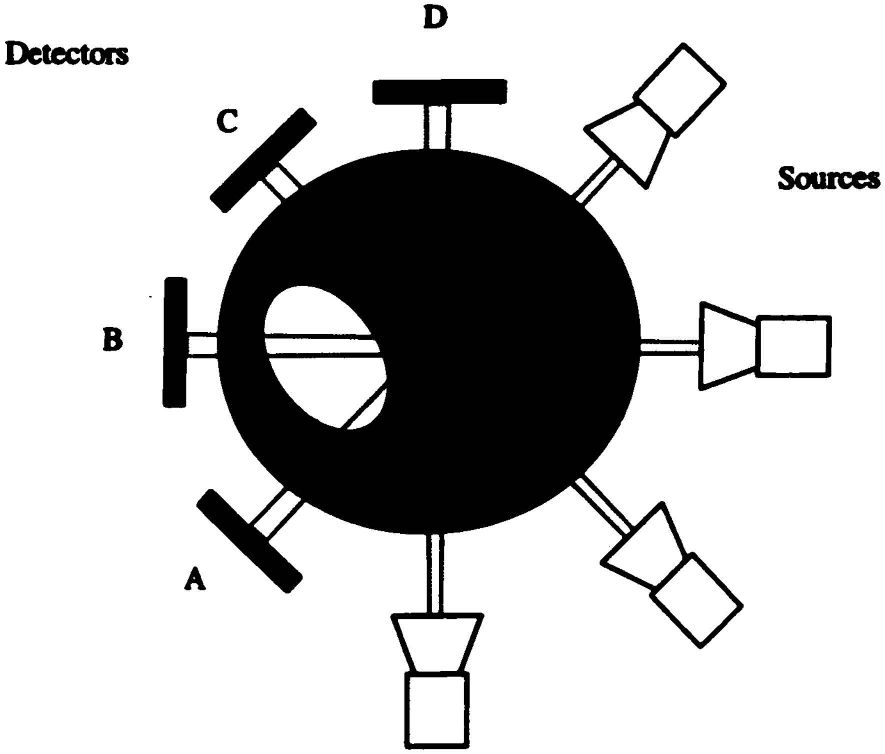

Figure 2.3 Schematic of Basic Tomographic Principles.

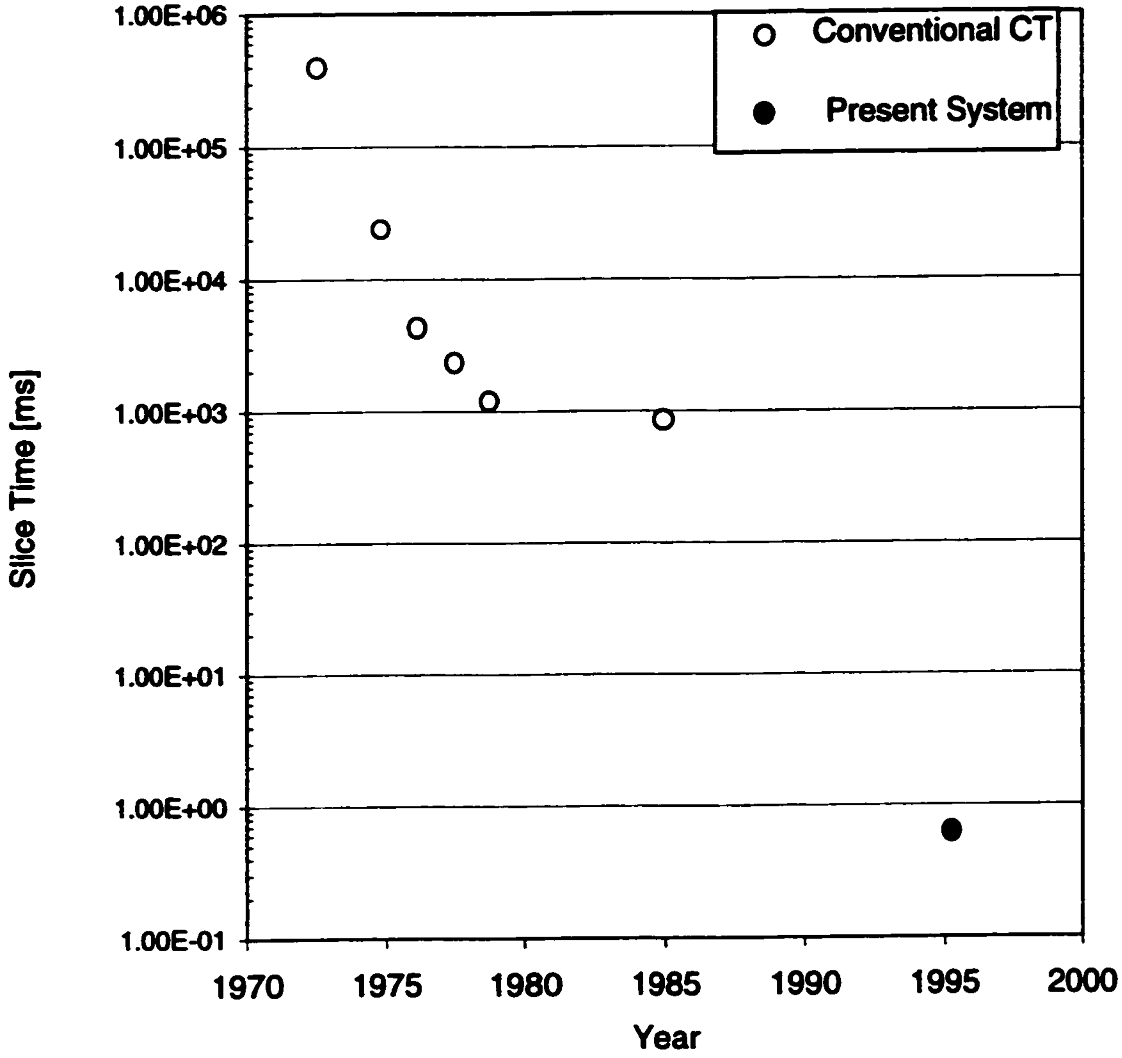

Figure 2.4 Advancements in XCT Scanning Time

CHAPTER 3 EXPERIMENTAL DETAILS

The experimental facilities used to measure the void distribution effects during flow boiling are discussed below. The major research facilities and equipment used to study void distribution during tube-side flow boiling were;

- Refrigerant 134a (CF_3CH_2F) flow loop used to study boiling phenomena.
- Real Time Neutron Radiography void measurement system.
- Refrigerant 123 flow loop, high capacity Refrigerant 123 flow loop used for ultra high speed X-Ray Computed Tomography studies.
- Ultra high speed X-Ray Computed Tomography system.
- A horizontal channel R134a boiling test section used for smooth and swirl-flow RTNR experiments.

- A vertical channel boiling test section also used to study smooth and swirl-flow of R134a and R123 using both RTNR and high speed X-Ray CT.

3.1 REFRIGERANT 134A BOILING EXPERIMENTS

3.1.1 Refrigerant 134a Flow Loop

The Refrigerant 134a flow loop is a small volume flow loop with total dimensions of 1.8 m high x 1 m width x 1 m length. The loop size was selected specifically for access into and out of the McMaster Nuclear Reactor (MNR) Neutron Radiography Shielding Room. Figure 3.1 shows a schematic of the flow system and diagnostic equipment. The flow loop was constructed from 12.5 mm O.D. (1.5 mm wall thickness) stainless steel tubing (SS316). The fluid properties used for Refrigerant 134a are shown in Appendix A for reference.

A magnetic driven centrifugal pump with a DC motor controller supplied refrigerant with mass flow rates from 0 to 60 l/min. A needle control valve was used to regulate the flow rate to the test section along with a bypass line and a separate bypass control valve. The refrigerant temperatures were regulated using external DC preheaters (AC heating tapes) located before the test section and surrounding the inlet piping. The flow rate was measured using a calibrated venturi flow meter and a differential pressure transmitter to measure the pressure drop across the venturi flow meter. System pressure was controlled using a pressurizer and external electrical heaters, with a maximum loop system pressure of 800 kPa. A horizontal or vertical test section can be installed after the flow meter. Heat was supplied to the test section using direct electrical heating or by means of indirect heating using a hot water supply loop (outlined below). The heated fluid may then be passed through a viewing section that contains a capacitance type multi ring transducer capable of measuring the transient volume averaged void fraction.

After the viewing section, the flow passed through a helical-counter flow heat exchanger. The heat was transferred to an open or closed loop cooling water system. The open loop water system supplied filtered city-main line water from 3 to 15 °C at flow rates up to 25 liters per minute. The closed loop system used a chiller with the temperature regulated using a thermostat and control valve. The chiller was capable of supplying water from 0 to 20 °C at flow rates up to 5 liters per minute.

3.1.2 Secondary Side Water Heating Loop

The vertical smooth and swirl flow experiments were conducted using a water heating jacket. The water was supplied from a secondary flow loop shown in Figure 3.2. This flow loop was capable of supplying heated water from 20 to 50 °C at flow rates from 2.5 to 30 liters per minute. A main needle flow control valve and bypass system were used to control the flow rate from an AC centrifugal pump. Heat was supplied using a 2 kW water heater and/or two separate 0.4 kW electrical heating tapes that were controlled using a variable transformer. For high power experiments, an optional 3-phase 4.8 kW water heater was available. Flow was measured using a turbine flow sensor with the calibration curve shown in Appendix B.

Water side temperature differences were used to calculate the test section power using an energy balance;

$$q'' = \frac{\dot{m}\, C_p \left(T_{in} - T_{out}\right)}{A_h} \qquad 3.1$$

where m and C_p are the mass flow rate and specific heat of water, A_h is the heat transfer area and T_{in} and T_{out} are the inlet and outlet water temperatures respectively. The test section was thermally insulated except for the RTNR measurement section. The portion of the test section under RTNR observation was not thermally insulated to reduce the scattering and interference affects on experimental observations. To account for natural convection losses from the outer water jacket to the atmosphere in this section, the correlation from Churchill and Chu[139] was used to calculate the average heat flux loss as;

$$q''_{loss} = \frac{k}{D}\left(T_{wall} - T_{atm}\right)\left[0.825 + \frac{0.387\,Ra_L^{1/6}}{\left(1+\left(0.492/Pr\right)^{9/16}\right)^{8/27}}\right]^2 \qquad 3.2$$

where k and Pr are the thermal conductivity and Prandtl number of air, T_{wall} and T_{atm} are the water jacket wall and atmospheric temperatures respectively and Ra is the Rayleigh number based on the length of exposed test section. Due to the low driving temperature difference in these experiments, the heat loss from the water side through the exposed section of tubing was less than 0.5% of the total applied heat flux for all experiments. However, all heat fluxes based on water temperature differences were corrected to account for this ambient loss term.

3.1.3 Direct Electrical Heating

The horizontal smooth and swirl flow experiments used direct electrical heating with a DC current. The heat flux to the test section was calculated using;

$$q'' = \frac{I^2 R}{A_h} \qquad 3.3$$

where I and R are the current and test section resistance respectively. Similar to vertical experiments, the portion of the test section examined using RTNR was not thermally insulated so a correction was required. The saturation temperature of Refrigerant 134a over the range of experimental conditions was less than the ambient room temperature so that the actual heat flux was slightly larger than that calculated using the above equation. The ambient heat input in this case was calculated using the correlation from Equation 3.2, modified for horizontal free convection with the Rayleigh number based on the tube outside diameter. This correlation was used to correct the measured heat flux for ambient conditions in the uninsulated region.

3.1.4 Surface Temperature Correction

The calculation of the direct electrical heating Refrigerant inside wall temperature based on outside wall temperature measurements were complicated because the heat flux is generated throughout the Inconel as a result of the current. Furthermore, the thermal conductivity of Inconel also changes with temperature. High heat flux or sub-cooling levels can lead to large temperature/conductivity gradients in the wall region. Therefore, it is necessary to calculate the wall to refrigerant temperature based on outside wall temperature measurements using the following;

$$q''' = \frac{1}{r}\frac{\partial}{\partial r}\left(k r \frac{\partial T}{\partial r}\right) \tag{3.4}$$

where k is the thermal conductivity, T the temperature and q''' the thermal generation per unit volume resulting from Joule heating. The boundary equations for this system are;

i) prescribed wall temperature($T_R = T_{wo}$).

ii) perfect outer wall thermal insulation.

Previous analysis used for high heat flux experiments solved Equation 3.4 assuming a constant thermal conductivity and evaluated the thermal conductivity at the average of the temperature profile. However, the thermal conductivity of Inconel is a strong function of temperature which may lead to over estimation of inside wall temperatures. In order to more accurately estimate the inside wall temperatures, Equation 4 can be non-dimensionalized by using the following definitions;

$$\bar{r} = \frac{r}{R} \qquad \bar{T} = \frac{T}{T_R}$$
$$\bar{k} = \frac{k}{k_{T=T_R}} \qquad \bar{q} = \frac{q'''R^2}{K_{T=T_R} T_R} \tag{3.5}$$

which gives;

$$\bar{q} = \frac{1}{\bar{r}} \frac{d}{d\bar{r}} \left(\bar{r}\bar{k} \frac{\partial \bar{T}}{\partial \bar{r}} \right) \tag{3.6}$$

Chang and Laframboise[140] have applied Kirchhoff transformations to heat conduction calculations in arbitrary shaped bodies. A similar transform in cylindrical coordinates between the inner and outer wall is;

$$\frac{dH}{d\bar{T}} = \bar{k} \quad ; \quad H = \int_{\bar{T}}^{1} \bar{k}\, d\bar{T} \tag{3.7}$$

Applying this transformation yields;

$$\bar{q} = \frac{1}{\bar{r}} \frac{d}{d\bar{r}} \left(\bar{r} \frac{\partial H}{\partial \bar{r}} \right) \tag{3.8}$$

This second order differential equation can be solved using the transformed boundary condition;

$$\bar{H} = \frac{\bar{q}}{4} \left(\bar{r}^2 - 2\ln(\bar{r}) - 1 \right) \tag{3.9}$$

Based on the thermal conductivity temperature dependance, a relationship for Inconel 600 thermal conductivity is as follows;

$$k_T = k_0 e^{\omega T} \qquad 3.10$$

where k_0 and ω are 11.8 W/m-K and 1.67×10^{-3} K^{-1} respectively. Integrating the original transformation, Equation 3.8, with Equation 3.10 gives;

$$H = \frac{1}{\omega T_R}\left(1 - e^{\omega T_R(\bar{T}-1)}\right) \qquad 3.11$$

Solving this for the inside wall temperature, and using Equation 3.9 gives;

$$\bar{T} = 1 + \frac{1}{\omega T_R}\ln\left(1 - \frac{\bar{q}\omega T_R}{4}\left(\bar{r}^2 - 2\ln(\bar{r}) - 1\right)\right) \qquad 3.12$$

which can be used to calculate the Inconel wall temperature at any location with internal heat generation.

3.1.5 Flow Diagnostics

Extensive flow diagnostic equipment was installed in the R134a Flow Loop. All measurements were recorded using a PC-based data acquisition system (Data Translation DT2835). A graphical data acquisition programing environment (HP VEE) was used to control the data acquisition, display and record the measured quantities in real time. A custom data acquisition program capable of 400 Hz sampling of all diagnostic equipment was developed and the program is shown in Appendix C. The recorded quantities were the

Refrigerant and water side flow rates, Refrigerant inlet and outlet temperatures, test section water side inlet and outlet temperature, Refrigerant system pressure, Refrigerant test section differential pressure and the Refrigerant pump side inlet temperature. As well the power to the electrical preheaters was measured using a total power meter (Simpson 390-2).

The system pressure was monitored using both a Bourdon type and a calibrated diaphragm type (Validyne DP15TL) pressure transducer that was located at the exit of the test section. The signal from the diaphragm sensor was converted into a proportional voltage signal and measured using the A/D system. Appendix B shows the calibration curve used for this sensor. A secondary Bourdon type pressure gauge was installed at the inlet of the test section. The test section differential pressure drop was measured using a second diaphragm type differential pressure sensor coupled immediately before and after the heated section. The calibration curve for this test section differential pressure transmitter is shown in Appendix C.

Fluid temperatures at the inlet and outlet of the test section were measured using the layout shown in Figure 3.3 . Thermocouples (3 mm diameter, K-Type) were inserted into 90 degree elbows so that the measurement point was approximately three tube diameters from the elbow center. The elbows were also thermal insulated from the environment to reduce errors caused by thermal losses. This assembly provided well-mixed fluid at the temperature measurement locations and therefore should yield accurate measurement of the average bulk fluid temperature. All thermocouple extension wires were shielded and grounded to prevent noise in the temperature measurements.

The refrigerant flow rate was measured using the venturi flow meter shown in Figure 3.4 in conjunction with a differential pressure transducer (Validyne DP15TL). The venturi entrance and throat diameter were 6.93 mm and 2.5 mm respectively. Four pressure taps were drilled circumferentially around the flow meter at each pressure measurement location to insure accurate measurements.

For some experiments a multi-ring type capacitance transducer was used to measure the test section outlet void fraction. Figure 3.5 shows a schematic of the multi-ring capacitance transducer used in these experiments. Alternating rings are connected in series and the capacitance was measured using a calibrated capacitance meter (Boonton 72B). The output of the capacitance meter was a proportional voltage in the range 0 to 1 V corresponding inversely to a void fraction between zero and one. These measurements were also recorded using the data acquisition system.

3.2 McMaster Nuclear Reactor

The McMaster Nuclear Reactor (MNR) is a 5 MW pool type research reactor located on the main campus of McMaster University in Hamilton, Ontario, Canada. It uses light water as a coolant and moderator and a combined natural and forced convective cooling system with a slightly enriched core. Currently the reactor operates at 2 MW thermal power for 16 hours, 5 days per week. Figure 3.6 shows the rectangular reactor core layout and beam tube locations (7 in total). These beam tubes can be used to extract a beam of radiation from the core to the location of a particular experiment. Beam Tube #2 supplies a filtered neutron beam to the RTNR experimental facility located in Beam Port #2. A steady supply of thermal neutrons at a flux of 3×10^6 neutrons/cm^2-s after collimation is supplied to the camera system.

3.2.1 Beam Port Facilities

Beam Port #2 is shown in Figure 3.7 with the Radiography Shielding Room. The walls of the shielding room were approximately 40 cm thick of concrete to provide adequate radiation shielding during beam operation. Access to the cave was through a 60 cm by 1.8 mm door that is also located off the beam center to reduce radiation leakage. The cave size and height (1.8 m) limit the size and volume of both the experimental test facility and the test section. A Cadmium collimator was used for main beam collimation and the shutter was constructed from a water-filled chamber and is raised with a mechanical crank and pulley system to activate the beam. The collimator L/D was approximately 90, with an aperture to object L/D of 200.

3.3 REAL TIME NEUTRON RADIOGRAPHY

The McMaster University Real Time Neutron Radiography system is a neutron imaging device for measuring two-phase flow parameters. Neutrons are converted into photons and recorded using a low level video camera system. The output of this system is a RS-330 video signal that can be recorded on a VHS system or passed directly into a digital image processing system. This allows for flexible processing either during or after experiments and allows for very long record lengths (2 hours maximum per standard video tape) at a frame speed of 33 ms.

Figure 3.8 shows a schematic of the RTNR system, neutron beam, incident object and the RTNR system. Different object materials and densities will differentially attenuate the thermal neutron beam and a Lithium doped ZnS (Ag activated) screen is used to convert the transmitted neutrons to photons. The photons produced in this convertor screen are then reflected off a mirror into a photo-intensifier system, which applies an intensity gain before the low light level video camera. To protect the camera electronics a mirror is used to deflect the photons so that the camera and sensitive electronics can be located outside the neutron beam path. The camera and electronics are also shielded from noise using a pressurized nitrogen jacket. To further reduce noise and allow changes in camera operation, the cooling system and focus controllers are located outside the beam room and are connected to the camera using electromagnetically shielded cables. The beam characteristics (gamma radiation, thermal neutron and fast neutron content) have been documented by Harvel[113]. Images produced can be recorded using an S-VHS video recorder (Mitsubishi HS-U69) for later analysis, or images can be directly analyzed in a computer system using a high speed PCI image processing board (DT3152). Interlaced images are produced at 16.5 ms per image, with a complete image being produced at a standard video signal rate of 33 ms. Chapter 4 shows the theoretical principles and technical details involved in the RTNR measurement of void distribution.

3.4 REFRIGERANT 123 FLOW BOILING FACILITY

3.4.1 Refrigerant 123 Flow Loop

The Refrigerant 123 and water heating flow loops were used for the ultra HS-XCT experimental investigation and are shown in the Figure 3.9. Hot water for indirect heating was supplied at 150 °C and 630 kPa. The water was heated using a large resistive electrical heater, with fine temperature adjustment using a smaller electrical preheater. Flow control of the water side was accomplished using a combination of a bypass valve and main control valve. Water flow was measured using an orifice flow meter coupled to a digital differential pressure transmitter. The high temperature water pump was also equipped with additional cooling to correct for pump heating effects during the experiment.

The Refrigerant 123 flow loop supplied liquid at test section inlet temperatures from 65 to 75 °C, mass fluxes from 750 to 1250 kg/m^2-s at a pressure of 630 kPa. Flow rates were measured using an orifice flow meter coupled to a digital differential pressure transmitter. A PID logic system controlled the flow using the output of the orifice flow meter and an actuated valve. Pressure was controlled through a large pressure vessel with an internal heating system.

The Refrigerant 123 properties used in this analysis are shown in Appendix A.

3.4.2 Ultra-High Speed X-Ray Computed Tomography System

A schematic of the ultra-high speed X-Ray Computed Tomography scanner, located at the Mitsubishi Heavy Industry's Takasago Research and Development Center, is shown in Figure 3.10. A total of 60 X-Ray tubes and 584 room temperature Cadmium Telluride X-Ray detectors are placed 360° around the test channel with the detector plane slightly below the source plane. The application of these detectors for fast X-Ray CT applications was described by Hori et al.[141]. During exposure, each X-Ray tube produces a 30° fan beam, with two sources (180° apart) operating simultaneously to reduce scanning time. The tubes operated at a potential of 110 kV with a maximum current of 17 mA. An electrically switched biasing grid was used to control the X-Ray timing and exposure from each tube. Switching the grid off allows X-Ray emission from the tube, while turning it on stops the beam. An electronic control system operates the grid switching and X-Ray exposure and allows the user to select any slice speed down to a minimum of 0.5 ms per slice. Figure 3.11 shows a sample of the timing control signals used for the XCT scanner for 0.9 ms slice speed.

The data acquisition system reads the signal from the detectors and stores the data into Random Access Memory (RAM). This data is then downloaded into a UNIX-based workstation that reconstructed the two-dimensional images based on the detector data. The data acquisition rate was approximately 60 MB per second for a maximum of 6 seconds, allowing approximately 6000 tomographic slices. Experiments performed previously on phantom sections indicate the system resolution is approximately a 1.5 mm minimum resolvable object size with a pixel size of 0.25 mm[142].

3.5 TEST SECTIONS

3.5.1 Horizontal Flow Test Section

Figure 3.12 shows a schematic of the horizontal flow-boiling test section. The test section was constructed from Inconel 600 alloy because its electrical resistivity remains constant over the range of temperatures considered, producing a constant heat flux over the test section length. A 550 mm (7.7 mm I. D., 1 mm wall thickness) tube was used with an L/D ratio of approximately 90. Wall temperatures were recorded using 6 thermocouples (0.5 mm O.D.) attached to the wall at various axial positions using high thermal conductivity cement. Thermal insulation was used to cover the entire test section except for the section being studied by RTNR. The differential test section pressure drop was measured using a diaphragm type differential pressure sensor. The Refrigerant was heated to boiling conditions and exits the heated section through a polyethylene viewing tube. A multi ring capacitance transducer measures the volume averaged instantaneous void fractions at the test section outlet and flow regime observations were made using a CCD camera.

Refrigerant 134a and 123 were selected as the working fluids due to low specific heat and saturation pressure that decreases the overall power requirements. The neutron attenuation ratio between the liquid and gas phases is high, as shown in Chapter 1, and provides for good contrast during RTNR of flow boiling experiments.

3.5.2 Vertical Flow Test Section

Figure 3.13 shows a schematic of the test section (16 mm I.D., 110 cm long) that was constructed from aluminum to reduce interaction with the X-Ray beam. Water flows counter currently in the outer jacket heating the Refrigerant that flows upwards in the center channel.

The water jacket was constructed from 23 mm I.D. tube to reduce the attenuation by water of x-rays and neutrons in this region. Also shown in this figure is the location of the XCT imaging location and the RTNR viewable area. The test section was positioned so that the X-Ray plane was approximately 10 cm from the outlet of the heated length, while the RTNR location covered an area from the outlet to the 30 cm upstream. A thermocouple was attached to the test section 10 mm downstream from the X-Ray plane to monitor the wall temperature.

The same vertical tube-side boiling test section was used for both the ultra-high speed XCT and RTNR experiments.

3.6 TWISTED-TAPE INSERTS

Schematics of the twisted tape inserts used to generate swirl-flow in these experiments are also shown in Figure 3.14 (75 cm and 100 cm for RTNR and XCT experiments respectively). The tape twist ratio is defined as,

$$y = \frac{L_{180^\circ}}{D} \tag{3.13}$$

where w is the tape width and l is the length of a 180° twist. Tapes were manufactured with widths approximately equal to the inner diameter of the test section. The tape width was 15.5 mm for both the vertical RTNR and XCT experiments (1 mm thickness) and was 7.2 mm for the horizontal direct heating test section. Experiments performed on horizontal flow boiling show that twist ratios above 4 do not significantly affect ONB or heat transfer performance.

Furthermore, small twist ratios (less than 2) may increase pressure drop to prohibitively high levels and are difficult to manufacture using conventional techniques. Due to these affects, most vertical RTNR and XCT experiments swirl-flow experiments were conducted at a twist ratio of 3.

For the direct electrical heating experiments the twisted tapes were hard anodized to prevent electrical conduction and heat generation within the twisted tape inserts.

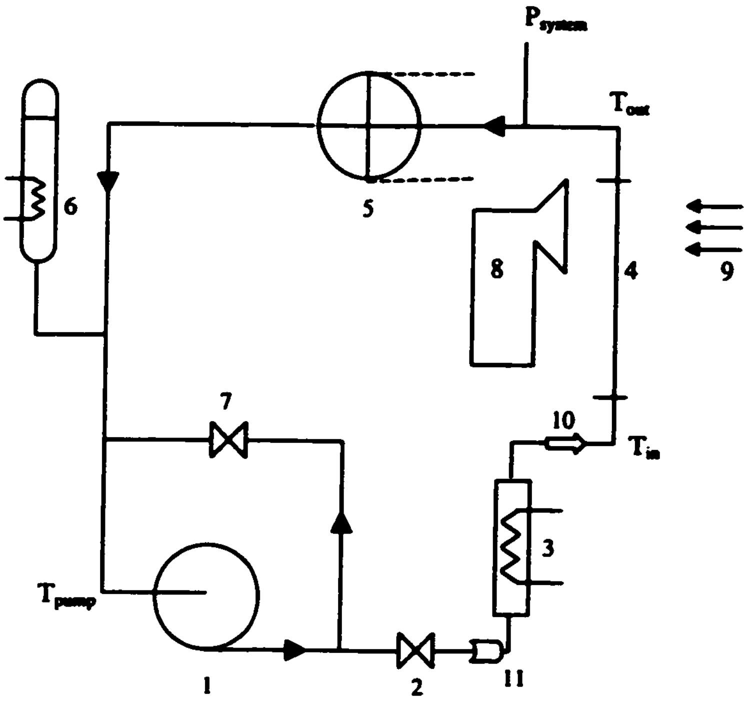

Figure 3.1 Schematic of Refrigerant 134a Flow Loop Used For RTNR Experiments (1. Refrigerant Pump, 2. Main Refrigerant Flow Control Valve, 3. Refrigerant Inlet Preheater, 4. Removable Test Section, 5. Refrigerant Condenser, 6. Refrigerant Pressurizer, 7. Bypass Refrigerant Control Valve, 8. RTNR Camera System, 9. Thermal Neutron Beam, 10. Venturi Flow Meter, 11. Refrigerant 134a Filter/Drier).

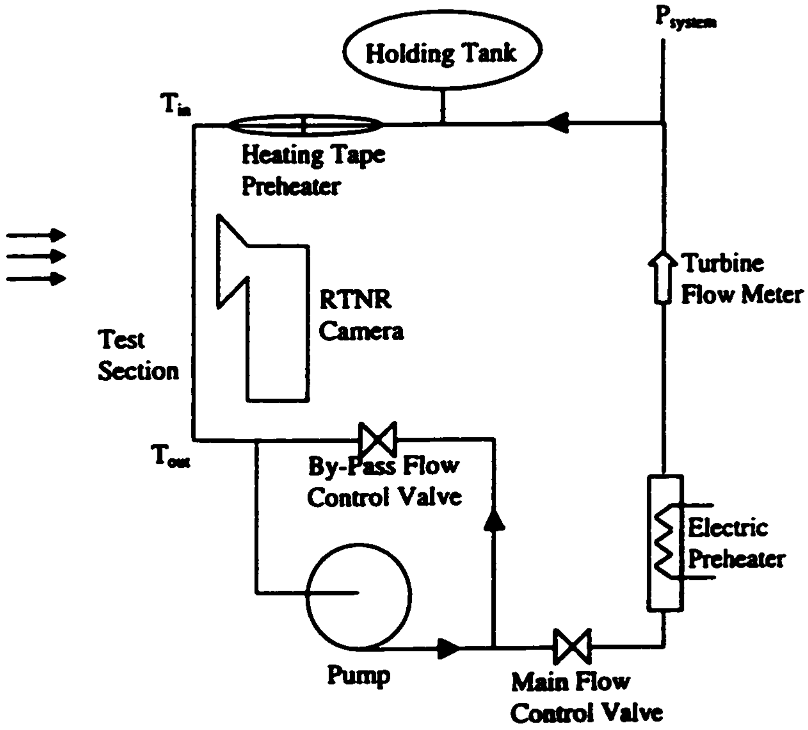

Figure 3.2 Schematic of the McMaster University Secondary Side Water Heating Loop.

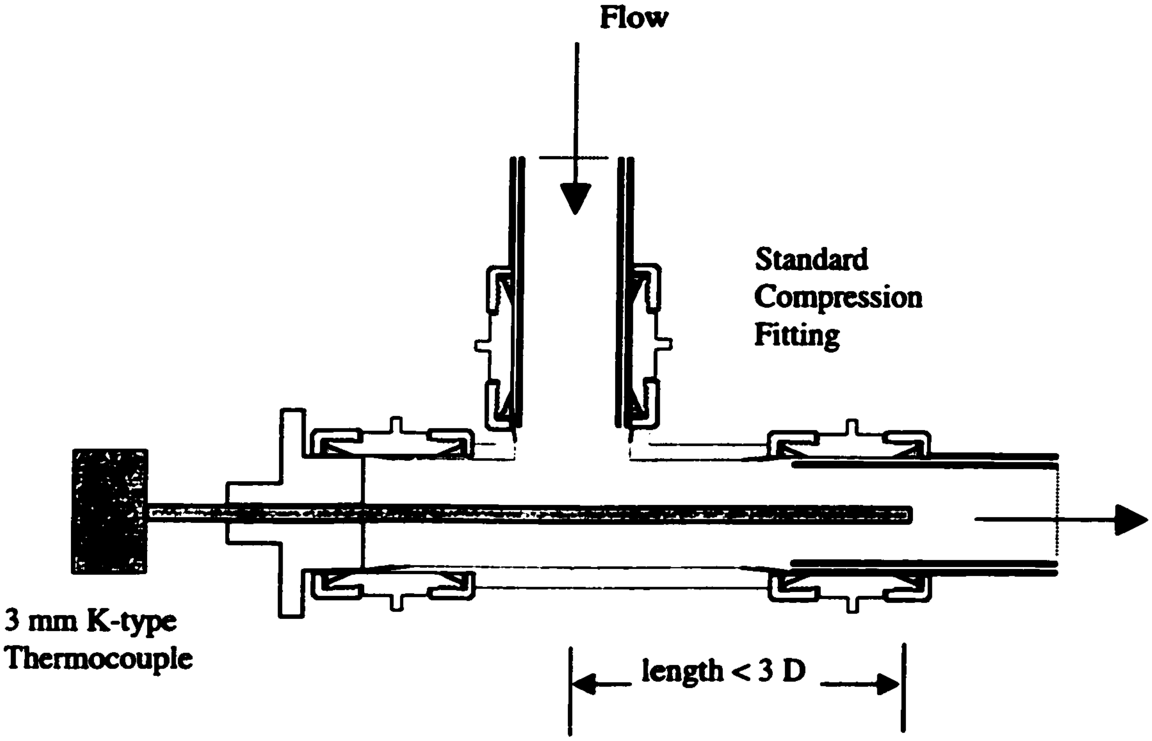

Figure 3.3 Schematic of the Bulk Fluid Thermocouple Measurement Assembly.

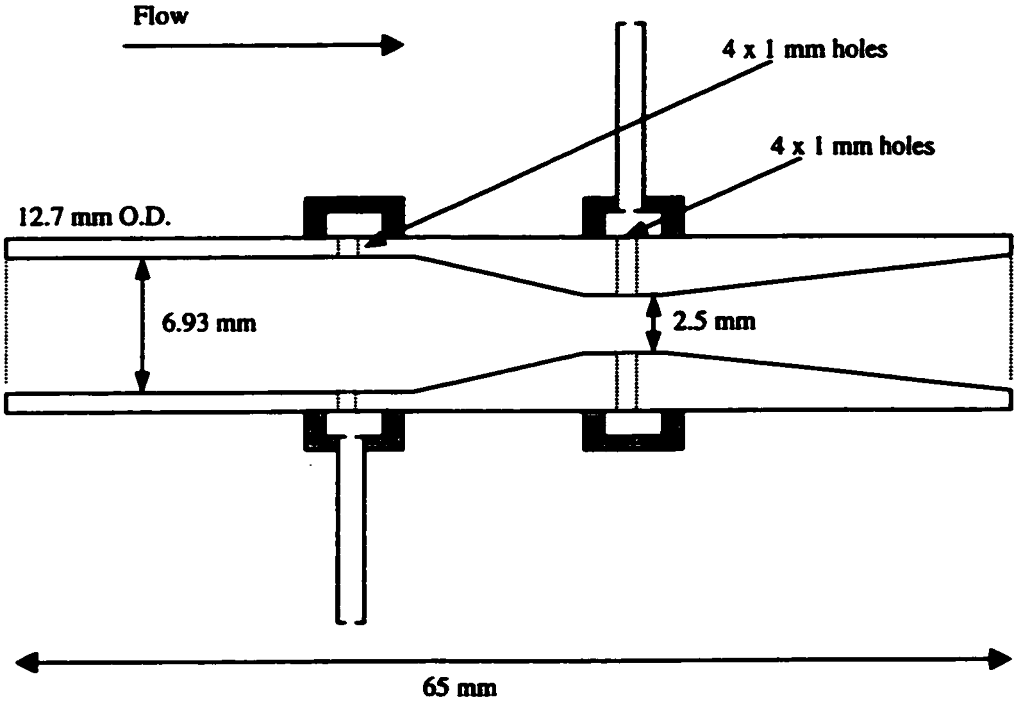

Figure 3.4 Refrigerant Side Venturi Flow Meter.

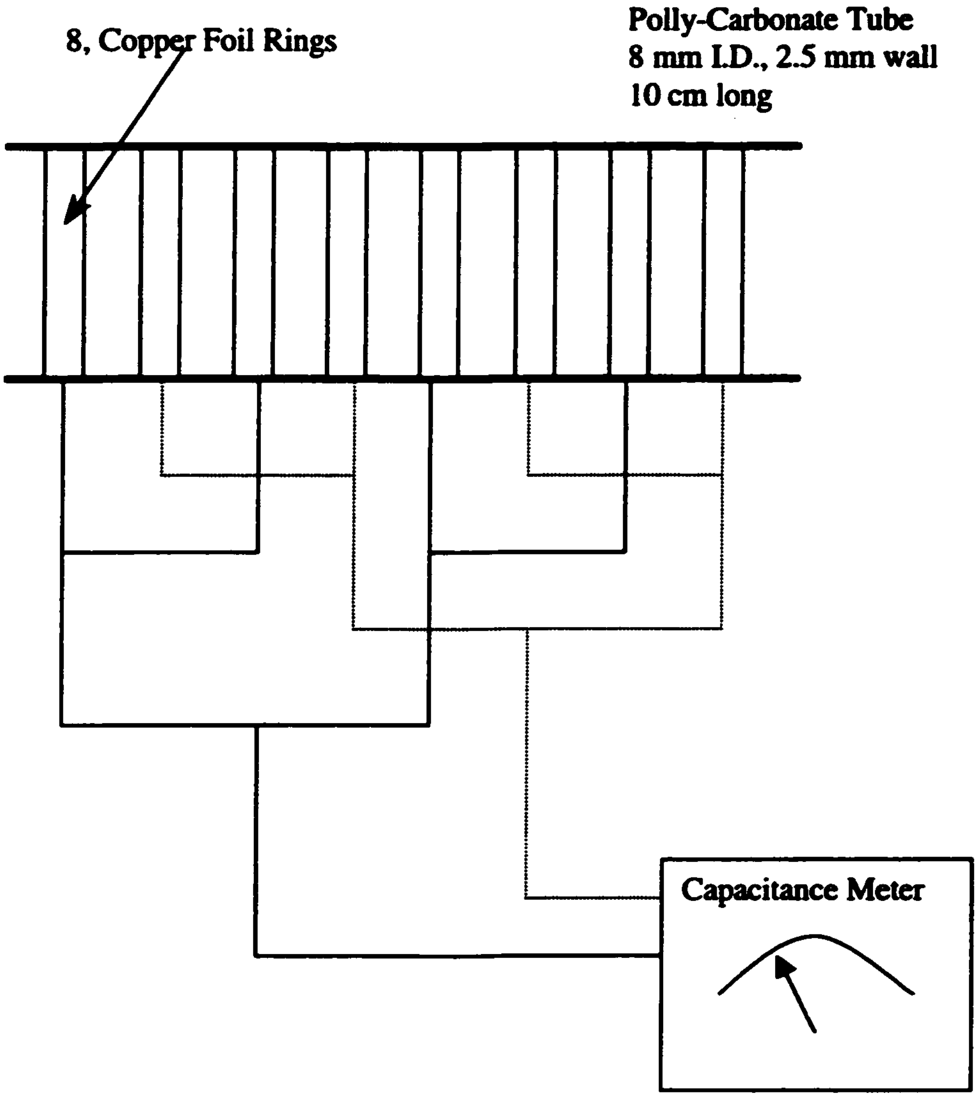

Figure 3.5 Schematic of the Multi-Ring Capacitance Flow Meter.

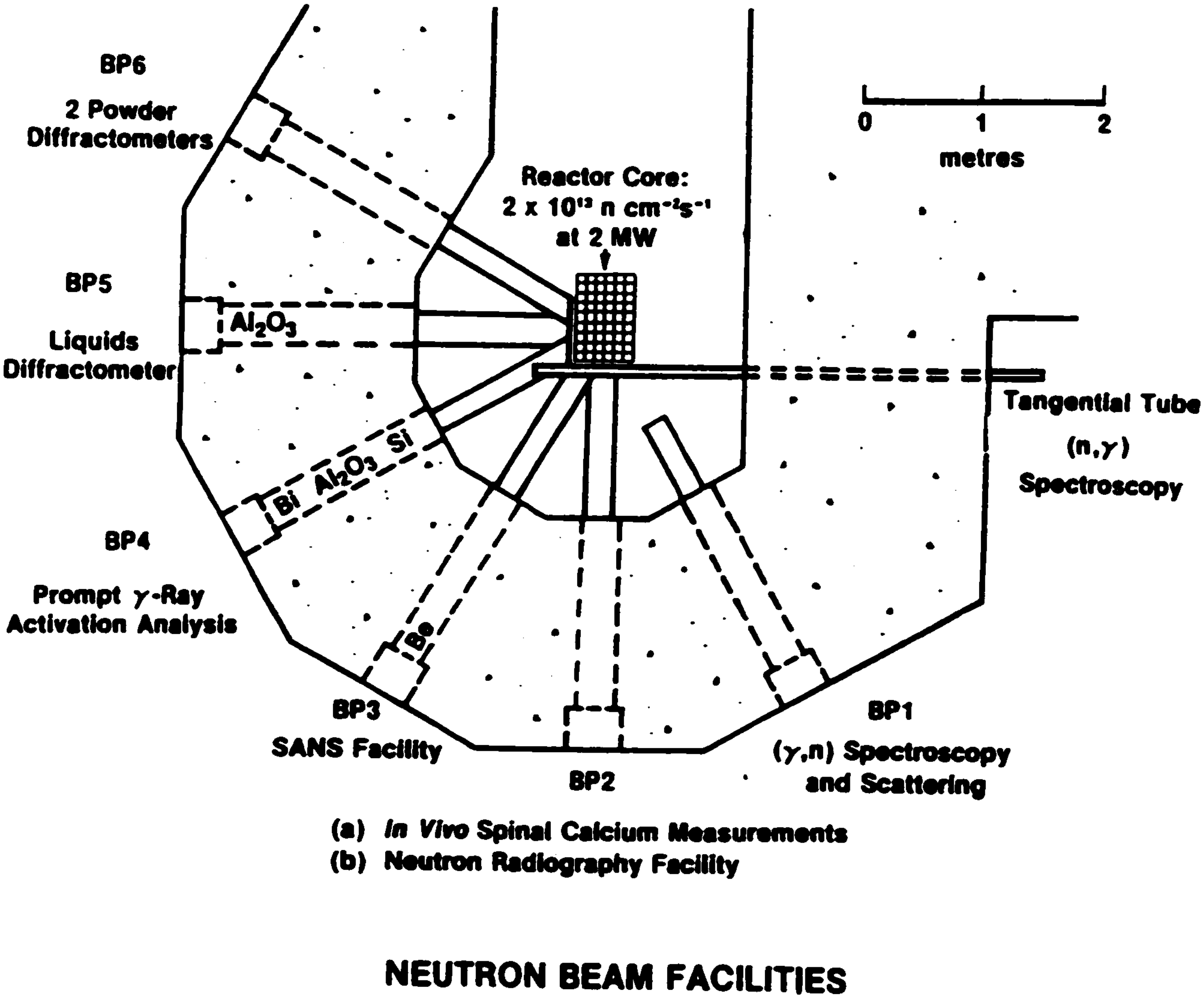

Figure 3.6 Schematic of the McMaster Nuclear Reactor Arrangement.

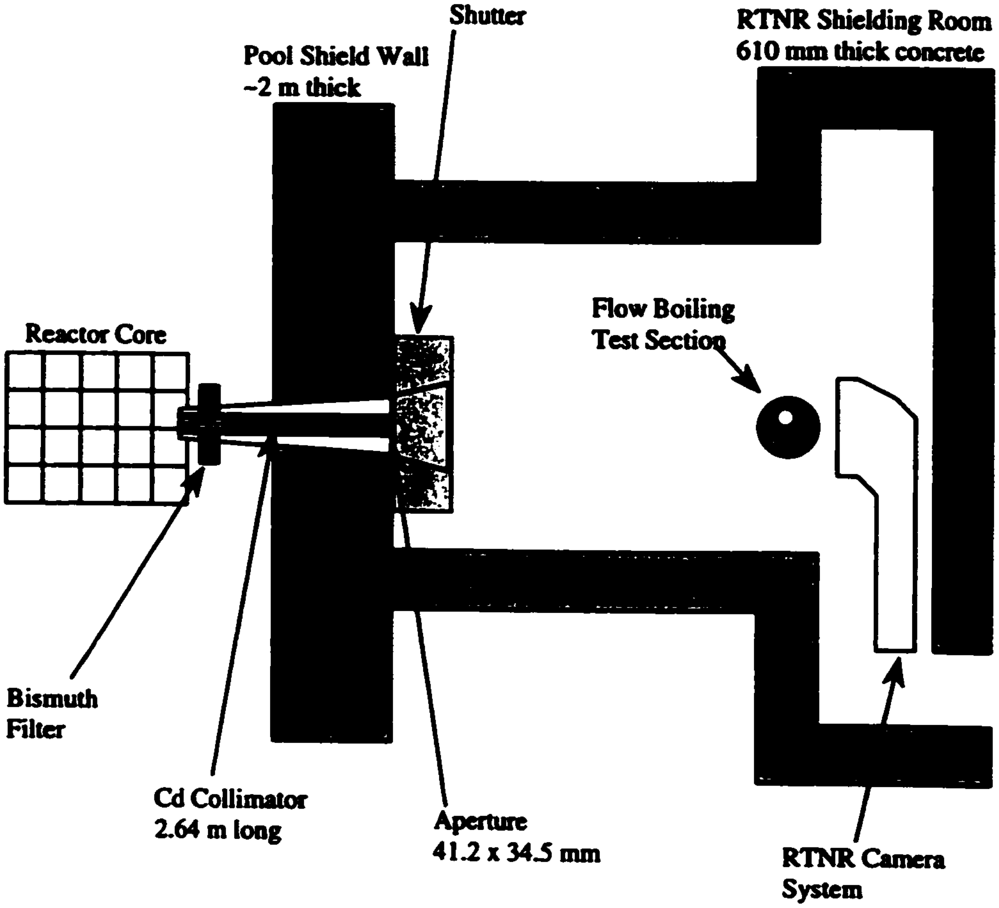

Figure 3.7 McMaster University Beam Port #2 Layout.

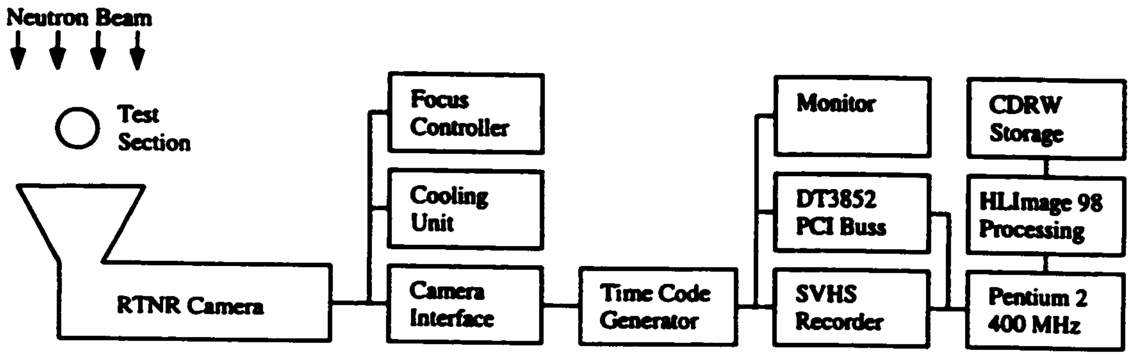

Figure 3.8 RTNR Void Distribution Measurement System.

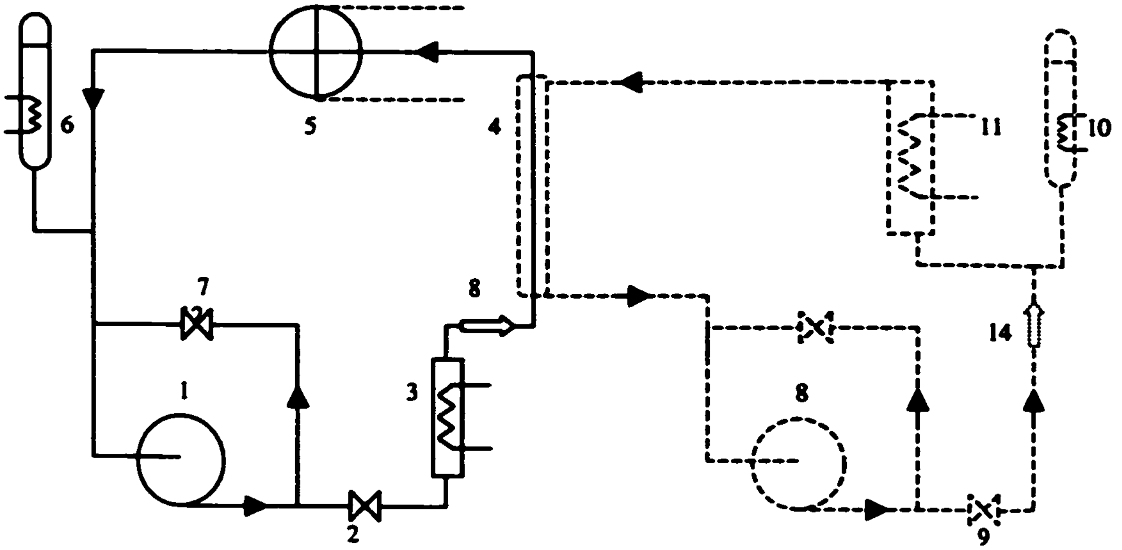

Figure 3.9 Schematic of Refrigerant 123 Flow Loop Used for Ultra-High Speed XCT Experiments (1. Refrigerant Pump, 2. Main Refrigerant Flow Rate Pneumatic Control Valve, 3. Refrigerant Inlet Preheater, 4. Removable Test Section, 5. Refrigerant Condenser, 6. Refrigerant Pressurizer, 7. Refrigerant Bypass Control Valve, 8. Refrigerant Orifice Flow Meter. 9. Water Pump, 10. Main Water Flow Control Pneumatic Valve, 11. Water Pressurizer, 12. Water Preheater, 13. Water Bypass Control Valve, 14. Water Orifice Flow Meter).

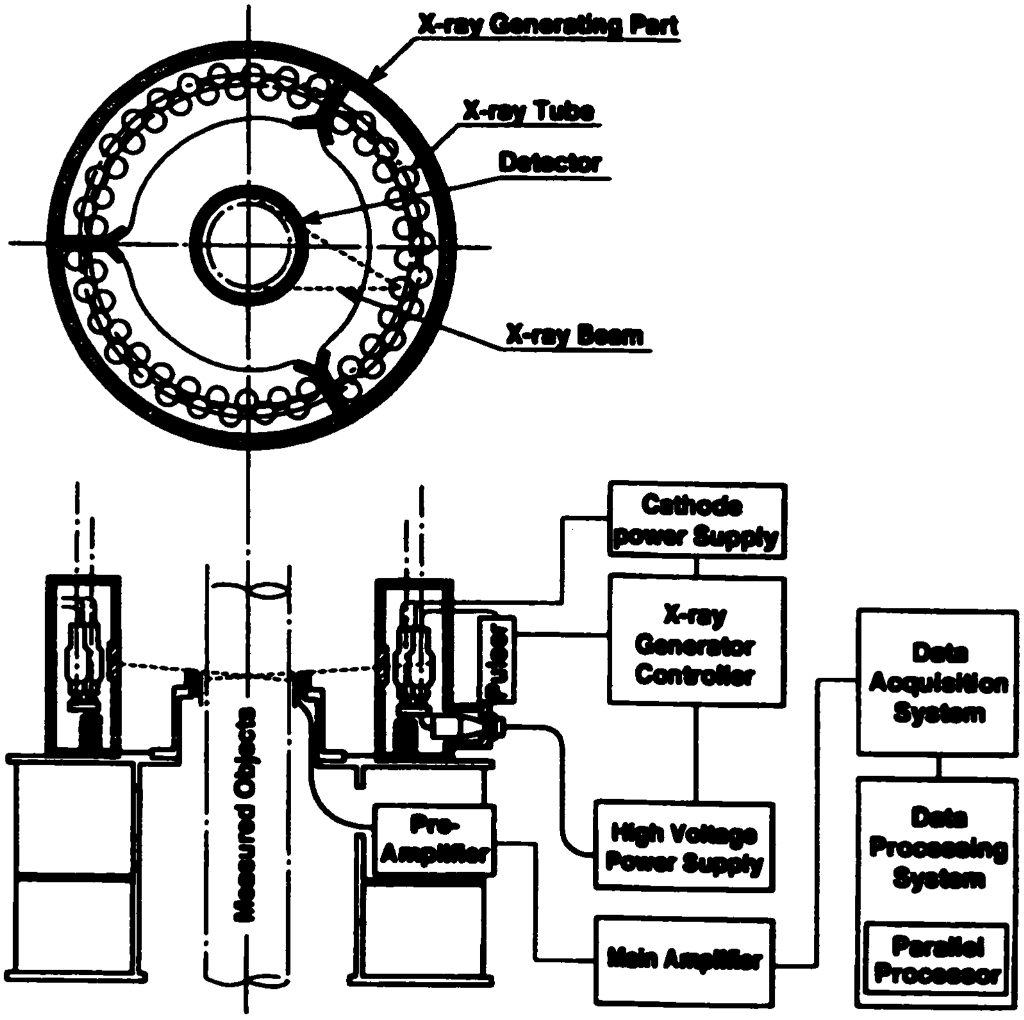

Figure 3.10 High Speed XCT Void Distribution Measurement System.

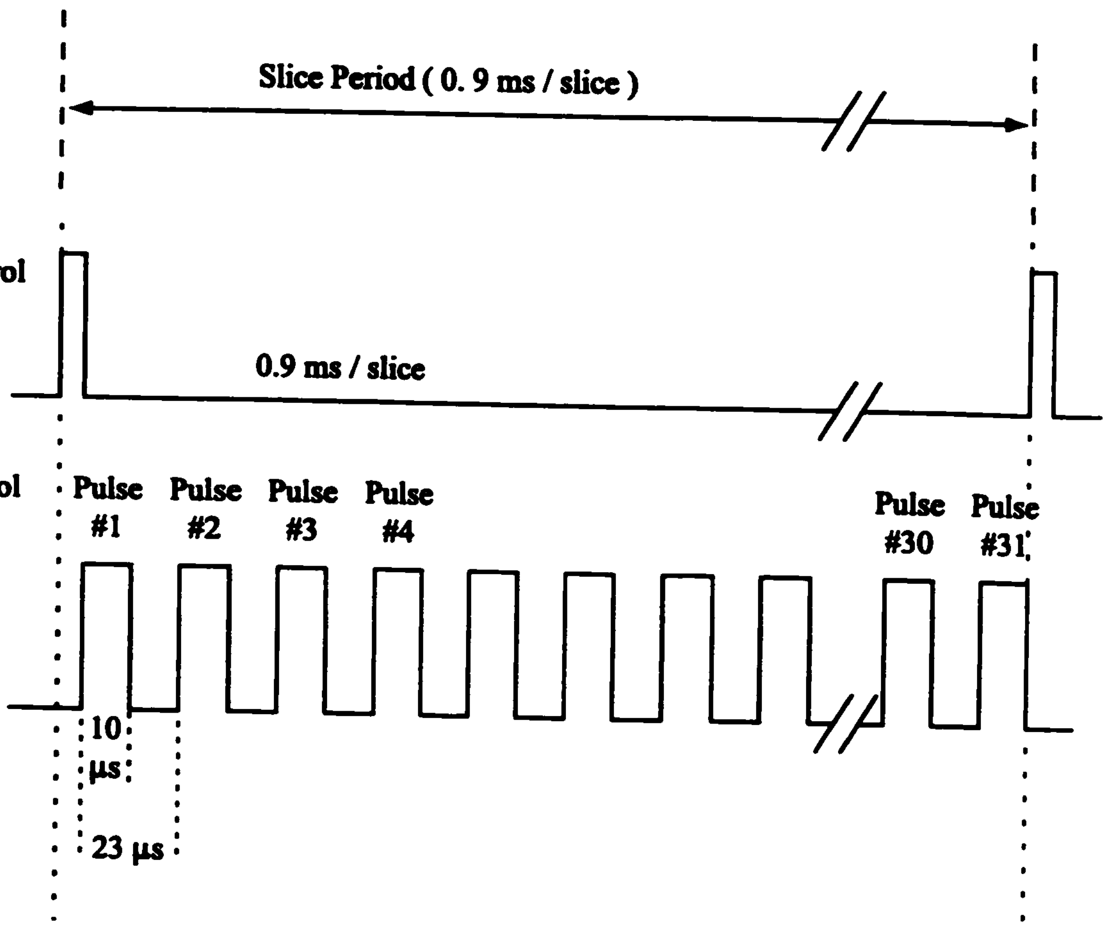

Figure 3.11 Timing Control Circuit for High Speed XCT .

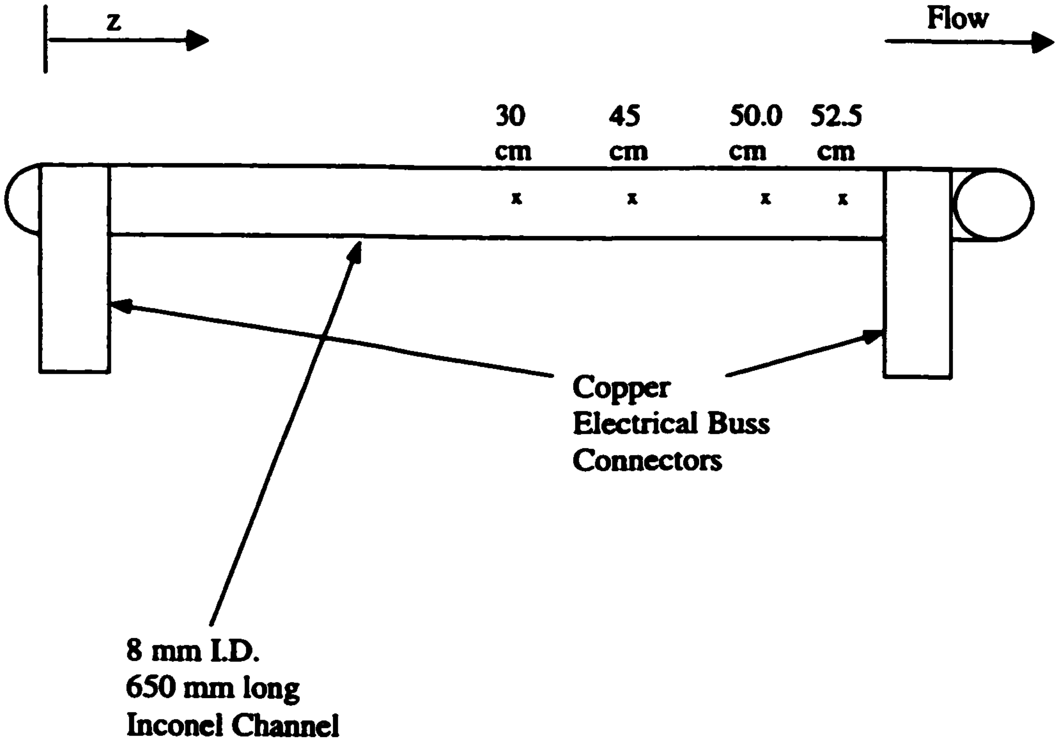

Figure 3.12 Schematic Horizontal Flow Boiling Test Section.

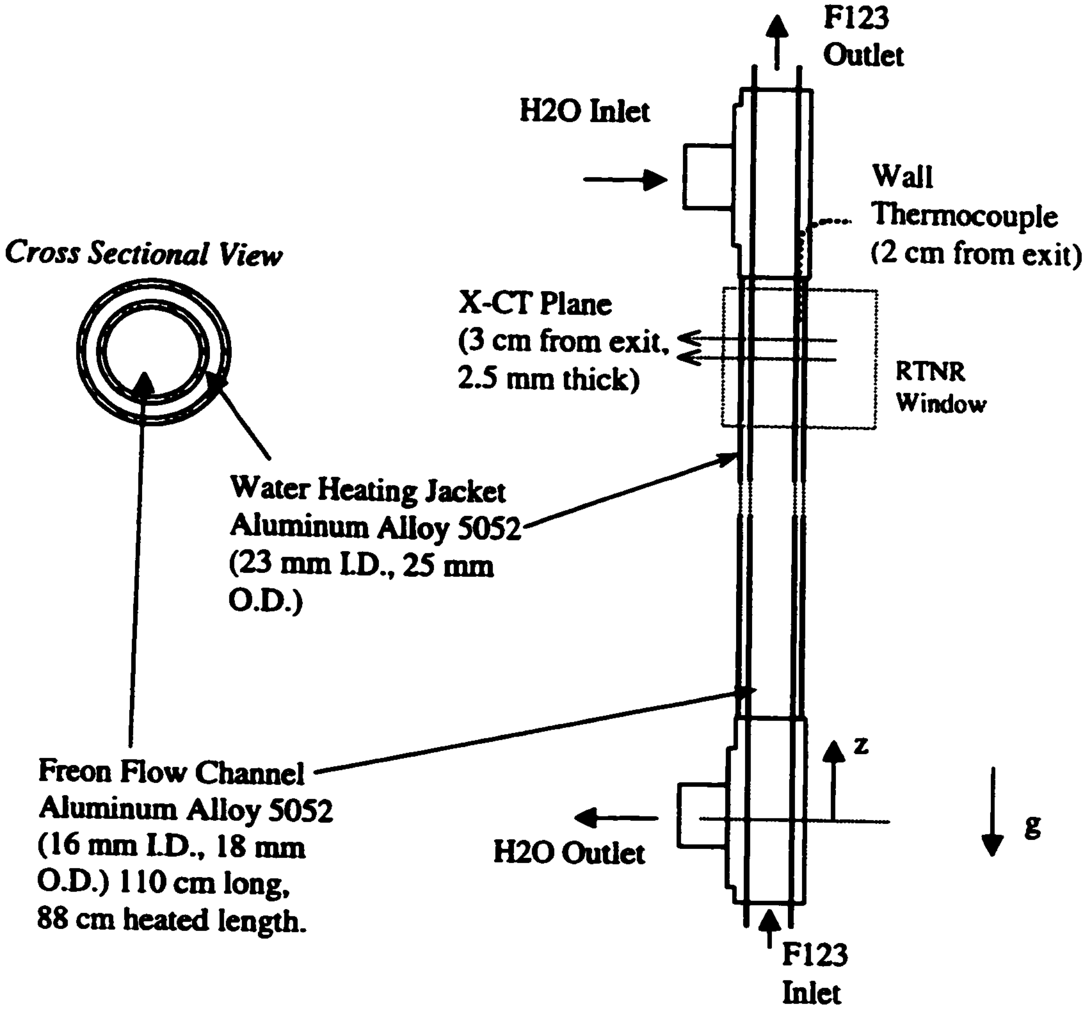

Figure 3.13 Schematic of Vertical Flow Boiling Test Section.

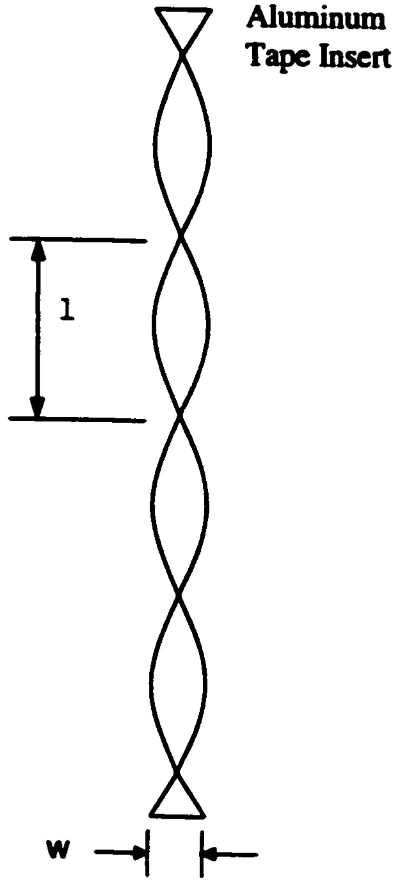

Figure 3.14 Twisted Tape Swirl-Flow Generating Inserts.

CHAPTER 4 RTNR VOID DISTRIBUTION MEASUREMENT THEORY

4.1 RADIOGRAPHIC PRINCIPLES

Radiography is the process of determining an object's internal structure through differences in radiation attenuation characteristics. These differences may result from geometrical changes (i.e. changes in thickness) or material/density changes (i.e. changes in the radiation attenuation characteristics). The transmitted radiation which passes through the object is used to create images on a recording medium that indicate its structure and organization. In general, the ideal attenuation of a radiation beam can be modeled using;

$$I = I_o e^{-\lambda y} \qquad 4.1$$

where I_0 and I are the incident and transmitted radiation intensities respectively, λ is an attenuation constant and y is the material thickness. The attenuation constant is a function of the scattering and adsorption mechanisms in a given material and the type of incident radiation. A schematic of the basic radiographic process is shown in Figure 4.1 for an object containing two differing attenuation materials.

In the case of medical X-Rays, a beam is passed through an object and the transmitted portion is used to expose photographic film. The image obtained gives a two-dimensional map of the structure of the incident object, based on the density and material in the object. For X-Ray radiographic and tomographic applications, attenuation in most materials is primarily due to photon-absorption[18]; hence elements with large atomic numbers and/or mass densities tend to attenuate X-Rays more efficiently than low density materials or low atomic elements. Furthermore, the attenuation of the beam can be accomplished by different materials or material densities, so that the measured attenuation using radiographic techniques represents the total contribution from all objects on a line between the source and the radiographic device. This means that each grain or pixel in the photographic film represents an integrated value of the material attenuation between the film and the source. At a given location, the measured attenuation is given as;

$$\overline{A} = e^{-\int_{\text{line}} A_{\text{material},\rho}\,dy} \qquad 4.2$$

where $\overline{A}$ is the chordal-attenuation, $A_{\text{material},\rho}$ is the contribution to attenuation from each material and density change in a line from the source to recording devices.

Neutron radiography is similar in many respects to modern medical X-Ray radiography. A beam of neutrons is directed at an object that attenuates part of the beam. The most common mechanism for neutron attenuation is through scattering events with neutron sized objects (i.e. hydrogen or low atomic number elements). In general, compounds with a large number of hydrogen nuclei (such as water, hydrocarbons etc.) tend to attenuate neutrons better than metals (high atomic number but neutrons and protons are concentrated in one nucleus). The attenuation of neutrons through a medium can be calculated using;

$$\frac{I}{I_0} = Bu \prod_{i=1}^{n} e^{-\Sigma_i^t y_i} \qquad 4.3$$

where Bu is the build-up factor, Σ^t_i is the thermal neutron attenuation coefficient for material i, y_i is the path length of material i with respect to the beam and n is the number of different materials. The build-up factor results from multiple neutron scattering events that may lead to scattering back into the beam path. For radiographic use, neutrons interact very little with photographic film or other direct detection methods, so convertor screens must be used to convert neutrons into a detectable medium (photons, electrons . . .). Gadolinium is often used to convert neutrons to photons for still radiography while Li^6 is used for real time applications.

The attenuation difference between the liquid and gas phases of water, Refrigerant 134a and Refrigerant 123 indicate that neutron and X-Ray radiography may be used to study the void distribution in thermalhydraulic experiments. The ability of neutrons to penetrate the metals used in high pressure/temperature systems makes it ideal for studying the internal void distribution in high temperature and pressure systems where the walls must be constructed from metal.

4.2 REAL TIME NEUTRON RADIOGRAPHY

The McMaster RTNR system is capable of producing motion pictures of the neutrons as they pass through the object of interest. The difference in neutron intensity at the RTNR system is recorded as a varying level of black and white intensity. Harvel[113] has demonstrated the practical application of this RTNR system on various flow geometries using air-water two-phase flow but the use of this system as a void distribution measurement device for flow boiling applications have not yet been studied. Equation 4.3 for a two-phase flow boiling system can be written as;

$$\frac{I}{I_o} = B u\, e^{-\Sigma'_{wall} y_{wall}} e^{-\Sigma'_l y_l} e^{-\Sigma'_v y_v} \qquad 4.4$$

where the subscripts w, l and v denote the wall, liquid and vapor contribution respectively. The thermal neutron attenuation of the gas phase is negligible compared to the other terms as shown in references[77]. Furthermore, for path lengths less than 2.5 cm the build-up factor does not significantly differ from unity so that;

$$\frac{I}{I_o} = e^{-\Sigma'_{wall} y_{wall}} e^{-\Sigma'_l y_l} \qquad 4.5$$

The liquid thickness can be calculated based on intensity measurements using;

$$y_l = -\frac{1}{\beta \Sigma'_l} \ln\left(G_w \frac{I}{I_o} \right) \qquad 4.6$$

where β is a calibration constant to account for neutron to photon conversion and photo-multiplier effects. G_w is the wall loss term given as;

$$G_w = e^{-\Sigma^t_{wall} y_{wall}} \tag{4.7}$$

For an RTNR image with a test section full of liquid, the measured liquid thickness is given as;

$$y_{full} = -\frac{1}{\beta \Sigma^t_l} \ln\left(G_w \frac{I_{full}}{I_{empty}} \right) \tag{4.8}$$

where I_{full} and I_{empty} are the full and empty measured intensities respectively. The measured liquid length in a two-phase image can be calculated using;

$$y_{tp} = -\frac{1}{\beta \Sigma^t_l} \ln\left(G_w \frac{I_{tp}}{I_{empty}} \right) \tag{4.9}$$

where I_{tp} is the measured two-phase intensity. The chordal void fraction can then be calculated using;

$$\tilde{\alpha} = 1 - \frac{y_{tp}}{y_{full}} = 1 - \frac{\ln\left(G_w \frac{I_{tp}}{I_{empty}} \right)}{\ln\left(G_w \frac{I_{full}}{I_{empty}} \right)} \tag{4.10}$$

This derivation combines the single-phase empty, full and two-phase images so that the calibration constant β is not required. Simplifying this expression gives;

$$\tilde{\alpha} = \frac{\ln\left(G_w I_{full}\right) - \ln\left(I_{tp}\right)}{\ln\left(G_w I_{full}\right) - \ln\left(I_{empty}\right)} = \Pi\left(1 - \frac{\ln\left(I_{tp}\right)}{\ln\left(G_w I_{full}\right)} \right) \tag{4.11}$$

where Π is an overall system array constant calculated based on the empty and full images as (no geometry information is required);

$$\Pi = \left(1 - \frac{\ln\left(I_{empty}\right)}{\ln\left(G_w I_{full}\right)} \right)^{-1} \qquad 4.12$$

The above calibration constant is fixed for a given test section geometry, beam position and camera setup. For thin, or low attenuation wall materials G_w is approximately 1. From Equation 4.11, the cross sectional averaged void fraction can be calculated as;

$$\alpha = \frac{\int L\tilde{\alpha}\, dy}{\int L\, dy} \qquad 4.13$$

where L is the total length of the flow channel at a given location.

The present RTNR system is capable of measuring the void fraction in a 27 cm x 27 cm viewing area, which is a significant area compared to other void fraction measurement techniques.

Figure 4.2 shows both an RTNR raw images (brightness and contrast enhanced for visibility). Figure 4.2a shows the empty vertical test section, and a portion of the test section enlarged to illustrate the tube walls and the water annulus while Figure 4.2b shows the full test section. Figure 4.2c and 4.2d show time averaged flow boiling results for smooth and swirl-flow boiling. An instantaneous RTNR image of swirl flow boiling is shown in Figure 4.2e.

4.2.1 Vertical RTNR Radial Void Distribution Reconstruction

For flow boiling in a vertical test section the radial distribution in the channel at a given axial location can be calculated based on the measured chordal void fractions from above. Figure 4.3 shows the cross sectional image of a vertical circular test section along with the camera surface, pixel locations and the neutron pathway for each pixel. The cross section is discretized into 26 half-ring sections with 1 pixel width. The average neutron path length in the center of each pixel location, i, across the whole channel is given as;

$$\xi_i^T = 2\sqrt{R^2 - \left(R - \frac{i-0.5}{n}D\right)^2} \qquad 4.14$$

where R and D are the tube radius and diameter respectively. At pixel location i, the individual path length in that specific ring is given as;

$$\xi_i = 2\sqrt{\left(R - \frac{i}{n}D\right)^2 - \left(R - \frac{i-0.5}{n}D\right)^2} \qquad 4.15$$

and the other path lengths at pixel i, can be calculated using;

$$\xi_j = 2\sqrt{\left(R - \frac{j}{n}D\right)^2 - \left(R - \frac{i-0.5}{n}D\right)^2} - \sum_{y=i}^{j} \xi_y \qquad 4.16$$

where j ranges between i-1 and 1. Using the relations given in Equation 4.15 and 4.16 the chordal void fraction can be formulated in terms of the contributions from the local void fraction α, in each ring;

$$\tilde{\alpha}_i = \sum_{y=2}^{i} \frac{\alpha_y \xi_y}{\xi_i^T} \qquad 4.17$$

where the void fraction in at the first pixel position (i = 1) is given by Equation 4.14. Inverting this relationship we can calculate the local void fraction in each ring. The local void fraction in ring segment i, is;

$$\alpha_i = \frac{\tilde{\alpha}_i \xi_i^T - \sum_{y=2}^{i-1} \alpha_y \xi_y}{\xi_i} \qquad 4.18$$

This process can be applied up to the center of the test section and is repeated on the adjacent side to provide the distribution across the entire channel, thus obtain the radial void fraction distribution at a given axial location. The center pixels can also be used to smooth the void values at the intersection of these two-half circles. For the results shown in Chapter 6 and 7, a three point averaging function based on the three pixels closest to the centerline was used to smooth the centerline void reconstructions to correct this discretization problem. These steps were iterated for each axial location to provide a complete reconstruction of the axial and radial void distribution.

4.2.2 RTNR Image Processing

The RTNR images are digitized using the DT3152 and computer hardware outlined in Chapter 3. Figure 4.4 shows the flow chart of image processing operations. The image acquisition is controlled using *HLImage++ 99* with the image capturing software add-on. This program is capable of acquiring up to 330 consecutive frames (10 seconds) of instantaneous results or continuous averaging for up to 5 minutes. The acquired grayscale images are 8 bits per pixel, providing 256 grey levels. To reduce noise, instantaneous images are filtered using a modified median filter at every pixel location based on the surrounding pixels;

$$I' = \frac{1}{48}\begin{bmatrix} 1 & 1 & 1 & 1 & 1 \\ 1 & 2 & 3 & 2 & 1 \\ 1 & 3 & 12 & 3 & 1 \\ 1 & 2 & 3 & 2 & 1 \\ 1 & 1 & 1 & 1 & 1 \end{bmatrix} I \qquad 4.19$$

where I and I' are the original intensity and filtered intensity respectively. This smoothing matrix accounts for proximity of adjacent pixels used for smoothing the center pixel. For time-averaged images a smaller smoothing matrix was used due to noise reduction already accomplished during averaging. The matrix used for time-averaged images is given as;

$$I' = \frac{1}{18}\begin{bmatrix} 1 & 2 & 1 \\ 2 & 6 & 2 \\ 1 & 2 & 1 \end{bmatrix} I \qquad 4.20$$

These images can be saved as bitmap (BMP) or tagged images (TIF) and exported into any image analysis program. To correct for small errors in camera orientation, such as the camera being off horizontal, the images can be processed in *Photoshop v5.01* and cropped to a 640 by 480 pixel image. The program CONV99.FOR, which is a DOS based FORTRAN 77 compatible program developed specifically to extract the integer values from the BMP or TIF images for each pixel and writes the integer representation of the intensity to an output file.

The integer based files can then be processed using VOID99.FOR, a second FORTRAN 77 program containing the routines necessary to calculate the chordal void fraction at each pixel, the cross sectional averaged void fraction axial distribution and the three dimensional void reconstruction using the inverse method described above.

Both the processed radial void distributions and raw digitized images can be saved in a compressed format know as GIF. This compression reduces the file size from approximately 300 KB to 5 KB, with some loss of detail. The advantage of this format is that these images can be loaded into an animation software program (*GIF-ANIMATE™*) that can play the images in sequence showing a movie of the void behavior as it travels through the channel. This type of analysis greatly simplifies the tracking of void pockets in the test section and therefore could reduce systematic errors in the calculation of void velocity and acceleration.

4.2.3 RTNR Void Distribution Dependencies

Figure 4.5 shows two types of flow patterns that show the effect of void distribution on RTNR measurement and for each case there is the same line integral void fraction. The accuracy of the idealized neutron attenuation approximation given in Equation 4.1 decreases with increased thickness with the effect of build-up factor being a non-linear function of thickness. This means that the neutron attenuation behavior may change depending on the liquid thickness and arrangement in the test section. Harvel[113] has shown that this effect is not significant in comparing bubbly to slug type flows, but may be more pronounced in comparing intermittent (where the liquid thickness alternates between a larger value when the liquid slug is present, and a lower value after the slug has passed) and annular flows (where there is a consistent liquid film on the wall). The non-linear build-up effect was also shown to contribute significantly to void measurement errors in water for liquid thicknesses over 2.54 cm. Harvel applies a different calibration factor for test sections larger than the 2.5 cm threshold, but this calibration factor can change as vapor causes the liquid thickness to decrease below this threshold during testing.

4.3 ACCURACY OF VOID RECONSTRUCTION METHODOLOGY

In addition to the errors resulting from the electronic noise, neutron backscatter (in the experimental section as well as from shielding walls), and camera intensity drift (which are minimized by warming the camera up for a minimum of 2 hours before experiments are begun) there are additional uncertainties. These uncertainties result from the afterglow (reset time) of the converter and photo-multiplier combination as well as the statistical nature of neutron-material interaction. Mishima and Hibiki have estimated the reset time at 100 μs for their system. No details were provided on whether this characterization was experimentally or analytically based, but Bossi et al.[143] presented the state of the art convertor technology decay coefficients for several doping concentration vs. intensifier screens. Given the lower Lithium doping in the current convertor, and the age of the image intensifier in the present system, it can be conservatively estimated that this system's convertor reset time is approximately 1 ms.

The statistical nature of neutron-material interactions was also quantified by Mishima and Hibiki as;

$$E = \sqrt{\frac{e^{\Sigma\delta}}{\phi_{th}\,\Delta t\,R^2\,N}} \qquad 4.21$$

where Σ is the cross section of the liquid phase (cm^{-1}), δ is the maximum liquid thickness (cm), ϕ_{th} is the thermal neutron fluence (n/cm^2), Δt is the frame speed, R is the length (in cm per pixel), and N is the number of averaging frames (if any). For the current frame rate (33ms), neutron flux at the test section (3×10^6 n/cm^{2}s), pixel size (0.1 cm/pixel) and liquid thickness (0.7 cm), the two-sigma statistical error calculated using Equation 4.21 will be less than 4%. However due to source of error resulting from convertor screen imperfections, biological shielding scatter, optical electronics and analogue video to digital conversion the uncertainty can be much higher as shown in Appendix D.

In general, the literature review has shown that time-averaged RTNR cross sectional averaged void fraction ranges from 4 to 8% depending on the facility, reconstruction techniques and test section geometries. Furthermore, Harvel[113] has shown that for some phase distributions (stratified horizontal flow), the local void fraction and liquid hold-up measured using RTNR, agrees with ultrasonic measurements to within 10 to 15%. It should be noted that most of these studies involved measurement of water-air two-phase flow, so the impact of void acceleration, generation and collapse on the accuracy is not included.

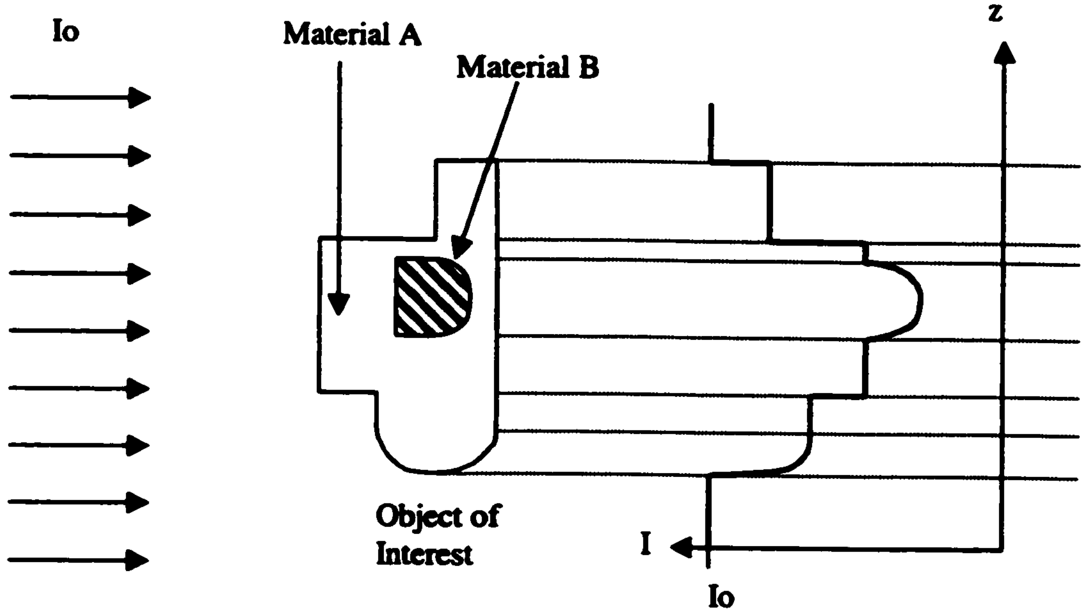

Figure 4.1 Schematic of Basic Radiographic Principles.

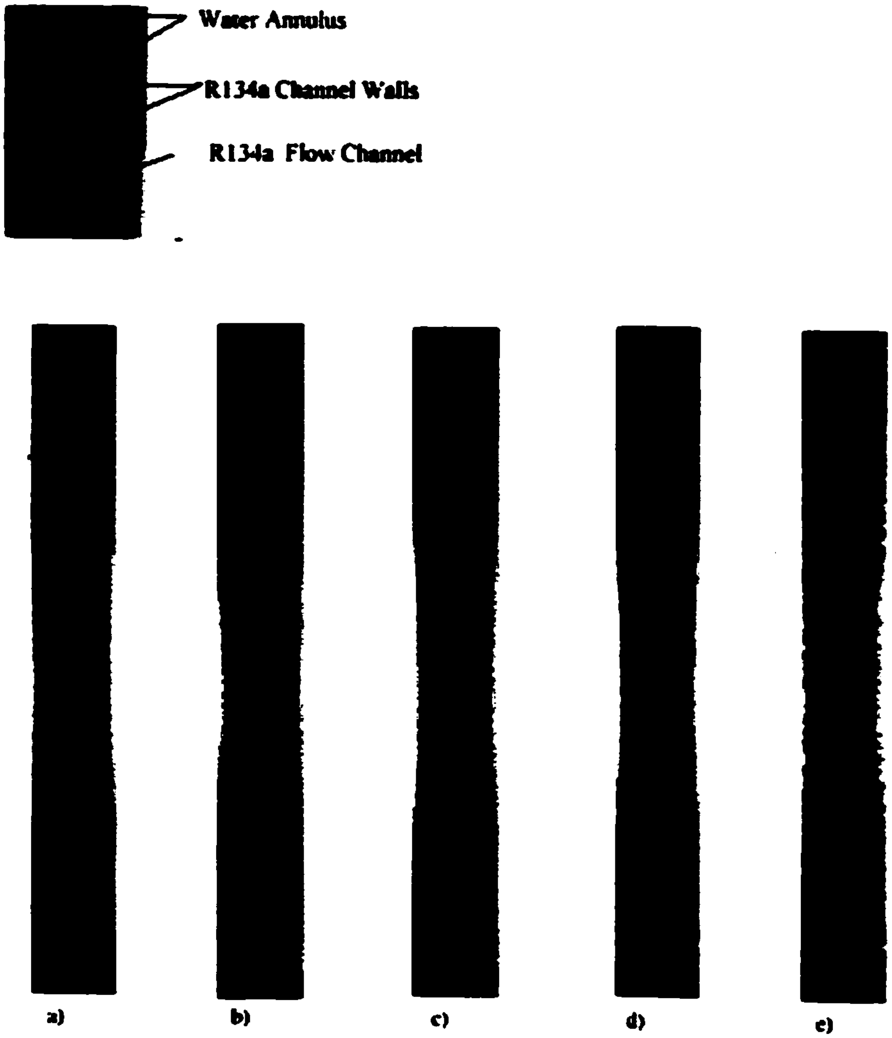

Figure 4.2 Unprocessed RTNR Images for an a) Empty Channel, b) Full Channel, c) Time Averaged Smooth-flow Boiling, d) Time Averaged Swirl-flow Boiling and e) Instantaneous Swirl-flow Boiling.

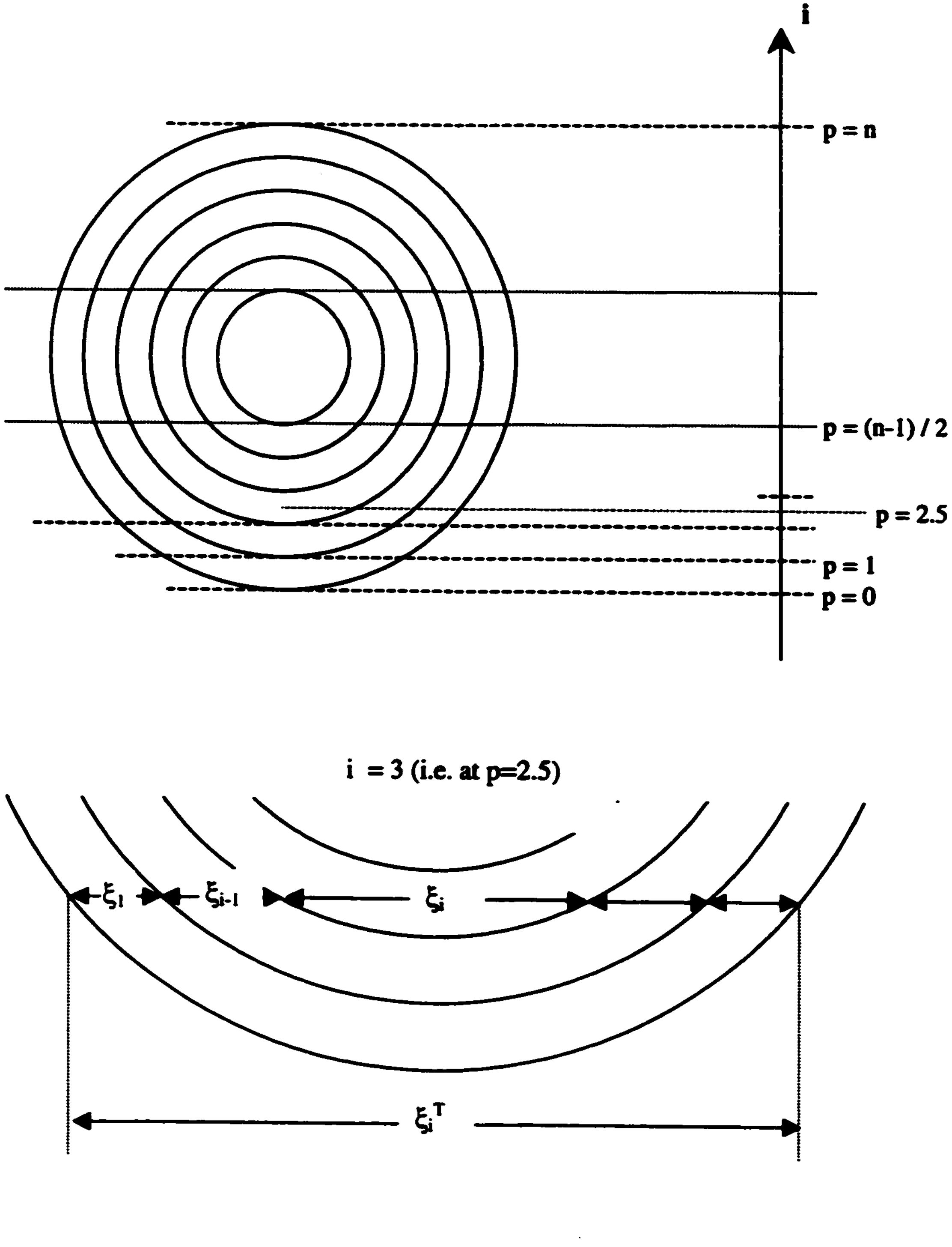

Figure 4.3 Radial RTNR Void Distribution Reconstruction Theory.

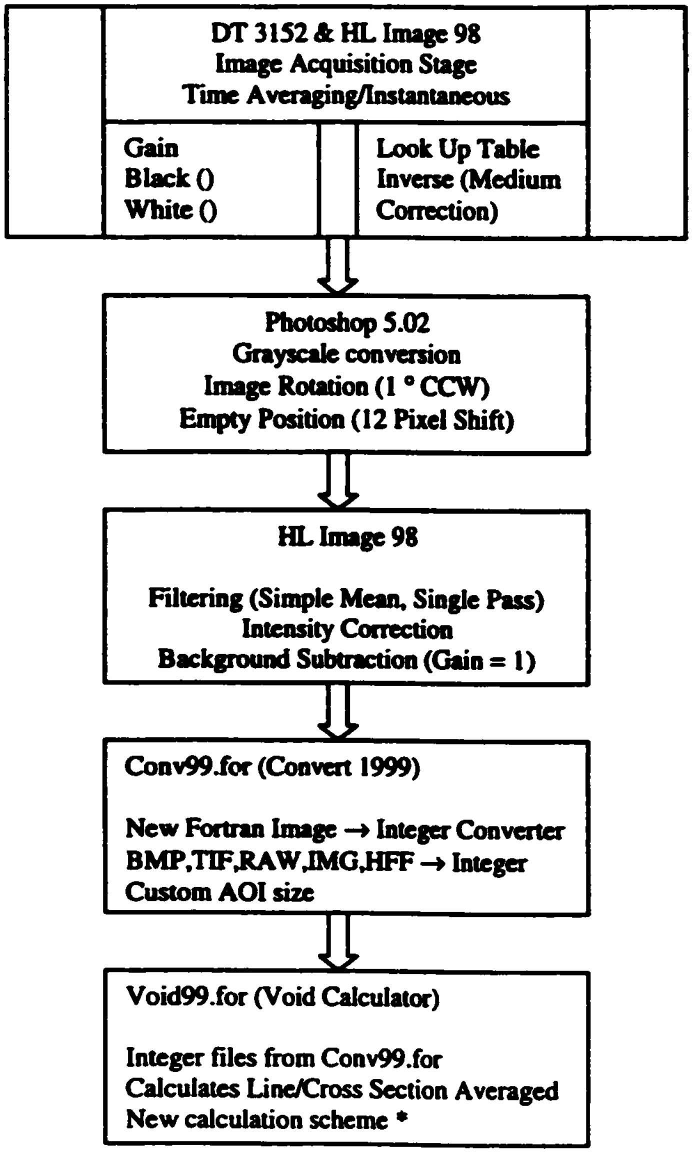

Figure 4.4 Image Processing Flow Chart.

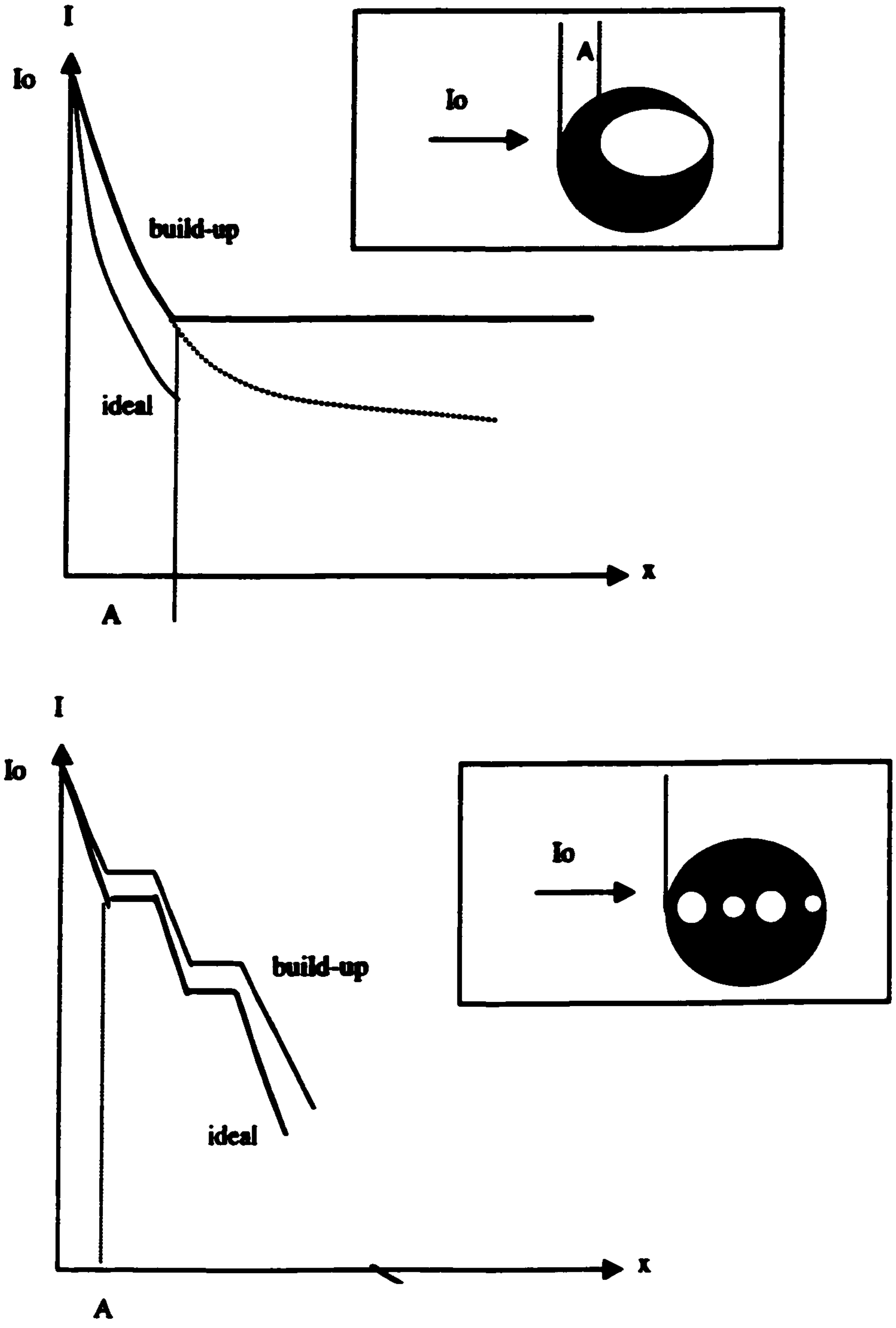

Figure 4.5 Effect of Flow Distribution on RTNR Void Measurement.

CHAPTER 5 HEAT TRANSFER AND PRESSURE DROP CHARACTERISTICS

The heat transfer and thermal performance characteristics of energy production, chemical processing or heat exchanger systems is influenced by the presence of two or more phases. For tube-side flow, the generation of a vapor phase through boiling can lead to either increases or decreases in the heat transfer depending on the void generation and distribution in the system. Therefore, predictive techniques used in operational or safety analysis often rely directly on void generation and distribution characteristics obtained from measurements. This chapter outlines the thermal performance characteristics of the tube-side flow boiling test sections described in Chapter 3. Chapters 6 and 7 provide void distribution measurements that relate directly to the heat transfer performance discussed below.

5.1 SMOOTH FLOW

The boiling curve for horizontal flow without a twisted tape insert is shown in Figure 5.1 at a mass flux of 100 kg/m^2-s, 630 kPa and 9 °C subcooling. During single-phase operation the heat flux increases with increasing wall superheat and the slope of the curve in this region can be used to experimentally determine the convective heat transfer coefficient for these conditions. As the heat flux and wall superheat increase further, the onset of nucleate boiling is reached resulting in a change of the heat transfer mechanism. This change in mechanism causes a change in the boiling curve slope that can be used to correlate the ONB heat flux and surface temperature condition. For increasing heat fluxes above ONB, the wall superheat increases and the curve can again be used to establish an experimentally based correlation for a given fluid, conditions, and geometry. These boiling curves provide important information on the mode of heat transfer taking place and are used in Chapter 6 and 7 to discuss the effects of void distribution on these systems.

Correlations established using the above techniques are not directly portable to other systems (i.e. different fluids, geometry etc.) and even for a specific fluid such as water, there can be a significant deviation between experiments[19, 41]. Furthermore, for safety analysis of complex system such as nuclear and conventional power generation systems, simple correlations for the overall heat transfer coefficient are not possible. To solve these systems multidimensional solution of the conservation equation is used with constitutive relationships describing the interchange of mass, momentum and energy between the phases as described in Chapter 1.

5.1.1 Effect of Mass Flux

The effect of mass flux on boiling curves is shown in Figure 5.2 for flow boiling at 630 kPa and 6 °C subcooling. The single phase heat transfer is significantly increased with increasing mass flux as expected due to increased turbulent heat transport. Figure 5.2 also shows an increase in the heat flux and wall superheat corresponding to ONB indicating that increasing the mass flux prolongs the single-phase liquid regime so that higher energy densities are required to initiate boiling. For two-phase flow boiling the mass flux does not significantly affect the heat transfer behavior of this system. Once subcooled boiling has been initiated, there is a large increase in the turbulence near the wall due to bubble creation and collapse. However other authors have shown a significant mass flux effect in higher heat flux experiments and near CHF that may result from a change in the void distribution with mass flux that has previously not been studied thoroughly[20].

5.1.2 Effect of Inlet Subcooling

Figure 5.3 shows the effect of inlet subcooling on the boiling curves for Refrigerant 134a at 100 kg/m^2-s and a system pressure of 630 kPa. The slopes for each single-phase portion of the curves are similar with the small changes resulting from changes in the wall-to-fluid temperature differences (which affects the total heat transfer) and/or changes in the heat transfer coefficient with changes in fluid properties (thermal conductivity, specific heat etc.). The ONB heat flux and wall superheat are significantly affected by inlet subcooling that may result from increased energy requirements to generate vapor for increasing subcooling. The subcooled boiling curves merge together indicating that during subcooled boiling there is no significant inlet subcooling effect indicating that the increased wall region turbulence previously discussed overrides any inlet subcooling effects. Again at higher heat flux conditions and near

CHF, inlet subcooling can significantly affect heat transfer performance which again indicates that subcooling may significantly affect void distribution.

5.1.3 Effect of System Pressure

System pressure affects ONB and flow-boiling behavior but does not significantly affect the single-phase heat transfer performance as shown in Figure 5.4 for an inlet subcooling of 6 °C and mass flux of 100 kg/m^2-s. During subcooled single phase flow of Refrigerant 134a, the fluid properties are relatively constant with respect to pressure and hence there is little effect on the heat transfer behavior. The ONB condition is significantly affected by pressure due to a shift in the saturation temperature and possible effects on the heat required to sustain vapor in a higher pressure system. Figure 5.4 also shows that system pressure significantly affects the flow-boiling heat transfer behavior as evident in the change of the slope in the two-phase region. This behavior may result from changes in the flow distribution and bubble size that can result in increased heat transfer coefficients.

5.2 SWIRL FLOW

The advantages of swirl-flow inserts were thoroughly discussed in Chapter 2. This section examines the thermal performance characteristics of internal twisted tape generated swirl-flow in a tubular channel. These enhancement devices can significantly enhance single phase heat transfer and ONB behavior but do not significantly enhance heat transfer during two-phase flow boiling. During nucleate boiling the intense wall turbulence caused by bubble creation, departure and collapse overrides the turbulence enhancement caused by flow swirling. However authors[49,50] have shown that swirl-flow can enhance very high heat flux behavior and

CHF by up to two times. This enhancement may be a result from changes in the void distribution as shown in Chapter 6 and 7. Below the heat transfer performance under various mass flux, inlet subcooling and pressures as well as twisted tape ratios are discussed.

5.2.1 Effect of Twist Ratio

The heat transfer performance gained by internal twisted tape generated swirl-flow is shown in Figure 5.5 for flow boiling at a constant mass flux, pressure and temperature of 100 kg/m^{2}s, 630 kPa and 9 °C subcooling. Single-phase heat transfer increases with decreasing twist ratio (i.e. since the twist ratio is inversely proportional to the number of pitch, a tube without an insert will have an infinite twist ratio and an insert with a high degree of twist will have a low twist ratio) that may be due to increased turbulence and the overall increase in the available heat transfer length over smooth flow caused by the helical fluid path. The heat flux and wall superheat required for ONB also increases with decreasing twist ratio that may be caused by centrifugal forces that drive cooler (more dense) liquid to the heat transfer surface and may also increase the local pressure in the wall region. This is evident from the rotational Bernoulli equation for a constant density fluid that states;

$$P - P_0 = \frac{\rho\omega^2 r^2}{2} - \rho g\left(z - z_0\right) \qquad 5.1$$

where P and P_0 are the local pressure and mean fluid pressure respectively, ω is the rotational velocity, r is the radial position, and ρ is the fluid density. From this equation it is evident that an additional pressure component is generated in swirl-flow by the angular velocity caused by the helical path. This tends to increase the local pressure in the wall region that may delay ONB to higher heat flux and wall temperature conditions.

5.2.2 Effect of Mass Flux

Figure 5.6 shows the flow boiling curves for a range of mass fluxes at a system pressure of 630 kPa and inlet subcooling of 9 °C. The heat transfer behavior is similar to the smooth-flow case shown previously. Increasing mass flux increases both the single-phase heat transfer and ONB heat flux/wall temperature respectively but does not significantly affect the subcooled boiling characteristics similar to the smooth-flow case.

5.2.3 Effect of Inlet Subcooling

The effect of subcooling on the swirl-flow boiling curves is shown in Figure 5.7. These figures show similar trends as the smooth-flow case with small single-phase heat transfer improvement, a large change in the ONB conditions and no significant two-phase flow boiling affect. Similar to the smooth-flow case, the small changes may result from changes in the driving temperature difference, or changes in the heat transfer coefficient with differing levels subcooling.

5.2.4 Effect of System Pressure

Figure 5.8 shows that the system pressure affects the flow boiling behavior of swirl-flow with similar mechanisms as the smooth-flow case at 630 kPa and 6 °C inlet subcooling. Fluid properties depend only weakly on pressure because the liquid is in a subcooled state and therefore only affects the single-phase heat transfer indirectly. The ONB heat flux and wall superheat significantly depend on the system pressure for the same reasons as discussed above for the smooth-flow case. System pressure does affect the flow boiling heat transfer rate that again may result from vapor size and distribution in the channel that varies with pressure.

These figures also show that swirl-flow does not significantly contribute to the heat transfer performance after ONB. However many authors[20] have shown that the very high heat flux behavior (near CHF) is strongly influenced by swirling flow as shown in Figure 5.9. This indicates that the void distribution in a swirl-flow channel has definite benefits at higher heat flux over the smooth-flow case and will be discussed in Chapter 7.

5.3 PRESSURE DROP RESULTS

The effect of mass flux on the test section pressure drop waveforms is shown in Figure 5.10 for smooth-flow at 9 °C inlet subcooling and 630 kPa. The pressure drop increases with increasing mass flux as expected but the intensity of the fluctuations decreases. For increasing mass flux, the forced convective heat transfer is improved and less energy is available to generate void and hence the amount of vapor present is reduced for the higher mass fluxes as compared to the lower mass flux case (as further discussed in Section 6.1.2). Also the increased mass flux means that the turbulence levels will be increased for the higher mass flux case which will work to reduce bubble diameters and thereby reduce the magnitude of the pressure loss fluctuations. For 55 kg/m^2-s, the smooth-flow pressure drop waveform appears to have some intermittent flow characteristics but the majority of fluctuations more resemble those of bubbly type flow. These trends were similar for both the smooth and swirl-flow experiments as shown in Figure 5.11. Although the absolute pressure drop for swirl-flow shows an overall increase, the magnitude of the fluctuations is less than for the smooth flow case. This phenomena was observed in most experiments and may result from the stabilizing effect of flow swirling that alters flow regime transitions and patterns and/or from the increased turbulence in swirling flow which acts to reduce bubble size and hence the magnitude of the pressure drop fluctuations.

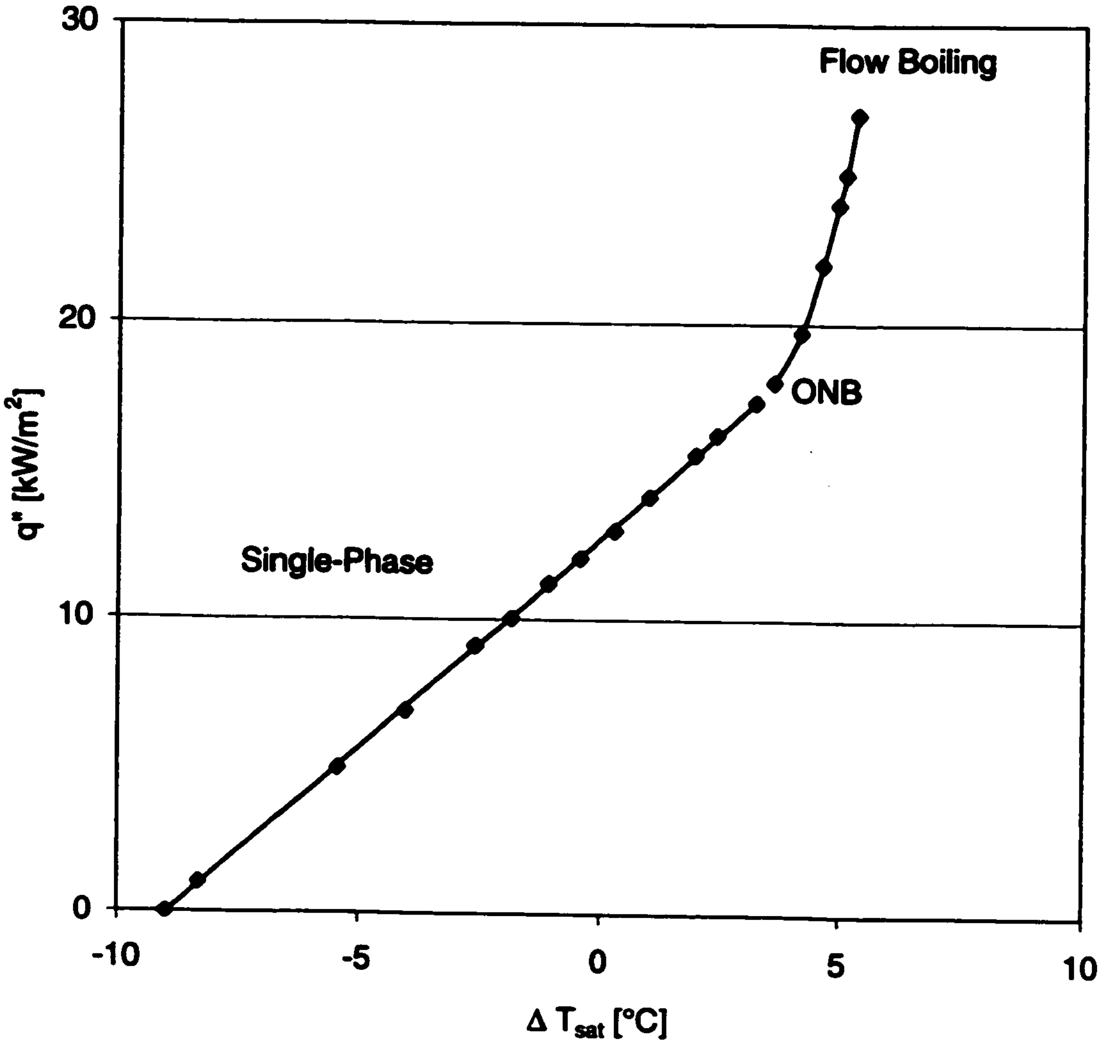

Figure 5.1 Horizontal Smooth-Flow Boiling Curve at 100 kg/m²-s, 630 kPa and 9 °C Subcooling.

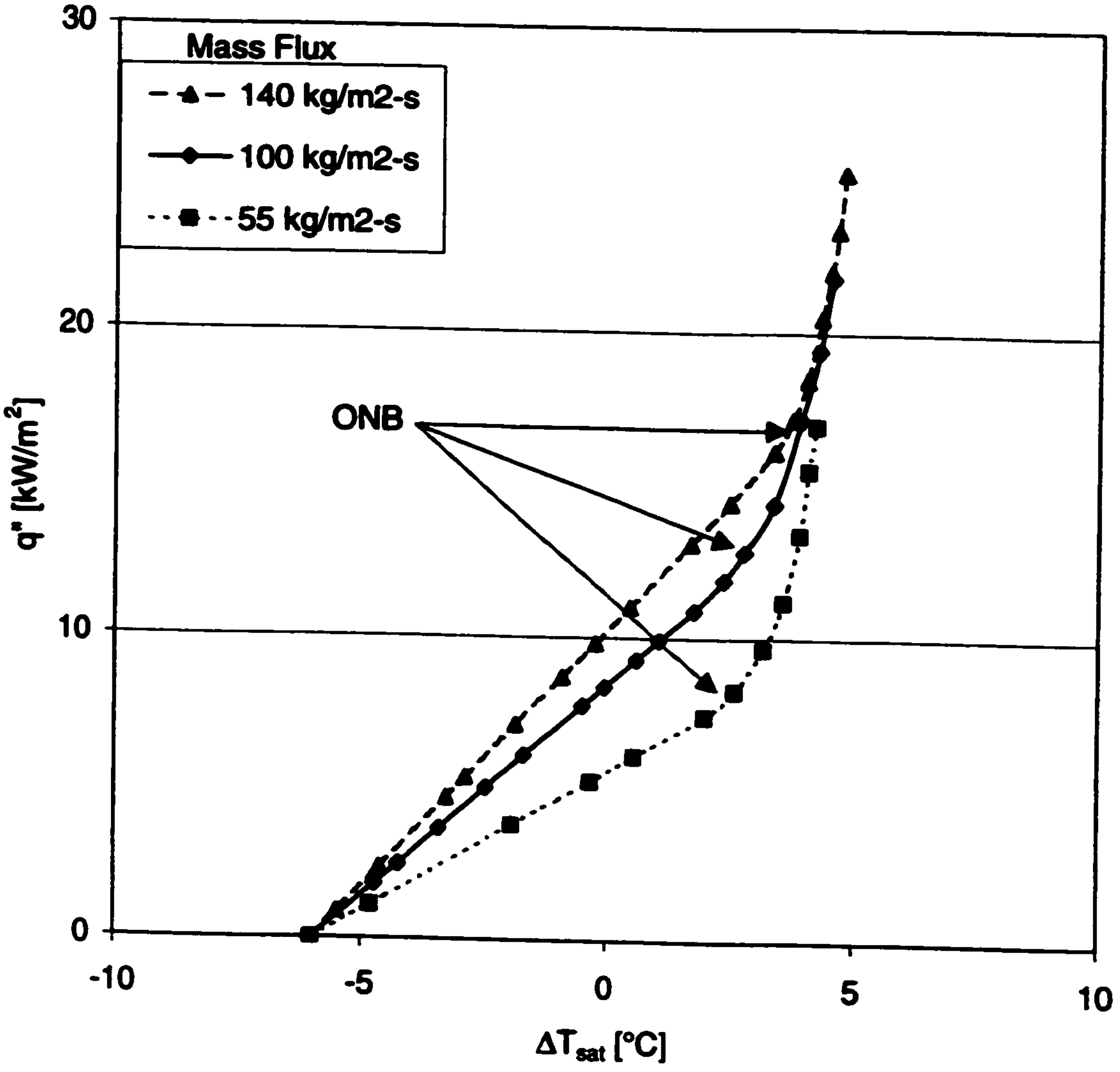

Figure 5.2 Effect of Mass Flux on Smooth-Flow Boiling of Refrigerant 134a at 630 kPa and 6 °C subcooling.

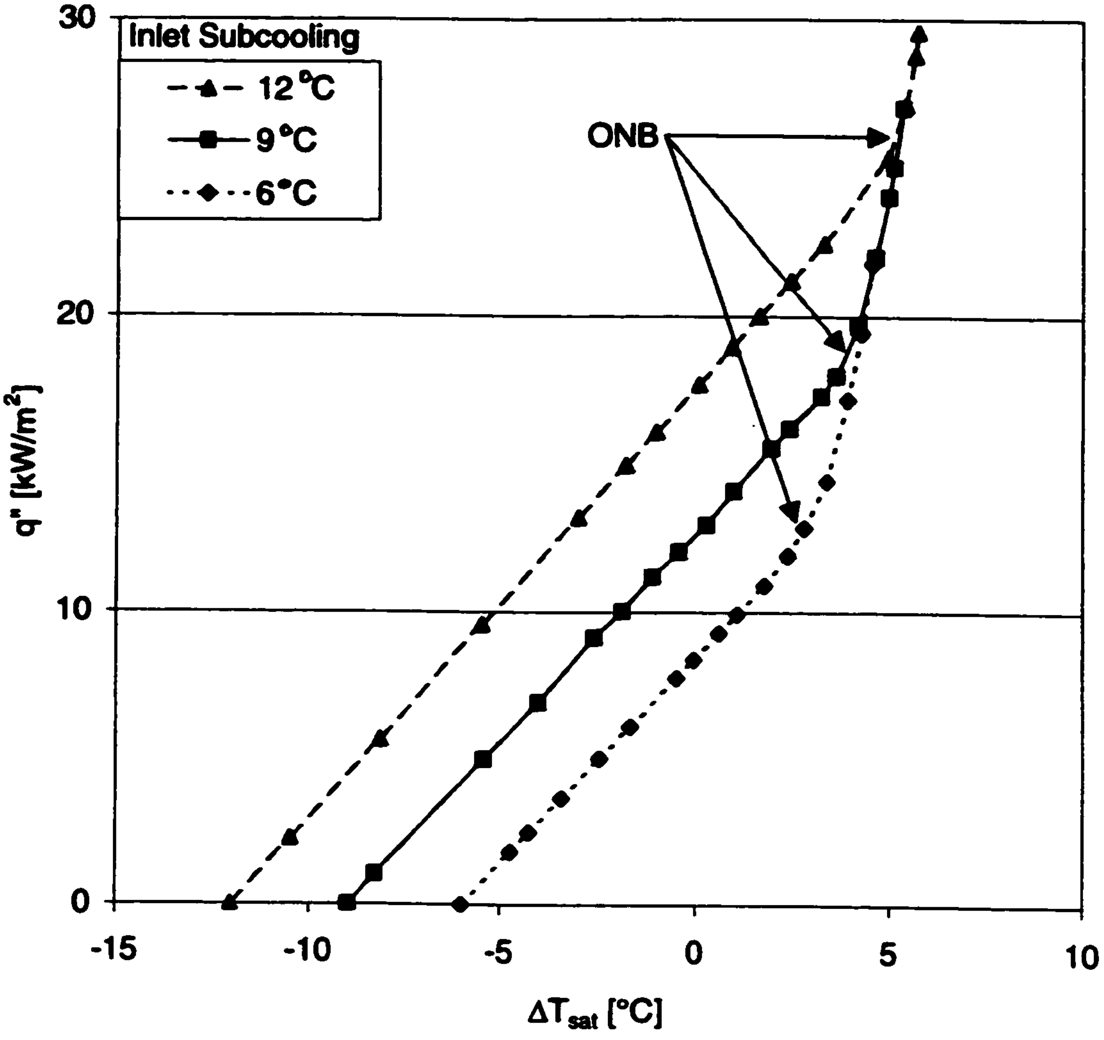

Figure 5.3 Effect of Inlet Subcooling on Smooth-Flow Boiling of Refrigerant 134a at 100 kg/m^2-s and 630 kPa.

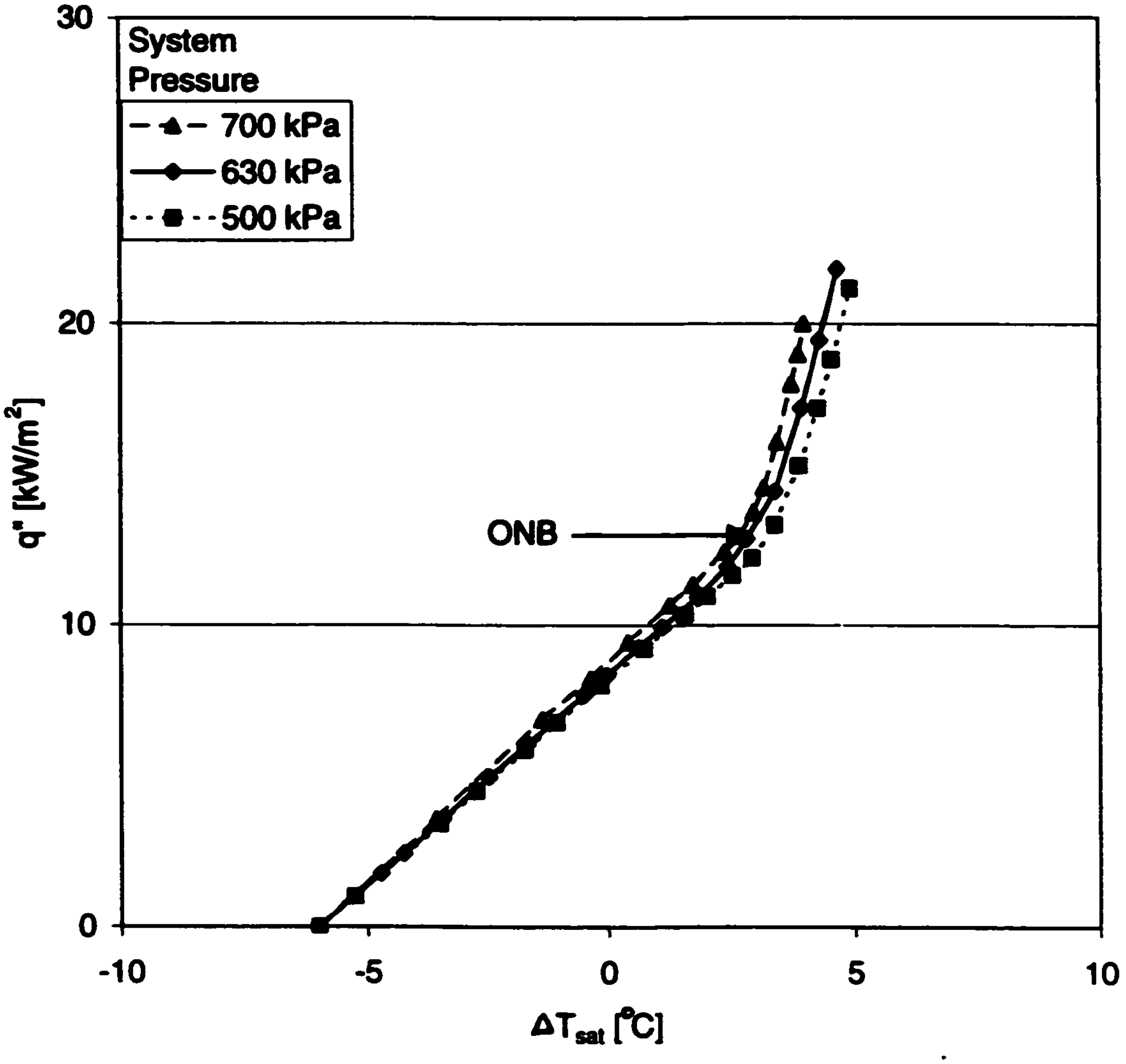

Figure 5.4 Effect of System Pressure on Smooth-Flow Boiling of Refrigerant 134a at 100 kg/m^2-s and 6 °C Subcooling.

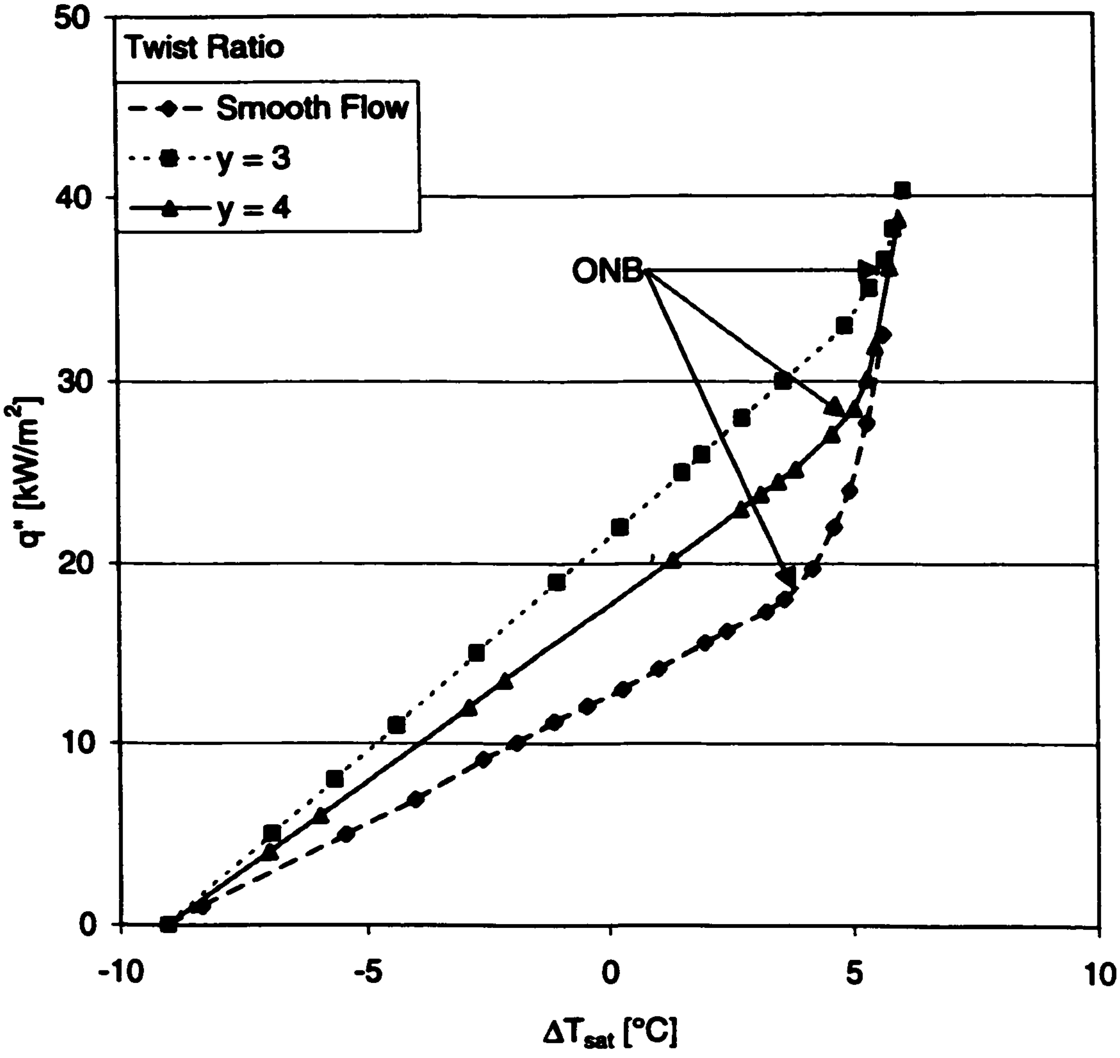

Figure 5.5 Effect of Twist Ratio on Swirl-Flow Boiling of Refrigerant 134a at 100 kg/m^2-s and 630 kPa.

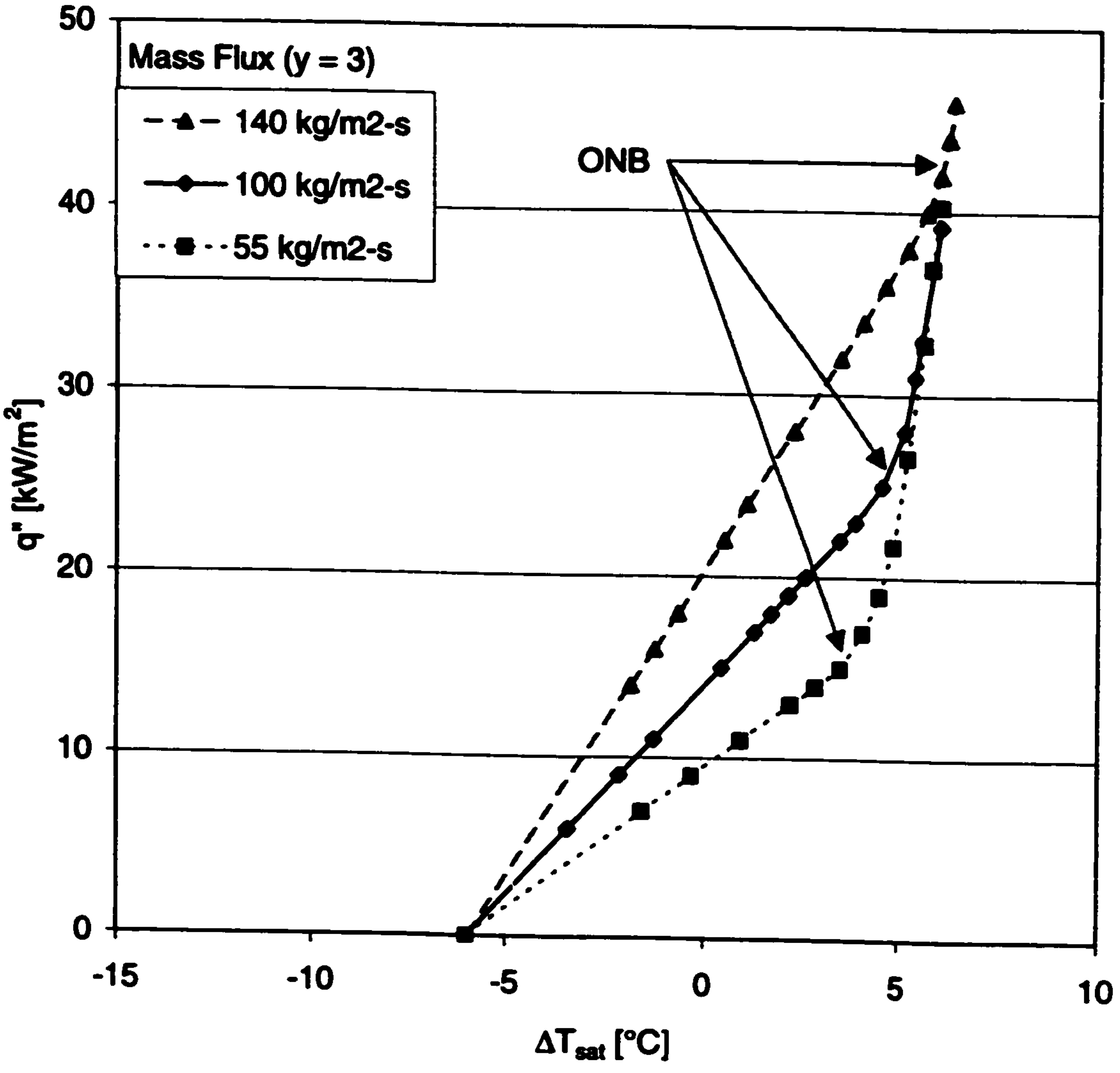

Figure 5.6 Effect of Mass Flux on Swirl-Flow Boiling of Refrigerant 134a at 630 kPa and 6 °C Subcooling.

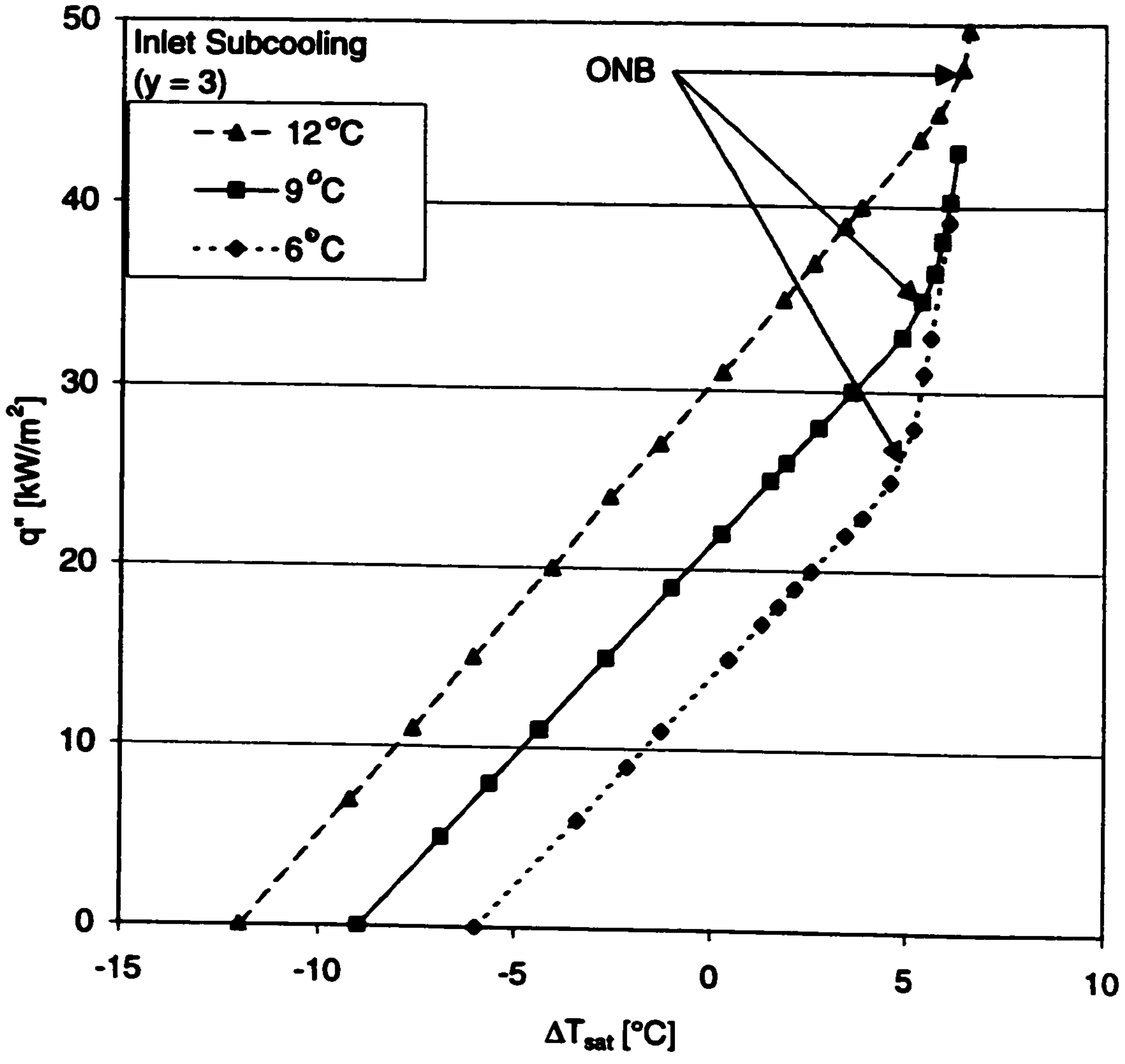

Figure 5.7 Effect of Inlet Subcooling on Horizontal Swirl-Flow Boiling of Refrigerant 134a at 100 kg/m^2-s, 9 °C Subcooling and 630 kPa.

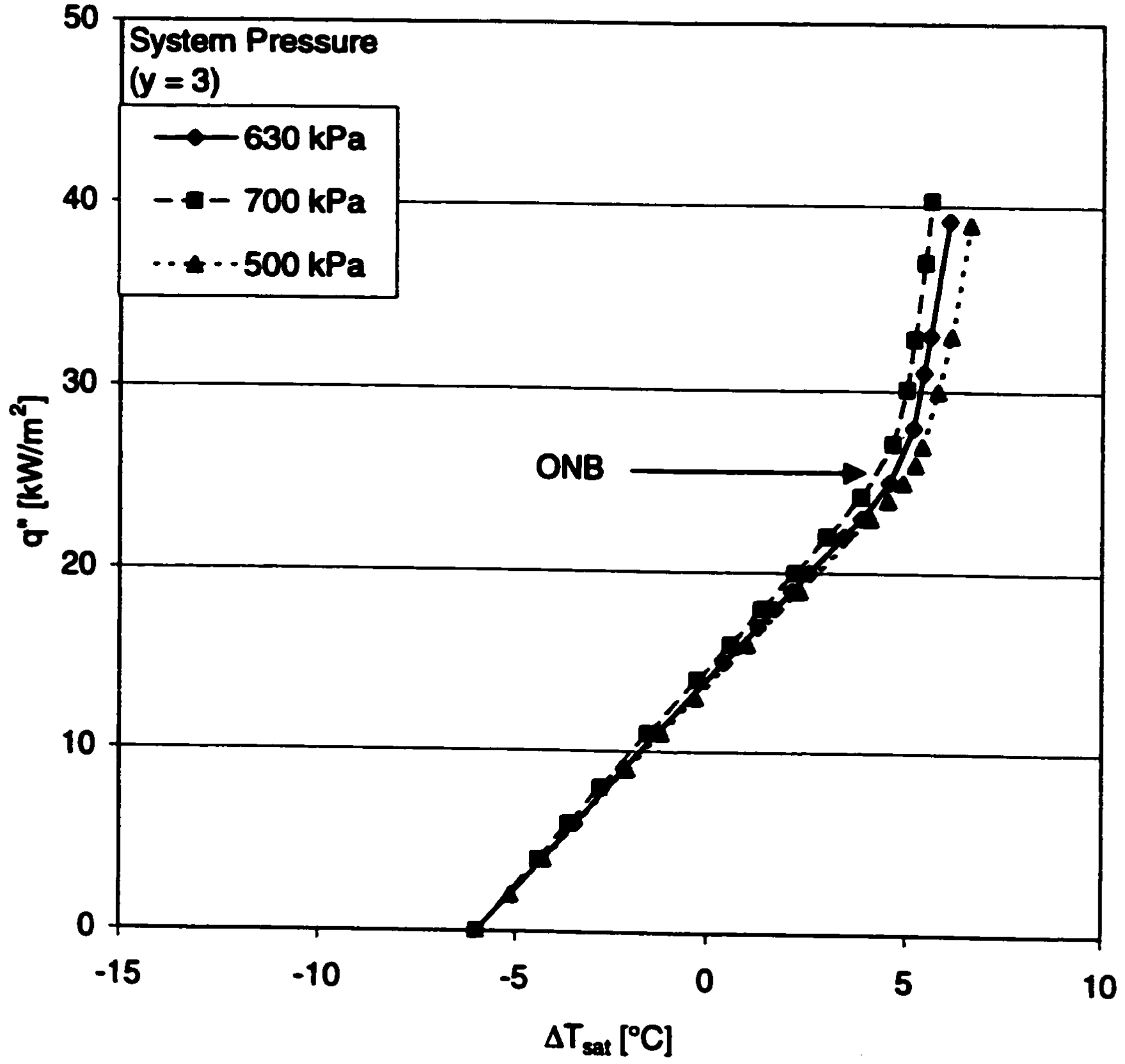

Figure 5.8 Effect of System Pressure on Horizontal Swirl-Flow Boiling of Refrigerant 134a at 100 kg/m^2-s and 6 °C Subcooling.

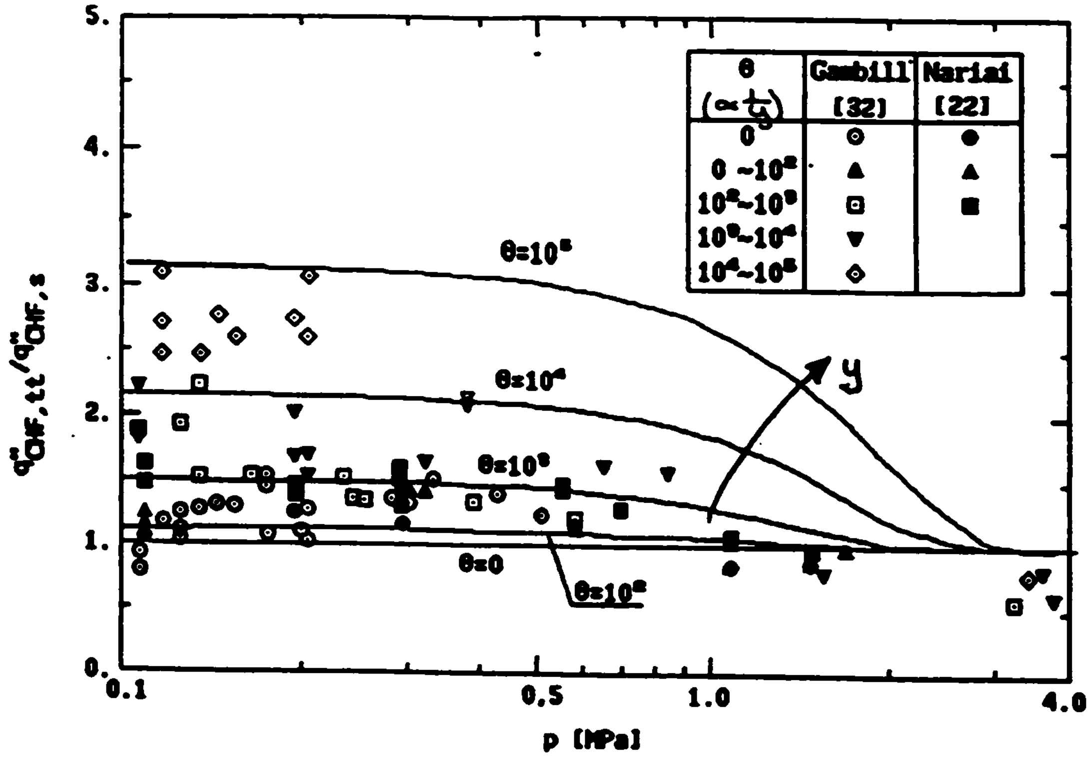

Figure 5.9 Effect of Twisted Tapes on CHF for Flow Boiling [Celata] (θ is inversely proportional to the twist ratio, hence an insert with a high degree of twist will have a high θ).

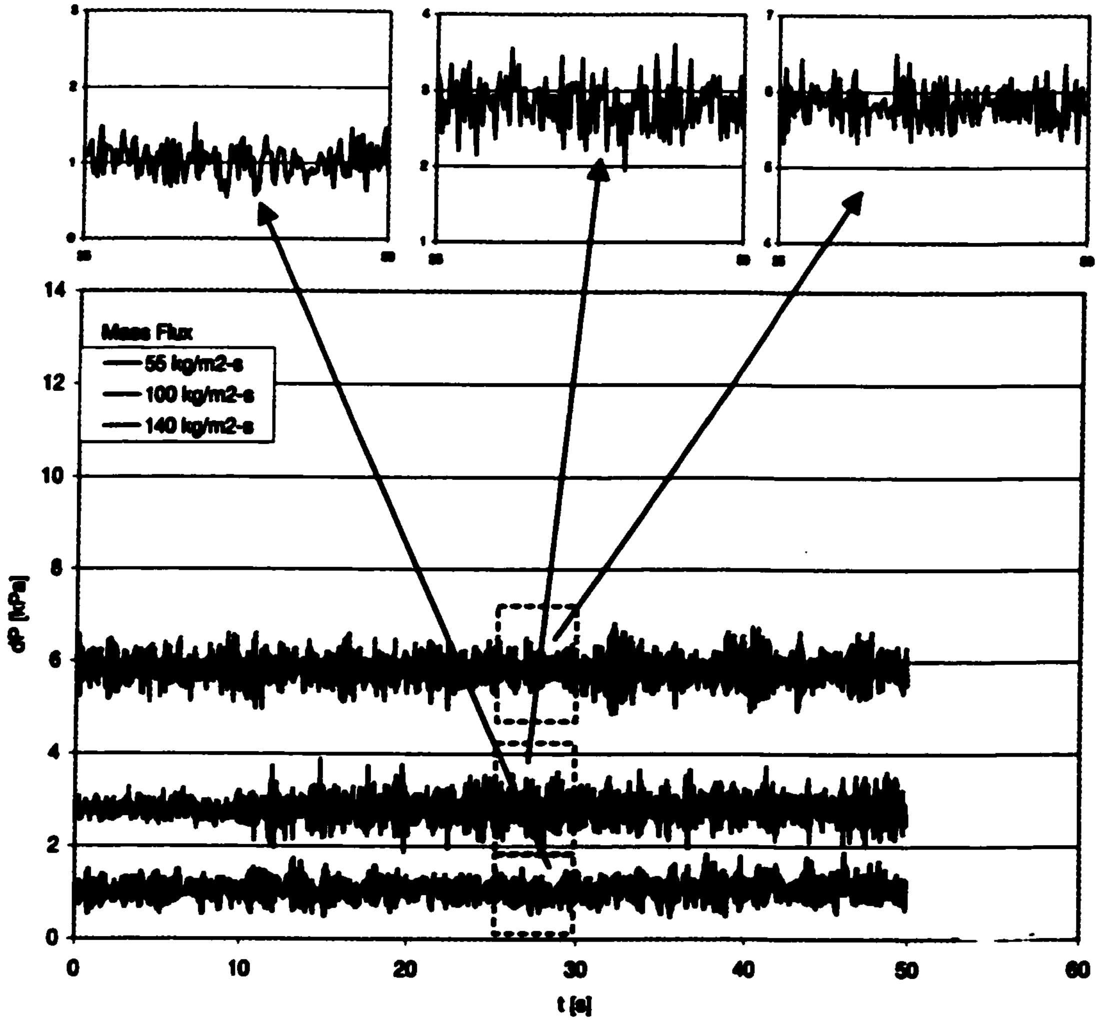

Figure 5.10 Effect of Mass Flux on Subcooled Boiling Pressure Drop Waveforms for Smooth-Flow.

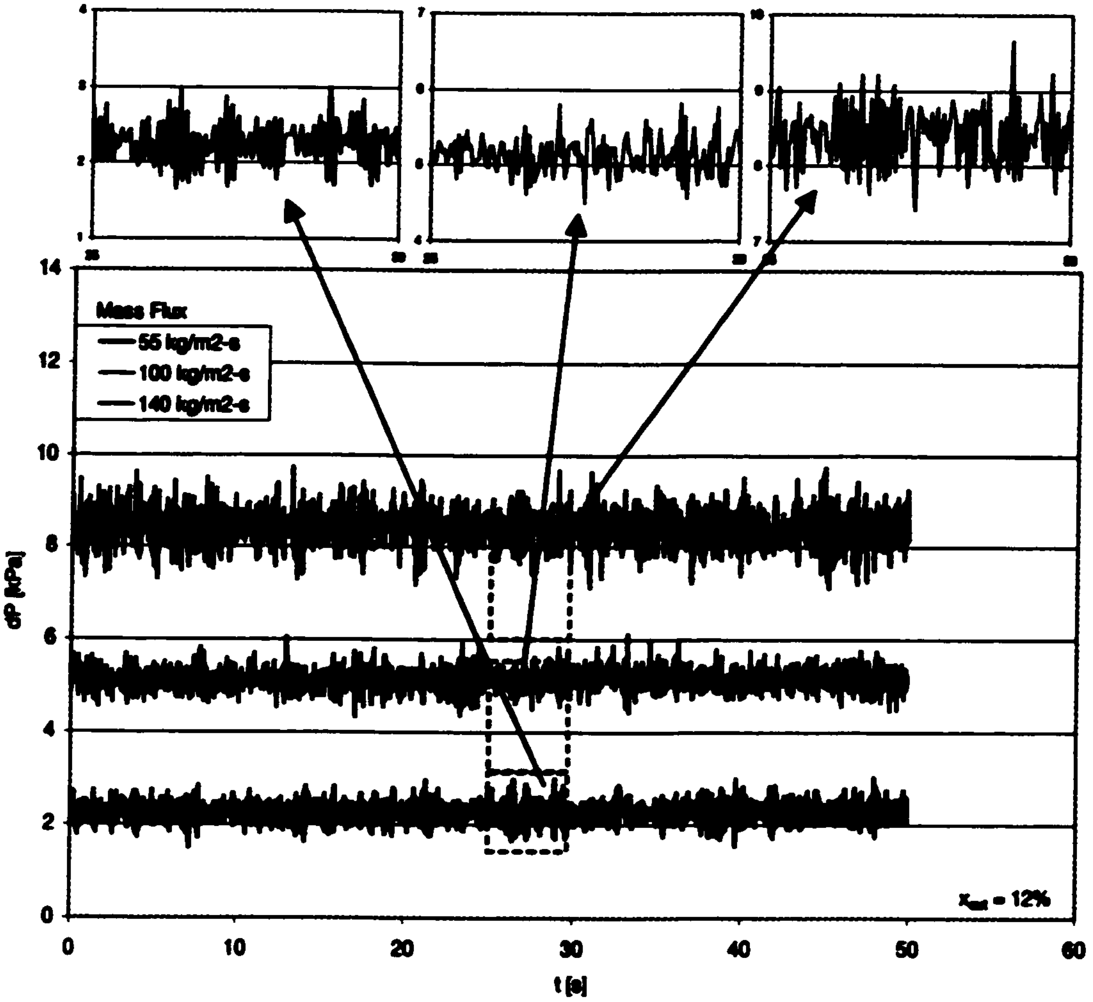

Figure 5.11 Effect of Mass Flux on Subcooled Boiling Pressure Drop Waveforms for Swirl-Flow.

CHAPTER 6 SMOOTH FLOW-BOILING VOID DISTRIBUTION MEASUREMENT

6.1 TIME AND CROSS SECTIONAL AVERAGED VOID FRACTION

Many of the techniques described in Chapter 2 for void fraction measurement obtain the cross sectional and time averaged void fractions. Using the techniques described in Chapter 4, the cross-sectional void fraction was calculated over the length of the test section using the RTNR method. These void fraction profiles provide the void fraction distribution in the axial directions as shown in Figure 6.1 for 9 °C subcooling, mass flux of 55 kg/m^2-s and system pressure of 630 kPa. The cross sectional averaged void fraction increases with increasing distance from the entrance of the heated length as expected. This results from the increase in the thermodynamic quality with increasing total heat transferred. The uncertainty of the cross-sectional and time averaged RTNR results was estimated based on repeat experiments to be ±5.6% with 95% confidence (see Appendix D). Also shown in Figure 6.1 are the void correlation predictions from Thom et al.[6], Wallis[126] and the homogenous equilibrium model for saturated flow boiling. These correlations tend to over-predict the axial void distribution because they neglect subcooling affects that tend to collapse void in the bulk liquid.

6.1.1 Effect of Inlet Subcooling

Figure 6.2 shows the cross sectional averaged void distribution profile for several liquid subcoolings at a mass flux of 55 kg/m^2-s and 630 kPa. The void fraction reduction with increased subcooling may result from both the change in the superheat required to initiate ONB, and/or the heat required to achieve similar vapor qualities.

Inspection of the axial void distribution trends shown in Figure 6.2 show that there is consistently a small change in slope at location A. This phenomena may result from a change in the flow regime which can lead to changes in the void production rate, or the slope change may result from changes in the void distribution leading to changes in the build-up or attenuation effects of neutrons in the liquid (i.e. changing the liquid thickness increases build-up). It is the authors opinion that the latter is the case, as discussed in Section 4.2.3.

6.1.2 Effect of Mass Flux

The effect of mass flux on the cross sectional averaged void fraction for smooth-flow at a pressure of 630 kPa and 6 °C subcooling is shown in Figure 6.3. The void fraction increases with decreasing mass flux which results from an increase in forced convective heat transfer and hence less energy is available for bubble nucleation. This may result in the significant reduction in the axial void fraction with increasing mass flux seen in Figure 6.3.

Figure 6.3 also shows that for mass fluxes of 55 and 100 kg/m^{2}s a similar change in slope to Figure 6.2 occurs in the slope of the axial void fraction profile. However, this effect is not present at the 140 kg/m^{2}s case. This higher inlet mass flux (and lower quality) may prevent flow regime transition and hence no significant change in neutron attenuation characteristics occurs.

6.1.3 Effect of System Pressure

Figure 6.4 shows the effect of system pressure on the cross sectional averaged void fraction for a mass flux of 55 kg/m^{2}s and inlet subcooling of 6 °C. This figure shows that the cross sectional averaged void fraction was not significantly affected by the system pressure; although for most experiments the void fraction was slightly higher for lower pressures. This discrepancy is well within the accuracy of the RTNR system for the maximum contrast ratio resulting from the test section thickness. The offset between these results is contrary to expectations because the fluid properties of Refrigerant 134a show that the latent heat decreases with increasing saturation which should result in an increase in axial void slope. From the uncertainty analysis shown in Appendix D the difference between these curves is within uncertainty range of these measurements but since the effect was reproducible and systematic further discussion is warranted. The saturation temperature of Refrigerant 134a decreases with decreasing pressure and this lower temperature may cause a larger temperature differential on the water heating side (which had a fixed inlet temperature). This increased temperature differential may increase the total heat transferred and therefore increase the cross sectional averaged void fraction. Similar to the lower mass fluxes in Figure 6.3 and the inlet subcooling in Figure 6.2, the axial void profiles show a change in slope part way along the test section. Again these changes most likely result from flow regime transitions and their impact on neutron build-up as discussed in Section 4.2.3.

6.1.4 Effect of Test Section Orientation

Finally, the effect of test section orientation is shown in Figure 6.5 for a mass flux of 80 kg/m^2-s, 9 °C inlet subcooling and a system pressure of 630 kPa. From this figure and in general, the void fractions measured for the horizontal test section are slightly higher than the vertical case for similar inlet conditions and heat flux. This may have resulted from gravity driven flow distributions in the horizontal case which can alter the build-up effects as discussed in Section 4.2.3.

Although the cross sectional analysis presented above for vertical and horizontal orientations provide excellent axial void information that is helpful in substantiating the heat transfer performance discussed in Chapter 5, it does not resolve void distribution issues such as centrifugal effects that are present in swirl flow. Furthermore the changes in pressure drop magnitude and fluctuations can not be explained fully given the time- and cross-sectional averaged results.

6.2 VOID QUALITY RELATIONSHIPS

The relationship between the cross-sectional averaged void fraction and the thermodynamic quality is useful for many homogeneous and separated flow simulations as discussed in Chapter 1. The axial quality can be calculated based on an energy balance shown in Chapter 3. Figure 6.6 shows the effect of subcooling on the relationship between void fraction and quality of several subcoolings at a system pressure of 630 kPa along with the void quality relationship from Wallis[126] evaluated at 630 kPa. The Wallis model is based on separated flow at thermal equilibrium and therefore may over predict the void fraction due to:

a) nonthermal equilibrium effects caused by liquid subcooling

b) void condensation and collapse in the liquid region

c) droplet evaporation in the vapor region

Figure 6.6 does show that void to quality relationship increases with increasing quality as expected, and the Wallis model provides a conservative estimate of the void fraction for thermalhydraulic predictive techniques.

6.3 INSTANTANEOUS CROSS SECTIONAL AVERAGED VOID FRACTION

The instantaneous cross sectional averaged void fraction provides critical information on the temporal behavior, and hence flow regimes. Tracking large increases in void over the length of the test section allows the void velocity, length and acceleration to be determined. From the void fraction waveforms and inspection of the videotaped experiments, the flow regime can also be described. RTNR images are captured in 33 ms time slices, and hence provide 33 ms axial images as shown in Figure 6.7 for a period of 99 ms at a mass flux of 55 kg/m^2-s and system pressure of 630 kPa. Through analysis of these profiles, specific void peaks that travel through the channel can be identified and used to calculate the void velocity. The void velocity has been calculated and normalized to the fluid velocity to describe the vapor to liquid velocity slip ratio as a function of mass flux and is shown in Figure 6.8. The slip ratio decreases with increasing mass flux, which may be the result of turbulence increasing with increasing flow velocity. This increased vapor-liquid mixing, equalizes the momentum of the flow, making it more homogeneous. Furthermore, the slope of the slip ratio changes for the highest mass flux experiments, indicating a transition to a more homogenous flow pattern. This slope change corresponds to experiments where there was also a significant change in the slope of the cross sectional averaged axial void profiles (see Sections 6.1.1 through 6.1.3).

Figure 6.9 shows the vapor slug slip ratio as a function of the inlet subcooling at a system pressure of 630 kPa. The slip ratio tends to increase with increasing subcooling. However the inlet subcooling show less effect than the mass flux as shown in Figure 6.8.

6.4 TIME AVERAGED LOCAL VOID DISTRIBUTION

The cross-sectional averaged void distribution provides axial void information but lacks detail on the specific behavior of vapor as it is generated and transported through the fluid. Accurate prediction of flow boiling systems requires complex models that rely heavily on constitutive relationships that model the void distribution (and/or interfacial area) in the channel. As described in Chapter 1, the interfacial area concentration describes the interfacial area in a given volume of fluid, and current two-phase methodology relies heavily on constitutive relationships for its prediction. Figure 6.10 shows a time averaged RTNR image of the void in the smooth-flow channel with the darker regions corresponding to higher void fractions at a mass flux of 55 kg/m^2-s, 6 °C inlet subcooling and 630 kPa. This image has been intensified to illustrate the path of void as it travels through the channel with the local void fraction tending to be greater near the center of the channel. The channel walls and water jacket have also been removed through image processing (image subtraction of an empty test section image).

Using the RTNR images, it is possible to reconstruct the radial void profile based on the convolution techniques outlined in Chapter 4. The time-averaged local void distribution is shown in Figure 6.11 for the same conditions as Figure 6.10. The void fraction is highest in the channel center and increases from the lower positions to 0.6 in the center of the channel near the outlet of the heated length. The wall void fraction is less than approximately 0.2 over the entire length of the test section. This lower void concentration in the wall region results from:

i smaller vapor bubbles (which are individually undetectable but have an integrated effect on the wall void fraction),

ii less coalescence in the wall region leading to a further effect as described in (i),

iii or reduced contrast caused by scattering from wall materials near the wall region.

The void fraction shown in Figure 6.11 is approximately symmetric with some deviations that can result from actual flow asymmetries and/or from error propagation in the reconstruction method as outlined in Chapter 4.

6.4.1 Effect of Mass Flux

Figure 6.12 shows the local void distribution for mass fluxes of 55, 100 and 140 kg/m^2-s at 6 °C inlet subcooling and 630 kPa. These figures show the increase in the void fraction at the channel center and wall regions with decreasing mass flux resulting from decreases in the overall quality with increased mass flux. Similarly, wall void distribution decreases significantly with increasing mass flux.

The increased slope in the axial flux profile described in Section 6.1.2 can be further examined by inspecting Figure 6.12 a). For this low mass flux, there is a significant increase in the void distribution in the wall regions. This may indicate a boiling mechanism transition from a nucleation to bulk boiling phenomena. Hence, this boiling transition may result in the change in axial void profile discussed in Section 6.1 . For Figure 6.12 c), the void distribution in the wall region is not significant but coalescence in the center of the channel is clearly evident.

6.4.2 Effect of Inlet Subcooling

Inlet subcooling effects are shown in Figure 6.13 for 12, 9, and 6 °C inlet subcoolings at 100 kg/m^2-s and 630 kPa. For most axial locations, the void concentration increases with decreasing radial distance similar to above. This may be due to decreased qualities, and increased vapor condensation in the bulk liquid caused by increases in subcooling.

6.4.3 Effect of System Pressure

The effect of pressure on the local void fraction distribution is shown in Figure 6.14 for 500, 630 and 700 kPa respectively at a mass flux of 55 kg/m^2-s and 6 °C subcooling. Cross-sectional averaged results shown previously indicate that the pressure did not significantly affect the void fraction, but from this figure it is clear that it does significantly affect the radial void distribution, and may account for the changes in pressure drop characteristics. The void distribution tends to shift to the wall region with increasing system pressure. This results from transitions in flow regime from a slug/annular type pattern to more bubbly flow pattern. The lower saturation temperature in Figure 6.14 c), also causes an increase in quality at a given location and this is clearly evident from comparisons for b) and c).

6.4.4 Effect of Orientation

The time averaged void distribution is shown in Figure 6.15 for a horizontal orientation at 100 kg/m^2-s, 6 °C inlet subcooling and 630 kPa. The horizontal image has been rotated to facilitate comparison with the vertical results (the gravity force direction is indicated). The stratified nature of the flow field is clearly shown in this case. The void fraction is largest at the top of the horizontal section and decreases to the bottom of the channel; in the vertical case the void is highest near the center and decreases with increasing radial distance. The cross sectional averaged results shown in Figure 6.5 show an increase in the void fraction for horizontal orientations at the same inlet conditions and heat flux. These local results clearly show that orientation effects (void distribution) can influence further void production and/or the neutron build-up behavior. Furthermore, the differences in test section geometry (diameter and length) may lead to changes in void distribution behavior.

6. 5 INSTANTANEOUS LOCAL VOID DISTRIBUTION

The instantaneous void fraction distribution is shown in Figure 6.16 over approximately 0.2 s at 55 kg/m^2-s, 6 °C inlet subcooling and 630 kPa. Each reconstruction represents the local void fraction distribution in one RTNR video image (33 ms), for 5 consecutive frames. Additional post-processing of the void images is possible so that they can be reassembled digitally into a video sequence of void images using the techniques described in Chapter 4. These radial and axial void fraction video sequences can be used to track vapor as it progresses through the channel and hence to measure the vapor slip ratio, volume and interfacial area. Figure 6.16 shows that for the instantaneous reconstruction, the void varies from zero to one. Theoretically, at each locality the void should discreetly vary as either 0 or 1. This effect is known as “smearing” and may result from;

i the reconstruction method and image processing techniques performed on the digital image involve some averaging to reduce noise levels and also allow some error propagation, thereby causing some void smearing.

ii Each pixel actually has a finite size, and therefore provides a volume averaged void, and hence can vary between 0 and 1.

iii the electronic image intensifier in the RTNR camera system may allow some photon "afterglow" or noise that may smear the analogue image before it is digitized[143].

iv noise sources including power supplied, image capture boards and very small movements of the test section during the testing program may also contribute to the smearing effect.

The author devised many image processing techniques involving thresholding of the digital image but all resulted in some gradients after the convolution algorithm was applied. Thus it was concluded that explanation i) and ii) above accounts for most of the smearing effect. Threshold techniques can be applied after the convolution algorithm (i.e. directly to Figure 6.16) to eliminate suspected artifacts but this would decrease the amount of information contained in all the material presented below so the author concluded it was best to leave the convolved images in their raw state.

Figure 6.17 shows the instantaneous void distributions for mass fluxes of 100 and 140 kg/m^2-s at similar pressures and temperatures as above. This figure clearly shows the effect of mass flux on the instantaneous void distribution is to decrease the overall void, specifically in the center of the channel, thereby making the overall flow more uniform in the radial direction.

The effect of pressure on the instantaneous void distribution is shown in Figure 6.18 for system pressures of 500 and 700 kPa respectively and a mass flux and inlet subcooling of 55 kg/m^2-s and 6 °C. From inspection of these local void distribution measurements, the void size tends to increase with decreasing pressure. Using the cross sectional averaged images from above show no significant change with pressure, which indicates that the lower pressure case has more and smaller void pockets and hence a larger interfacial area concentration. This increase may result in the increase in subcooled boiling heat transfer performance with decreasing pressure as shown in Chapter 5. Figure 6.19 shows the instantaneous void fraction distributions for inlet subcoolings at 100 kg/m^2-s and 630 kPa. It is evident from these reconstructed radial void distributions that the size and behavior of vapor in the channel changes with inlet subcooling.

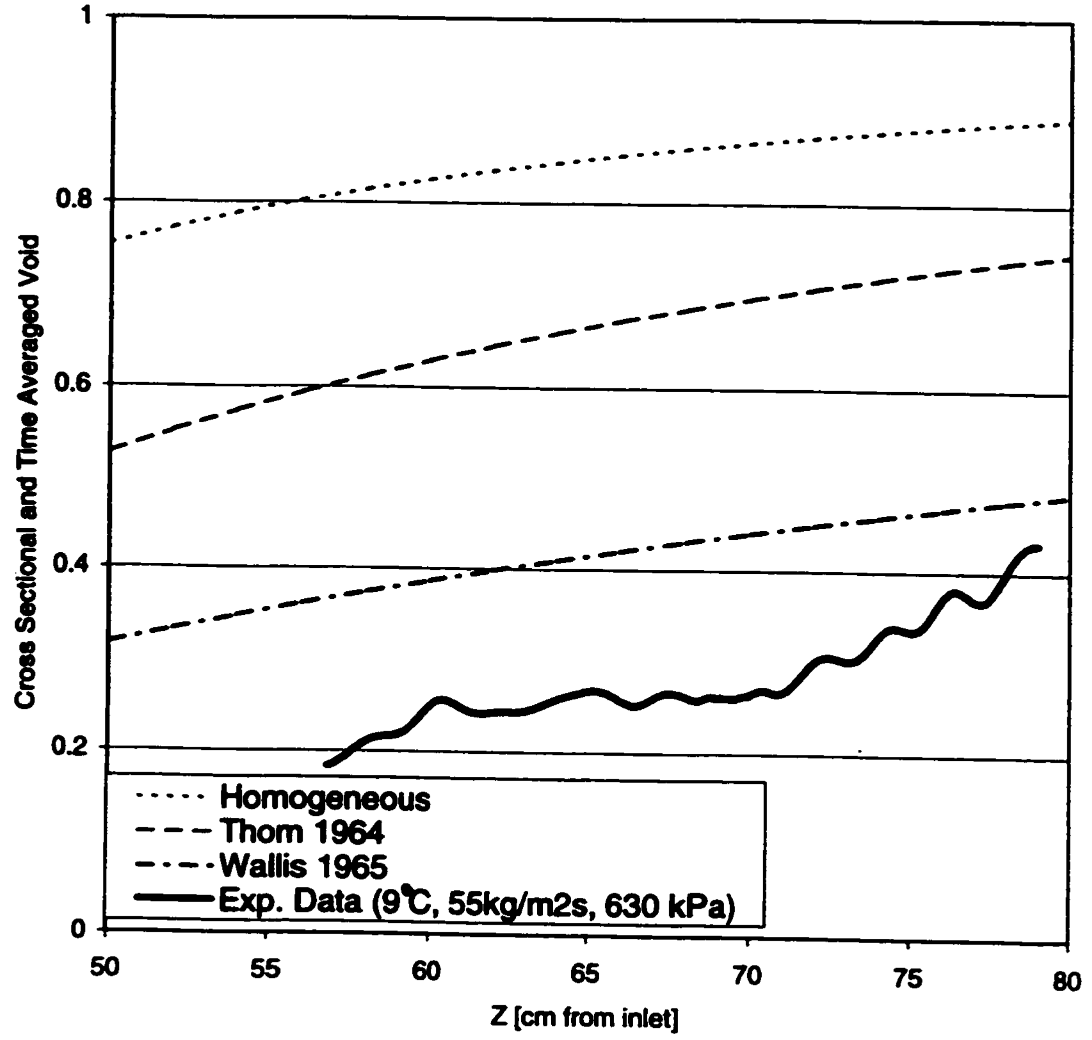

Figure 6.1 Refrigerant 134a Smooth-Flow Cross Sectional and Time Averaged Void Fraction Distribution and Comparison with Correlations from Wallis, Thom et al. and the Homogeneous Equilibrium Model.

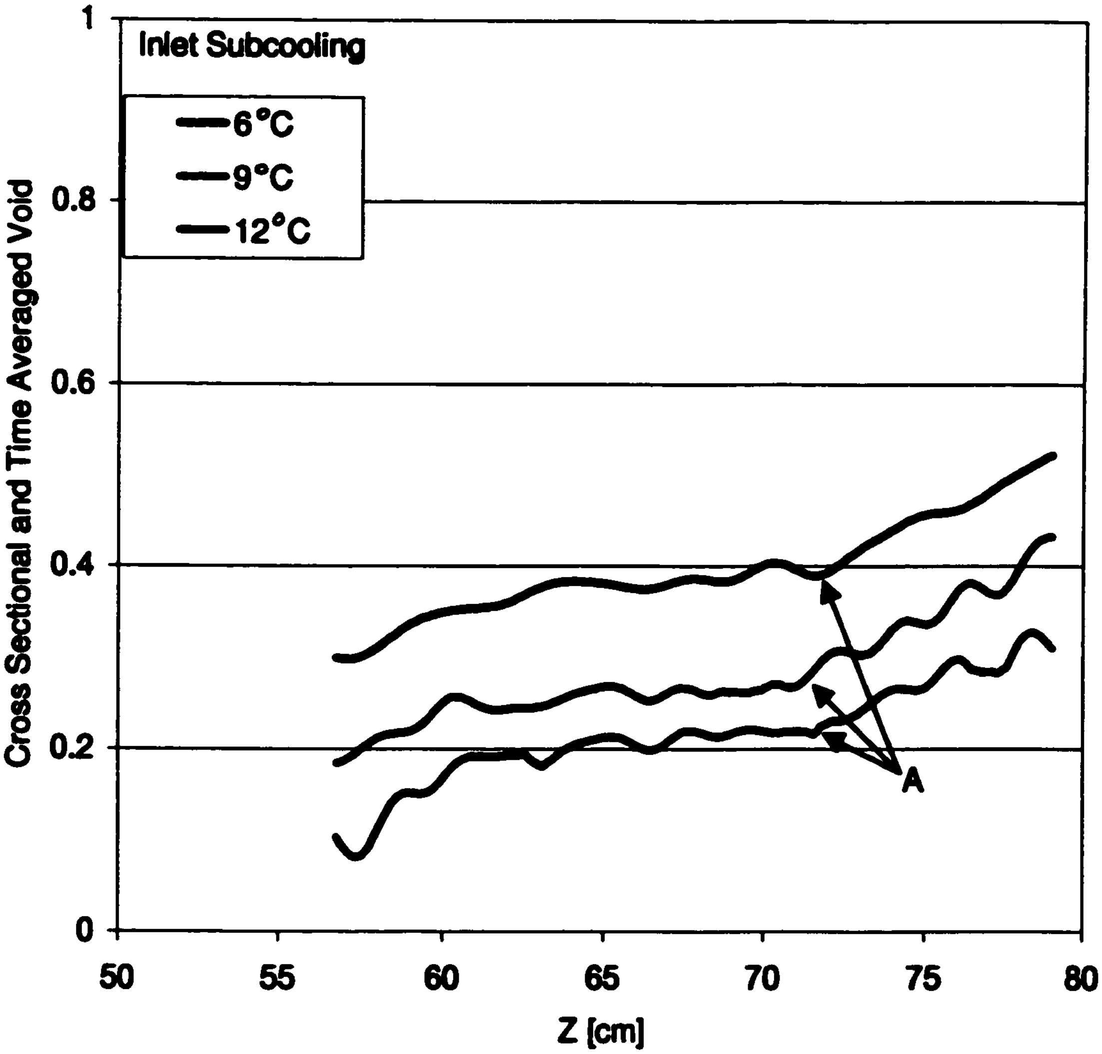

Figure 6.2 Effect of Inlet Subcooling on Cross Sectional and Time Averaged Void Distribution for Refrigerant 134a Smooth-Flow Boiling at 55 kg/m^2-s and 630 kPa.

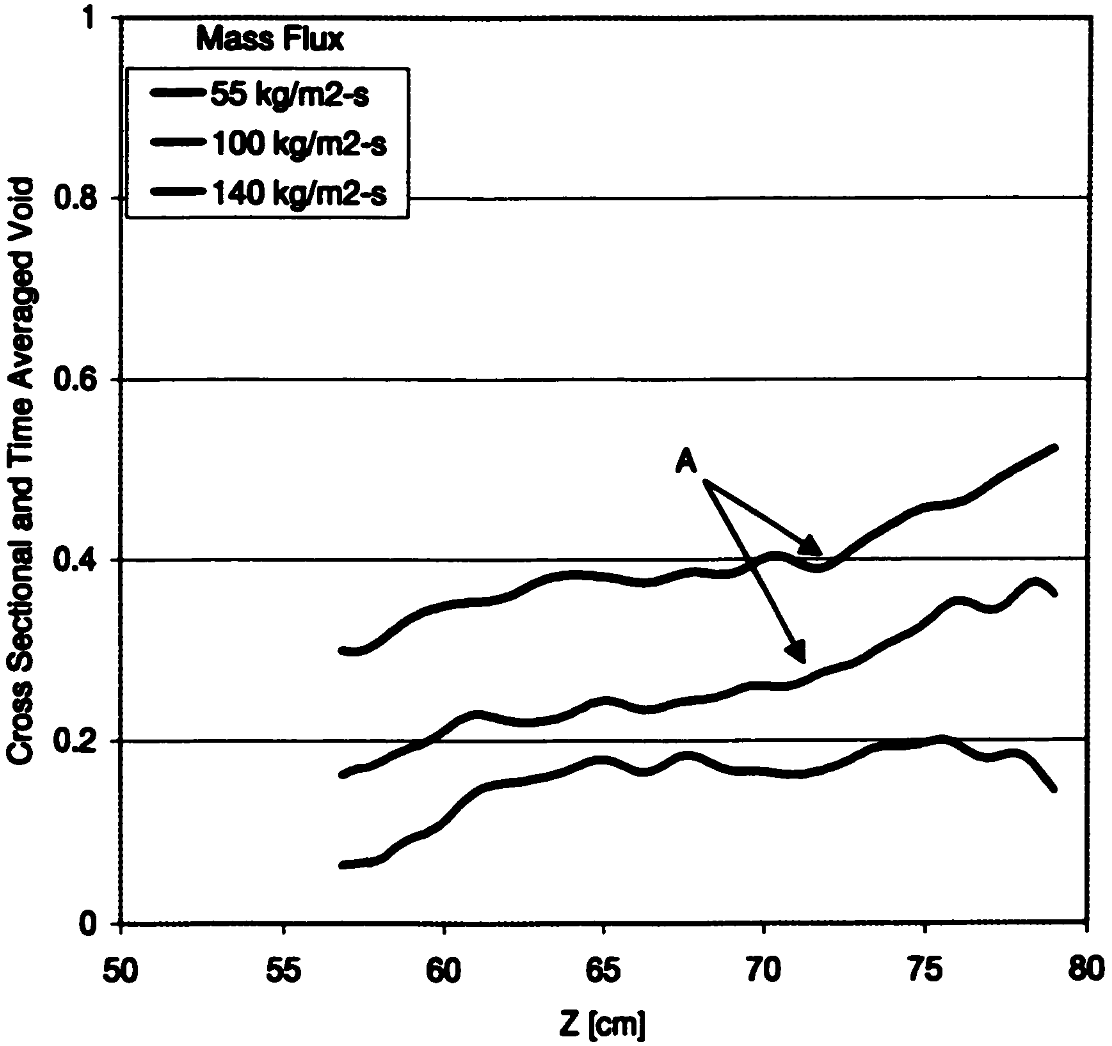

Figure 6.3 Effect of Mass Flux on Refrigerant 134a Cross Sectional and Time Averaged Void Distribution for Refrigerant 134a Smooth-Flow Boiling at 6 °C Inlet Subcooling and 630 kPa.

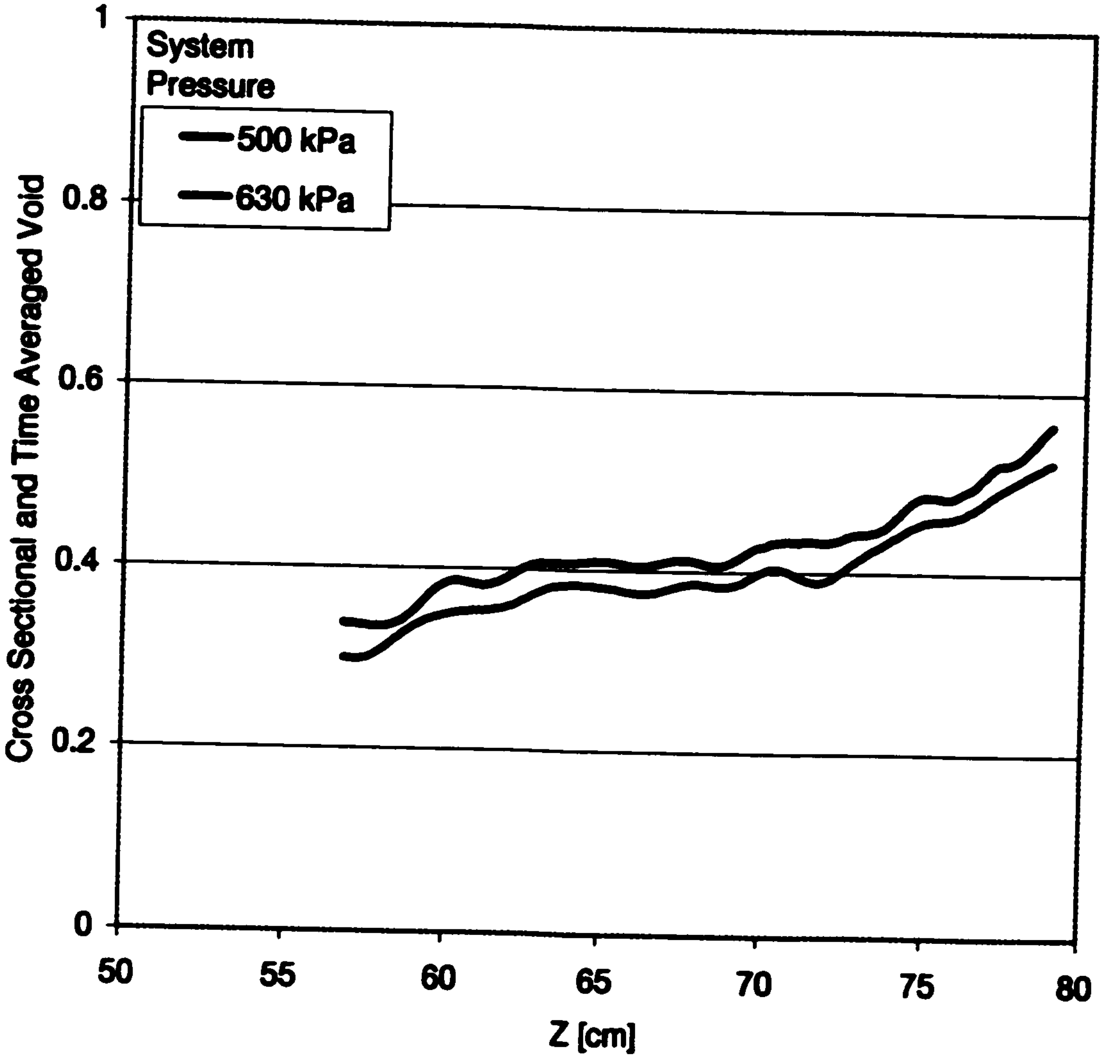

Figure 6.4 Effect of System Pressure on Cross Sectional and Time Averaged Void Distribution for Refrigerant 134a Smooth-Flow Boiling at 6 °C Subcooling and 55 kg/m^2-s.

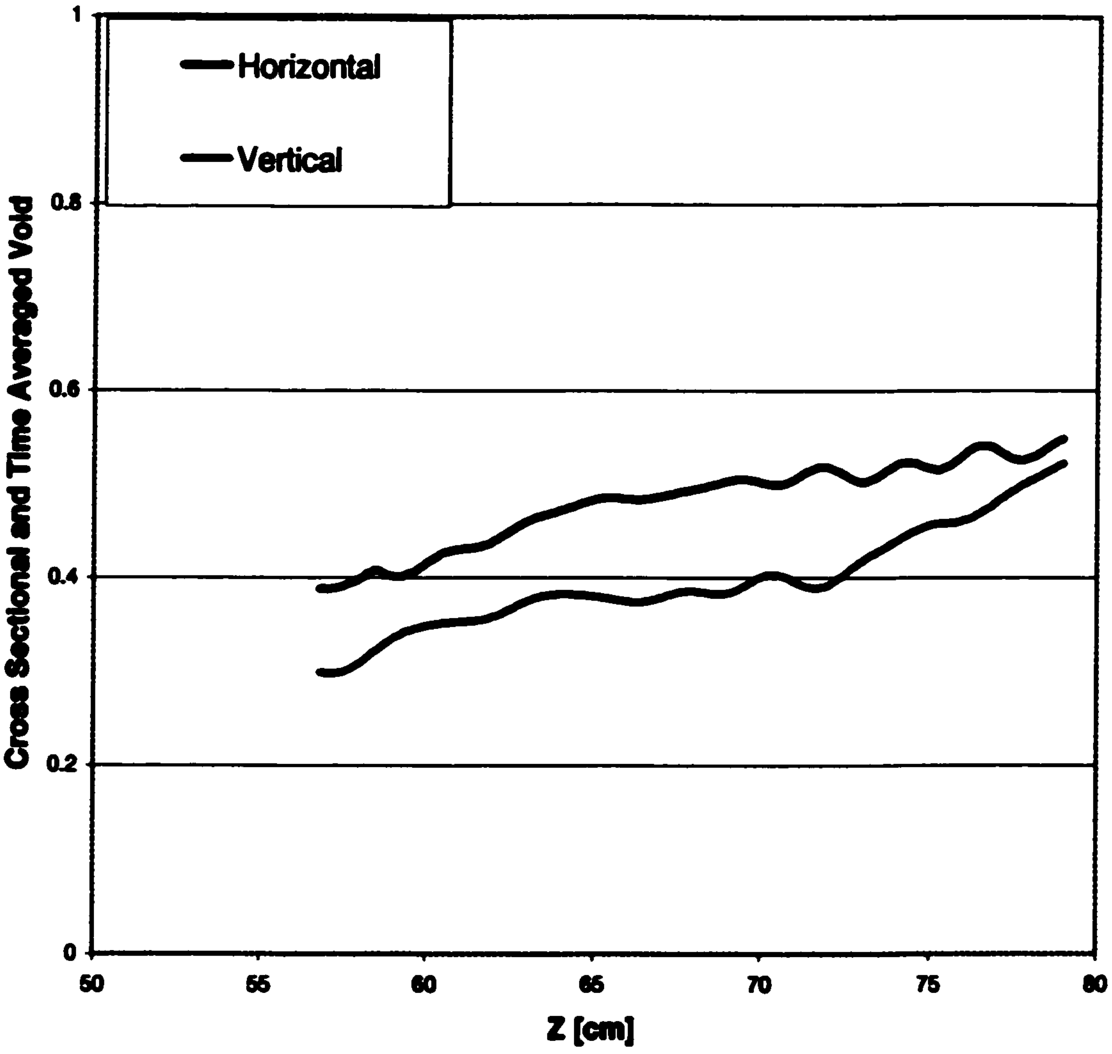

Figure 6.5 Effect of Test Section Orientation of Cross Sectional and Time Averaged Void Distribution for Refrigerant 134a Smooth-Flow Boiling at 630 kPa and 55 kg/m^2-s.

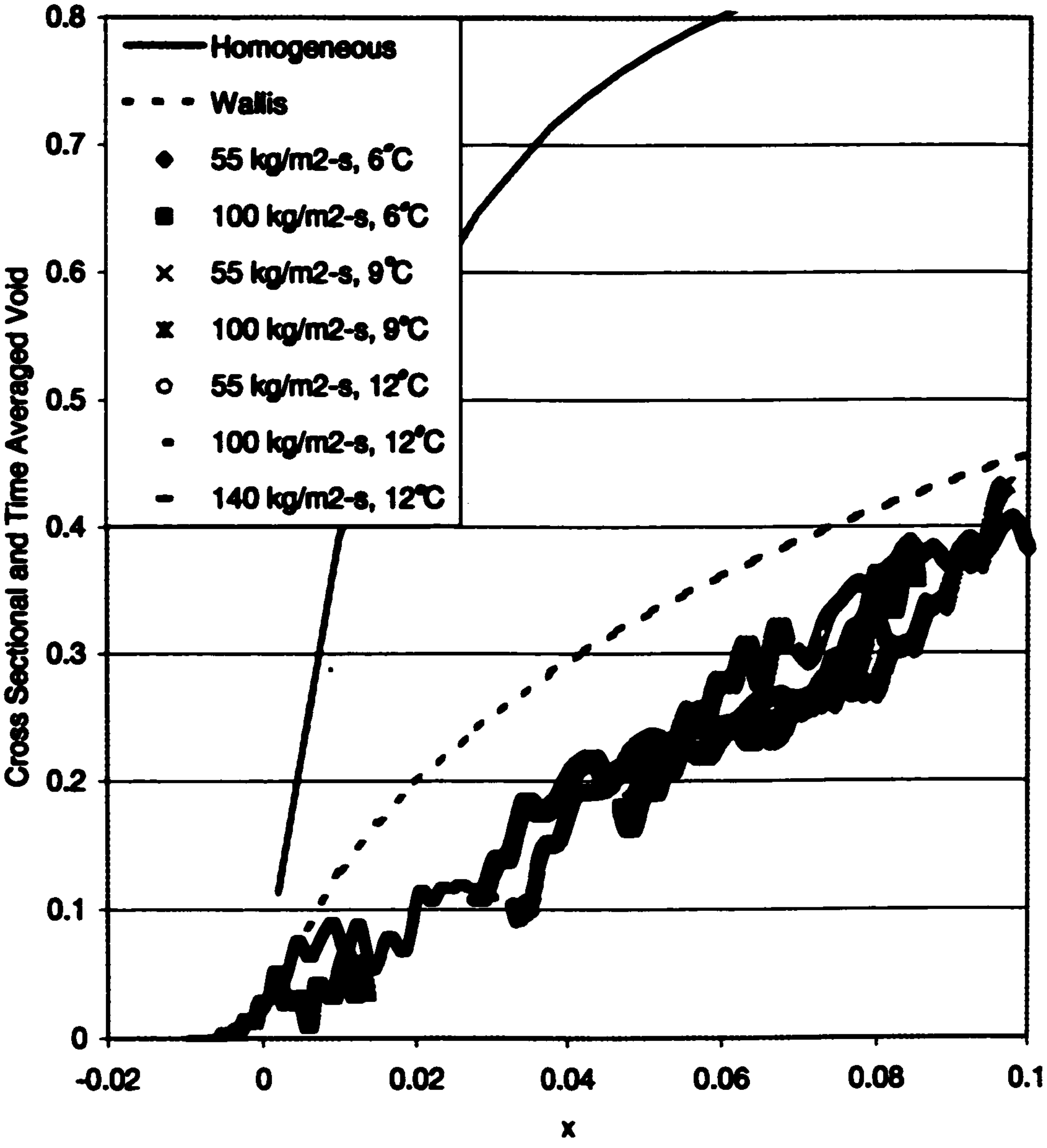

Figure 6.6 Smooth Flow Void to Quality Relationship at 630 kPa and Comparison to Wallis Correlation.

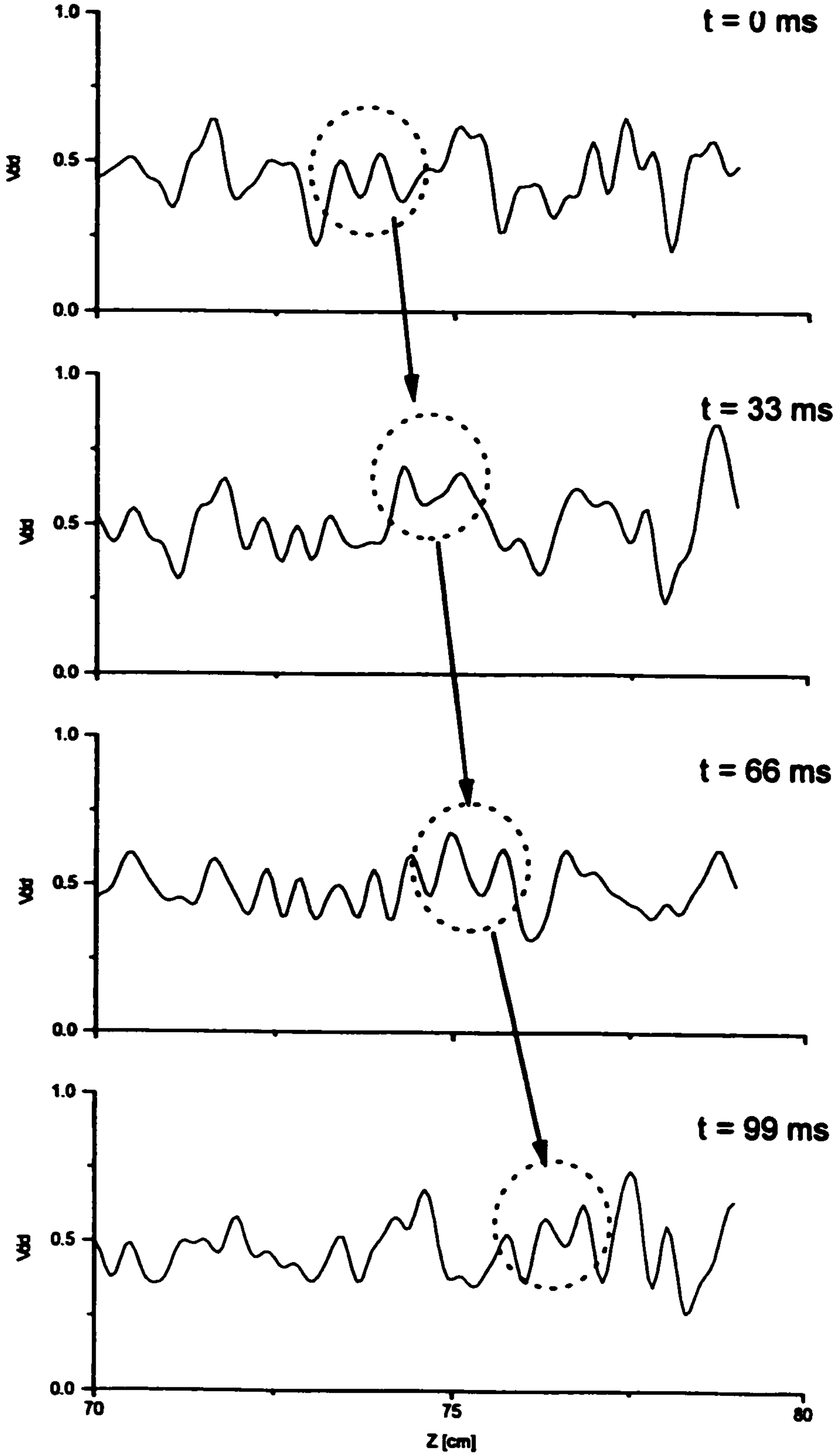

Figure 6.7 Instantaneous Cross Sectional Void Fraction Distribution.

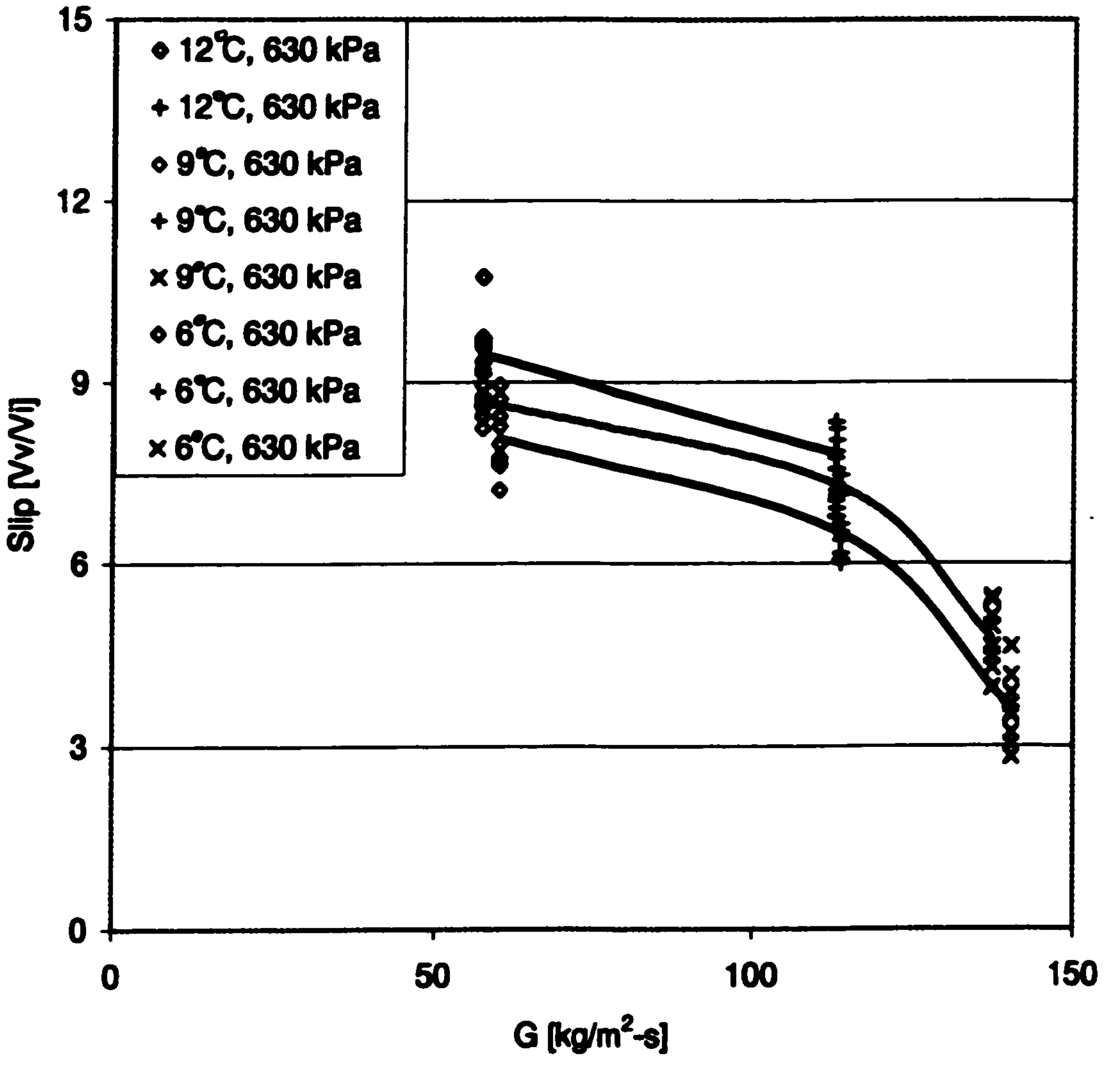

Figure 6.8 Effect of Mass Flux on the Vapor Slug Slip Ratio.

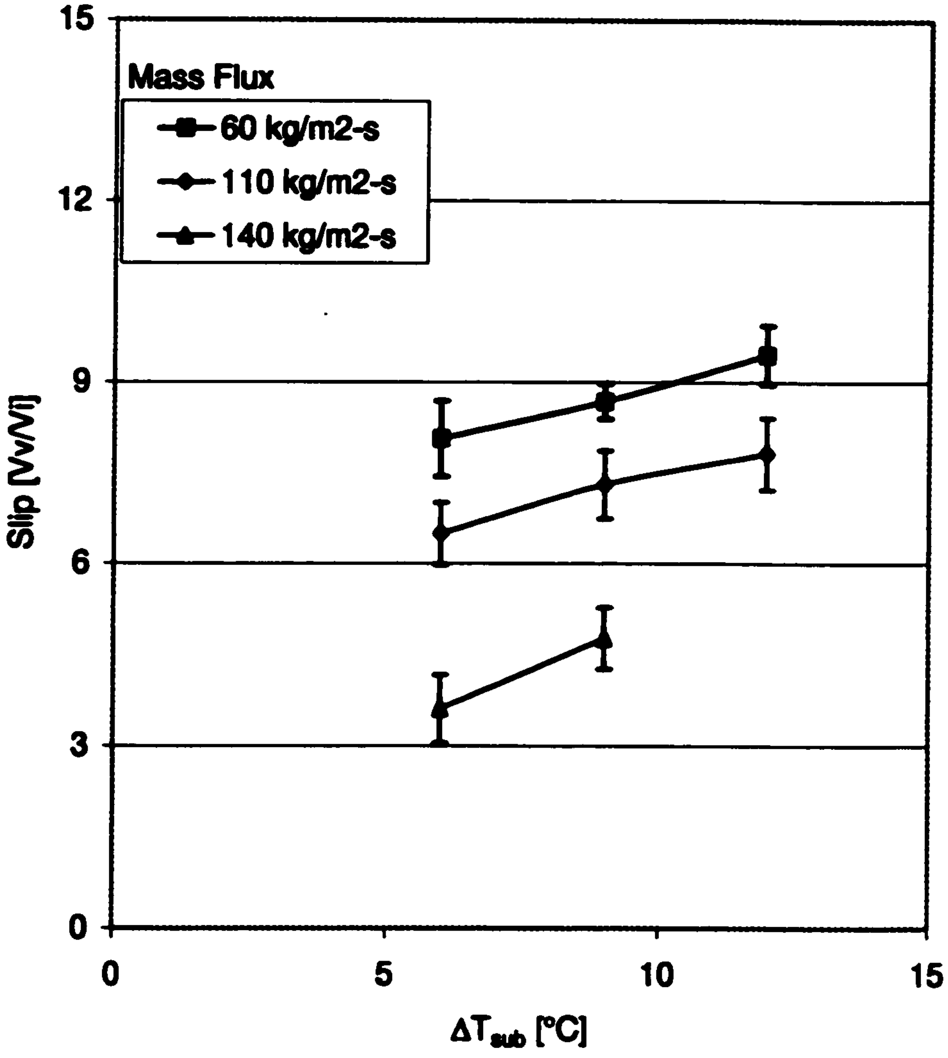

Figure 6.9 Effect of Inlet Subcooling on Vapor Slug Slip Ratio.

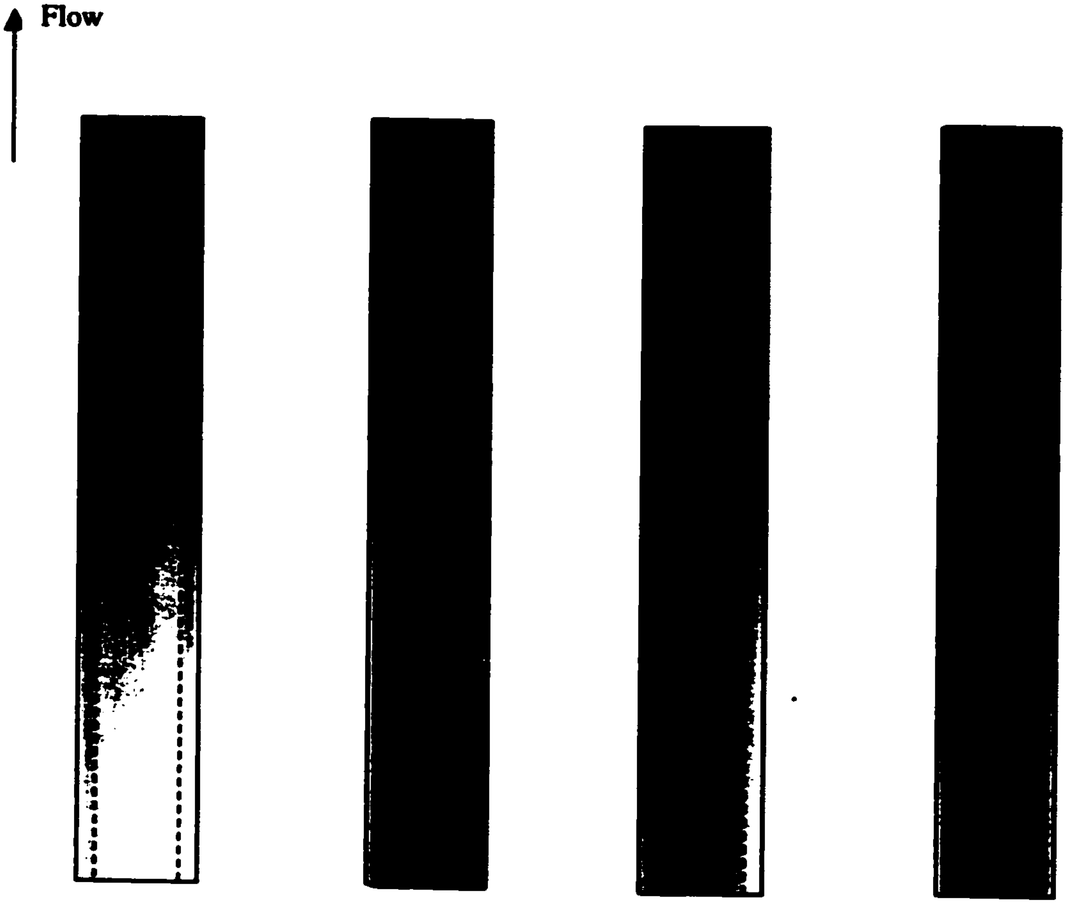

Empty Channel

Full Channel

Flow Boiling
(High Power)

Flow Boiling
(Lower Power)

Figure 6.10 RTNR Processed Image of Flow Boiling at 55 kg/m^2-s, 6 °C Inlet Subcooling and 630 kPa.

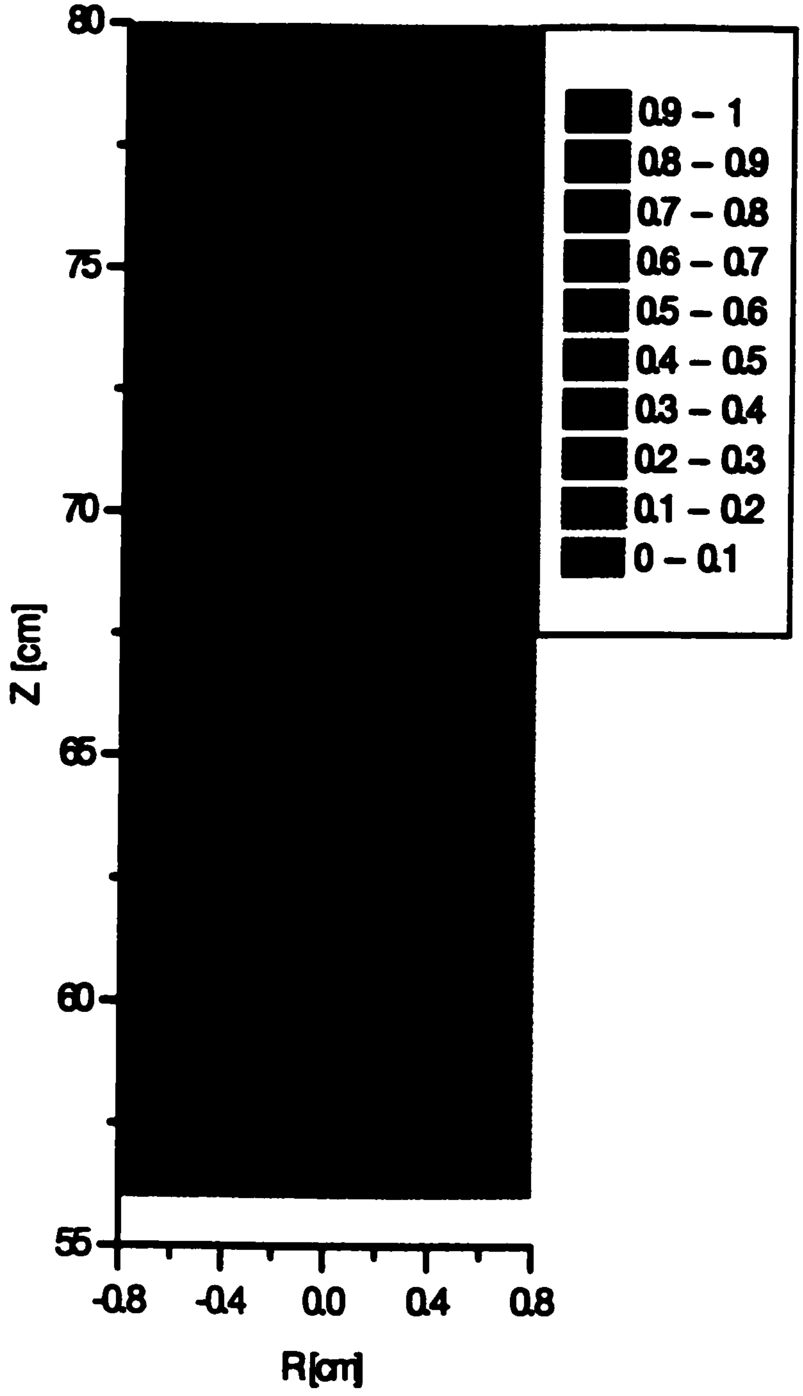

Figure 6.11 Time Averaged Local Void Fraction Distribution for Refrigerant 134a Smooth-Flow Boiling at 55 kg/m^2-s, 6 °C Inlet Subcooling and 630 kPa.

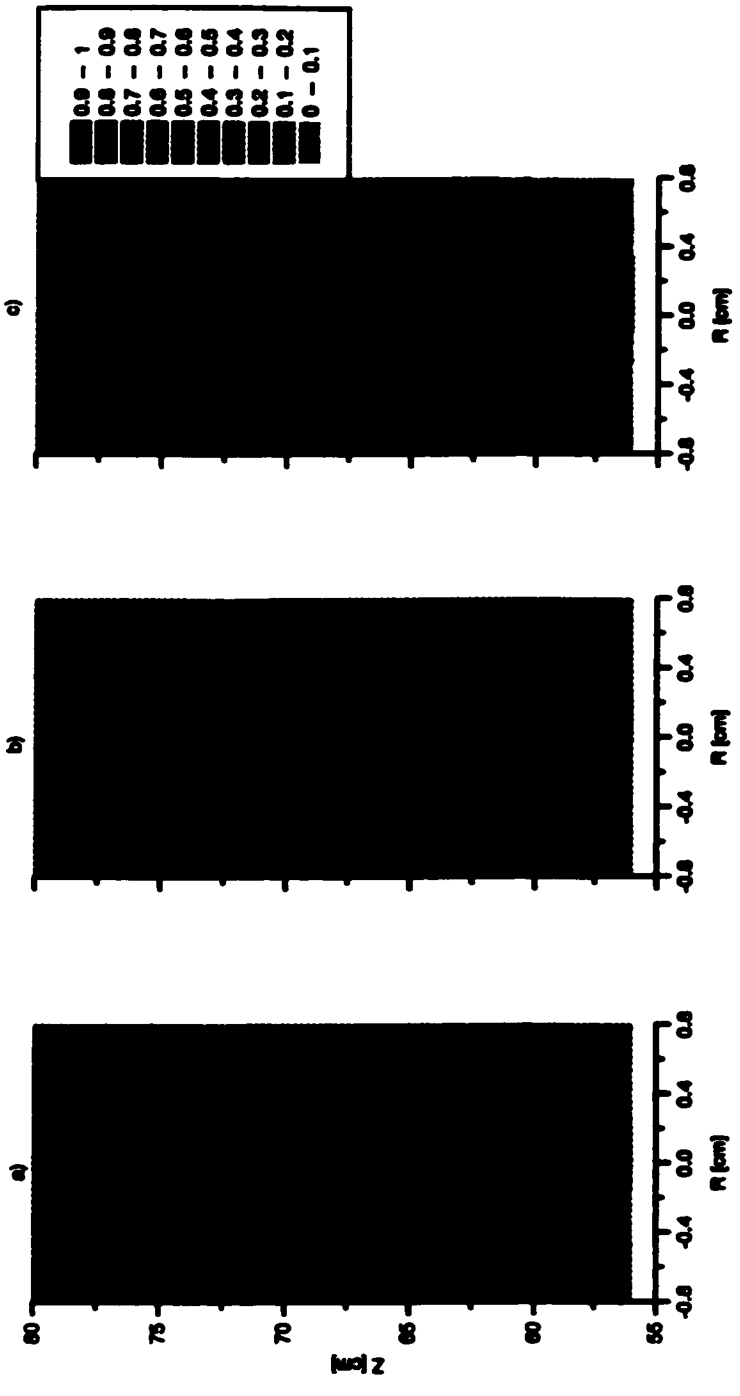

Figure 6.12 Effect of Mass Flux on the Time Averaged Local Void Fraction Distribution for Refrigerant 134a Smooth-Flow Boiling at 6 °C Inlet Subcooling, 630 kPa and a)55, b) 100 and c) 140 kg/m^2-s.

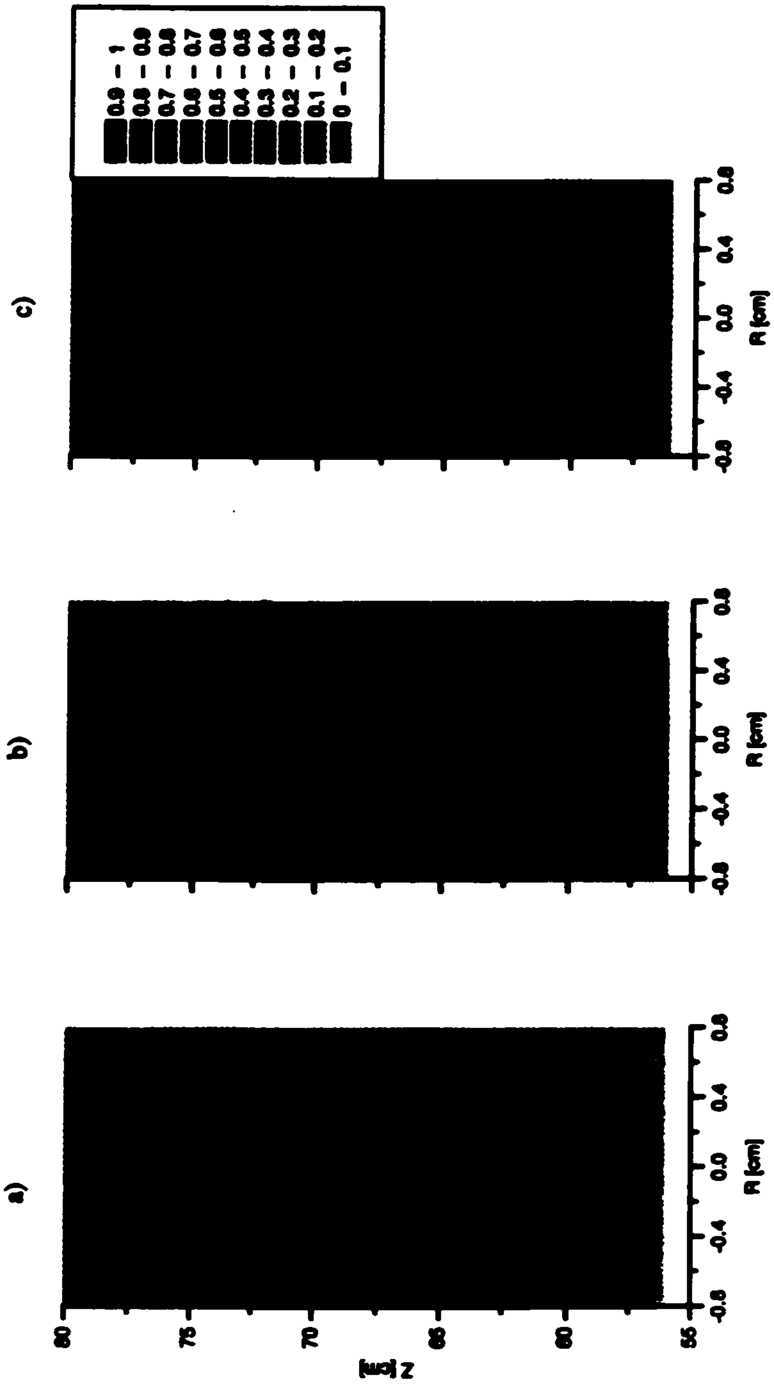

Figure 6.13 Effect of Inlet Subcooling on the Time Averaged Local Void Distribution at 100 kg/m^2-s and 630 kPa for a) 12 , b) 9 , and c) 6 °C Inlet Subcooling.

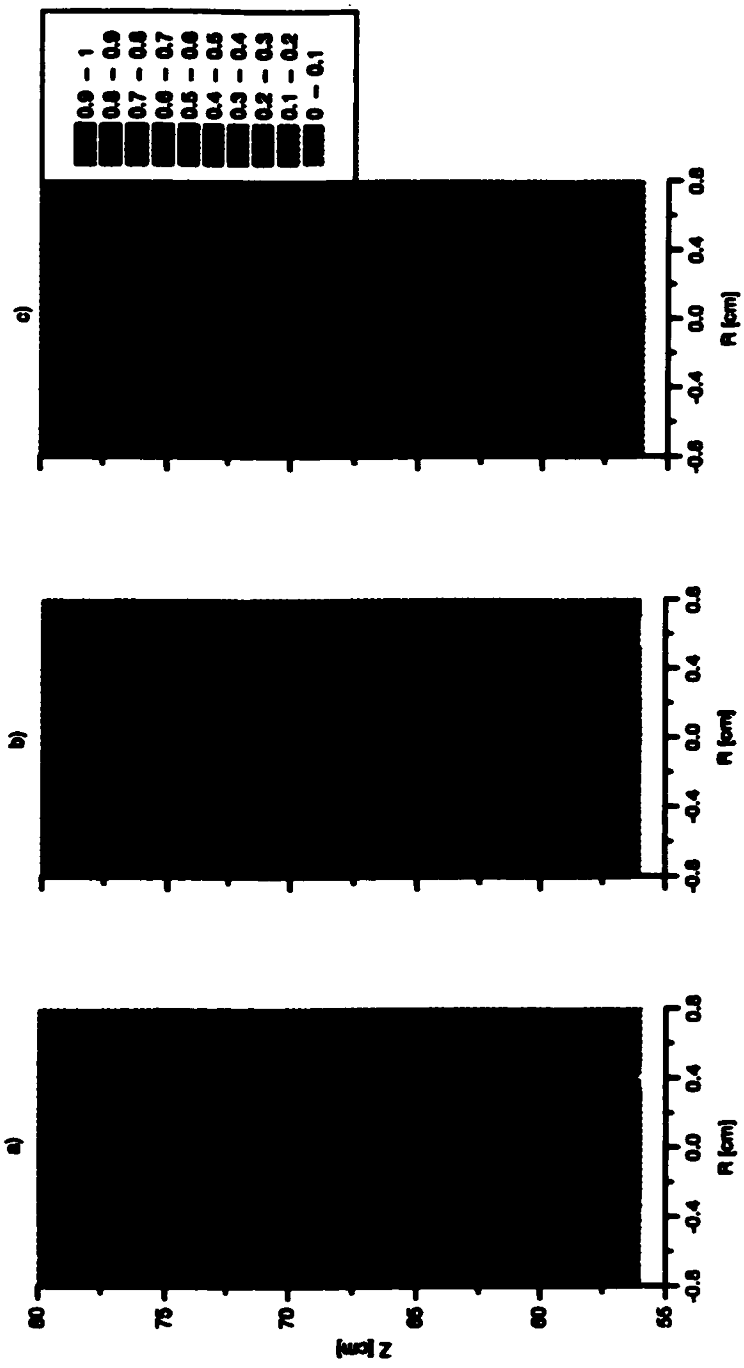

Figure 6.14 Effect of System Pressure on the Time Averaged Local Void distribution at 1000 kg/m^2-s and 9 °C Inlet Subcooling at a) 500 , b) 630 , and c) 700 kPa.

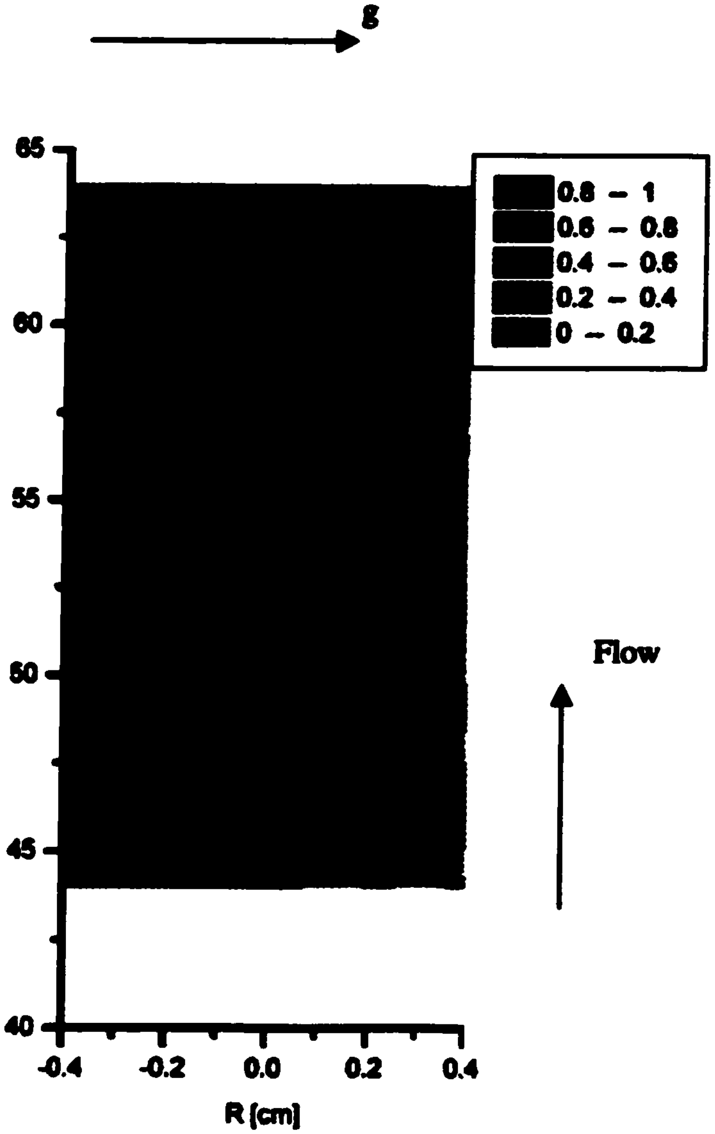

Figure 6.15 Effect of Orientation on Void Distribution at 100 kg/m^2-s, 630 kPa and 6 °C Subcooling for a Horizontal Orientation

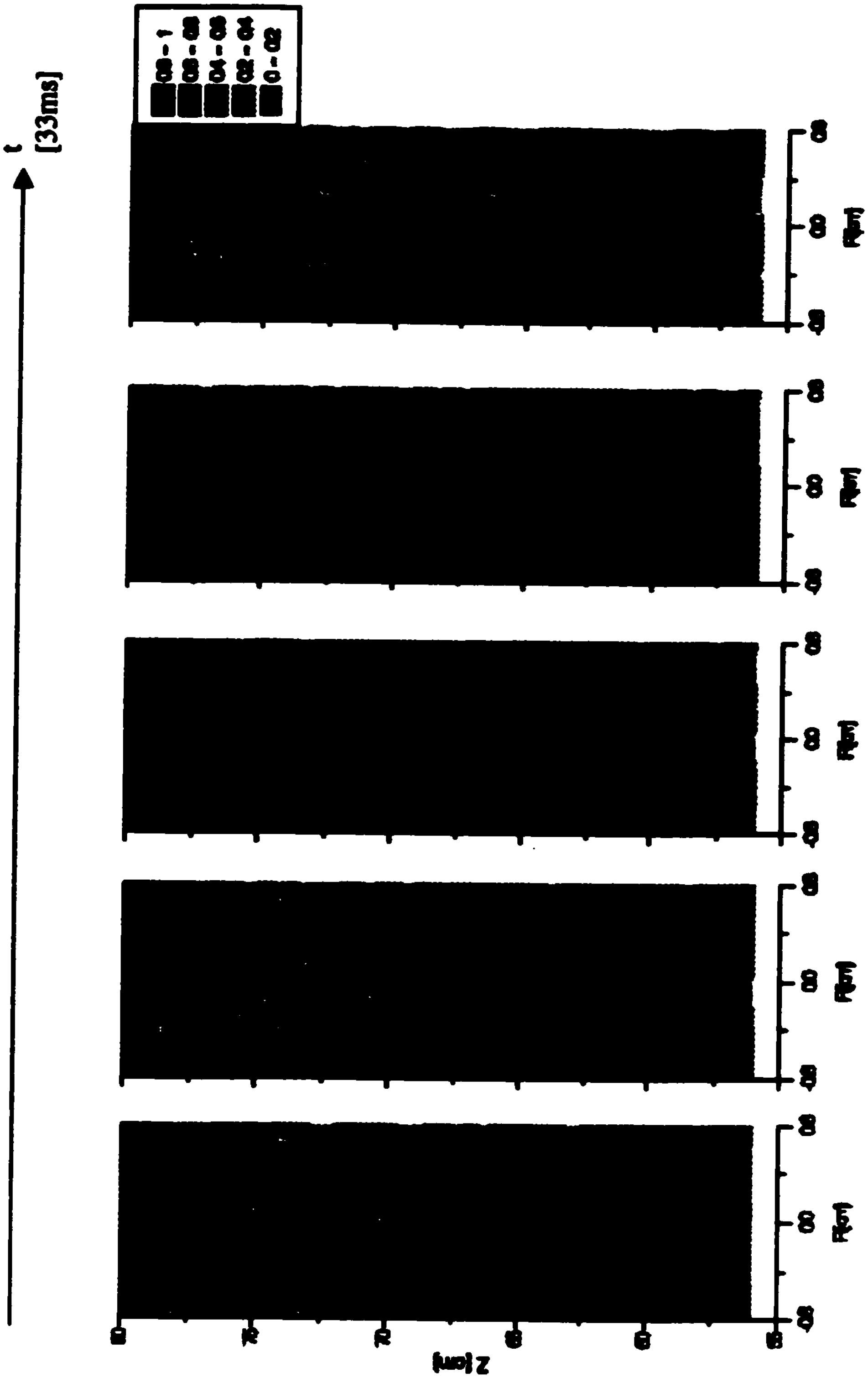

Figure 6.16 Instantaneous Local Void Distribution for Smooth-Flow Boiling of Refrigerant 134a at 55 kg/m^2-s and 630 kPa.

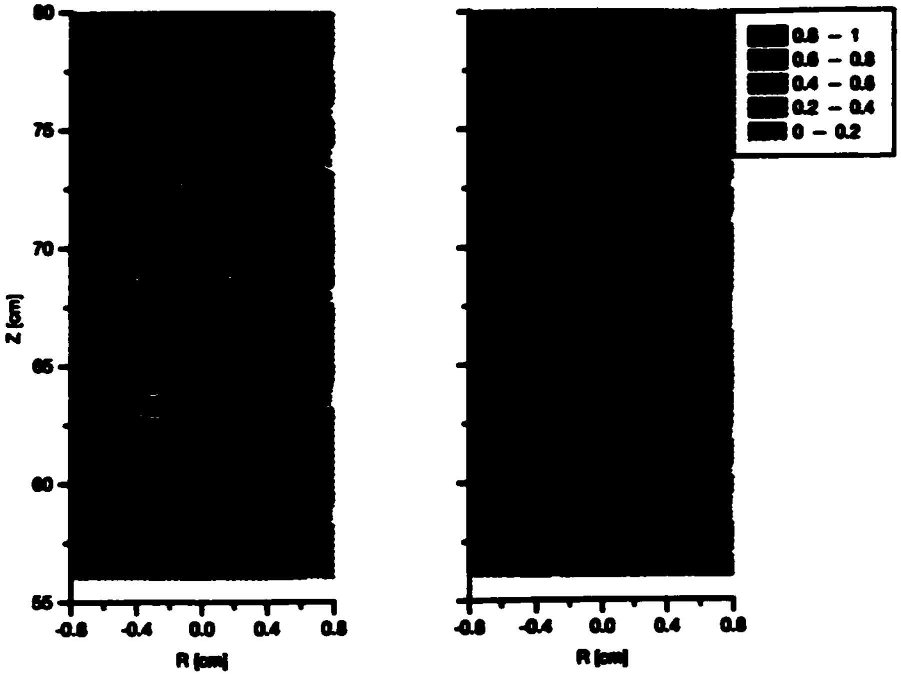

a) 140 kg/m^2-s

b) 100 kg/m^2-s

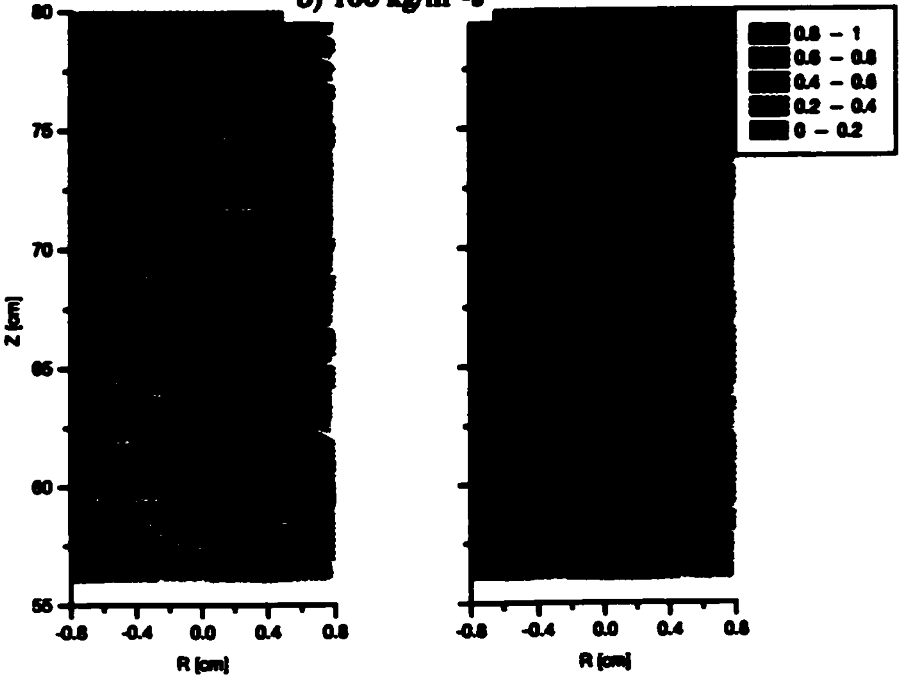

Figure 6.17 Effect of Mass Flux on the Instantaneous Local Void Distribution for Smooth-Flow Boiling of Refrigerant 134a at 630 kPa and 6 °C Inlet Subcooling for a) 140 and b) 100 kg/m^2-s.

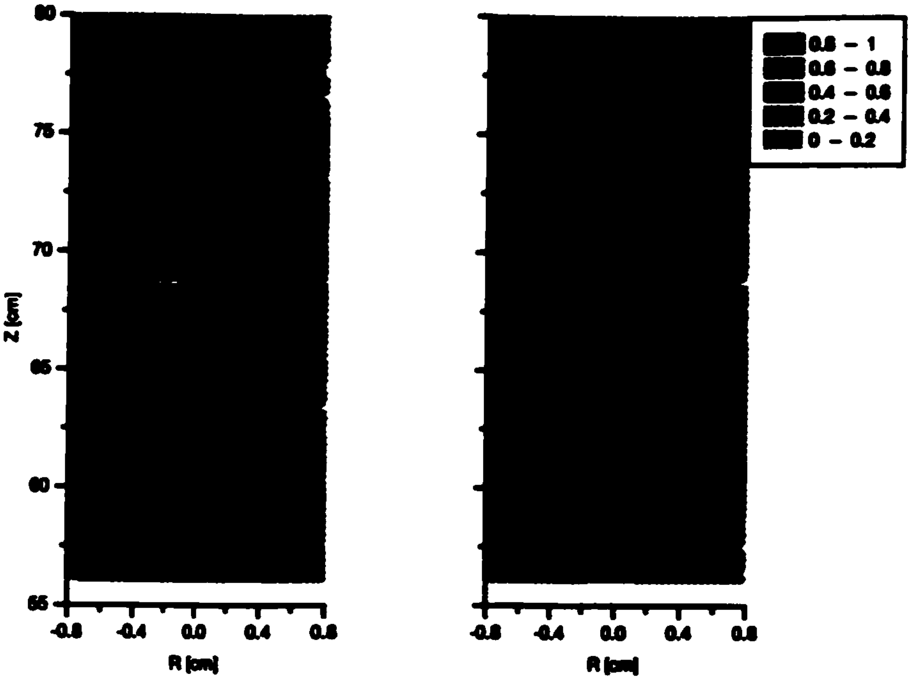

a) 500 kPa

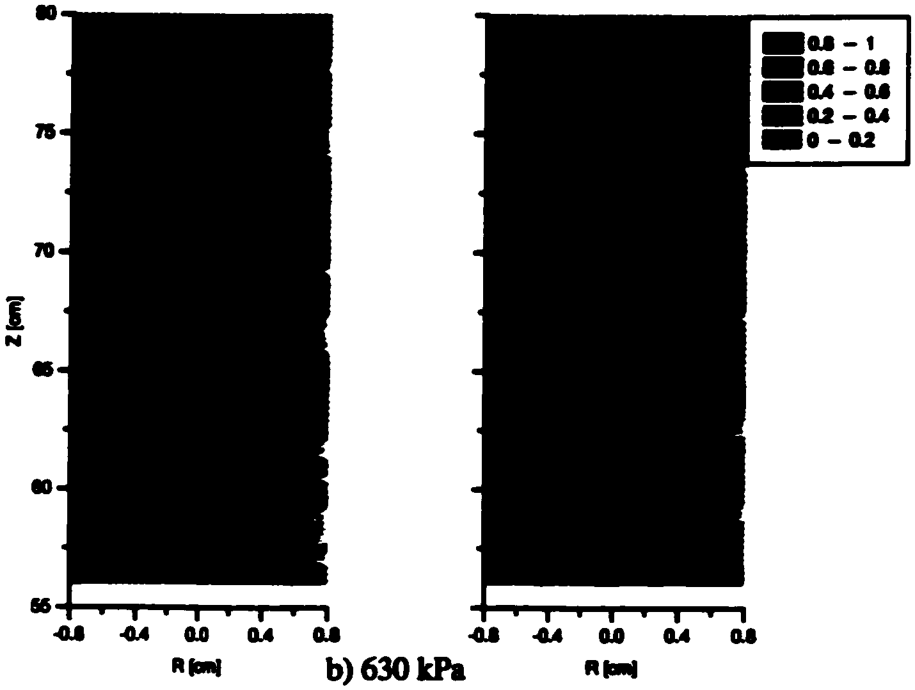

b) 630 kPa

Figure 6.18 Effect of System Pressure on Instantaneous Local Void Distribution at 55 kg/m^2-s and 6 °C Inlet Subcooling for a) 500 kPa and b) 630 kPa.

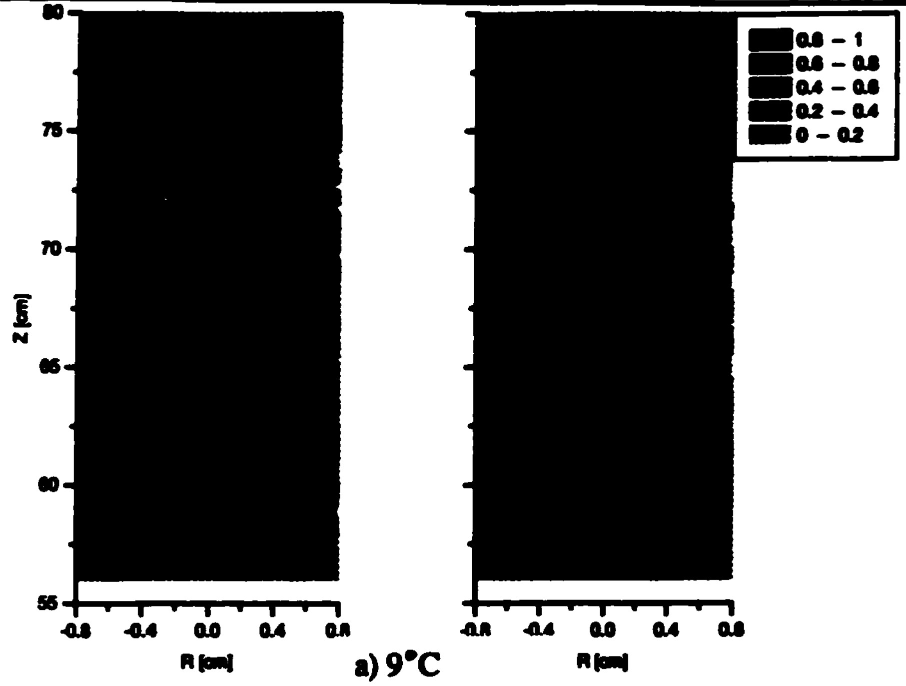

a) 9°C

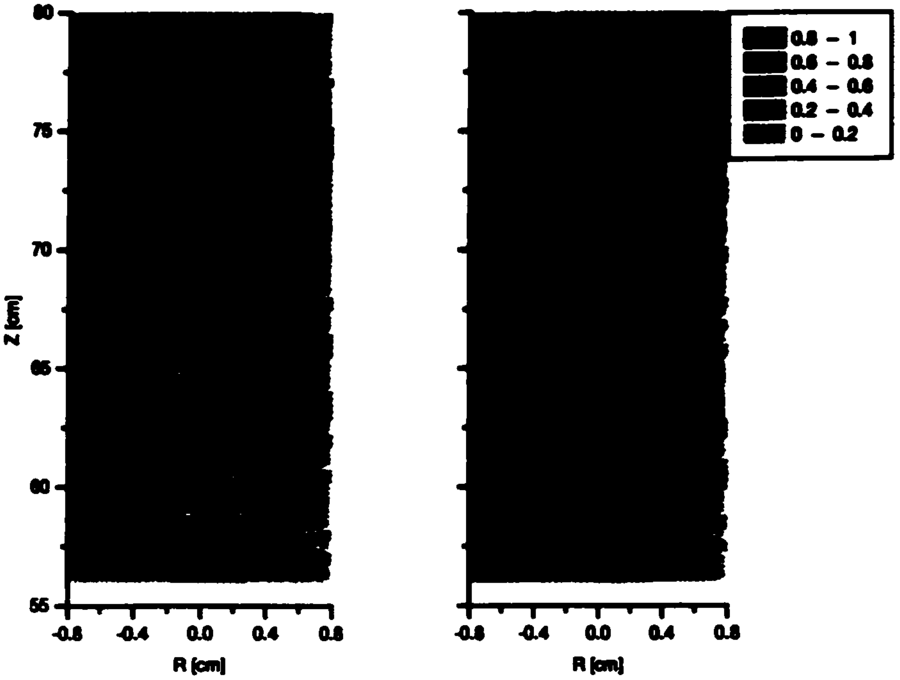

a) 12°C

Figure 6.19 Effect of Inlet Subcooling on Instantaneous Local Void Distribution at 100 kg/m^2-s and 630 kPa for a) 9 °C and b) 12 °C Inlet Subcooling.

CHAPTER 7 SWIRL FLOW VOID DISTRIBUTION MEASUREMENT

Swirl-flow heat transfer behavior was outlined in Chapter 5 for various system conditions but the complex behavior observed in these experiments requires understanding of the distribution of the void inside the channel. RTNR and high speed XCT techniques were adopted to demonstrate the importance of void distribution and trajectory in a flow boiling system. These complementary techniques were able to determine the void distribution in the smooth and swirl-flow channels so that quantified measurements could be used as a basis for future simulations and predictive methods. This chapter compares smooth and swirl-flow measured void distributions using these techniques and demonstrates their effectiveness as diagnostic devices during flow boiling.

7.1 TIME AND CROSS SECTIONAL AVERAGED RESULTS

Figure 7.1 and 7.2 compare the time and cross sectional averaged void distributions for smooth and swirl vertical flow at a mass flux of 55 kg/m^2-s, 630 kPa and for 6 °C and 9 °C subcooling respectively. The introduction of swirling increases the void fraction slightly compared to the smooth-flow case that may result from;

- increased overall heat transfer coefficient, U, that for a given water and Refrigerant 134a temperature difference tends to increase the heat flux, and hence the total quality.
- increased conduction effects that transfer heat from the walls into the center of the channel using the twisted tape itself as a heat transfer fin.
- decreased wall temperatures at a given heat flux due to cooler, and therefore heavier fluid, being forced to the walls by centrifugal forces. This lower wall temperature maintains a larger temperature differential with the outside water heating jacket and therefore can increase the local heat flux that increases the thermodynamic quality. This effect cannot be proven using simple cross sectional averaged void fraction results and below the local distribution effects are measured and discussed.
- Future experiments should include experiments at similar local qualities, in addition to similar inlet conditions examined in this work. This type of quality comparison is difficult to achieve along the test section length because of the different vapor production rates for smooth and swirl-flow.

Figure 7.3 shows the smooth and swirl-flow axial void distributions for 6 °C subcooling, 630 kPa and 100 kg/m^2-s. This figure again shows a small increase in the axial void fraction for the swirl flow case as discussed above.

These figures also show that for the swirl flow case there is no significant change in slope of the axial void distribution, contrary to the smooth flow case. These results may be a combination of the following phenomena:

i the large radial velocities generated in swirl flow with the twisted tape increase flow mixing and hence make the flow more homogeneous over the range of conditions tested,

ii addition of a centrifugal force caused by swirling flow may prevent or delay flow regime transitions.

iii the internal twisted tapes effectively divide the channel into two subchannels.

These may explain the continuous slope observed in the swirl-flow case as compared to smooth-flow.

7.1.1 Inlet Subcooling Effects

Inlet subcooling similarly affects the swirl-flow cross sectional and time averaged void fraction distribution as smooth-flow as shown in Figure 7.4 at 630 kPa and 100 kg/m^2-s. The axial void fraction decreases with increasing inlet subcooling, perhaps the result of decreases in the bulk liquid temperature at each location that tends to collapse void as it moves from the wall.

7.1.2 Mass Flux Effects

The effect of mass flux on cross-sectional and time averaged void fractions is shown in Figure 7.5 at 630 kPa and 6 °C subcooling. This figure shows that the axial void distribution decreases with increasing mass flux as expected. This results from a strong decrease in the quality with increased flow velocity as shown in the smooth flow case in Chapter 6.

7.1.3 System Pressure Effects

Figure 7.6 shows the axial void fraction as a function of system pressure for swirl-flow at a mass flux of 55 kg/m^2-s and 6 °C subcooling. Similar to the smooth flow case, the axial void was not significantly affected by the change in pressure but tended to decrease with increasing pressure. This may result from a similar mechanism as described in Chapter 6.

7.1.4 Effect of Test Section Orientation

The effect of test section orientation on the cross sectional averaged void fraction are shown in Figure 7.7 for horizontal swirl-flow boiling at 80 kg/m^2-s, 6 °C inlet subcooling and 630 kPa. Compared to the smooth-flow results presented in Section 6.1.4, there is no significant axial void distribution difference between the vertical and smooth flow cases. The significant radial velocities and momentum generated during swirl-flow significantly reduced the flow stratification in the horizontal test section. This effect is discussed below in terms of local void measurements.

7.2 INSTANTANEOUS CROSS SECTIONAL AVERAGED VOID FRACTION

Four instantaneous cross sectional averaged void distributions are shown in Figure 7.8 for swirl-flow at 630 kPa and 3 °C subcooling. Using the techniques described in Chapters 4 and 6, the slug velocity slip ratio was calculated and shown in Figure 7.9 for a system pressure of 630 kPa as a function of mass flux. The slip ratio decreases with increased mass flux similar to the smooth flow case. Figure 7.10 compares the smooth and swirl-flow slug velocity slip ratio as a function of mass flux. The swirl-flow slip ratio is smaller than the smooth flow case for all the conditions tested and may result from the imposed helical motion of the fluid in the channel.

7.3 TIME AVERAGED LOCAL VOID DISTRIBUTION

The ability of RTNR to reconstruct the axial and radial void distribution provides information on the behavior of the flow boiling system. Figure 7.11 shows the time-averaged image over two seconds for swirl flow boiling where the darker regions correspond to higher void at a mass flux of 55 kg/m^2-s, clearly showing the helical motion of the void. The smooth flow image is also shown for comparison in Figure 7.11

Using the void fraction calculation techniques and convolution algorithm shown in Chapter 4, the local void distribution can be calculated based on time averaged images. Figure 7.12 shows the reconstructed void distributions for vertical swirl and smooth-flow at the same condition as the images shown above. The line shown in the swirl-flow reconstruction is the centroid of the twisted tape. These figures clearly show the changes in the void distribution caused by the internal twisted tape generated swirl-flow. The distribution changes from the smooth-flow case where there is maximum void near the center of the channel that decreases monotonically towards the tube wall, to the swirl-flow case where void is concentrated near the center of each separate sub channel with a lower void at the tube center and a very low in the wall region (a double peak profile).

Figure 7.13 shows the effect of mass flux on the swirl-flow boiling time averaged local void distributions for mass fluxes of 55, 100 and 140 kg/m^2-s. In all of these reconstructed images, the void distribution behavior demonstrates trends similar to Figure 7.12. The RTNR void distribution measurements show that swirl-flow establishes void concentrations at the center of each subchannel and that the wall region void is considerably less than that for the smooth-flow case. These phenomena may be caused by the centrifugal forces generated during swirl-flow boiling that cause liquid to be forced into the wall region and vapor to collect at the center of each subchannel. Furthermore, the void fraction near the wall region seems to increase with decreasing mass flux which may result from;

i increased thermodynamic quality in the entire channel leading to increased void fraction at all locations.

ii a decrease in the centrifugal force caused by less swirling that allows vapor into the wall region.

Inlet subcooling affects on swirl-flow time averaged void distribution is shown in Figure 7.14 for 6 °C, 9 °C and 12 °C at 100 kg/m^2-s and 630 kPa. The distribution seems to depend on inlet subcooling in a similar manner as described for smooth flow in Chapter 6. Furthermore, the system pressure effects shown in Figure 7.15 again shows trends similar to those discussed for smooth flow in Chapter 6.

Finally, the effect of orientation on the void distribution during swirl flow is shown in Figure 7.16. These reconstructions show that although the flow was more homogenous than the smooth-flow case, some stratification still remained near the exit of the test section. This may have resulted from gaps between the twisted tape and channel walls that allows the flow to remain stratified. Furthermore, the range of mass fluxes examined was low in comparison to other tests[19] and this low velocity could mean that centrifugal forces generated by swirling were not significant compared to gravitational forces.

7.4 INSTANTANEOUS SWIRL FLOW LOCAL VOID DISTRIBUTION

The instantaneous void distribution for swirl-flow boiling is shown in Figure 7.17 for a 133 ms time frame at 100 kg/m^2-s, 6 °C inlet subcooling and 630 kPa. The instantaneous results show a bubbly-type flow regime with bubbles tending to concentrate in the center of each subchannel. Bubble agglomeration may be reduced due to;

i the physical presence of the twisted tape which prevented bubbles in each subchannel from interacting with bubbles on the other side.

ii the increased turbulence caused by flow swirling could prevent agglomeration and/or help to break larger bubbles into smaller sizes.

These effects may significantly alter the behavior of flow boiling in the channel and may explain the large increases in CHF encountered during flow swirling.

Figure 7.18 shows the effect of mass flux on the instantaneous swirl flow local void fraction for 100 and 140 kg/m^2-s at 9 °C inlet subcooling and 630 kPa. The effect of inlet subcooling and system pressure on the instantaneous void distribution are also shown in Figure 7.19 and 7.20 respectively for swirl-flow boiling. Figures 7.18, 7.19 and 7.20 show similar behavior to the smooth flow instantaneous void distributions shown in Chapter 6.

7.5 ADVANCED XCT RESULTS

An experimental program was undertaken to provide detailed cross-sectional void distribution information for smooth and swirling-flows. At the time of publication, results were not available for the smooth-flow case. However, the swirl-flow results discussed below further add to the void distribution information discussed above and further substantiate the need for this information.

7.5.1 XCT Cross Sectional Averaged Void Distribution

The radial void distributions obtained using RTNR provide valuable information on the behavior of void during swirling flow. However, as discussed in Chapter 4, these reconstructions require assumptions on the partial symmetry in the flow channel. To validate and quantify this assumption and to obtain a clearer picture of the void behavior, ultra-high speed XCT was used on the flow channel. Figure 7.21 shows the time averaged void distribution for swirl-flow obtained using 2000 slices of Refrigerant 123 flow boiling over a period of 2 seconds with the darker regions corresponding to higher void fractions. This figure shows the vapor regions near the center of each subchannel and a permanent liquid layer at the wall region similar to the RTNR results discussed above.

7.5.2 XCT Instantaneous Void Distribution

Figure 7.22 shows consecutive XCT slices over a period of 15 ms for swirl-flow boiling of Refrigerant 123 at a mass flux of 700 kg/m^2-s with dark regions corresponding to vapor pockets. These images show a bubbly flow pattern (images #1-12) with periodic agglomeration to form slugs (images 13-15). Furthermore, these images can be shown consecutively to form a void distribution slow motion video movie as described in Chapter 4. Inspection of this video shows very little void in the wall region that further supports the RTNR analysis previously discussed. To show this video sequence the cross sectional images have been assembled and void regions connected to form the 3-dimensional image shown in Figure 7.23.

The cross-sectional void distributions obtained with high speed XCT provide angular in addition to radial void measurements that strongly support the RTNR experiments conducted. These results also show that the circular symmetry used in the RTNR radial convolution algorithm is valid.

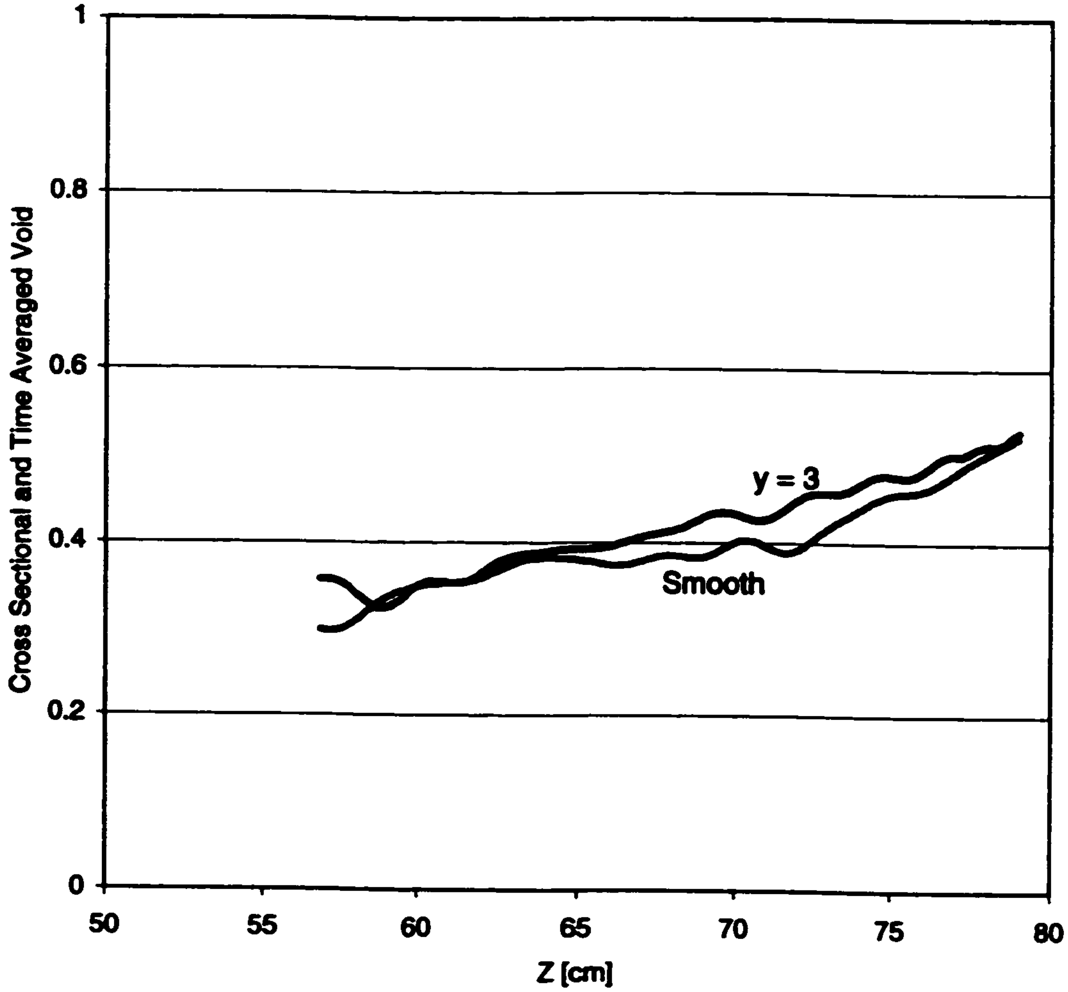

Figure 7.1 Effect of Swirl Flow on the Time and Cross Sectional Averaged Void Distribution at 55 kg/m^2-s, 6 °C Inlet Subcooling and 630 kPa.

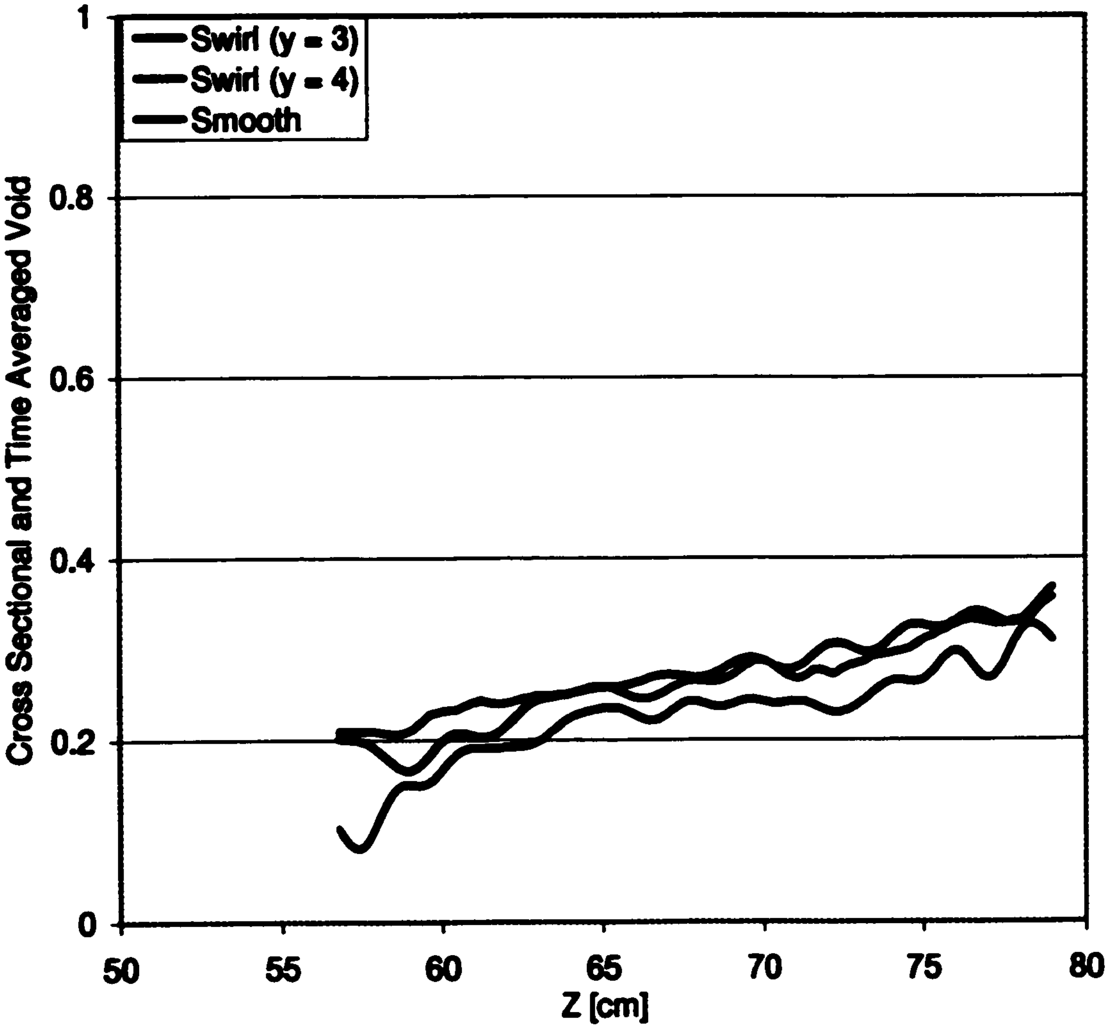

Figure 7.2 Effect of Swirl Flow on the Time and Cross Sectional Averaged Void Distribution 55 kg/m^2-s, 12 °C Inlet Subcooling and 630 kPa.

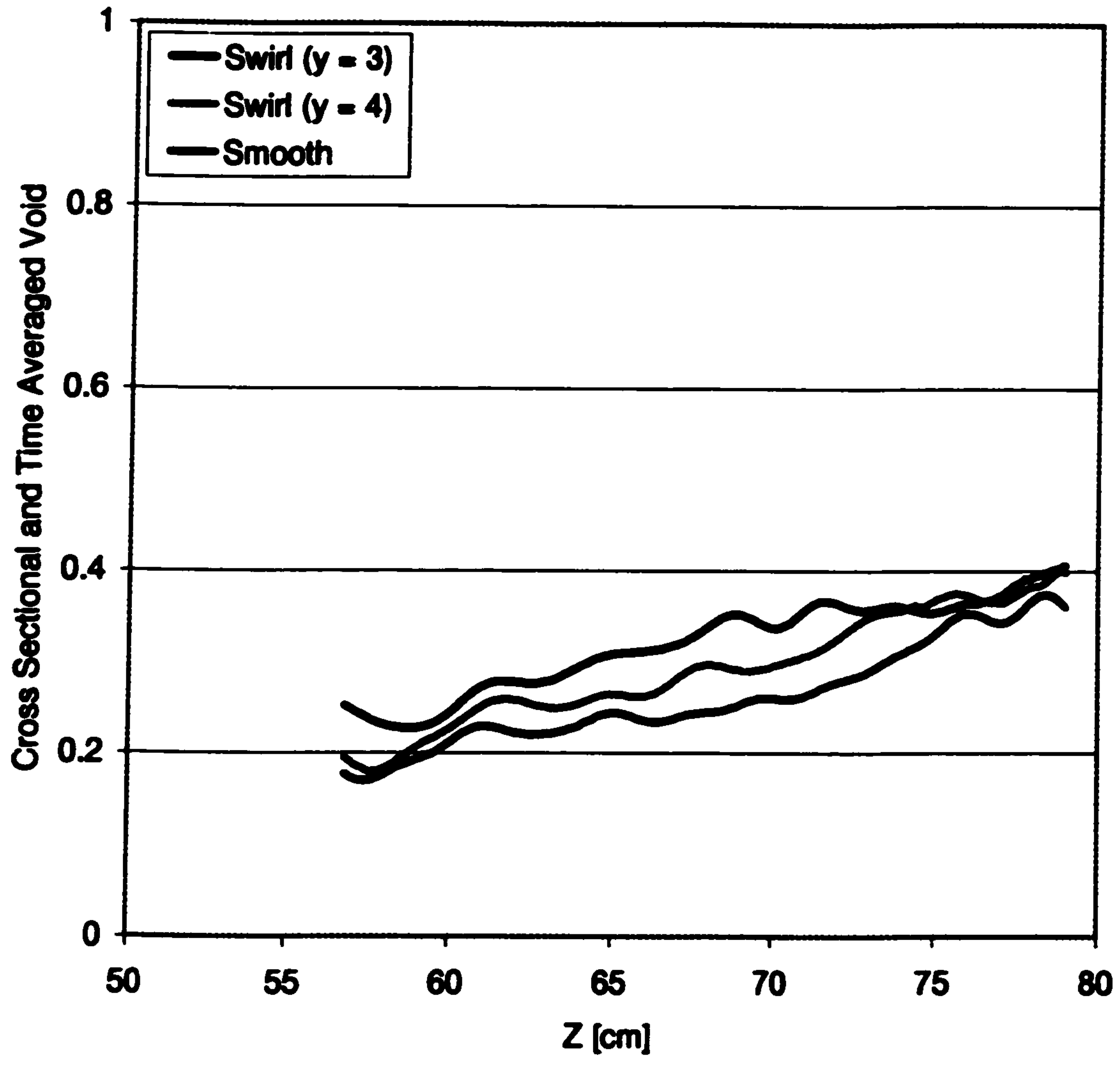

Figure 7.3 Effect of Swirl-Flow on the Time and Cross Sectional Averaged Void Fraction Distribution at 100 kg/m^2-s, 6 °C Inlet Subcooling and 630 kPa.

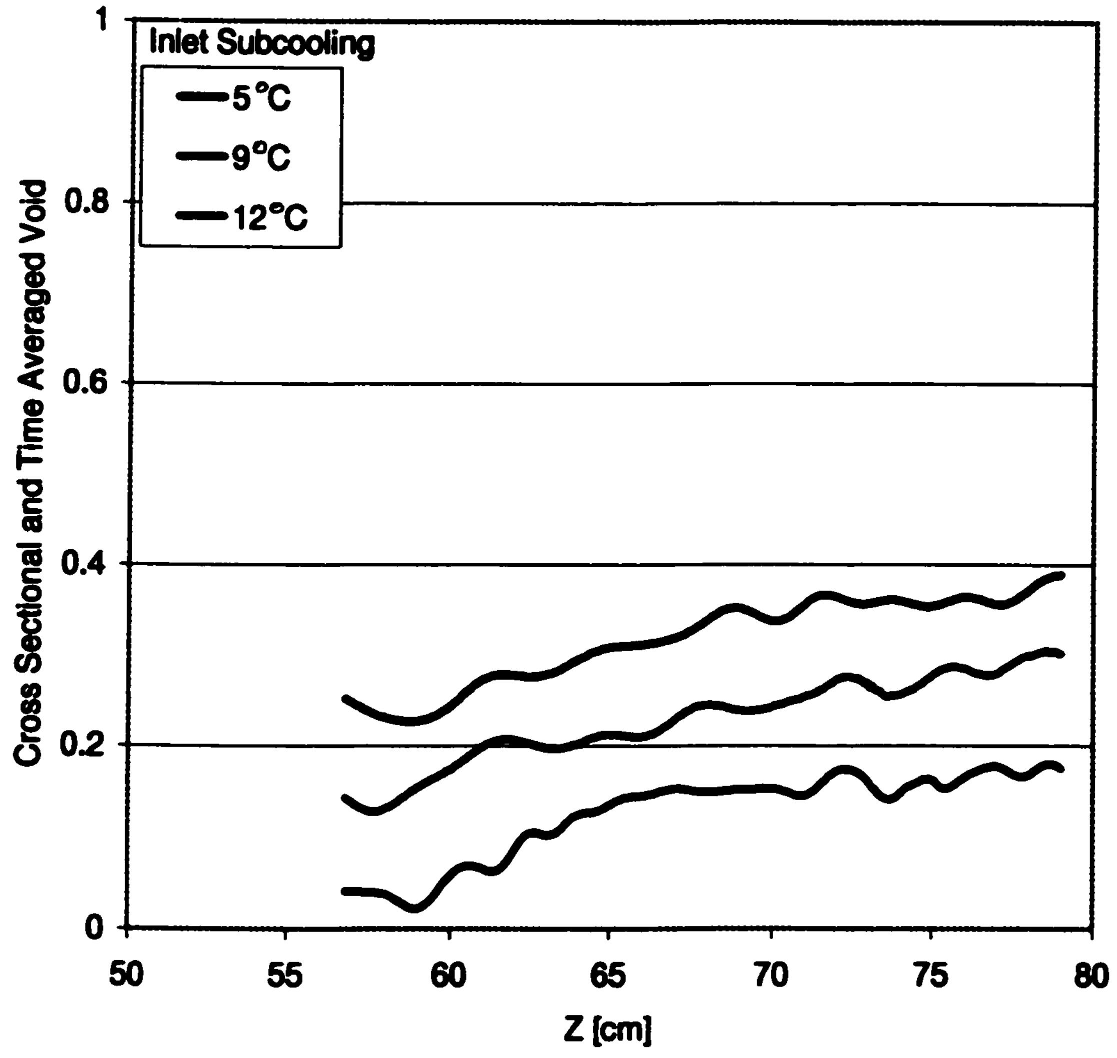

Figure 7.4 Effect of Inlet Subcooling on Cross Sectional and Time Averaged Void Distribution for Refrigerant 134a Smooth-Flow Boiling at 100 kg/m^2-s and 630 kPa.

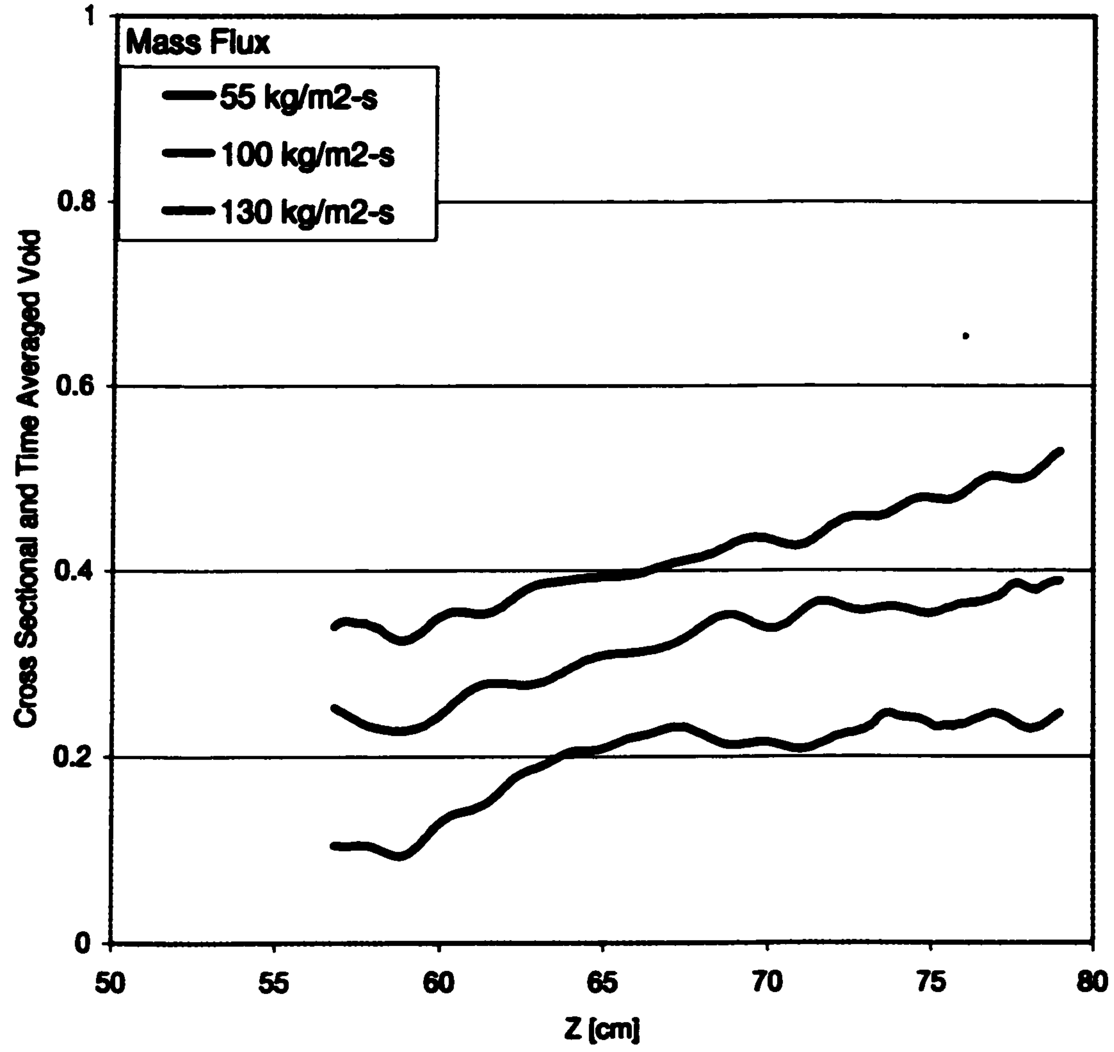

Figure 7.5 Effect of Mass Flux on Refrigerant 134a Cross Sectional and Time Averaged Void Distribution for Refrigerant 134a Swirl-Flow Boiling at 6 °C Inlet Subcooling and 630 kPa.

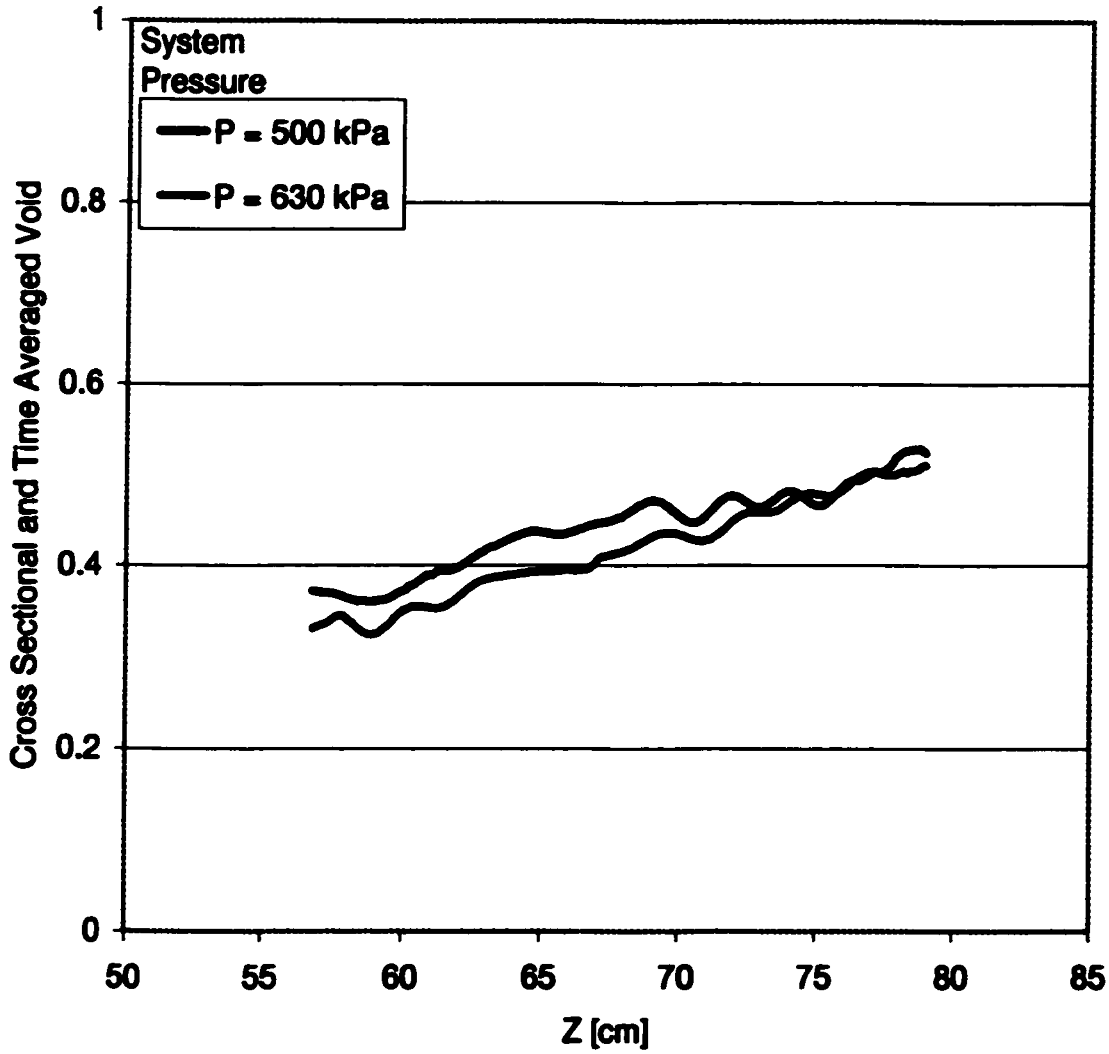

Figure 7.6 Effect of System Pressure on Cross Sectional and Time Averaged Void Distribution for Refrigerant 134a Swirl-Flow Boiling at 55 kg/m^2-s and 6 °C Inlet Subcooling.

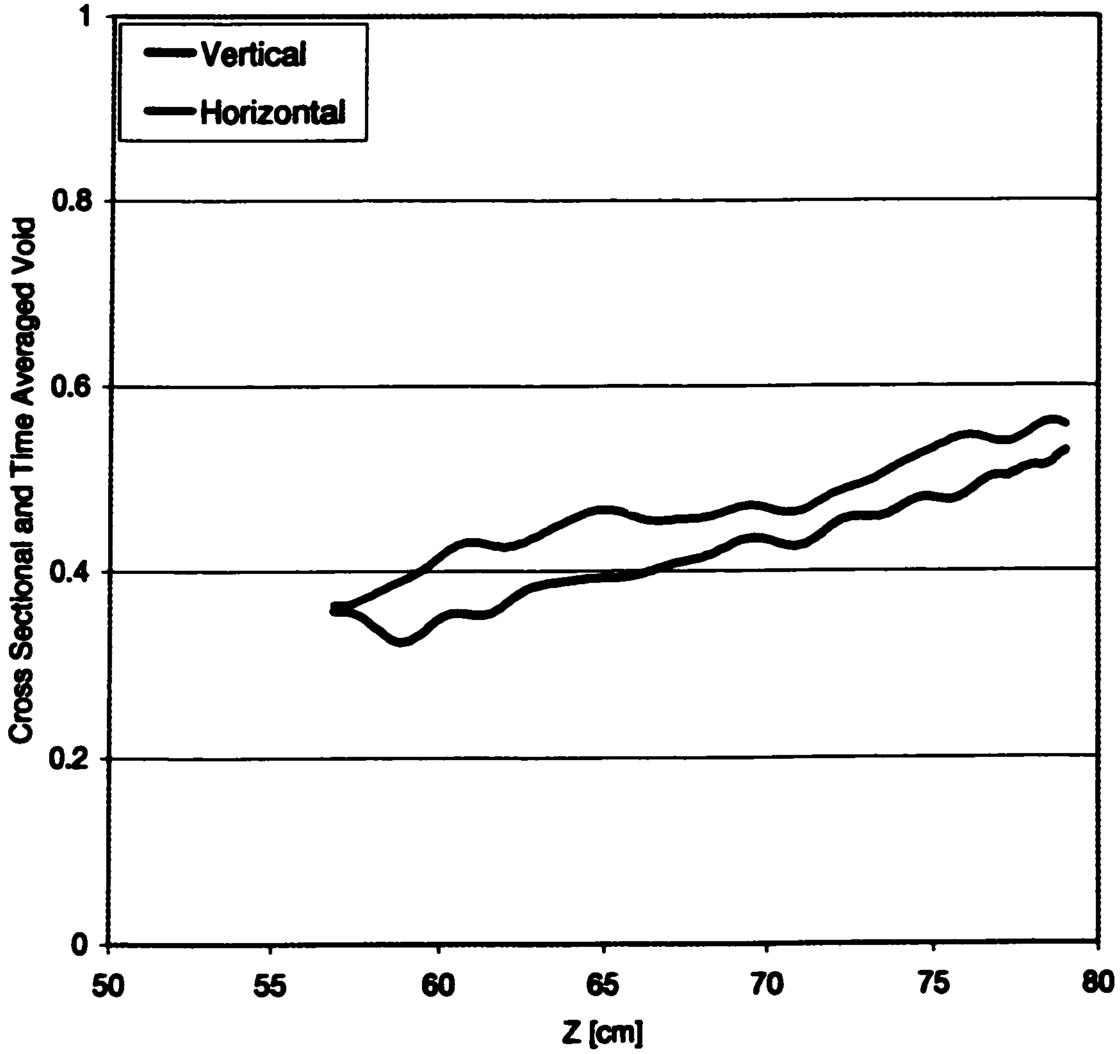

Figure 7.7 Effect of Test Section Orientation of Cross Sectional and Time Averaged Void Distribution for Refrigerant 134a Swirl-Flow Boiling at a twist ratio of 3, 630 kPa and 55 kg/m^2-s.

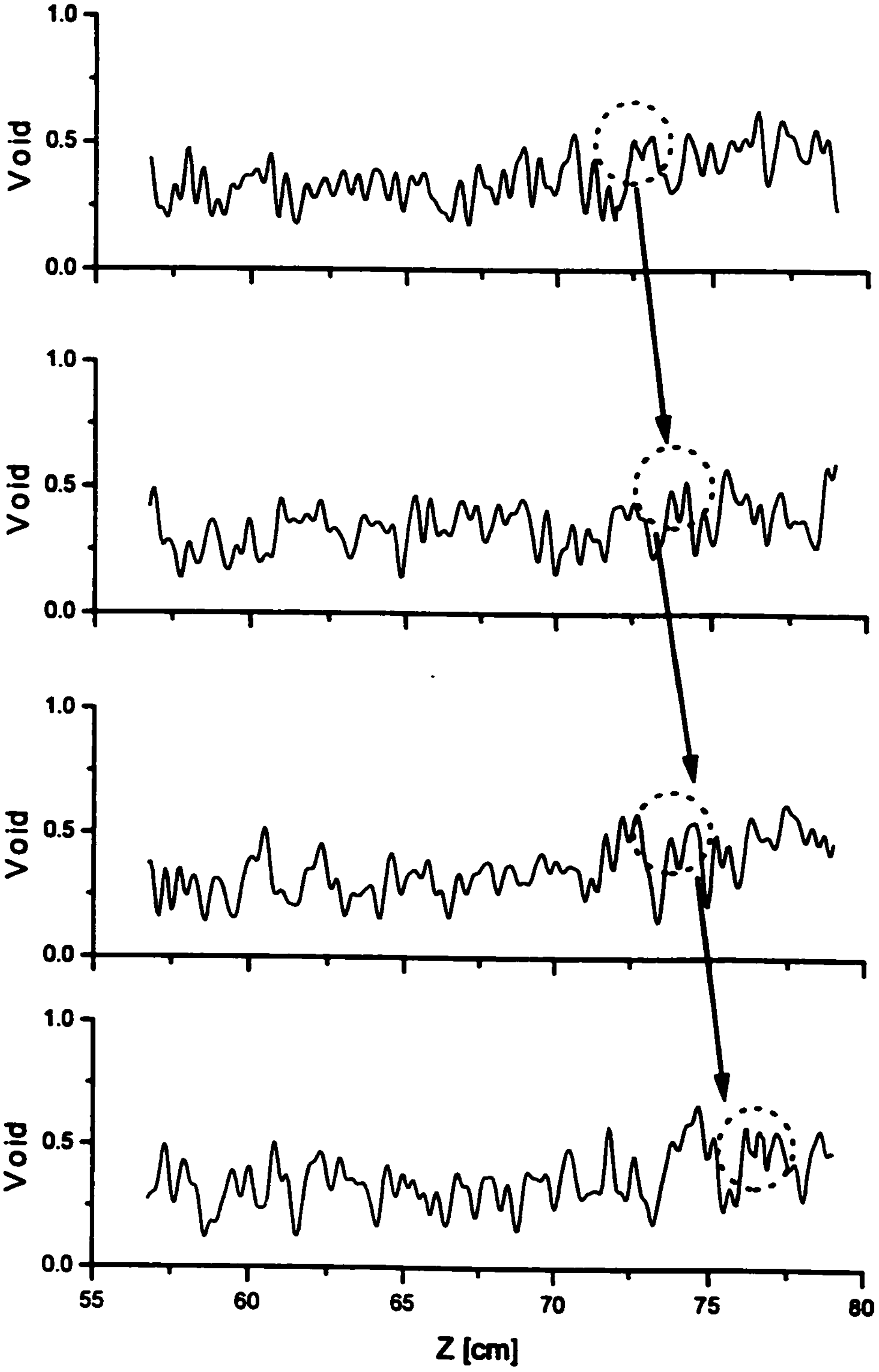

Figure 7.8 Instantaneous Cross Sectional Void Fraction Distribution for Swirl Flow at 55 kg/m^2-s, 9 °C Inlet Subcooling and 630 kPa.

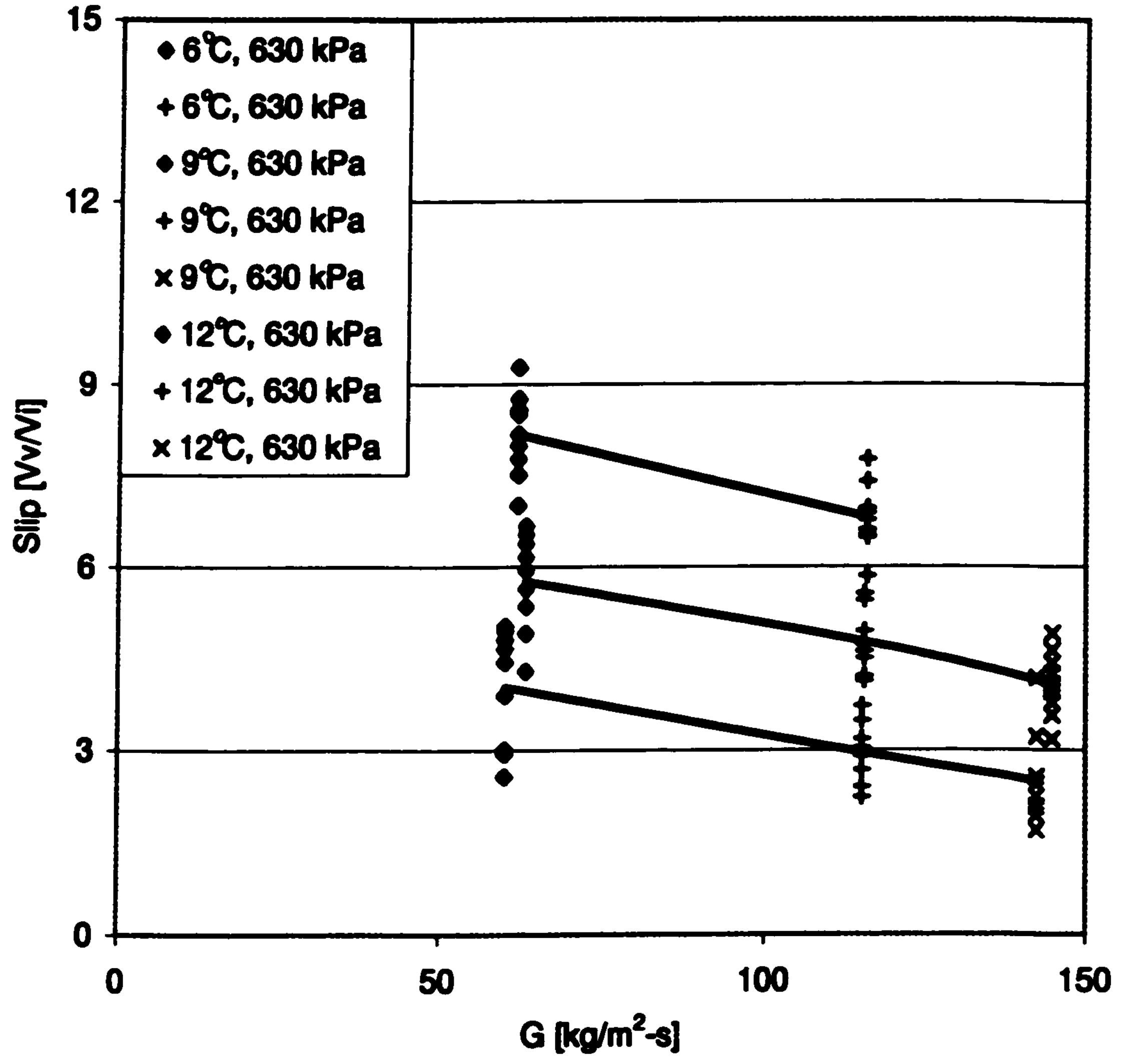

Figure 7.9 Effect of Mass Flux on the Vapor Slug Slip Ratio at 630 kPa for Swirl Flow.

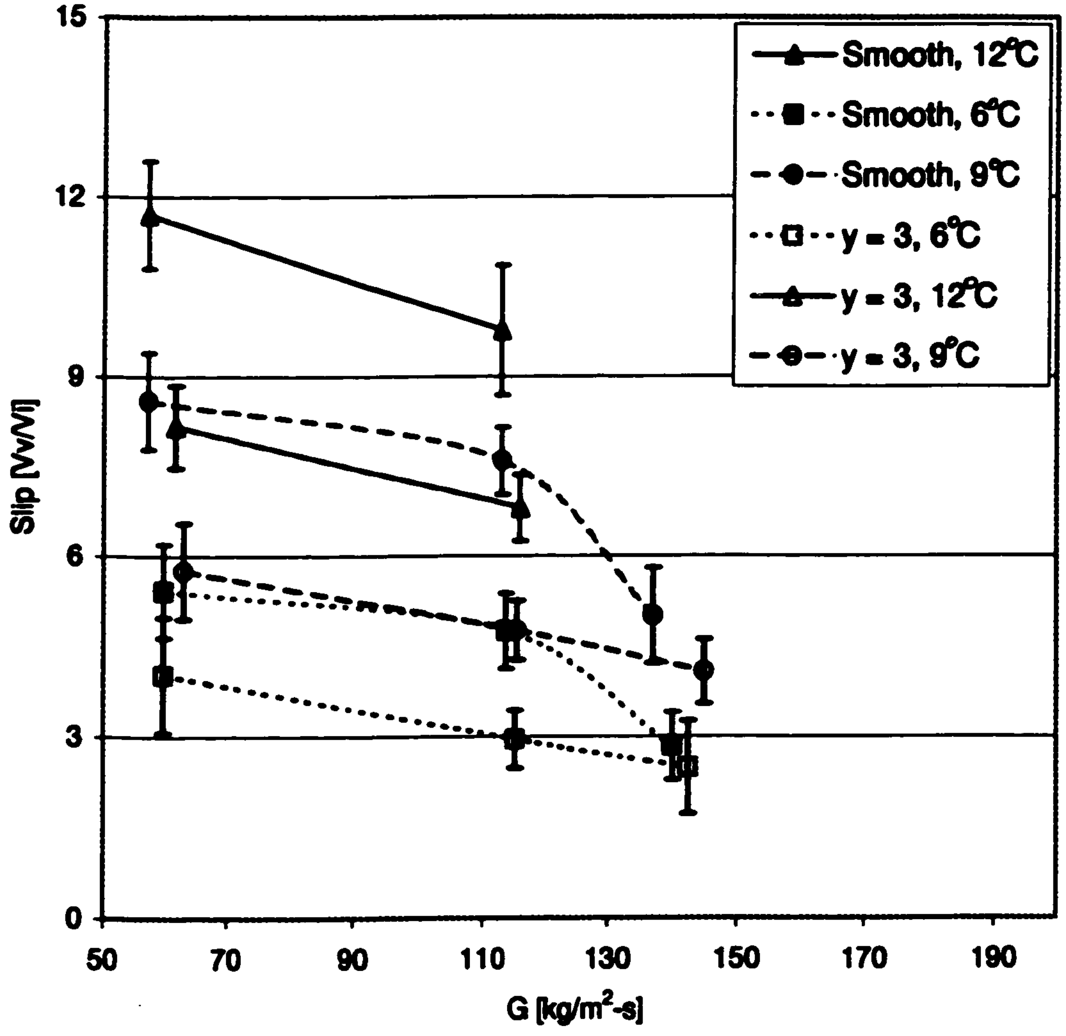

Figure 7.10 Effect of Swirl-Flow on the Vapor Slug Slip Ratio at 630 kPa.

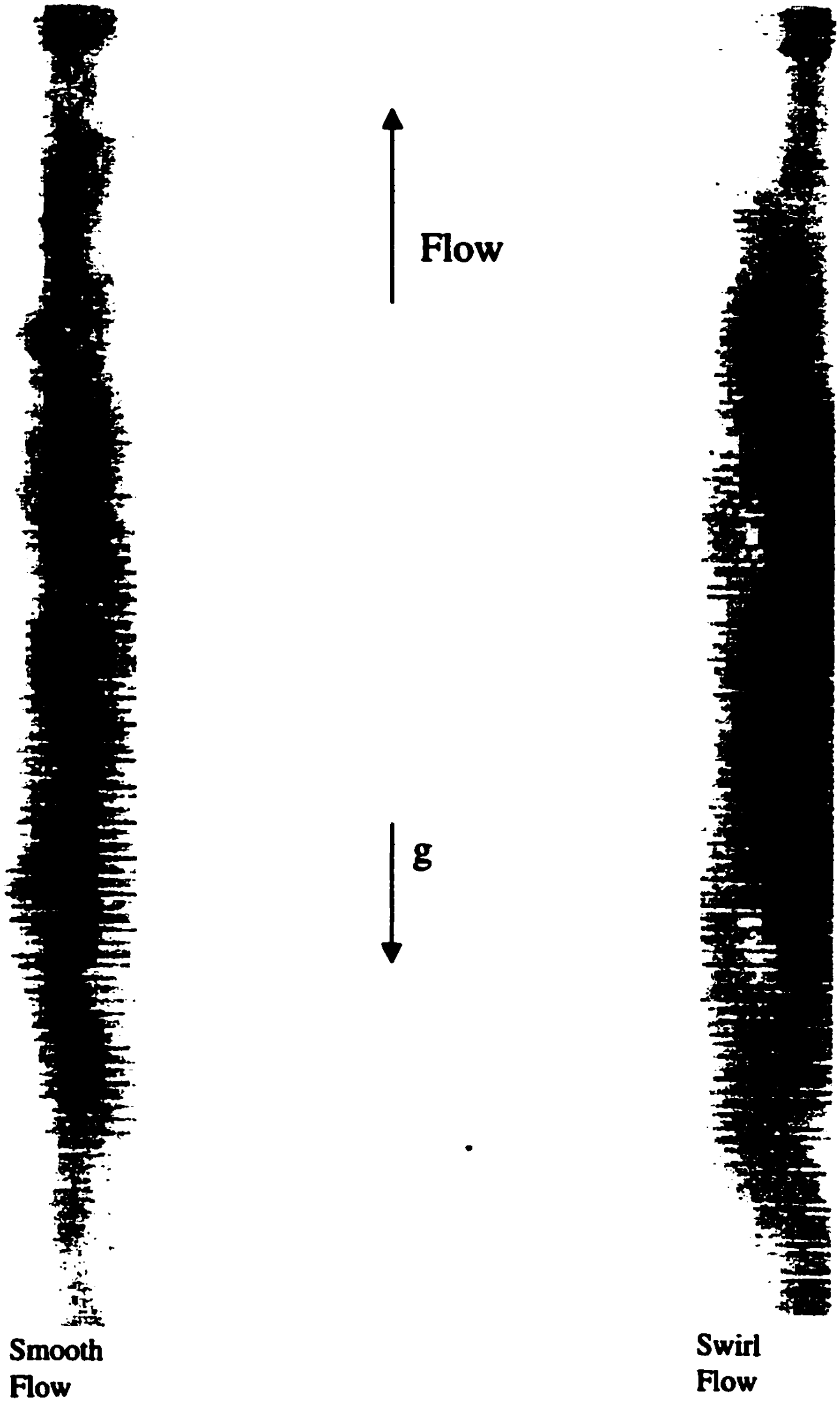

Figure 7.11 Time Averaged Local Void Fraction Distribution for Refrigerant 134a Swirl-Flow Boiling at 55 kg/m^2-s.

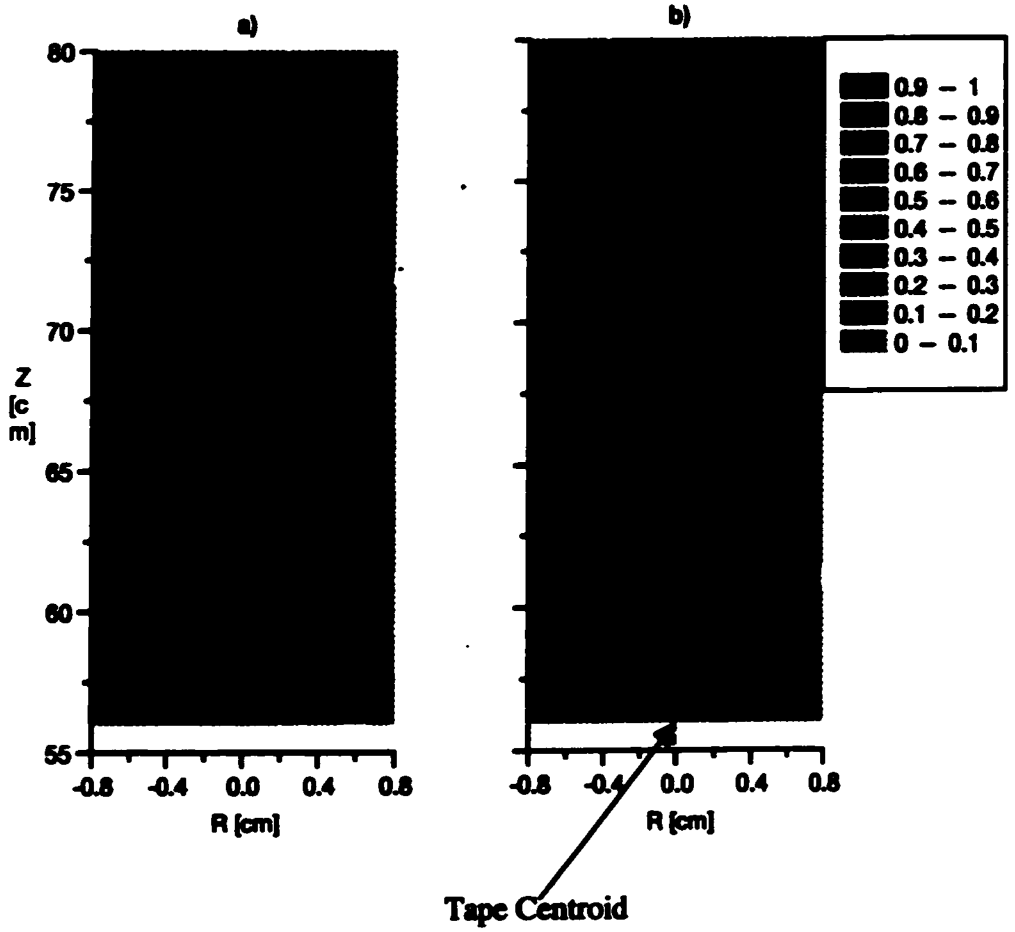

Figure 7.12 Time Averaged Local Void Fraction Distribution for Refrigerant 134a a) Smooth-Flow and b) Swirl-Flow Boiling at 55 kg/m^2-s, 9 °C Inlet Subcooling and 630 kPa.

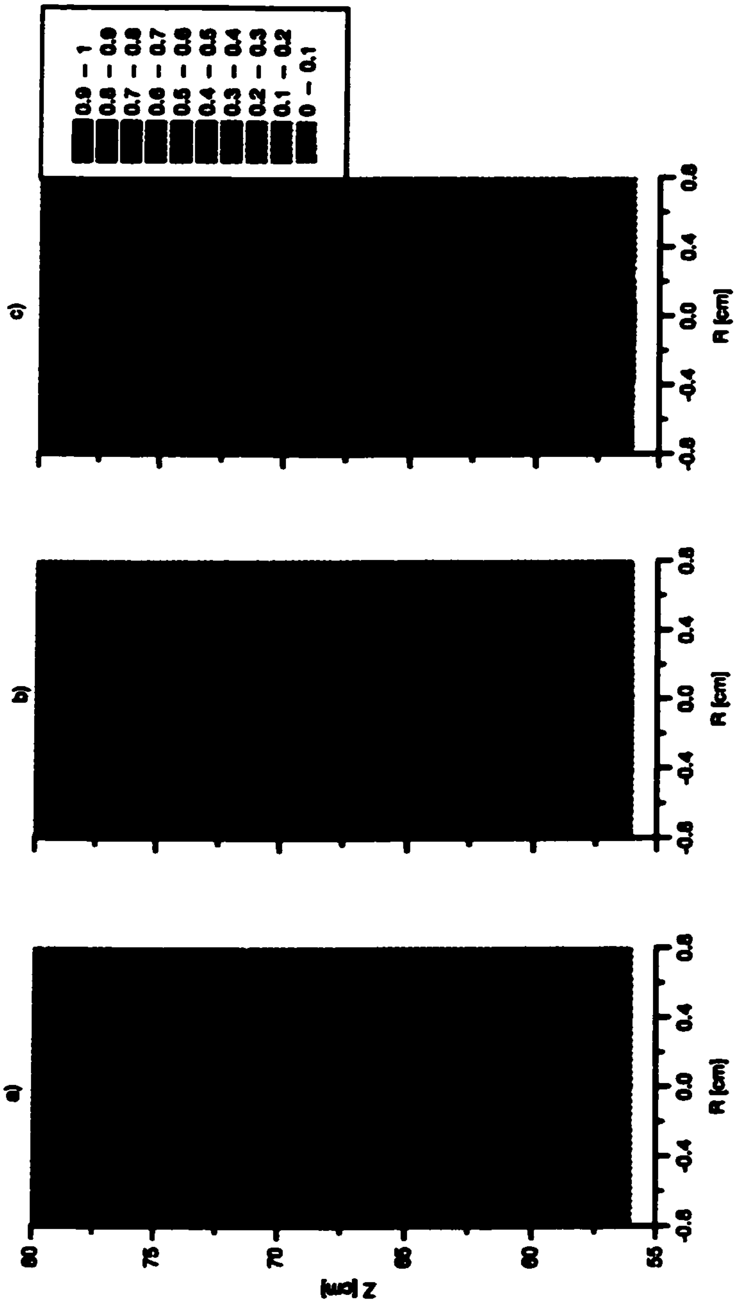

Figure 7.13 Effect of Mass Flux on Swirl Flow Boiling Time Averaged Local Void Distribution for a) 55 , b) 110 and c) 140 kg/m^2-s at 630 kPa and 6 °C Subcooling.

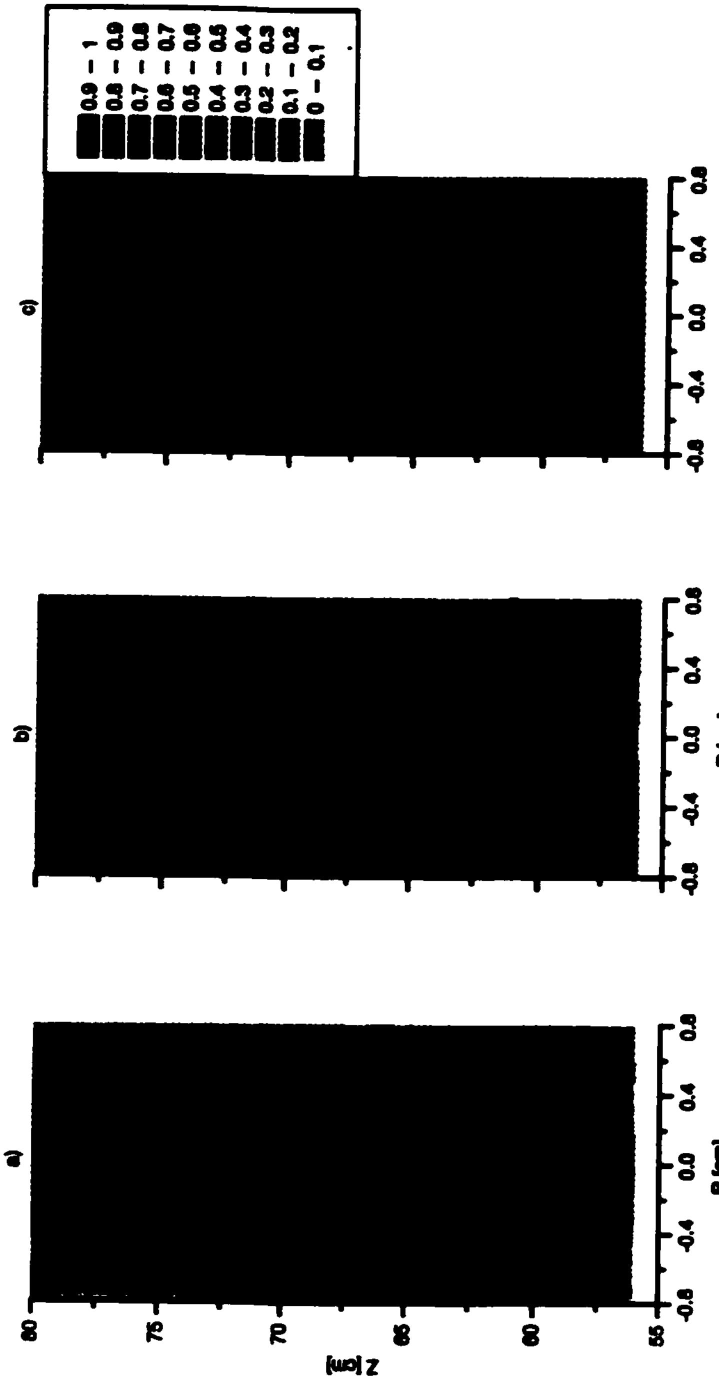

Figure 7.14 Effect of Inlet Subcooling on Swirl Flow Boiling Time Averaged Void Distribution for a) 12 , b) 9 and c) 6 °C Inlet Subcooling at 110 kg/m^2-s and 630 kPa.

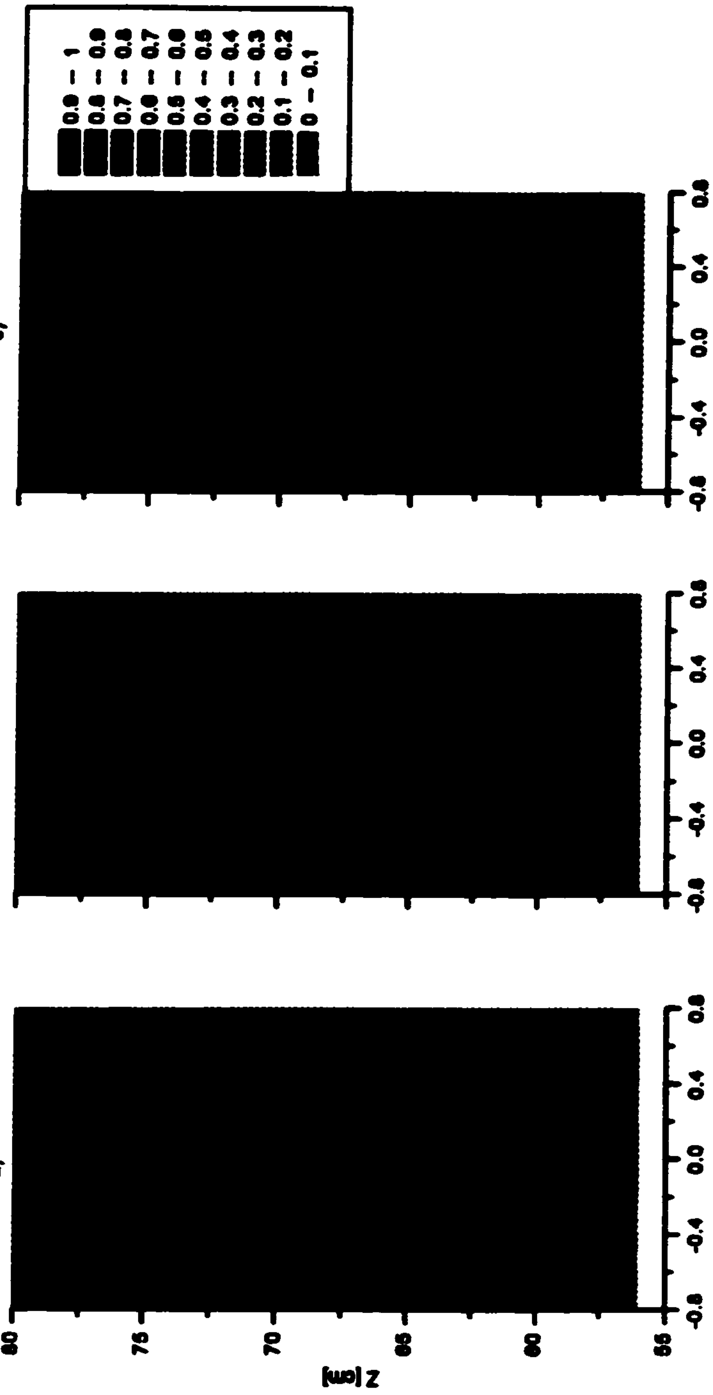

Figure 7.15 Effect of System Pressure on Swirl Flow Boiling Time Averaged Void Distribution for a) 500 , b) 630 and c) 700 kPa at 55 kg/m^2-s and 9 °C Inlet Subcooling.

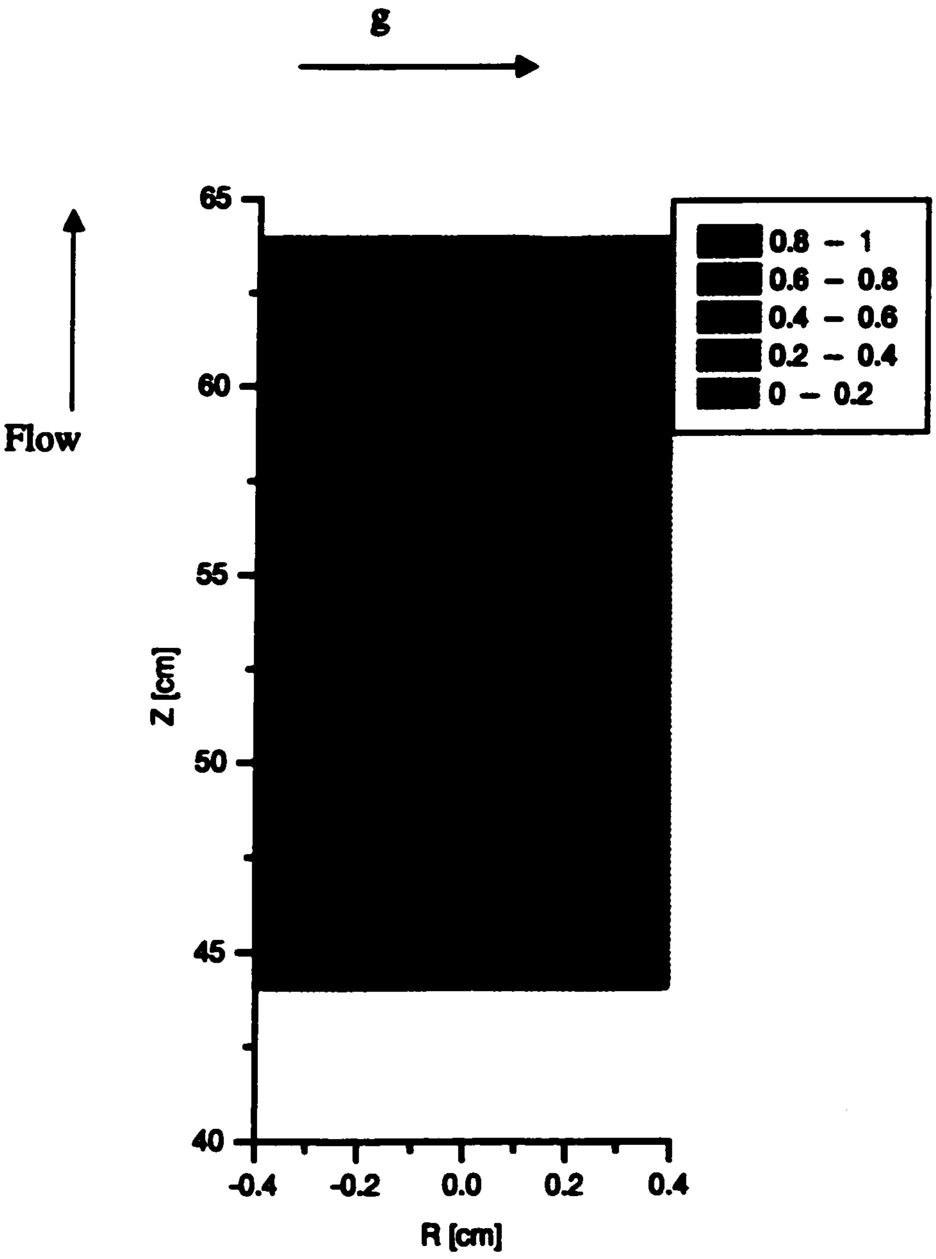

Figure 7.16 Orientation on Swirl-Flow Boiling Time Averaged Void Fraction Distribution at 100 kg/m^2-s and 6 °C Inlet Subcooling.

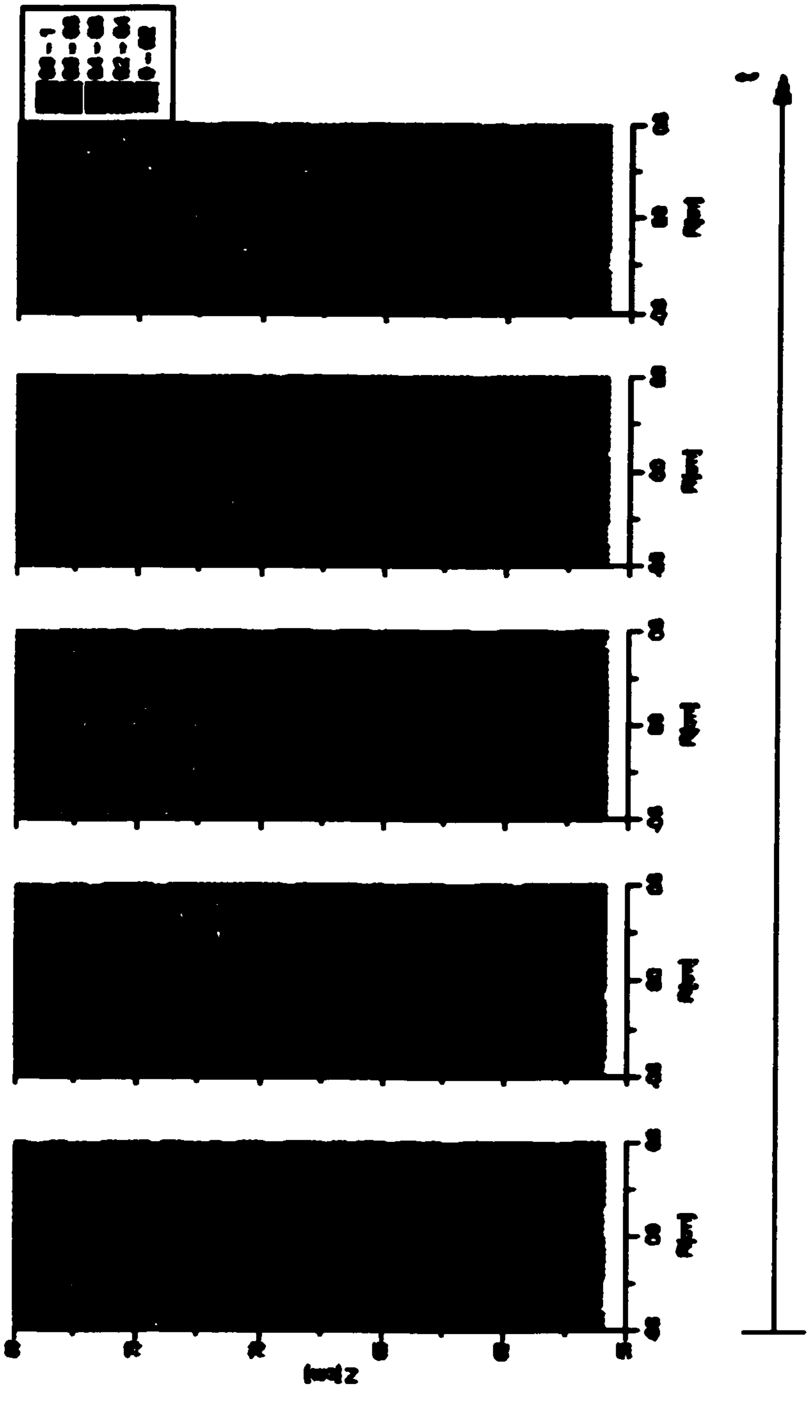

Figure 7.17 Instantaneous Local Void Distribution for Swirl-Flow Boiling of Refrigerant 134a at 55 kg/m^2-s, 6 °C Inlet Subcooling and 630 kPa.

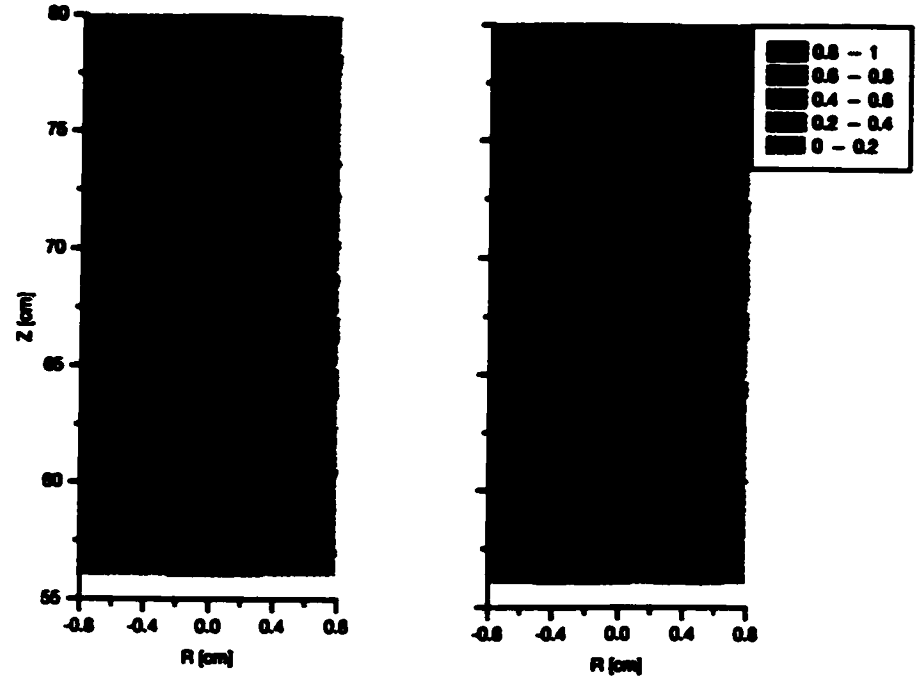

a) 100 kg/m^2-s

b) 140 kg/m^2-s

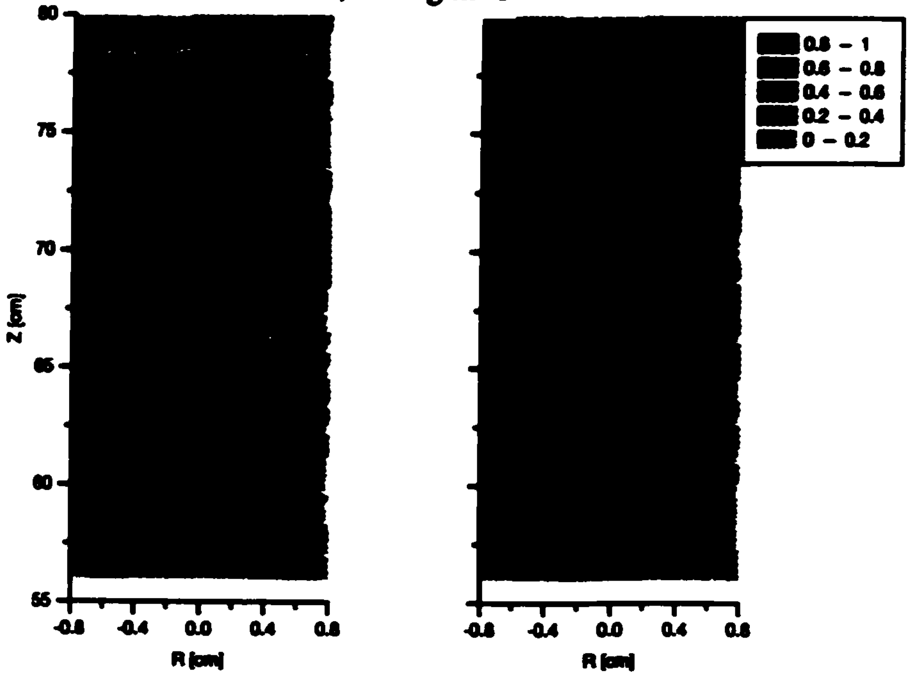

Figure 7.18 Effect of Mass Flux on the Instantaneous Local Void Distribution for Swirl-Flow Boiling of Refrigerant 134a for a) 100 kg.m2-s and b) 140 kg/m^2-s at 9 °C Inlet Subcooling and 630 kPa.

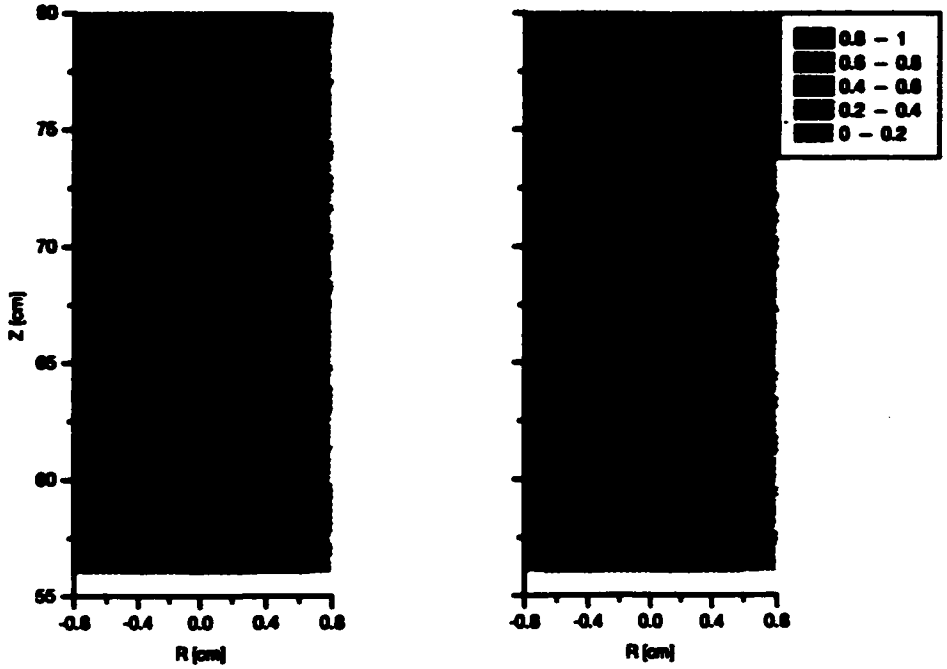

a) 9 °C

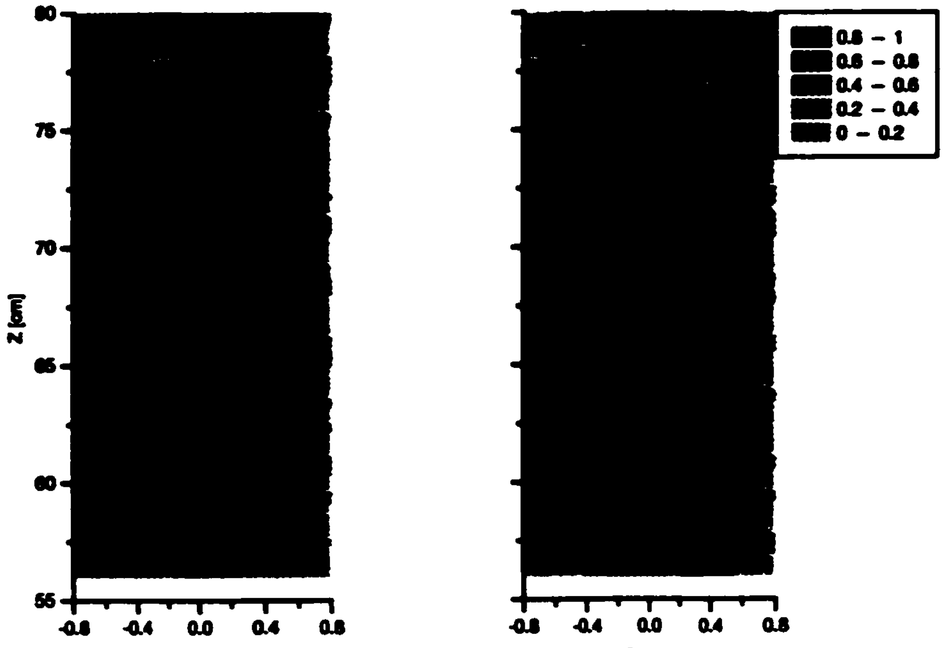

a) 12 °C

Figure 7.19 Effect of Inlet Subcooling on Instantaneous Local Void Distribution at 55 kg/m^2-s and 630 kPa at a) 9 and b) 12 °C Subcooling.

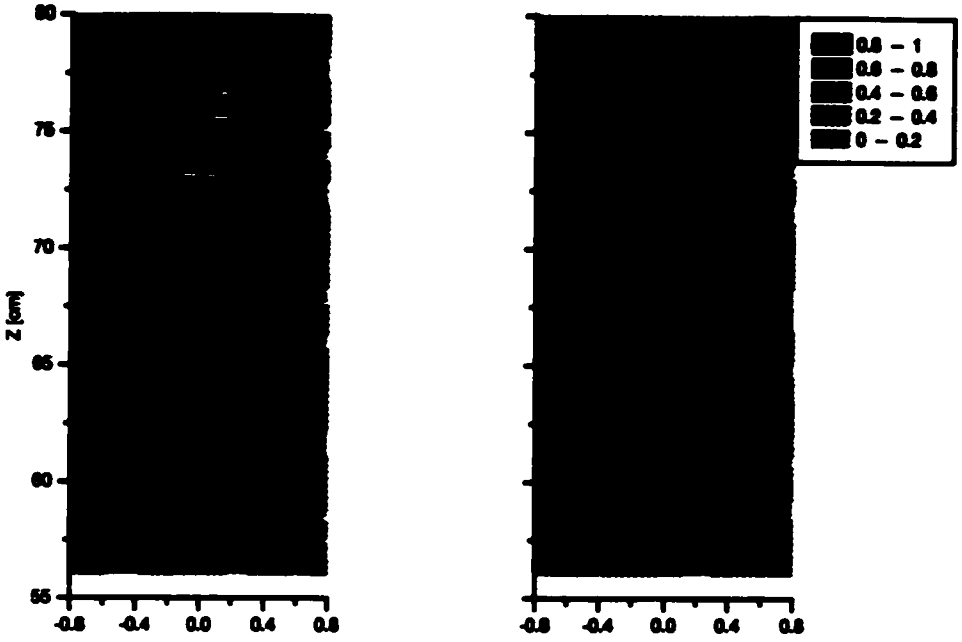

b) 500 kPa

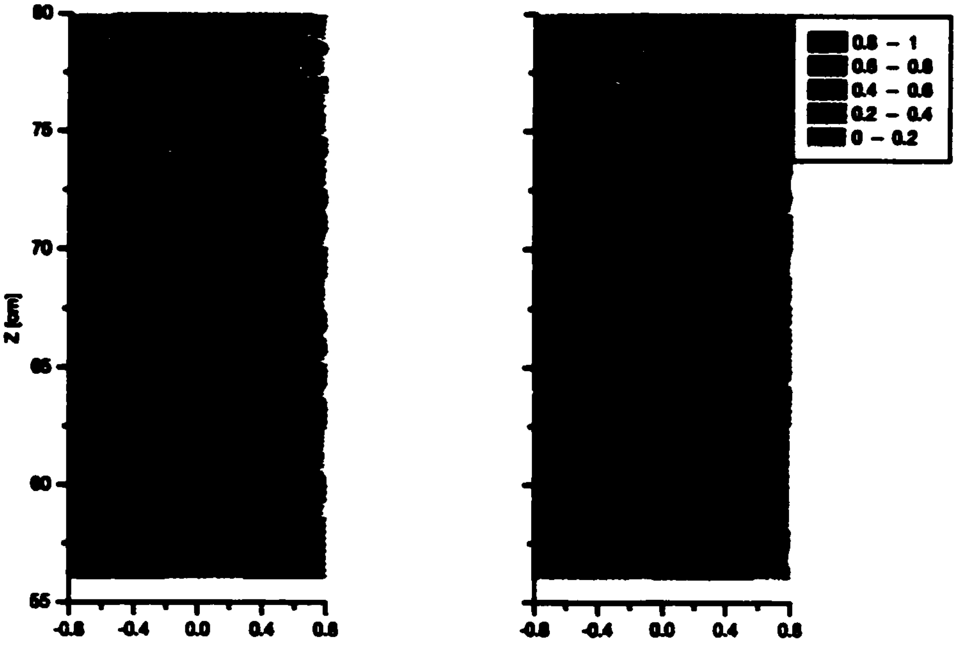

b) 630 kPa

Figure 7.20 Effect of System Pressure on Instantaneous Local Void Distribution at 55 kg/m^2-s and 6 °C Inlet Subcooling for a) 500 and b) 630 kPa.

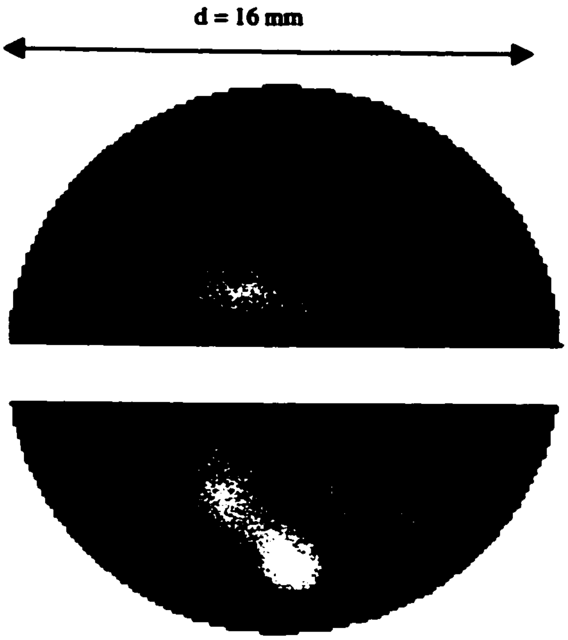

Figure 7.21 Time Averaged XCT Measurement of Swirl Flow Boiling of Refrigerant 123 at 750 kg/m^2-s and 630 kPa.

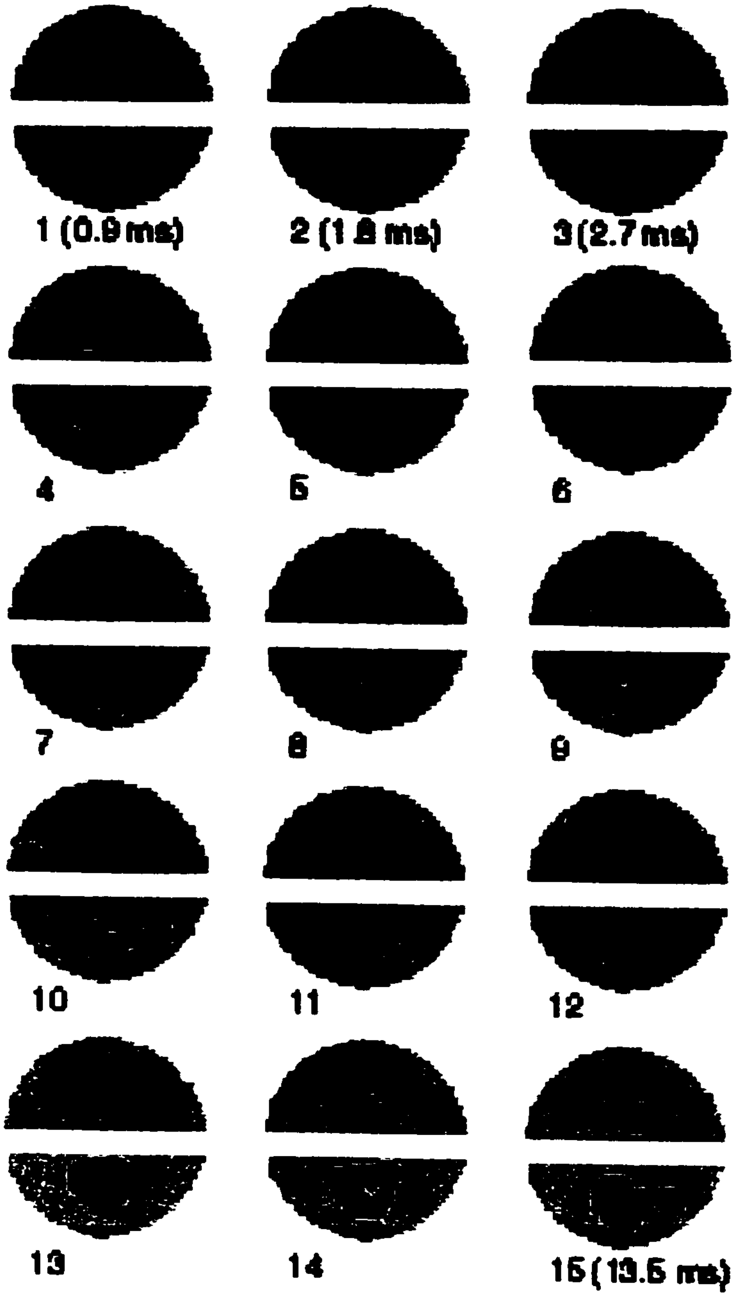

Figure 7.22 Instantaneous Void Distribution Measurement (0.9 ms per slice) of Swirl Flow Boiling of Refrigerant 123 at 750 kg/m^2-s and 630 kPa Using High Speed XCT.

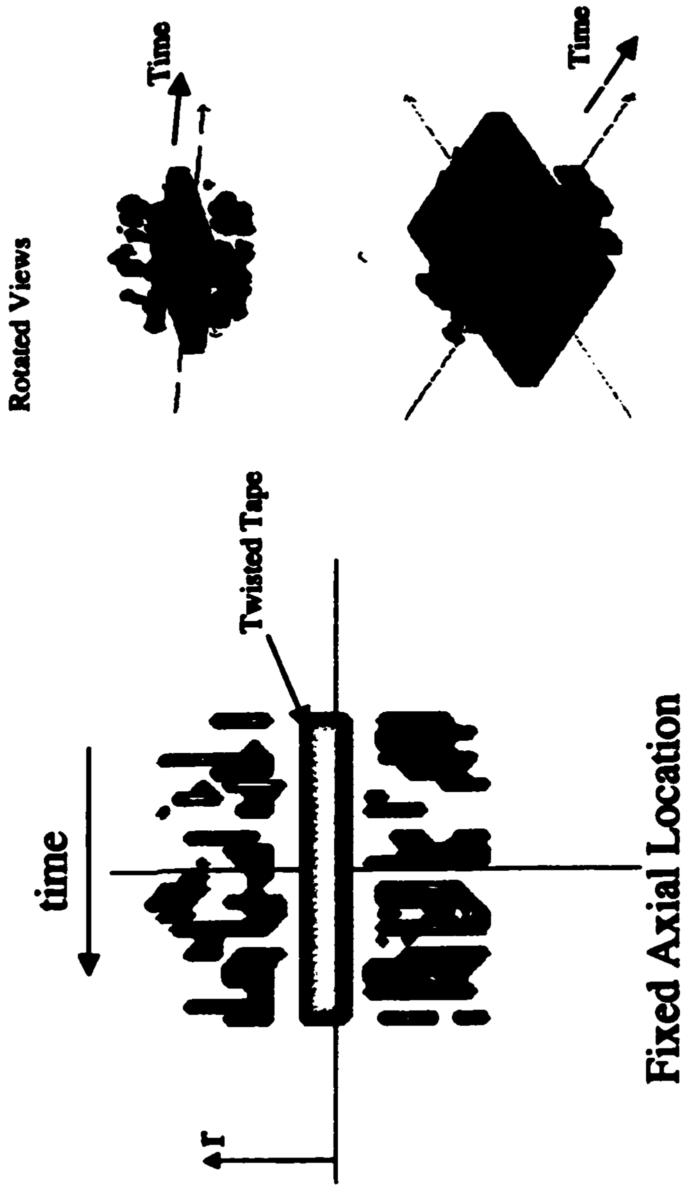

Figure 7.23 Instantaneous 3-Dimensional Reconstruction of Refrigerant 123 Flow Boiling at 750 kg/m^2-s and 630 kPa Based on 300 High Speed XCT Slices (shown in Figure 7.22).

CHAPTER 8 CONCLUSIONS

The insitu measurement of void distribution during flow boiling using Real Time Neutron Radiography has been demonstrated for smooth-tube and swirl-flow conditions. Its importance in understanding heat transfer and pressure drop performance has also been established. Current predictive techniques for two-phase flow boiling rely heavily on constitutive relationships describing void behavior, and this thesis has clearly demonstrated the application of RTNR for time dependent measurement for this purpose.

8.1 SMOOTH FLOW TIME AND CROSS SECTIONAL AVERAGED RESULTS

From the cross and time averaged analysis of the smooth-tube flow experiments shown in Chapter 6, it can be concluded that;

- the change in slope of the measured axial void distributions under smooth-flow in a round tube with lower flows and subcoolings, may be the result of a transition in flow-regime.
- the measured void fraction was bounded by the simple correlations developed by Wallis, Thom et al. and the homogeneous mixture model. All correlations significantly over predicted the cross section and time averaged void fractions with the Wallis correlation most closely predicting the measured trends. The over predictions resulted from non-thermodynamic equilibrium effects which are not accounted for in these models.
- the measured vapor slip ratio show that a mixture type void fraction model is not appropriate for the entire range of conditions tested and that this slip ratio(momentum non-equilibrium) contributed to the over-prediction of the models above.
- the cross-sectional and time averaged void fraction decreases significantly with increasing mass flux. This phenomenon resulted from a combination of increased forced convection heat transfer (i.e. less energy is available for void production), and/or from further changes in the vapor slip ratio, and/or a further transition to a more homogenous mixture. A transition to a homogenous mixture results in:

  i decreased bubble coalescence

  ii increased mixing causing large bubble fragmentation

These two factors mean that the bubble size may decrease to the extent that individual bubble measurement using the current RTNR system is difficult.

iii the void fraction increases with decreased subcooling due to a shift in the location of ONB toward the exit of the channel.

In general, the time and cross sectional results show the basic trends and behavior expected during subcooled boiling. The axial void profiles clearly showed flow regime or boiling mechanism transition, with more detail being obtained using the transient and local measurements.

8.2 INSTANTANEOUS AREA AVERAGED VOID FRACTION MEASUREMENT

The instantaneous void fraction measurements discussed in Chapter 6 provide detail on the vapor movement in the channel during flow boiling. From these experiments, it can be concluded that;

- the measured void fraction waveforms have peaks that are quasi-periodic indicating a slug-type flow. However, the base void fraction is significantly greater than zero for all cases, indicating the presence of a large number of bubbles or even a transition to an annular type flow pattern in the channel.
- the vapor slip ratio decreases with increasing mass flux. The increased fluid turbulence with increasing mass flux prevent large bubble formation and works to reduce bubble size through agitation. With a reduction in bubble size the flow becomes more homogeneous and hence the vapor slip ratio should decrease.
- the vapor slip ratio increases with decreasing subcooling. Under similar conditions, more void is generated for lower subcooling levels which leads to increases in bubble coalescence, and a shift away from thermodynamic equilibrium.

These instantaneous results provide vapor slug velocities that are typically used in two-phase flow prediction methodology. The vapor slip ratio of these slugs ranged from 2.5 to 15 for the range of conditions tested which indicates a significant deviation from homogenous behavior.

Furthermore, predictive techniques must consider these fluctuations which have magnitudes that may cause damage to system components.

8.3 LOCAL TIME AVERAGED VOID DISTRIBUTION RESULTS

The local void distribution behavior was calculated based on the principles discussed in Chapter 4 and the results shown in Chapter 6. These time-averaged results show the regions of high and low void concentration in relationship to the heat transfer surface. From these results it can be concluded that;

- the local void fraction is highest near the center of the channel and decreases with increasing radial distance from the center. The wall void fraction is significantly lower than that at the channel centerline indicating that wall bubbles are small and significant agglomeration occurs along the test section length.
- the centerline void fraction increases with decreasing mass flux. This resulted from increases in the local thermodynamic quality as discussed previously and/or increased bubble agglomeration. These local and instantaneous results discussed below, suggest that agglomeration is significant as shown by large diameter bubbles traveling near the center of the test section.

8.4 INSTANTANEOUS LOCAL VOID FRACTION DISTRIBUTION

One of the most valuable applications of RTNR is the measurement of the instantaneous void distribution during flow boiling. The visualization of bubbles as they evolve in the channel provides information on bubble size, position and velocity. From the experimental results shown in Chapter 6 it can be concluded that;

- near the wall region there are significantly fewer void pockets. This may result from bubbles that are too small to be detected with the present system or from a change in the flow boiling behavior to a slug type annular or annular mist flow regime. The decrease in contrast near the wall caused by neutron scattering from the channel walls and water jacket may cause some smearing of bubble measurements near the wall.
- it is possible to track specific void pockets over a period of time to determine their shape, position and growth in addition to the slip velocity ratio using cross sectional averaged results previously discussed.

8.5 SWIRL FLOW VOID DISTRIBUTION MEASUREMENT

The application of RTNR to an enhanced heat transfer flow boiling device was demonstrated in Chapter 7. These results further emphasize the need and application of local void measurements during flow boiling. The cross-sectional and time averaged void fraction distribution was not significantly affected by swirling flow in the channel. The minor increases in void for the swirl-flow case may have resulted from heat conduction from the walls to the center of the tape, an increased overall liquid path length or non equilibrium effects such as changes in the void velocity caused by helical motion. The instantaneous void distributions were used to approximate the vapor slip ratio for slugs in the channel. The swirl flow slip ratio was less than the smooth-flow case and may have resulted from the helical motion as compared to pure axial in the smooth case.

The time averaged local void distribution was significantly different from that corresponding to the smooth-flow case. The void concentrated in the center of each subchannel showed the impact of the twisted tape geometry on flow distribution. The wall void was also significantly less than that encountered in the smooth flow case, resulting from centrifugal forces pushing heavier liquid to the heat transfer surface or from increased turbulence which may reduce bubble agglomeration in this region.

Ultra-high speed computed tomography experiments were used for comparison to the RTNR results. These experiments showed that void tended to concentrate near the center of each subchannel, further supporting the RTNR results previously discussed. The advantage of this system is its extremely fast temporal response and detailed cross sectional local void distribution but it lacks the axial void distribution information necessary to calculate void velocity and size.

CHAPTER 9 RECOMMENDATIONS FOR FUTURE WORK

During the course of this research, the author has made several advances in the measurement of void distribution using Real Time Neutron Radiography. It has also become apparent that some areas of research regarding RTNR remain that would benefit by further work in this area. These areas include;

- addition of a platform that can move the test section in the axial direction. The current RTNR experiments were limited to observation of approximately the last 25 cm of heated length and hence for the fixed power levels, the observation of ONB was missed.
- the power supply for heating, monitoring, pressurizing and heating requirements was limited in the RTNR beam port. The addition of a 5kW power supply terminal helped achieve much higher test section powers, but adequate control requires further

development. Furthermore, this 5kW power supply, although large, is not sufficient for future CHF experiments.

- introduction of a secondary RTNR imaging system with a beam at an acute angle to the present beam (although the practicality of obtaining this beam is limited). This dual RTNR system could provide full three-dimensional reconstructions of void distribution through registration image processing techniques. These techniques use the two separate images and locate the exact location in space based on the changes in relative position from one image to the other. The present system could be modified by using a beam splitter and directing the neutron beam 90 degrees from the present system to impact on a second camera system at right angles to the existing facility.

- the experiments for this dissertation were accomplished by recording the RTNR images with a VHS recorder and then laboriously processing the images after completion of the experiment. Through parallel processing and the advances in computing power it is possible to do this image processing in an automated fashion using the DT3152 data acquisition board. The data acquisition system would be activated, monitored, controlled and recorded using one system processor. Secondary processors could then apply the image processing procedures discussed in Chapter 4 and give real time cross sectional, time averaged, local and instantaneous local void distributions. The output of this system could then be recorded to CD ROM, or it could be sent as a video signal to a VHS tape. This tape would then have a record of processed void information, not raw RTNR images.

- the recent advances in neural network processing and fuzzy logic could be applied to the present system in order to improve the tracking of vapor in the channel, and can even be employed in real time analysis using the above mentioned advanced imaging system.

- The effect of scattered neutrons from the test section wall should be investigated further to ascertain whether or not bubbles in this region are being obscured by these effects.

- Advances in semi-conductor and CCD camera technology allow for much faster acquisition of images in a digital format. A new RTNR based on CCD technology with digital outputs directly to a computer system would remove the errors that can result in this process.

RTNR has been developed into an excellent method for void distribution measurement during flow boiling. The use of the present system to examine theoretical aspects of flow boiling is now possible including:

- the fluid to fluid scaling of Refrigerant to Water void distribution. The substitution of Refrigerant for water as a working fluid in thermalhydraulic experiments can significantly reduce the power requirements, pressures, temperatures and hence the overall cost. However the effect of the differences in the surface tension, enthalpy and density of the liquid and vapor phases on the void distribution should be investigated.

- with the present Refrigerant loop and a high power heating system, it would be possible to reach CHF conditions in a flow boiling channel. Presently the mechanism and behavior of CHF is not thoroughly understood. Current CHF prediction methodologies rely on empirical correlations based on fluid conditions in the channel. The void distribution at or near CHF conditions would provided much needed insight to boiling crisis phenomena.

- The effects of geometry on void distribution and the subsequent changes in CHF could be examined in order to ascertain the mechanisms involved and to develop predictive techniques under these conditions.

- With the ability to measure the local void distribution, local heat transfer and pressure drop, development of mechanistic models or semi-empirical correlations based on local phenomena are possible for interfacial area concentration and transport, bubble diameter, void effects on heat transfer, and two-phase pressure drop beyond the current formulations.

REFERENCES

1. Incopera, F.P. and Dewitt, D.P., Fundamentals of Heat and Mass Transfer, John Wiley and Sons, Toronto, 1990.

2. Leppert, G. and Pitts, C.C., Boiling, *Advances in Heat Transfer*, **1**, pp. 185-266, 1964.

3. Ishii, M., Thermo-Fluid Dynamic Theory of Two-Phase Flow, Eyrolles, Paris, 1975.

4. Boure, J.A., Constitutive Equations for Two-Phase Flows, from Two-Phase Flow and Heat Transfer with Application to Nuclear Reactor Design Problems, Von Karman Istitute, Hemisphere, New York, 1978.

5. Dukler, A.E., Wicks, M., Cleveland, R.G., Pressure Drop and Hold-Up in Two-Phase Flow, Part A and B, *AIChE J.*, **10**, pp. 38-51, 1964.

6. Collier, J.G., Convective Boiling and Condensation, McGraw Hill, New York, 1981.

7. Donevski, B., Chang, J.S. and Groeneveld, D.C., Prediction Methods for Interfacial Parameters Used in Inverted Annular Film Boiling, *International Journal of Heat and Technology*, **10**, pp. 43-70, 1992.

8. Knoll, G.F., Radiation Detection and Measurement, John Wiley, New York, 1989.

9. Hibiki, T., Mishima, K., Yoneda, K., Fujine, S., Tsuruno, A., Matsubayashi, M., Visualization of Fluid Phenomena Using High Frame Rate Neutron Radiography with a Steady Thermal Neutron Beam, *Nuclear Instruments and Methods in Physics Research*, **351**, pp. 423-436, 1994.

10. Dittus, F.W. and Boelter, L.M., University of California Publications on Engineering, **2**, p. 443, Berkley, 1930.

11. Allen, R.W. and Eckert, E.R., *J. Heat Transfer*, **86**, 1964.

12. Deissler, R.G., *Transactions ASME*, **73**, pp. 101-107, 1951.

13. Petukhov, B.S., Heat Transfer and Friction in Turbulent Pipe Flow with Variable Physical Properties, *Advances in Heat Transfer*, **6**, pp. 503-564, 1970.

14. Gnielinski, V., *Int. Chemical Engineering*, **16**, p. 359, 1976.

15. Karman, T., *Transactions ASME*, **61**, pp. 705-710, 1939.

16. Sieder, E.N. and Tate, G.E., *Ind. Eng. Chem.*, **28**, p. 1429, 1936.

17. Krieth, F. and Summerfield, M., *Transactions ASME*, **71**, 1949.

18. Fox, R.W. and McDonald, A.T., Introduction to Fluid Mechanics, John Wiley and Sons, New York, 1985.

19. Novog, D.R., Yin, S.T. and Chang, J.S., High Heat Flux Subcooled Boiling Heat Transfer and Pressure Drop Under Smooth and Swirl Flow Conditions, *Proc. of the U.S. National Heat Transfer Conference*, ANS Publishing Inc., Illinois, **HTC-Vol. 8**, p.139 - 146, 1995.

20. Tain, R., CHF Fluid to Fluid Scaling , *PhD. Thesis*, University of Ottawa, 1994.

21. Taitel, Y. and Dukler, A.E., Flow Regime Transitions for Vertical Upward Gas-Liquid Flow: A Preliminary Approach Through Physical Modeling, 70th AIChE Meeting, New York, 1977.

22. Carey, V.P., Liquid - Vapor Phase Change Phenomena, Hemisphere, New York, 1992.

23. Hewitt, G.F., and Roberts, D.N., Studies of Two-Phase Flow Patterns by Simultaneous X-Ray and Flash Photography, Report AERE-M 2159, HSMO, England, 1969.

24. Taitel, Y. and Dukler, A.E., A Model for Predicting Flow Regime Transitions in Horizontal and Near Horizontal Gas-Liquid Flow, *AIChE Journal*, **22**, pp. 47-55, 1976.

25. Baker, O., Simultaneous Flow of Oil and Gas, *Oil and Gas J.*, **53**, pp. 185-195, 1954.

26. Mandhane, J.M., Gregory, G.A. and Aziz, K., Flow Pattern Map for Gas-Liquid Flow in Horizontal Pipes, *Int. J. Multiphase Flow*, **1**, pp. 537-553, 1974.

27. Taitel, Y. and Dukler, A.E., A Model For Predicting Flow Regime Transitions in Horizontal and Near Horizontal Pipes, *AIChE J.*, **22**, pp. 47-55, 1976.

28. Harvel, G.D., Chang, J.S., and Krishnan, V.S., A Two-Phase Flow Regime Map for a Maple-Type Nuclear Research Reactor Fuel Channel: Effect of hexagonal Finned Bundle, *Nuc. Technology*, **118**, pp. 151-161, 1997.

29. Westwater, J.W., Things We Don't Know About Boiling Heat Transfer, *Proc. 1960 ASME Winter Meeting*, New York, pp. 61-73, 1960.

30. Tong, L.S., Flow Boiling, Boiling Heat Transfer and Two-Phase Flow, Chapter 5 John Willey and Sons, New York, pp.111-175, 1965.

31. Spindler, K., Flow Boiling, *ASME Publication* GK-12, pp. 349-368.

32. Harvey, E.N., Barnes, D.K., McElroy, W.D., Whiteley, A.H. and Pease, D.C., *J. American Chemical Society*, **67**, p. 156, 1945.

33. Knapp, R.T., *Transactions ASME*, **80**, p. 1315, 1958.

34. Corty, C. and Foust, A.S., *Chemical Eng. Progress Symposium Series*, **51**, No. 17, p. 1, 1955.

35. Cole, R., Boiling Nucleation, *Advances in Heat Transfer*, **10**, pp.85 - 166, 1974.

36. Novog, D.R., Judd, R.L.and Chang, J.S. , Subcooled Flow Boiling Hysteresis Characteristics for Freon 134a in a Tubular Channel, *Proc. of the 17th Japanese Multiphase Flow Symposium*, Tokyo, Japan, July 23-24, 1998.

37. Hsu,Y.Y., On the size of active nucleation cavities on a heating surface, *J. Heat Transfer*, Vol. 84, pp. 207-213, 1962.

38. Sato, T. and Matsumura, H., On the Conditions of Incipient Subcooled Boiling and Forced Convection, *Bulletin of JSME*, **7**, pp. 392-398, 1964.

39. Davis, E.J. and Anderson, G.H., The Incipience of Nucleate Boiling in Forced Convection Flow, *AIChE J.*, Vol. 12, pp. 774-780, 1966.

40. Frost, W., Dzakowic, G.S., An Extension of the Methods of Predicting Incipient Boiling on Commercially Finished Surfaces, ASME paper 67-HT-61, National Heat Transfer Conference, Seattle, Washington, 1967.

41. Bergles, A.E., and Rohsenow, W.M., The Determination of Forced Convection Surface Boiling Heat Transfer, *J. of Heat Transfer*, Vol. 86, pp. 365-372, 1964.

42. Yin, S.T., Jin, Z., Abdelmessih, A.H., and Gierszewski, P.J., Prediction of Highly Subcooled Flow Boiling For Cooling of High Heat Flux Components in Fusion Reactors, NURETH 6, **1**, Courtaud and Delhaye Ed., p. 733, 1993.

43. Shah, M.M, Generalized Prediction of Heat Transfer During Subcooled Boiling in Pipes and Annuli, *ASHRAE Transactions*, **83**, 1977.

44. Kutateladze, S.S., Boiling Heat Transfer, *Int. J. of Heat and Mass Transfer*, **4**, pp. 31-45, 1961.

45. Jens, W.H., and Lottes, P.A., Analysis of Heat Transfer Burnout, Pressure Drop, and Density Data for High Pressure Water, ANL-4627, 1951.

46. Del Valle, V., and Kenning, D.B., Subcooled Boiling at High Heat Flux, *Int. J. Heat Mass Transfer*, **28**, pp. 1907-1920, 1985.

47. Novog, D.R., High Heat Flux Subcooled Boiling of Water Under Smooth and Swirl Flow Conditions, *Masters Thesis*, McMaster University, May, 1995.

48. Percupile, J.C., Riedle, K., and Schmidt, F.K., Experimental Investigation: Boiling Heat Transfer in Evaporator Tubes - Vertical Up-flow, *AIChE Symposium Series*, **70**, pp. 91-97, 1971.

49. Yin, S.T., Cardella, A., Abdelmessih, Jin, Z., Bromley, B.P., Assessment of a Heat Transfer Correlation Package for Water Cooled Plasma-Facing Components in Fusion Reactors, *Nuclear Engineering and Design*, **146**, pp. 311-323, 1994.

50. Celata, G.P., Recent Achievements in the Thermalhydraulics of High Heat Flux Components in Fusion Reactors, *Experimental Thermal and Fluid Science*, **7**, pp. 263-278, 1993.

51. Rohsenow, W.M. and Clark, J.A., A Study of the Mechanism of Boiling Heat Transfer, *Trans. ASME*, **73**, July, pp. 609- 620, 1951.

52. Kolev, N.I., How Accurately Can we Predict Nucleate Boiling, *Experimental Thermal and Fluid Science*, **10**, pp. 370-378, 1995.

53. Forster, H.K. and Zuber, N., Dynamics of Vapor Bubbles and Boiling Heat Transfer, *AICHE Journal*, **4**, pp. 531-535, 1972.

54. Gunther, F.C., Photographic Study of Surface Boiling Heat Transfer to Water With Forced Convective Cooling, *Trans. ASME*, **73**, Feb., pp. 115-122, 1951.

55. Nishikawa, K. and Fujita, Y., Nucleate Boiling Heat Transfer and its Augmentation, *Advances in Heat Transfer*, **20**, pp. 1-82, 1990.

56. Bankoff, S.G., and Miksel, R.D., Bubble Growth Rates in Highly Subcooled Nucleate Boiling, *Chemical Engineering Progress Symposium*, 55, No. 29, pp.95-102.

57. Jiji, L.M., and Clark, J.A., Bubble Boundary Layer and Temperature Profiles for Forced Convection in Channel Flow, *J. of Heat Transfer*, **86**, pp. 50-58, 1964.

58. Bhatia, R.M., Kumar, P., and Sud, Y.C., Contribution to Swirl-Flow Heat Transfer and Friction Factor Calculations, *The India Institution of Engineers*, U.D.C. 531.46, pp. 34-47, 1967.

59. Kumar, P. and Judd, R.L., Heat Transfer with Coiled Wire Turbulence Promoters, *The Canadian J. Chem. Eng.*, **48**, pp. 378-383.

60. Seymour, E.V., Fluid Flow Through Tubes Containing Twisted Tapes, *The Engineer*, Oct., pp. 634-640, 1966.

61. Backshall, R.G., and landis, F., The Boundary Layer Velocity Distribution in Turbulent Swirling Pipe Flow, *Transactions of ASME*, Paper 69-FE-14, pp. 1-6, 1969.

62. Lopina, R.F., and Bergles, A.E., Heat Transfer and Pressure Drop in Tape-Generated Swirl Flow of Single-Phase Water, *J. of Heat Transfer*, **91**, pp. 434-445, 1969.

63. Marner, W.J., and Bergles, A.E., Augmentation of Highly Viscous Heat Transfer Inside Tubes with Constant Wall Temperature, *Experimental Thermal and Fluid Science*, pp. 252-261, 1964.

64. Wantanbe, K, Taira, T., and Mori, Y., Heat Transfer Augmentation in Tubular Flow by Twisted Tapes at High Pressures and Optimum Performance, *Heat Transfer Japanese Research*, **12**, pp. 1-31, 1991.

65. Gambill, W.R., Bundy, R.D., and Wansbrough, R.W., Heat Transfer, Burnout, and Pressure Drop for Water in Swirl-Flow Tubes with Internal Twisted Tapes, *Chemical Engineering Progress Symposium*, **57**, pp. 127-137, 1961.

66. Gambill, W.R., Subcooled Swirl-Flow Boiling and Burnout With Electrically Heated Tapes and Zero Wall Heat Flux, *Procs. of the 1964 ASME Winter Meeting*, New York, paper 64-WA/HT-2, 1964.

67. Smithberg, E., and Landis, F., Friction and Forced Convection Heat Transfer Characteristics in Tubes With Twisted Tape Generators, *J. of Heat Transfer*, pp. 39-48, 1964.

68. Lopina, R.F., and Bergles, A.E., Subcooled Boiling of Water in Tape-Generated Swirl-Flow, *J. of Heat Transfer*, 95, pp. 281-283, 1973.

69. Cumo, M., Farello, G.E., Ferrari, G., Palazzi, G., The Influence of Twisted Tapes in Subcritical, Once-Through Vapor Generators in Counter Flow, *J. of Heat Transfer*, pp. 365-370, 1974

70. Gambill, W.R., Subcooled Swirl-Flow Boiling and Burnout With Electrically Heated Twisted Tapes With Zero Wall Flux, *Procs. of the 1964 ASME Winter Meeting*, 64-WA/HT-42, 1964.

71. Jensen, M.K., and Bensler, H.P., Saturated Forced Convective Boiling Heat Transfer With Twisted Tape Inserts, *J. of Heat Transfer*, **108**, pp. 93-99, 1986.

72. Agrawal, K.N., Varma, H.K., and Lal, S., Heat Transfer During Forced Convective Boiling of R-12 Under Swirl Flow, *J. of Heat Transfer*, **108**, pp. 567-573, 1986.

73. Agrawal, K.N., Varma, H.K., and Lal, S., Pressure Drop During Forced Convective Boiling of R-12 Under Swirl-Flow, *J. of Heat Transfer*, **104**, pp. 758-762, 1982.

74. Royal, J.H. and Bergles, A.E., Augmentation of Horizontal In-Tube Condensation by Means of Twisted Tape Inserts and Internally Finned Tubes, *J. of Heat Transfer*, **100**, pp. 17-23, 1978.

75. Manglik, R.M., and Bergles, A.E., Heat Transfer and Pressure Drop Correlations for Twisted-Tape Inserts in Isothermal Tubes: Part -1 Laminar Flows, *J. of Heat Transfer*, **115**, pp. 881-889, 1993.

76. Plessis, J.P., and Kroger, D.G., Friction Factor Prediction for Fully Developed Laminar Twisted-Tape Flow, *J. of Heat and Mass Transfer*, **27**, pp. 2095-2100, 1984.

77. Chang, J.S., Girard, R., Raman, R, and Tran, F., Measurement of Void Fraction in Vertical Gas-Liquid Two-Phase Flow by Ring-Type Capacitance Transducers, *Mass Flow Measurement*, ASME Press, New York, pp. 93-99, 1984.

78. Cimorelli, L., Evangelisti, The Application of the Capacitance Method for Void Fraction Measurements in Bulk Boiling Conditions, *Int. J. of Heat and Mass Transfer*, **10**, 277-278, 1967.

79. Auracher, H. and Daubert, J., A Capacitance Method for Void Fraction Measurements in Two-Phase Flow, *Proc. of 2nd Int. Conf. on Multi-Phase Flow*, pp. 425-441, 1985.

80. Huang, S.M., Plaskowski, A.B., Xie, C.G. and Beck, M.S., Tomographic Imaging of Two-Component Flow Using Capacitance Sensors, *J. of Physics E*, **22**, pp. 173-177, 1989.

81. Chang, J.S., Myint, T.A., Donevski, B., Berezin, A.A., Irons, G.A., and Lu, W.K., Determination of the Interfacial Parameters in Gas Solid Two-Phase Pipe Flow by Capacitance Transducers, Particulate and Multi-Phase Processes - Colloidal and Interfacial Phenomena, Ariman and Veziroglu Ed., Springer-Verlag, New York, pp. 173-187, 1985.

82. Oyvind, I., A Review of Reconstruction Techniques for Capacitance Tomography, *Measurement Science and Technology*, **7**, pp. 325-337, 1996.

83. Barber, D.C., Quantification of Impedance Imaging, *Clinical Physics and Physiology Measurements*, **8A**, pp. 45-56, 1990.

84. Huahun, G. and Chuanjing, T., Use of Conductance Probe Method to measure Two-Phase Flow Patterns, Selected Papers of Two-Phase Flow and Heat Transfer, , Engineering Thermophysics Research Institute, Xian Jiaotong University, 23-1, 1984.

85. Andreussi, P., Donfrancesco, A., Messia, M., An Impedance Method for the Measurement of Liquid Hold-up in Two-Phase Flow, *Int. J. of Multi-Phase Flow*, **14**, pp. 775-785, 1988.

86. Ishii, M., and Revankar, S.T., Measurement of Local Interfacial Area and Velocity in Bubbly Flow, *Proc. 1991 National Heat Transfer Conference*, pp. 181-189, 1991.

87. Klung, F. and Mayinger, F., Impedance Based Flow Reconstruction, a Novel Flow Composition Measuring Technique for Multi-Phase Flows, *Nuclear Engineering and Design*, **146**, pp. 35-42, 1995.

88. Brooks, R.A. and DiChiro, G., Theory of Image Reconstruction in Computed Tomography, *Radiology*, **117**, pp. 561-572, 1975.

89. Narabayashi, T., Tobimasu, T., Nagasaka, H. and Kagawa, T., Measurement of Transient Flow Patterns by High Speed Scanning X-Ray Void Fraction Meter, Measurement Techniques in Gas-Liquid Flows, pp. 259-280, Verlag, 1984.

90. Narabayashi, T., Ishiyama, T., Miyano, H. and Nei, H., Measurement of Void Distribution in High Pressure Steam Water Two-Phase Flow Using High Speed X-Ray Scanner, *Proc. of First International Conference on Multiphase Flows*, **1**, Tsukuba, Japan, pp. 241-246, 1991.

91. Hori, K., Kawanishi, K., Hamamura, H., Ochi, M., and Akai, M.,A High Speed X-Ray Computed Tomography Scanner for Multipurpose Flow Visualization and Measurement, *Proc. of 4th International Topical Meeting on Nuclear Thermalhydraulics, Operations and Safety*, pp. 43-D-1, April, 1994.

92. Hori, K., Fujimoto, T., Kawanishi, K., and Nishikawa, H., Advanced High Speed X-Ray CT Scanner for Measurement and Visualization of Multi-phase Flow, *OECD/CSNI Specialists Meeting on Advanced Instrumentation and Measurement Techniques*, Santa Barbara, Ca., 1997.

93. Hori, K., Fujimoto, T. and Kawanishi, K., Development of ultra-fast X-Ray computed tomography system, *Proc. IEEE Medical Imaging Conference*, 1997.

94. Hori, K., Fujimotot, T., and Kawanishi, K., Application of cadmium telluride detectors to high speed X-Ray CT scanners, *Nuclear Instruments and Methods in Physics Research A*, **380**, p. 397, 1996.

95. Chang, J.S., and Morola, E.C., Determination of Two-phase Interfacial Areas by an Ultrasonic Technique, *Nuclear Engineering and Design*, **112**, pp. 143-156, 1990.

96. Matikainen, L., Irons, G.A., Morala, E.C. and Chang, J.S., Ultrasonic System for Detection of Transient Liquid-Gas Interfaces Using a Pulse Echo Technique, *Review of Scientific Instruments*, **57**, pp. 1661-1666, 1986.

97. Whitehouse, J.C., Eghbali, D.A., Flitton, V.E. and Anderson, D.G., Measurement of Two-component Flow Using Ultrasonic Flowmeters, *ASME Winter Meeting*, WSRC-MS-91-261, p. 5, 1991.

98. Annunziato, M., Bitonti, P., and Giammartini, S., Gamma-Densitometer: Methods for Signal Processing and Systematic Error Correction, *Proc. 2nd International Symposium on Multiphase Flow*, Xian China, Ed. Xue-Jun Chen, p. 70, 1989.

99. Chan, A.M., and Banerjee, S., Design aspects of Gamma Densitometers for Void Fraction Measurement in Small Scale Two Phase Flow, *Nuclear Instruments and Methods*, **190**, pp. 135-148, 1981.

100. Edelman, Z., and Elias, E., Void Fraction Distribution in Low Flow Rate Subcooled Boiling, *Nuclear Engineering and Design*, **66**, pp. 375-382, 1981.

101. Fung, K.K. and Groeneveld, D.C, Measurement of Void Fraction in Steady-State Subcooled and Low Quality Flow Film Boiling, *Int. J. Multiphase Flow*,**6**, pp.357-361, 1980.

102. Pan, L., and Hewitt, G.F., Precise measurement of Cross Sectional Phase Fractions in Three-Phase Flow Using a Dual-Energy Gamma Densitometer, *Proc. of the 1995 National Heat Transfer Conference*, ANS Publication, pp. 71-78, 1995.

103. Oyedele, J.A., Statistical Errors in Void Fraction Determinations in Voided Liquids Employing Radiation Beams, *Int. J. of Radiation Applications and Instrumentation: A*, **43**, pp. 537-542, 1992.

104. Palazzi, G., and Savelli, D., Advanced Two-phase Measurements Developed at ENEA Laboratories, *Proc. 2nd International Symposium on Multiphase Flow*, Xian China, Ed. Xue-Jun Chen, p. 63, 1989.

105. Augousti, A.T., Mason, J. and Grattan, K.T., A Simple Fiber Optic Level Sensor Using Fluorescent Fibers, *Rev. Sci. Instrumentation*, **61**, pp. 3854-3858, 1990.

106. Cartellier, A., Optical Probes for Local Void Fraction Measurements: Characterization of Performance, *Rev. Sci. Instrumentation*, **61**, pp. 874-886, 1990.

107. Bakshi, B.R., Zhong, H., Jiang, P. and Fan, L.S., Analysis of Flow in Gas-Liquid Bubble Columns Using Multi-Resolution Methods, *Trans. International Chemical Eng.*, **73**,pp. 608-614, 1995.

108. Cimbala, J., Sathianathan, D., Cosgrove, S., Levine, S., "Neutron Radiography as a Flow Visualization Tool", *Neutron Radiography*, **3**, pp. 497-504, 1990.

109. Fairholm, W.H., Harvel, G.D., Campeau, J.C., Chang, J.S., "Visualization of Two-Phase Interfaces in a Natural Circulation Loop by a Real Time Neutron Radiography Imaging System, *ANS 1991 National Heat Transfer Conference*, pp. 199-206, 1991.

110. Carlisle, B.S., Johns, R.C., Hassan, Y.A., Two-phase Fluid Flow Measurements in Small Diameter Channels Using Real Time Neutron Radiography, *Proc. 4th International Meeting on Nuclear Thermalhydraulics, Operations and Safety*, 43-B-1, Taipei, Taiwan, 1994.

111. Dance, W.E., and Carollo, S.F., High Sensitivity Electronic Imaging System for Reactor and Non-reactor Neutron Radiography, *Neutron Radiography*, **2**, pp. 415-422, 1986.

112. Takenaka, N., Fujii, T., Ono, A., Turuno, A., Real Time Neutron Radiography as a Flow Visualization and Measurement Tool for Nuclear Thermalhydraulic

Research, *Proc. 4th International Topical Meeting on Nuclear Reactor Thermalhydraulics, Operations, and Safety*, 43-C-1, 1994.

113. Harvel, G.D., Determination of Two-Phase Flow Parameters for Nuclear Fuel Channels Using a Real-Time Neutron Radiography Method, *PhD. Thesis*, McMaster University, Hamilton, Ontario, Canada, 1995.

114. Beck, M.S., Plaskowski, A.B. and Green, R.B., Imagining for Measurement of Two-Phase Flow, *Proc. of Process Flow Visualization 4*, Paris 26-29, pp. 585-588, 1986.

115. Chang, J.S., and Harvel, G.D., Determination of Gas Liquid Bubbly Column Instantanious Interfacial Area and Void Fraction by a Real Time Neutron Radiography Technique, *Chem. Eng. Sci.*, **47**, p. 3639, 1992.

116. Harvel, G.D., Chang, J.S., and Krishnan, V.S., Determination of Time Dependent Void Fraction Distribution in Bubbly Flow by a Real Time Neutron Radiography Technique, NURETH 6, Grenoble, France, 1993.

117. Harvel, G.D., Hori, K., Kawanishi, K., and Chang, J.S., Cross Sectional Void Fraction Distribution Measurement in a Vertical Annulus Two-Phase Flow by a High Speed X-Ray Computed Tomography and Real Time Neutron Radiography Techniques, NURETH 7, Saratoga Springs, New York, USA, 1995.

118. Hibiki, T., Mishima, K., Yoneda, K., Fujine, S., Tsuruno, A, Matsubayashi, M., Visualization of fluid phenomena using a high frame rate neutron radiography with a steady thermal neutron beam, *Nuclear Instruments and Methods in Physics Research A*, **351**, pp. 423-436, 1994.

119. Hibiki, T., Mishima, K. and Matsubayashi, M., Application of High Frame Rate Neutron Radiography With a Steady Thermal Neutron Beam to Two-Phase Flow Measurements in a Metallic Rectangular Duct, *Nuclear Technology*, **110**, pp. 422-434, 1995.

120. Hibiki, T., Mishima, L., Feasibility of High Frame Rate Neutron Radiography by Using a Steady Thermal Neutron Beam With 10^6 n/cm^2-2 Flux, *Nuclear Instruments and Methods in Physics Research A*, **369**, pp. 186-194, 199.

121. Robinson, A.H., and Wang, S.L., High Speed Motion Neutron Radiography of Two-phase Flow, *Neutron Radiography*, pp. 653-659, 1983.

122. Uchimura, K., Harvel, G.D., Matsumoto, T., Kanzaki, M., and Chang, J.S., An Image Processing Approach for Two-phase Interfaces Visualized by a Real Time Neutron Radiography Technique, *Flow Measurement and Instrumentation*, **9**, pp. 203-210, 1998.

123. Osuwa, J., Neutron Radiographic Unsharpness and Dimensional Analysis, *Ph.D. Thesis*, McMaster University, Hamilton, Ontario, Canada, 1982.

124. Wyman, D.R., Neutron Transport in Radiography, *Ph.D. Thesis*, McMaster University, Hamilton, Ontario, Canada, 1984.

125. Mishima, K. and Hibiki, T., Quantitative Limits of Thermal and Fluid Phenomena Measurements Using Neutron Attenuation Characteristics of Materials, *Exp. Thermal and Fluid Sci.*, to be published.

126. Wallis, G.B., One Dimensional Two Phase Flow, McGraw-Hill, New York, 1969.

127. Zivi, S.M., Estimation of Steady State Steam Void Fraction by Means of the Principle of Minimum Entropy Production, *J. of Heat Transfer*, **86**, pp. 247-252, 1964.

128. Lockhart, R.W., and Martinelli, Proposed Correlation of Data for Isothermal Two-Phase, Two-Component Flow in Pipes, *Chem. Eng. Progress*, **45**, pp. 39-48, 1949.

129. Martinelli, R.C., and Nelson, D.B., Prediction of Pressure Drop During Forced Circulation of Boiling Water, *Trans. ASME*, **70**, pp. 695-70, 1948.

130. Thom, J.R., Prediction of Pressure Drop During Forced Circulation Boiling of Water, *J. of Heat and Mass Transfer*, **7**, pp. 709-724, 1964.

131. Baroczy, C.J., A Systematic Correlation for Two-Phase Pressure Drop, 8th International Heat Transfer Conference, Los Angeles, August, 1965.

132. Butterworth, D., A Comparison of Some Void-Fraction Relationships for Co-current Gas-Liquid Flow, *Int. J. Multiphase Flow*, **1**, pp. 845-850, 1975.

133. Griffith, P., Clark, J.A. and Rohsenow, W.M., Void Volumes in Subcooled Boiling Systems, Paper 58-HT-19, 1958 National Heat Transfer Conference, Chicago, 1958.

134. Kroger, P.G. and Zuber, N., An Analysis of the Effects of Various parameters on the Average Void Fractions in Subcooled Boiling, *Int. J. of Heat and Mass Transfer*, **11**, pp. 211-223, 1968.

135. Abdul-Razzak, A., Shoukri, M., and Chang, J.S., Characteristics of Refrigerant R-134a Liquid Vapor Two-Phase Flow in a Horizontal Pipe, *ASHRAE Transactions: Symposia*, CH-95-12-1, 1995.

136. Abdul-Razzak, A., Shoukri, M., and Chang, J.S., Measurement of Two-Phase Refrigerant Liquid Vapor-Mass Flow Rate - Part 1: Venturi and Void Fraction

Meters, *ASHRAE Transactions*, **101**, Pt. 2, SD-95-17-1, 1995.

137. Abdul-Razzak, A., Shoukri, M., and Chang, J.S., Measurement of Two-Phase Refrigerant Liquid Vapor-Mass Flow Rate - Part 2: Turbine and Void Fraction Meters, *ASHRAE Transactions*, **101**, Pt. 2, SD-95-17-2, 1995.

138. Abdul-Razzak, A., Shoukri, M., and Chang, J.S., Measurement of Two-Phase Refrigerant Liquid Vapor-Mass Flow Rate - Part 3: Combined Turbine and Venturi Meters and Comparison With Other Methods, *ASHRAE Transactions*, **101**, Pt. 2, SD-95-17-3, 1995.

139. Churchill, S.W. and Chu, H.H.S., "Correlating Equations for Laminar and Turbulent Free Convection", *Int. J. of Heat and Mass Transfer*, **18**, p. 1323, 1975.

140. Chang, J.S., and Laframboise, J.G., *Int. J. of Heat and Mass Transfer*, **38**, p. 360-362, 1978.

141. Hori, K., Fujimoto, T., and Kawanishi, K., Application of Cadmium Telluride Detector To High Speed X-Ray CT Scanner, *Nuclear Instruments & Methods in Physics Research A*, **380**, pp. 397-401, 1996.

142. Hori, K., Fujimoto, T., and Kawanishi, K., Development of Ultra-Fast X-Ray, Computed Tomography Scanner System, IEEE 1997 Medical Imaging Conference, 1997.

143. Bossi, R.H., Robinson, A.H., Barton, J.P., High Speed Motion Neutron Radiography, *Nuclear Tech.*, **81**, pp. 435-445, 1982.

APPENDIX A. FLUID PROPERTIES

Refrigerant 134a Liquid Density vs. Temperature

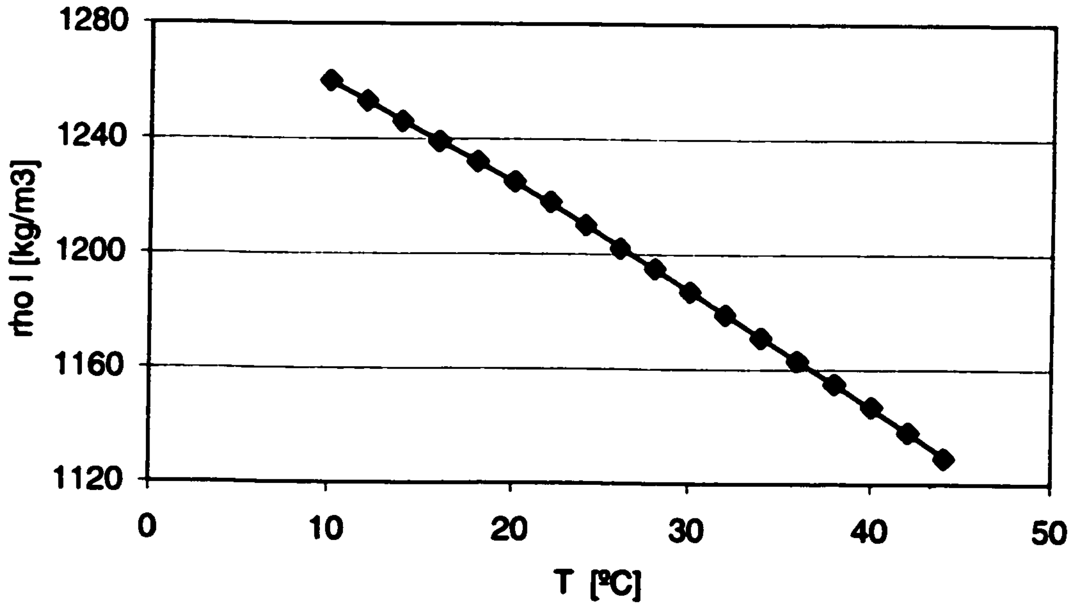

Refrigerant 134a Liquid Enthalpy vs Temperature

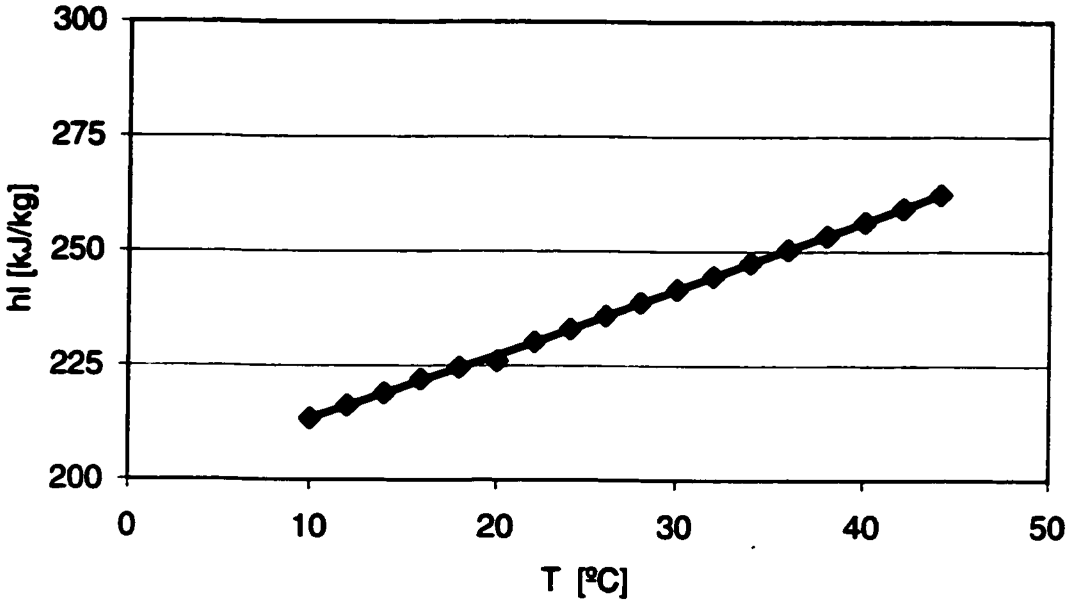

Figure A.1 Refrigerant 134 Liquid Density and Enthalpy as a Function of Temperature.

Refrigerant 134a Latent Heat vs. Temperature

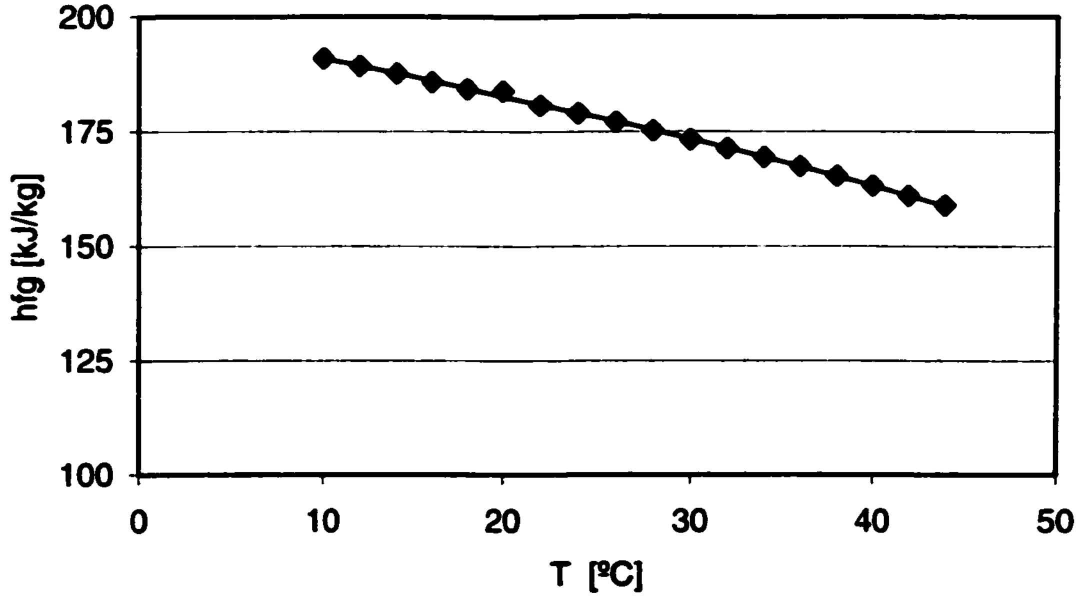

Refrigerant 134a Liquid Viscosity vs Temperature

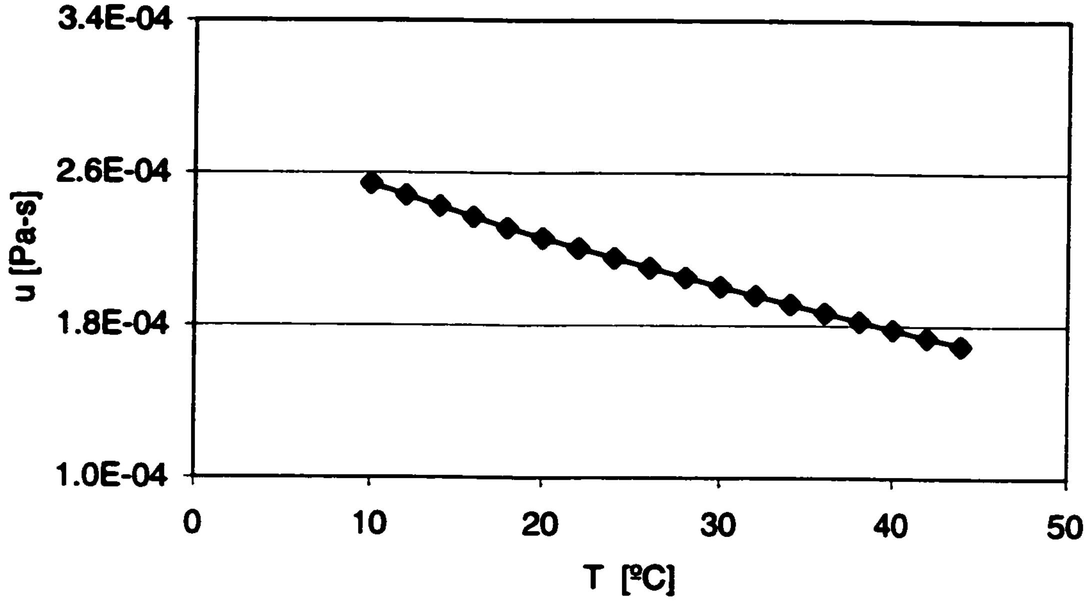

Figure A.2 Refrigerant 134 Latent Heat and Liquid Viscosity as a Function of Temperature.

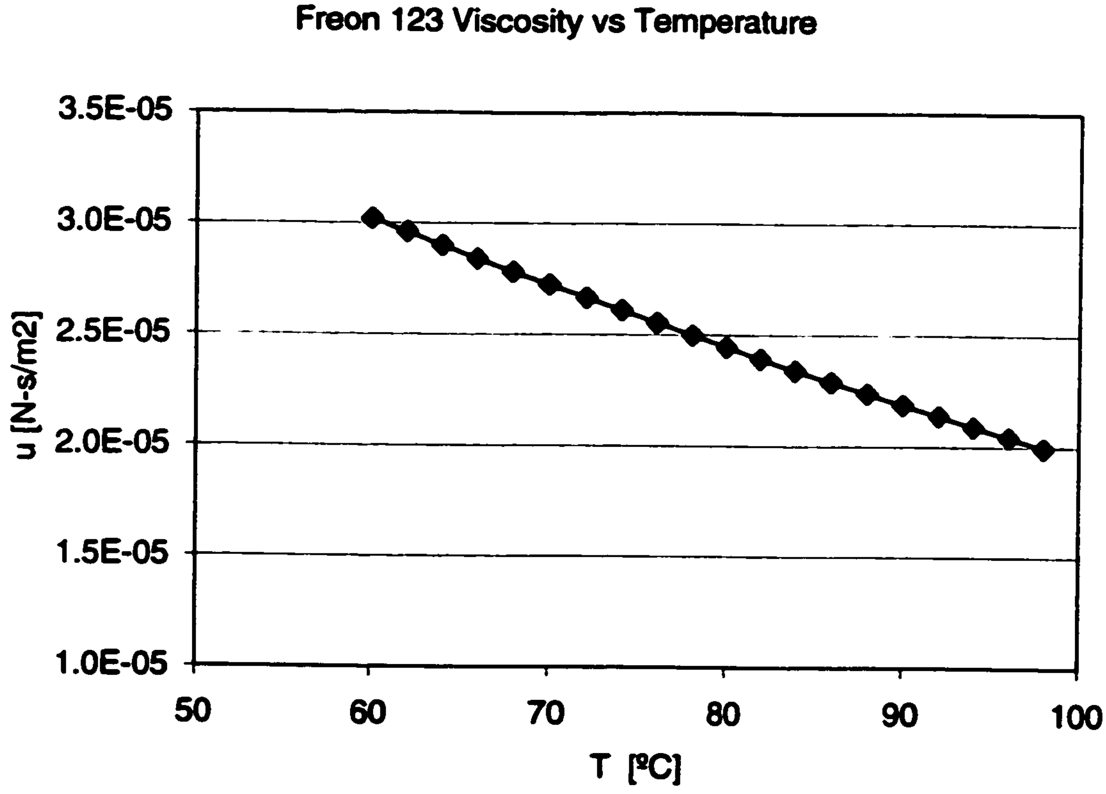

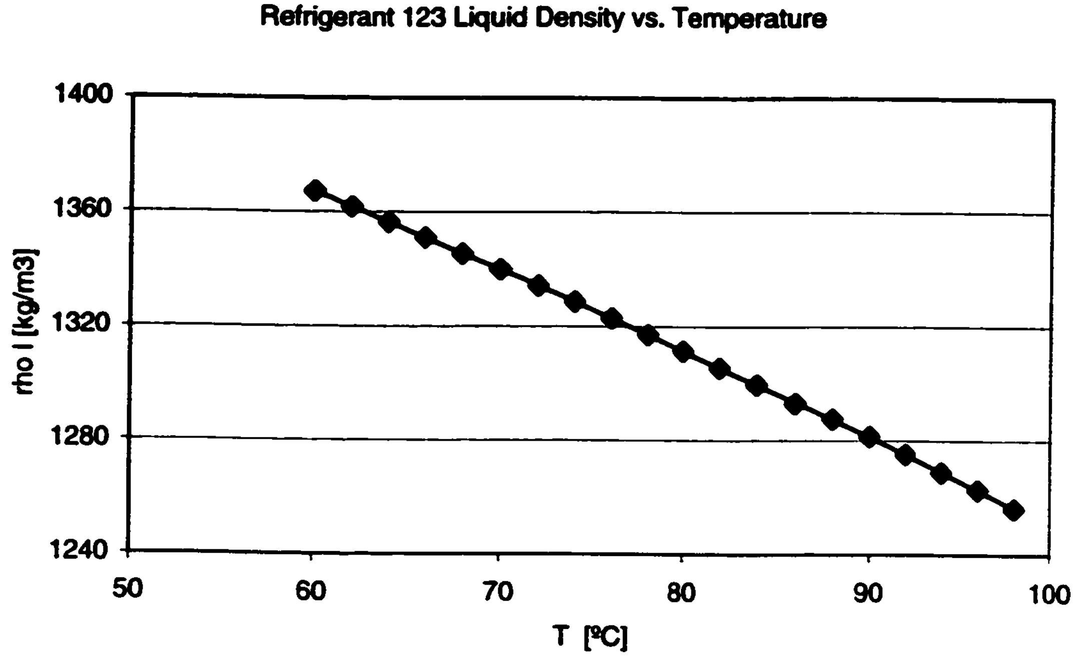

Figure A.3 Refrigerant 123 Liquid Density and Enthalpy as a Function of Temperature.

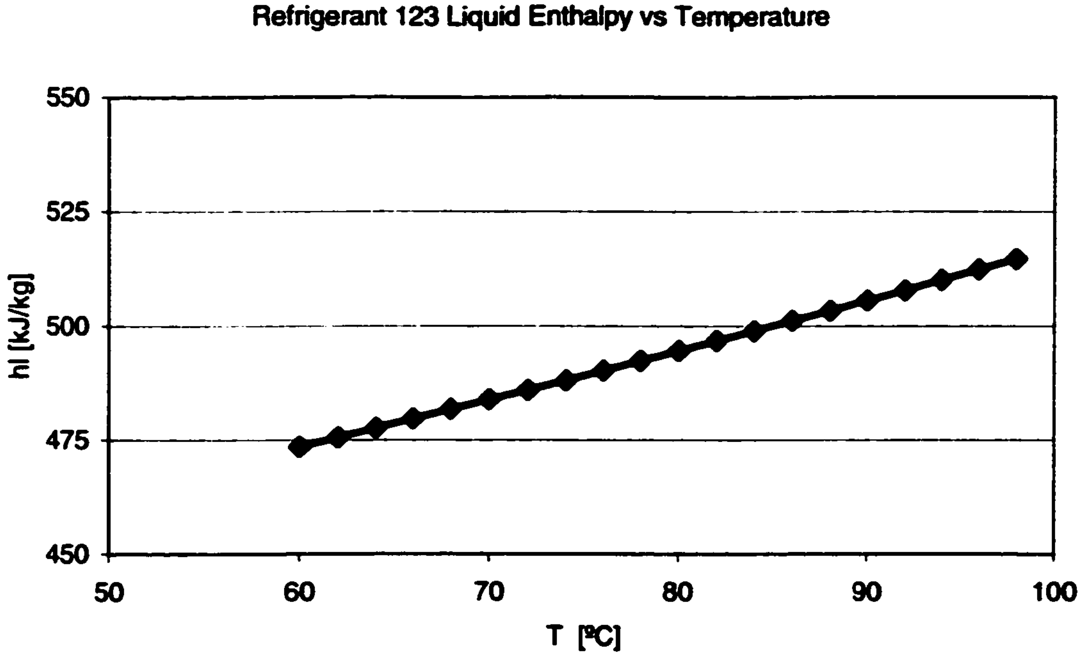

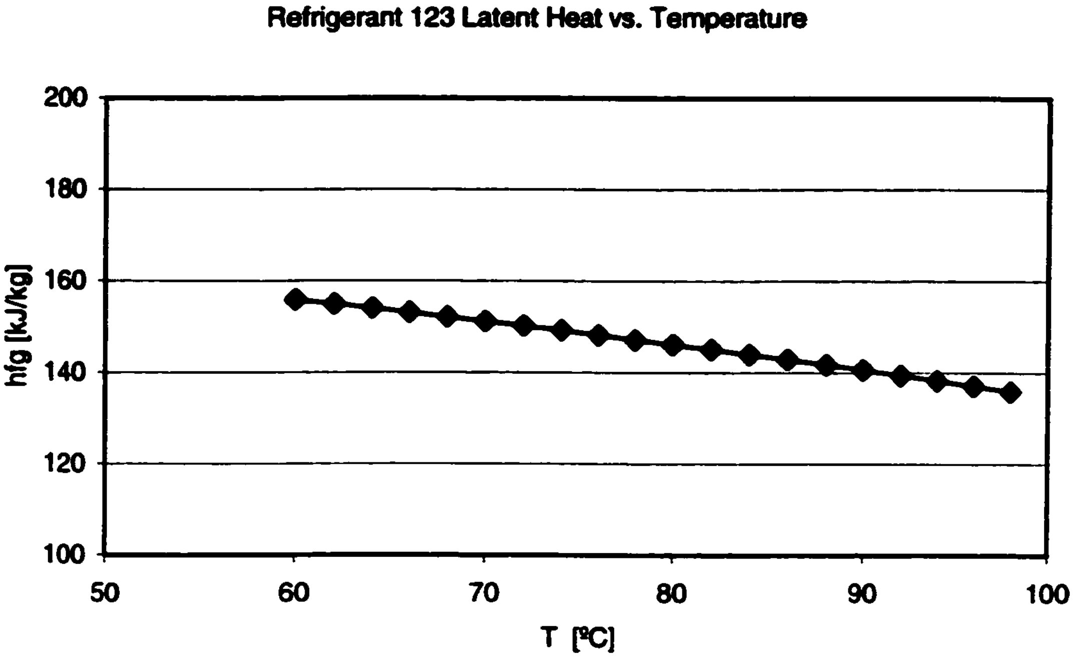

Figure A.4 Refrigerant 123 Latent Heat and Liquid Viscosity as a Function of Temperature.

APPENDIX B. APWR FUEL RTNR VOID MEASUREMENTS

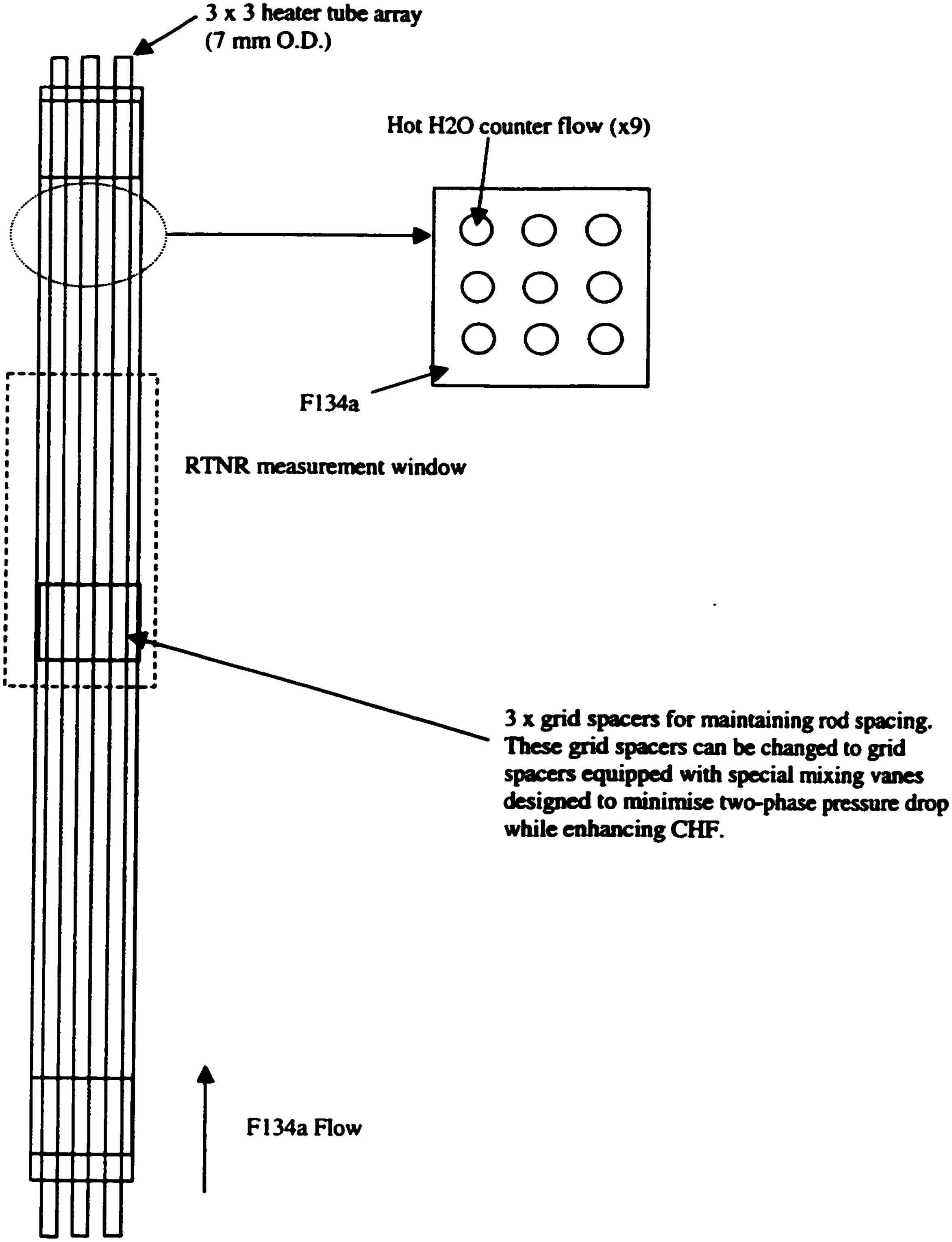

3 x grid spacers for maintaining rod spacing. These grid spacers can be changed to grid spacers equipped with special mixing vanes designed to minimise two-phase pressure drop while enhancing CHF.

Figure B.1 Schematic of the APWR 3 x 3 Rod Bundle with Grid Spacers (With and Without Mixing Vanes).

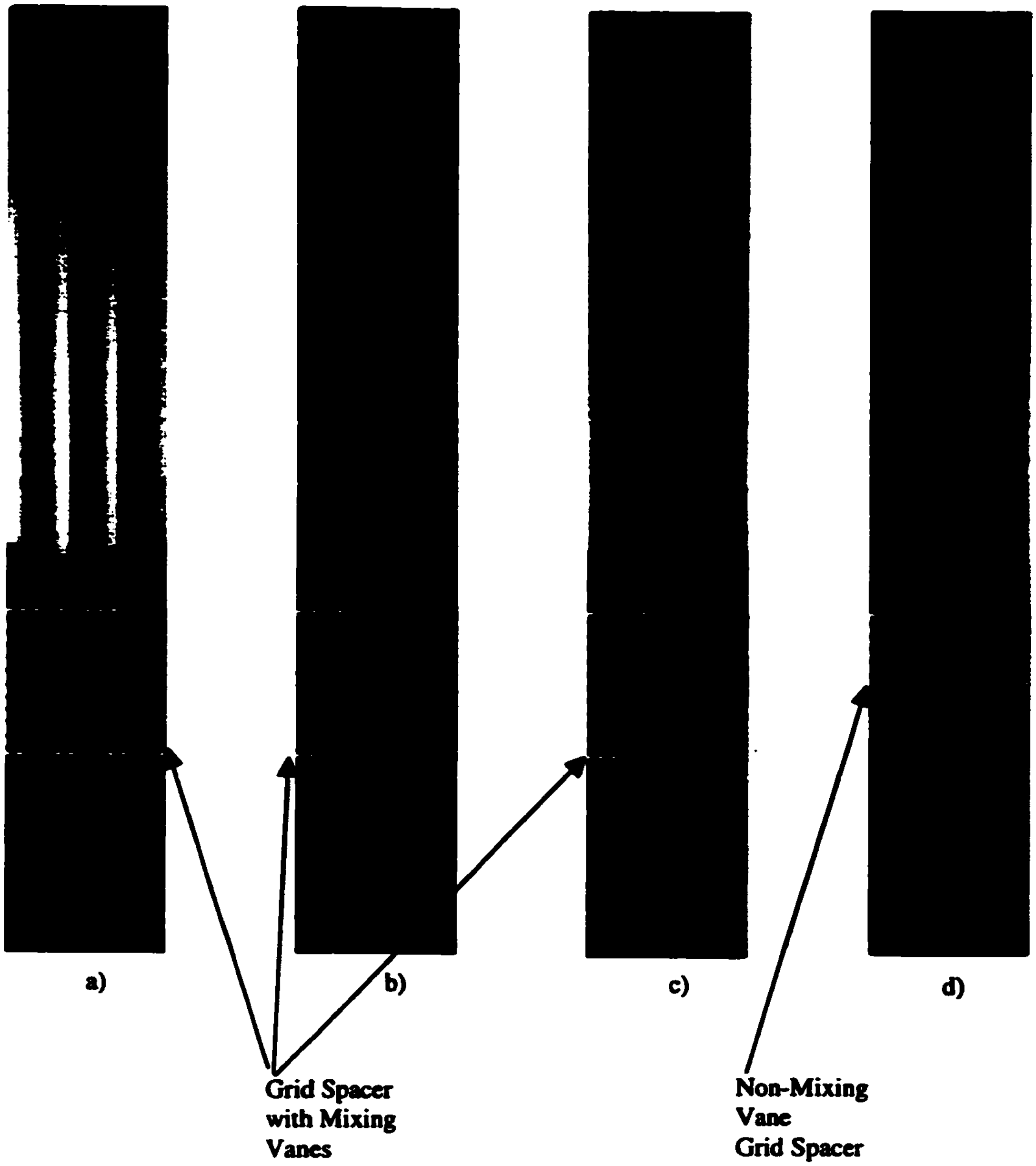

Figure B.2 RTNR Measurements of an APWR Simulated 3 x3 Rod Bundle *(a. empty test section with mixing vane grid spacers, b. full test section with mixing vane grid spacers, c. two-phase flow boiling with mixing vane grid spacers and d. two-phase flow boiling with non-mixing vane grid spacers).*

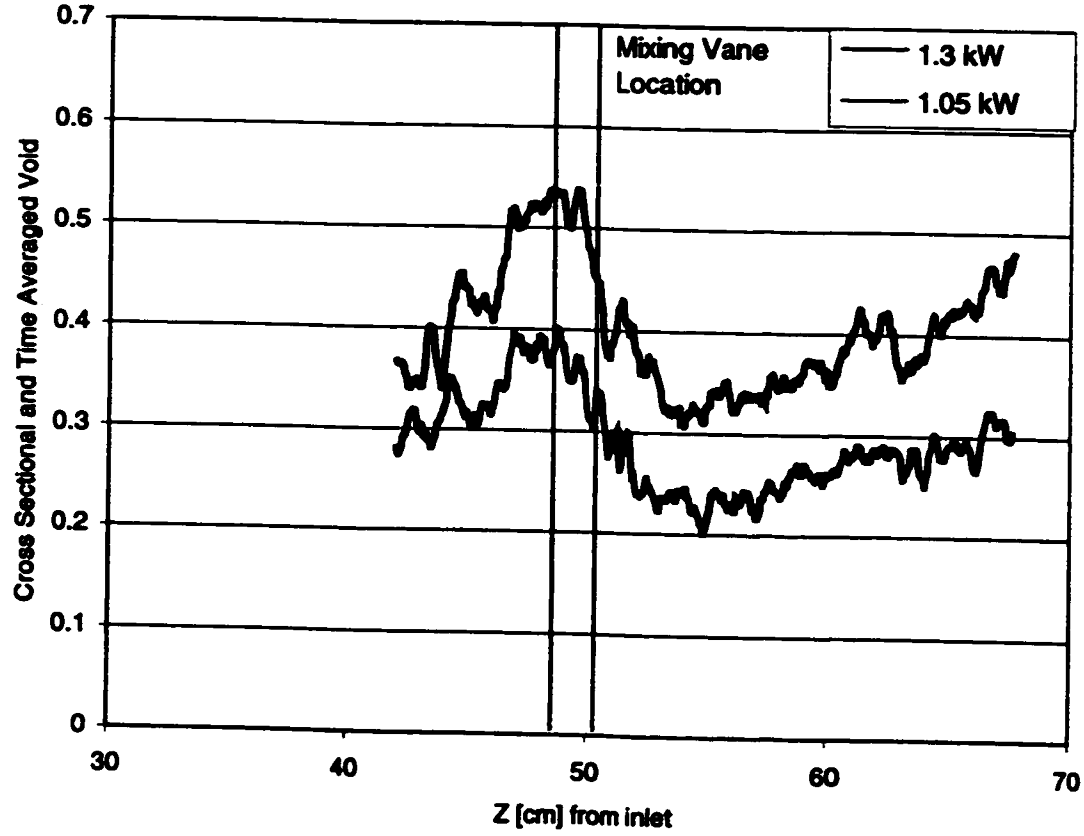

Figure B.3 Cross-Sectional and Time Averaged Void Fraction for an Simulated APWR 3 x 3 Rod Bundle with Mixing Vane Grid Spacers.

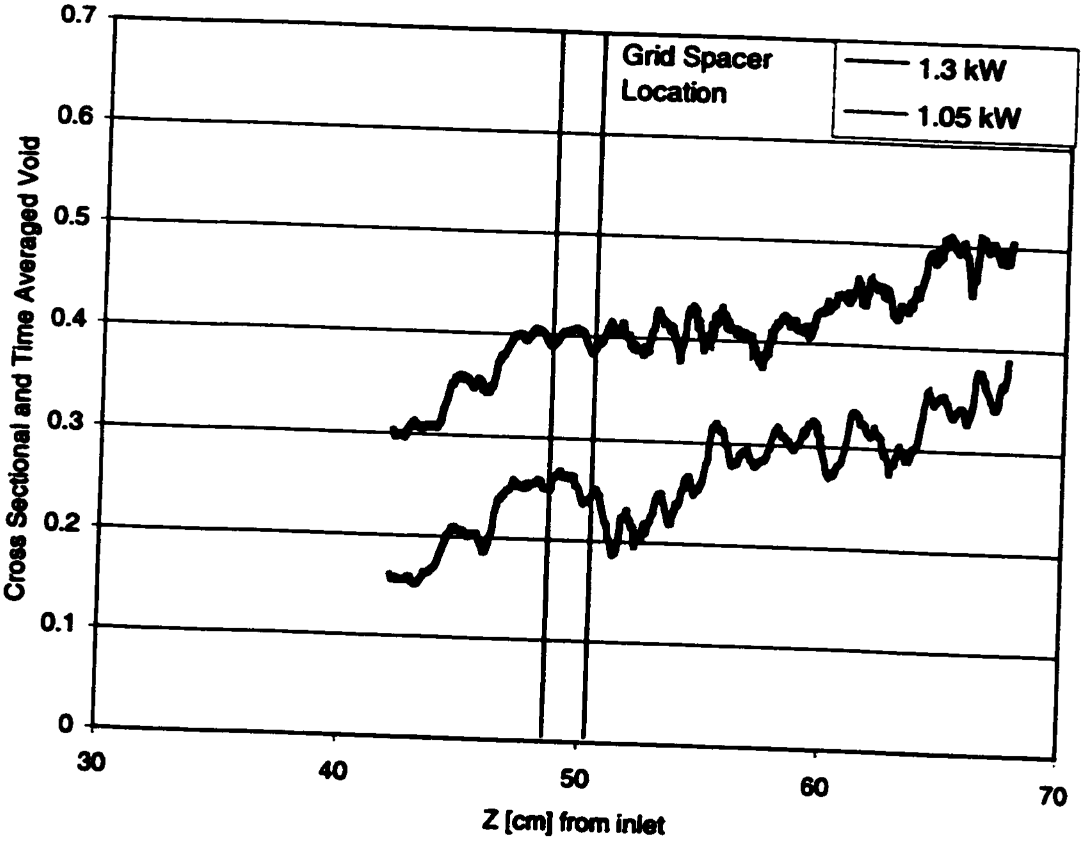

Figure B.4 Cross-Sectional and Time Averaged Void Fraction for an Simulated APWR 3 x 3 Rod Bundle with Normal Grid Spacers (no Mixing Vanes).

APPENDIX C. CALIBRATION INFORMATION

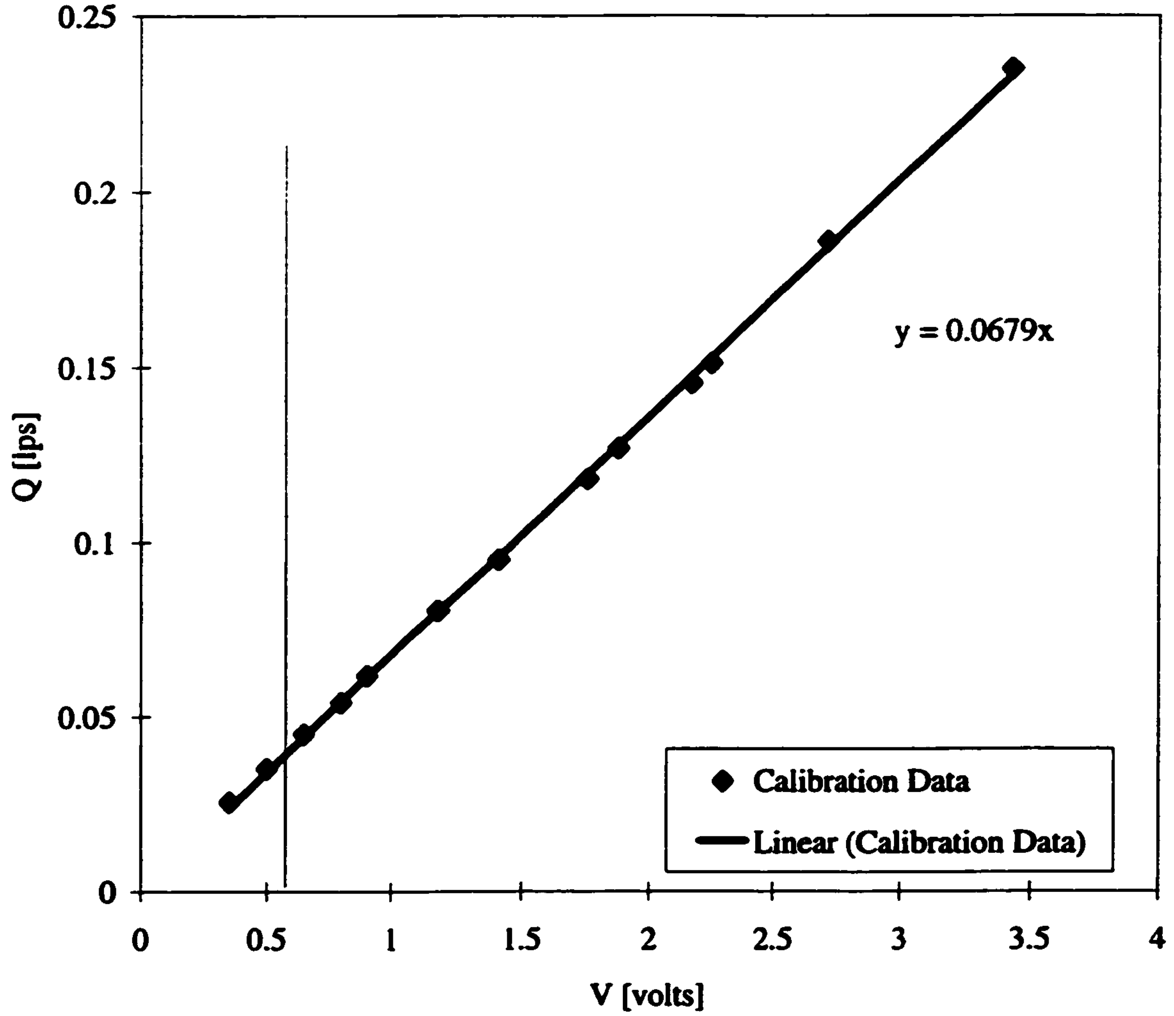

Figure C.1 Calibration Curve for RTNR Experiments Water Side Turbine Flow Meter.

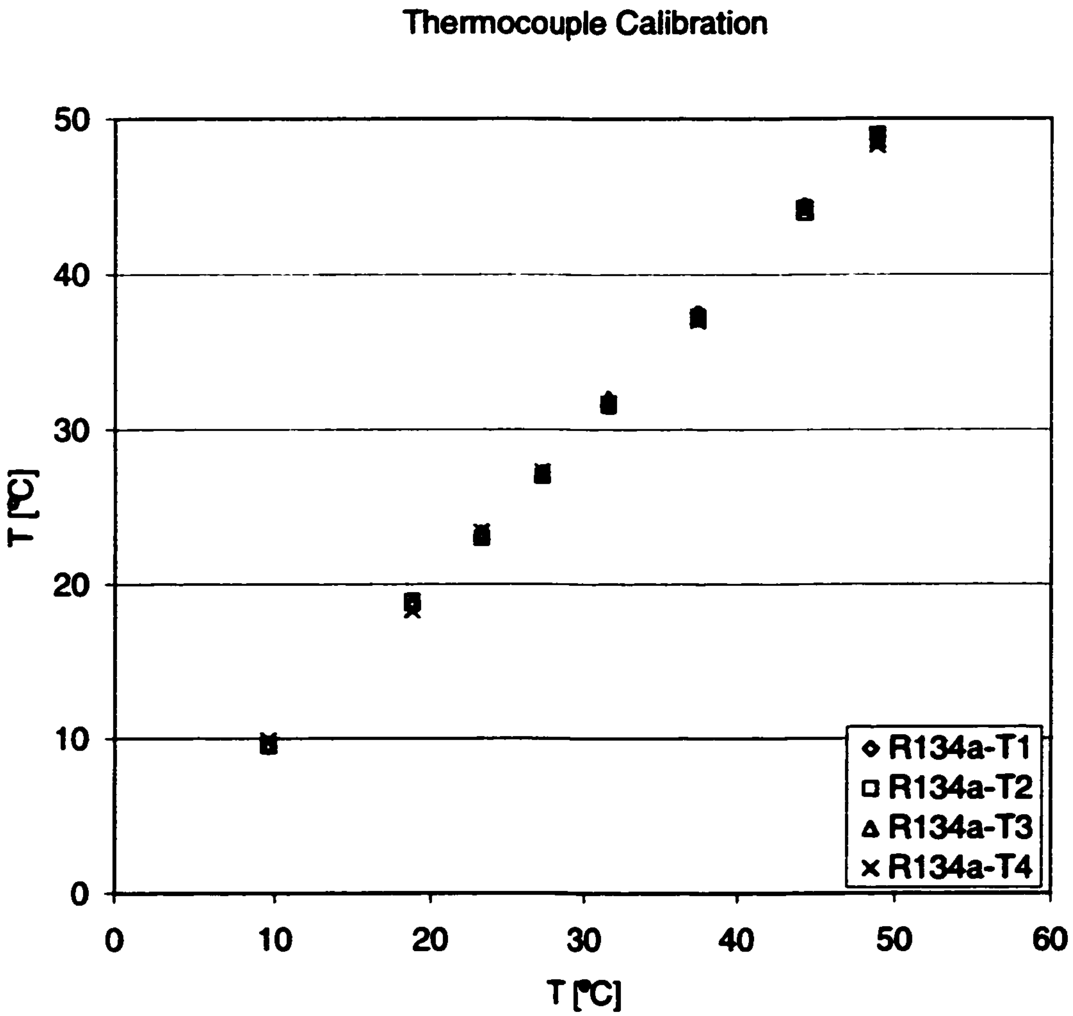

Figure C.2 Thermocouple Calibration - Comparison of Measured Thermocouple Readings to Known Temperature Water Baths.

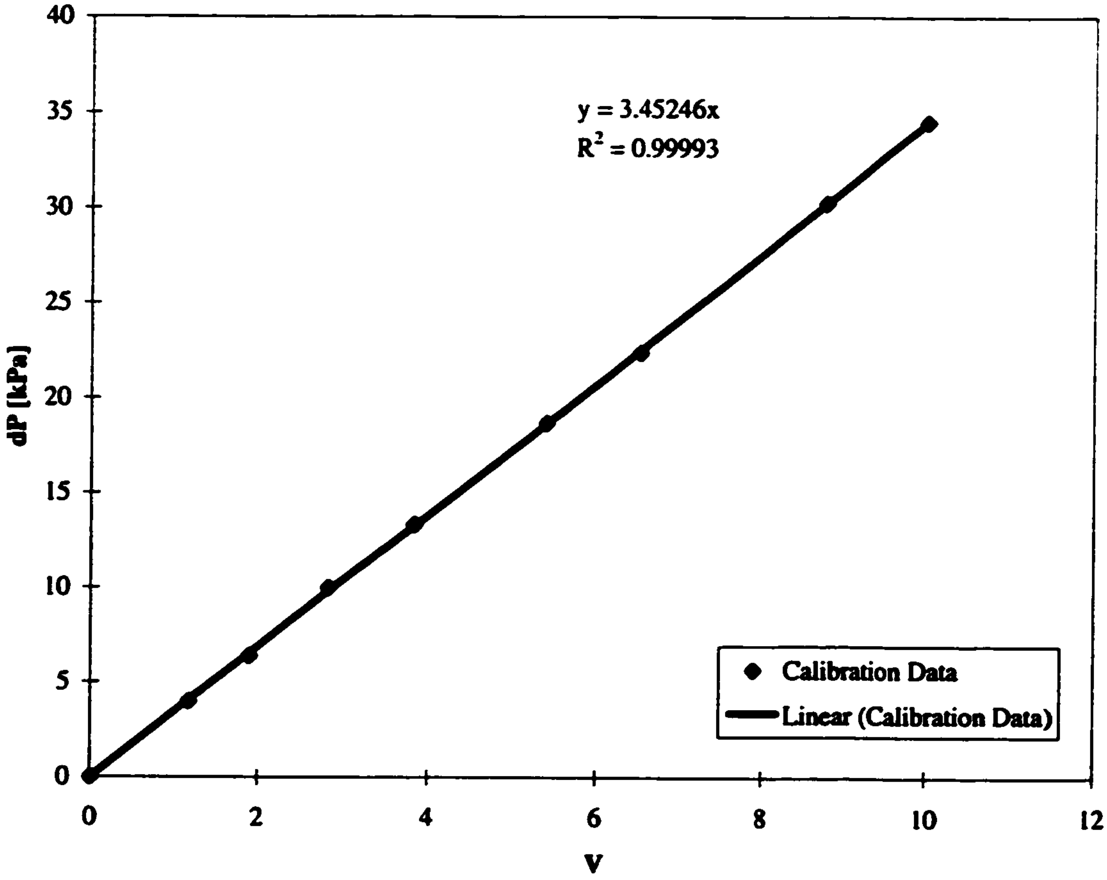

Figure C.3 Text Section Differential Pressure Sensor Calibration Curve.

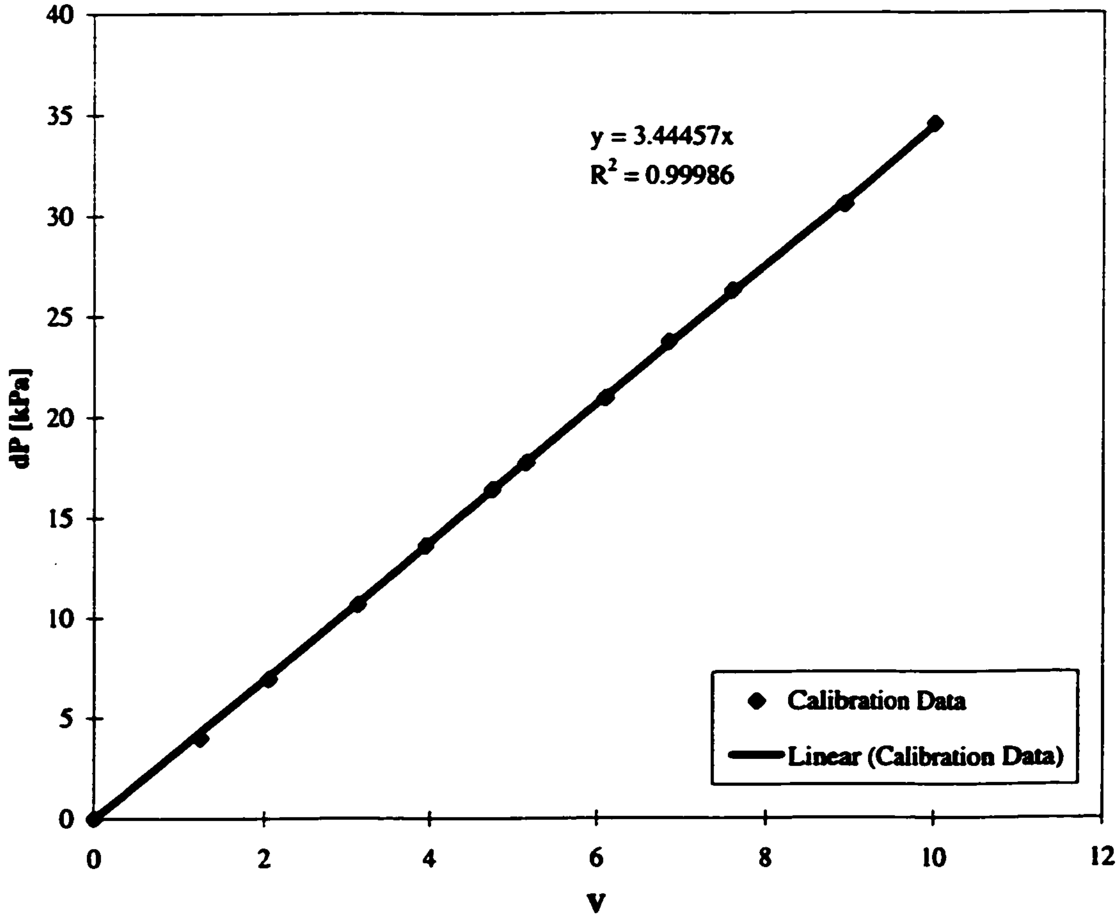

Figure C.4 Refrigerant 134a Venturi Pressure Drop Sensor Calibration Curve.

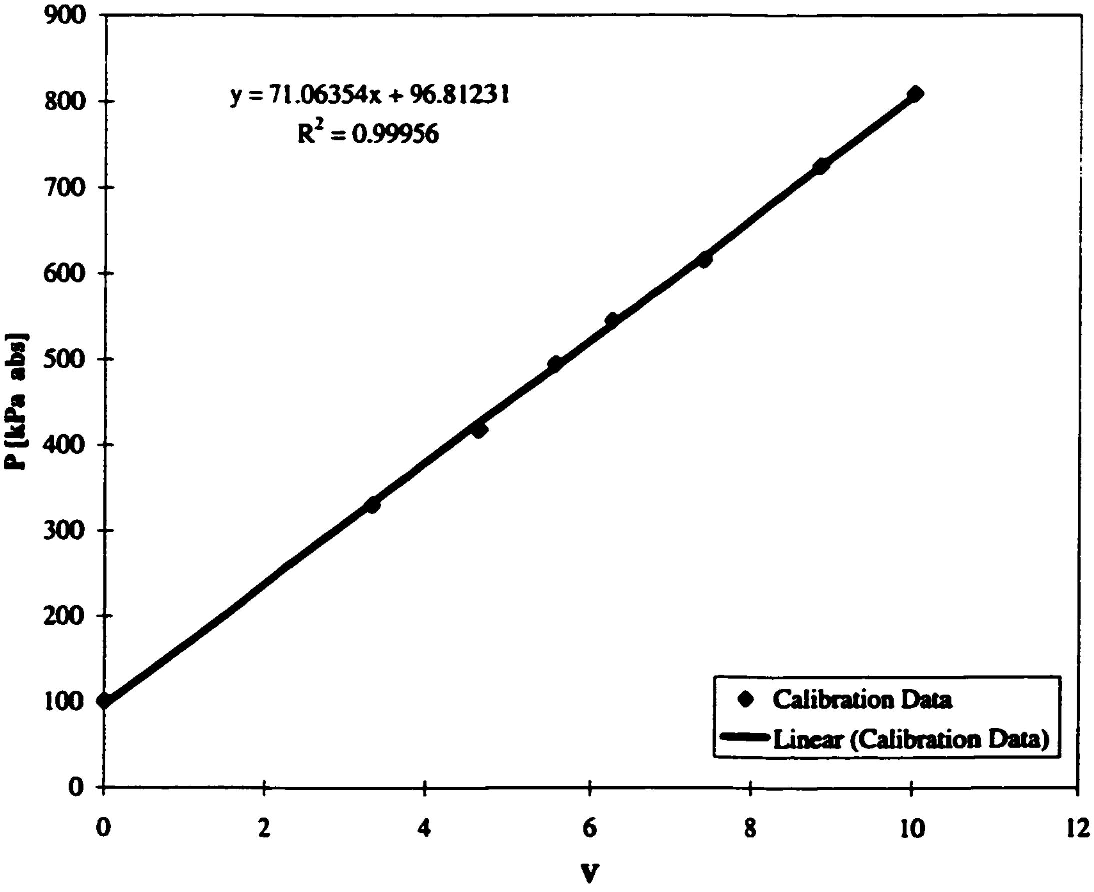

Figure C.5 System Pressure Sensor Calibration Curve.

APPENDIX D. RTNR UNCERTAINTY DETERMINATION

The uncertainty in cross sectional averaged axial void distribution RTNR measurements was established using comparisons of four sets of experimental results. The average void distribution for these using the standard deviation in the four data sets. Figure D.1 shows the four experimental used to establish the void measurement uncertainty. These results show that the uncertainty in these measurements is ±5.1% with 95% confidence with a maximum uncertainty of approximately 18%.

Figure D.2. shows the time averaged local distribution scatter for two experiments conducted at similar conditions. The figure shows the measured local void fraction from Experiment 1 versus the local void measured in the second experiment. Since each time averaged reconstruction contains approximately 5500 local void measurement (22 x 220 pixels in each RTNR image) locations are compared.. The uncertainty is estimated as ±10.2% at 95% confidence with a maximum uncertainty of 31%.

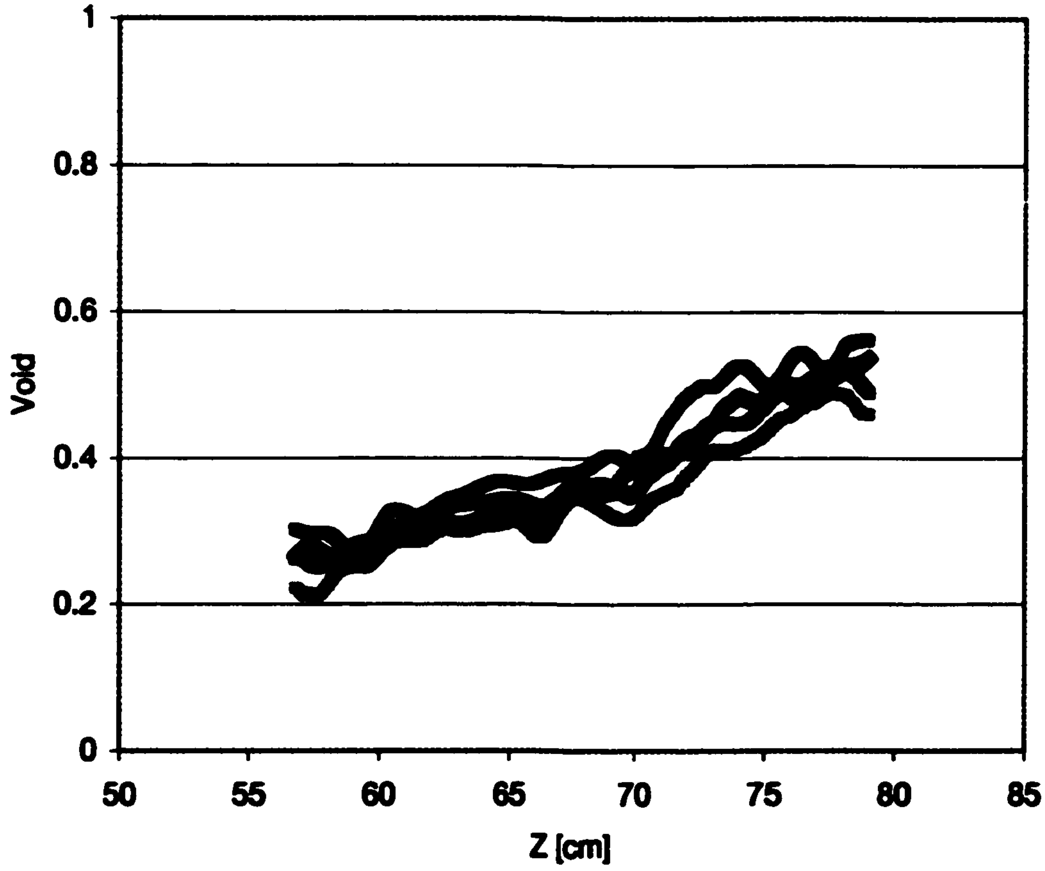

Figure D.1 Cross Sectional and Time Averaged Void Distribution Repeat Measurements at 500 kPa, 55 kg/s and 6 °C Inlet Subcooling. *The cross sectional and time average void fraction uncertainty based on repeat measurements is ±5.1 % at 95 % confidence with a maximum uncertainty of ±18 %.*

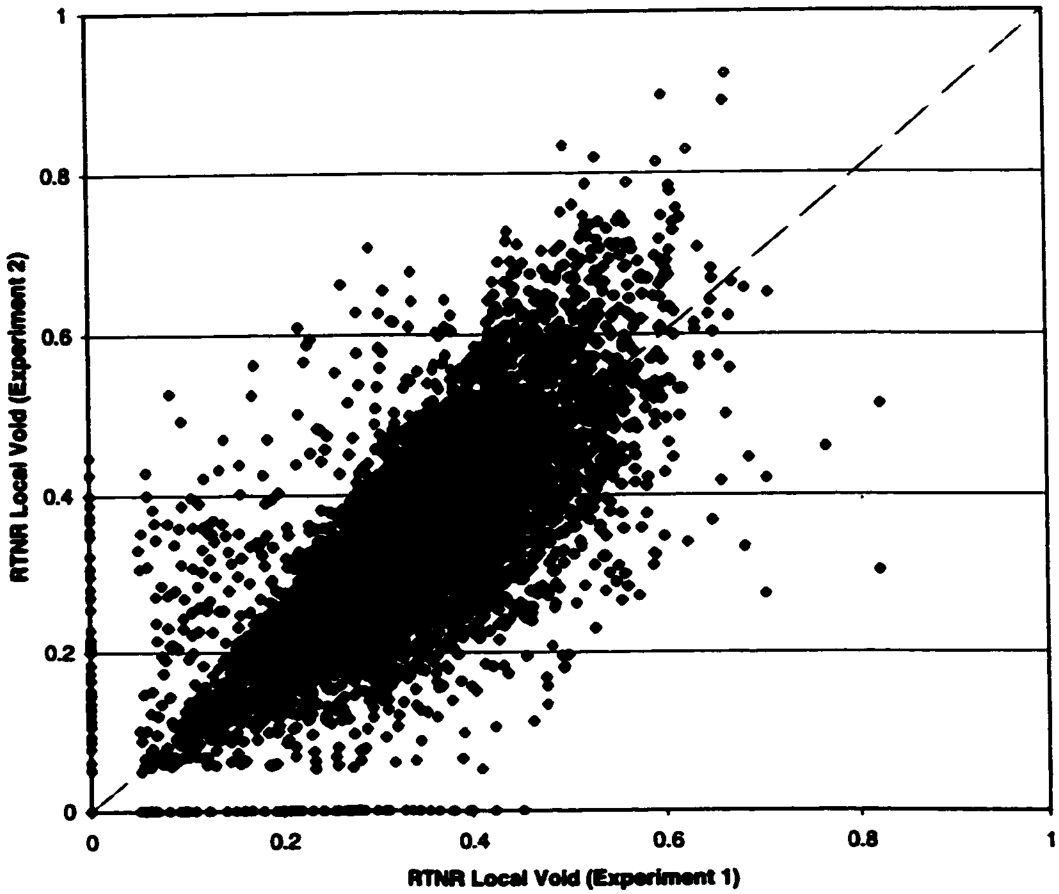

Figure D.2 Comparison of Time Averaged Local Void Distribution at 630 kPa, 55kg/m^{2}s and 6 °C - Comparison of Measured Void for Each Pixel on Two Separate Tests at the Same Conditions and Power. (*The local time average void fraction uncertainty based on these repeat measurements is ±10.1 % at 95 % confidence level*)

APPENDIX E. HP VEE DATA ACQUISITION PROGRAM

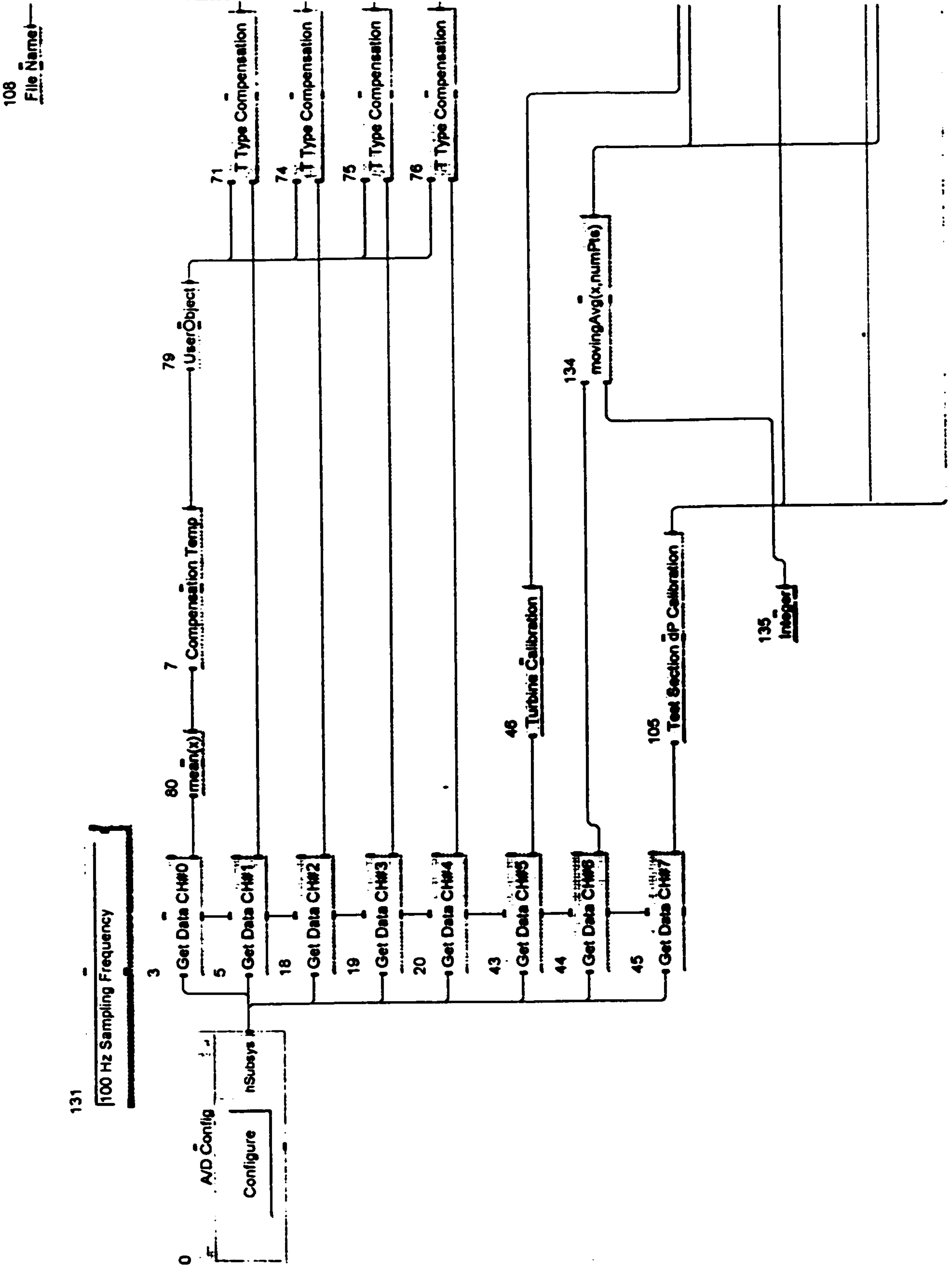
108
File Name
71
T Type Compensation
74
T Type Compensation
75
T Type Compensation
76
T Type Compensation
79
UserObject
134
movingAvg(x,numPts)
7
Compensation Temp
80
mean(x)
46
Turbine Calibration
105
Test Section dP Calibration
135
Integer
131
100 Hz Sampling Frequency
3
Get Data CH#0
5
Get Data CH#1
18
Get Data CH#2
19
Get Data CH#3
20
Get Data CH#4
43
Get Data CH#5
44
Get Data CH#6
45
Get Data CH#7
0
A/D Config
Configure
hSubsys

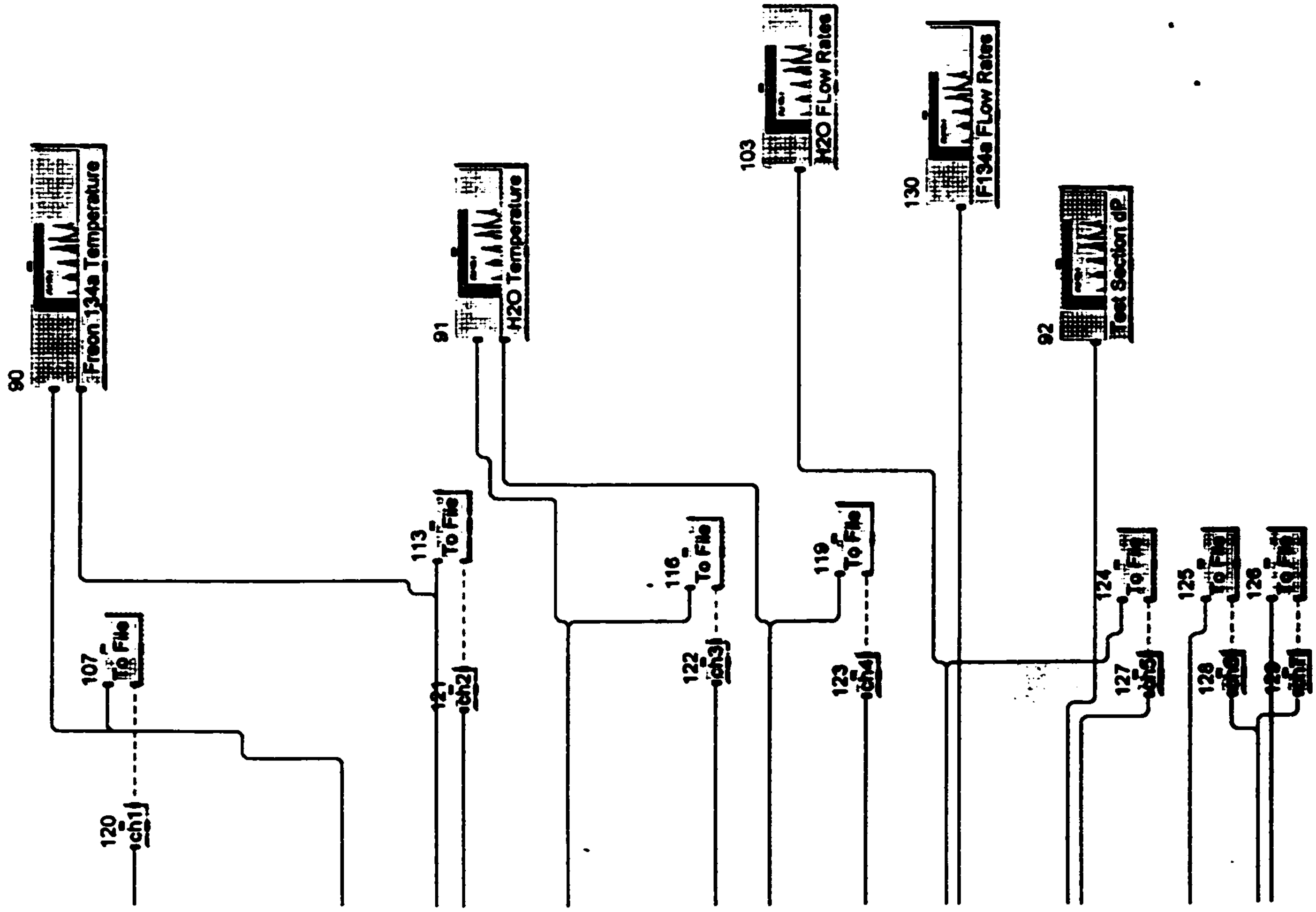
90
Freon 134a Temperature
91
H2O Temperature
103
H2O FLow Rates
130
F134a FLow Rates
92
Test Section dP
107
To File
113
To File
116
To File
119
To File
124
To File
125
To File
126
To File
120
ch1
121
ch2
122
ch3
123
ch4
127
ch5
128
ch6
129
ch7

Untitled: Get Data CH#7 (45)

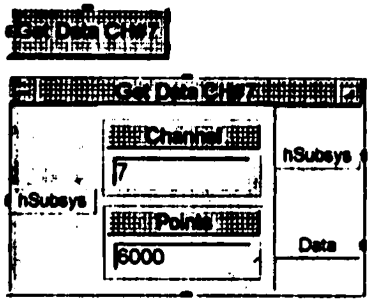

Channel: 7

Points: 6000

Untitled: Get Data CH#7 <Network>

Untitled: Turbine Calibration (46)

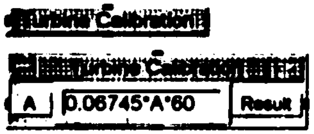

0.06745*A*60

Untitled: T Type Compensation (71)

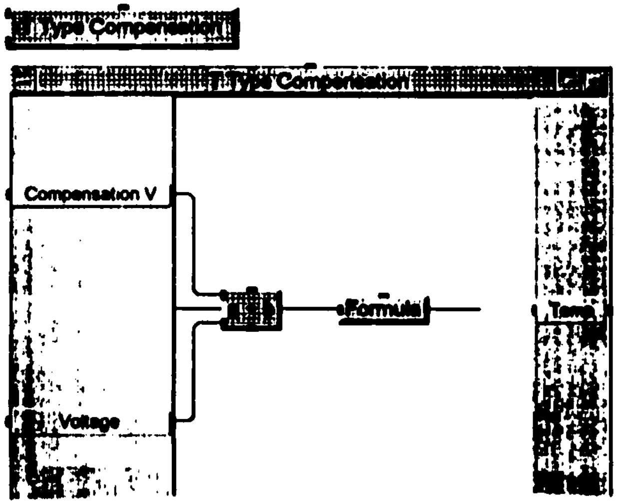

Untitled: T Type Compensation <Network>

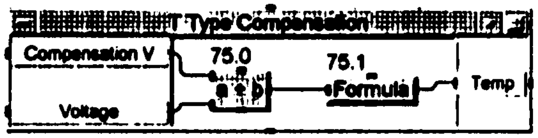

Untitled: T Type Compensation: a + b (75.0)

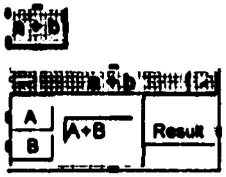

A+B

Untitled: T Type Compensation: Formula (75.1)

-a^2*5.6183e5+a*2.5715e4+2.8304e-3

Untitled: T Type Compensation (76)

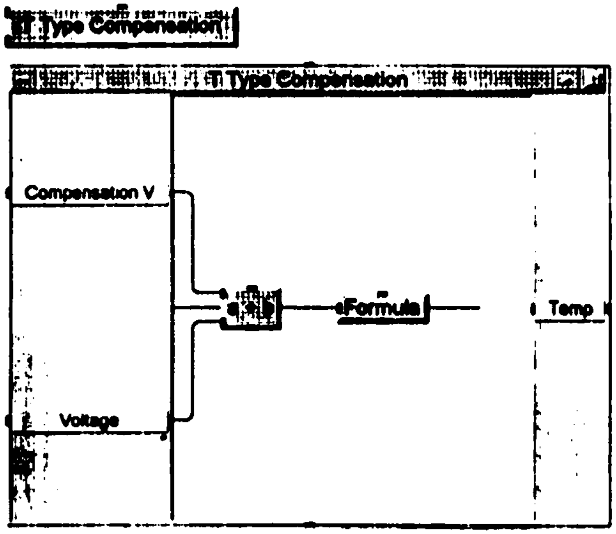

Untitled: CompensationVolts (F1)

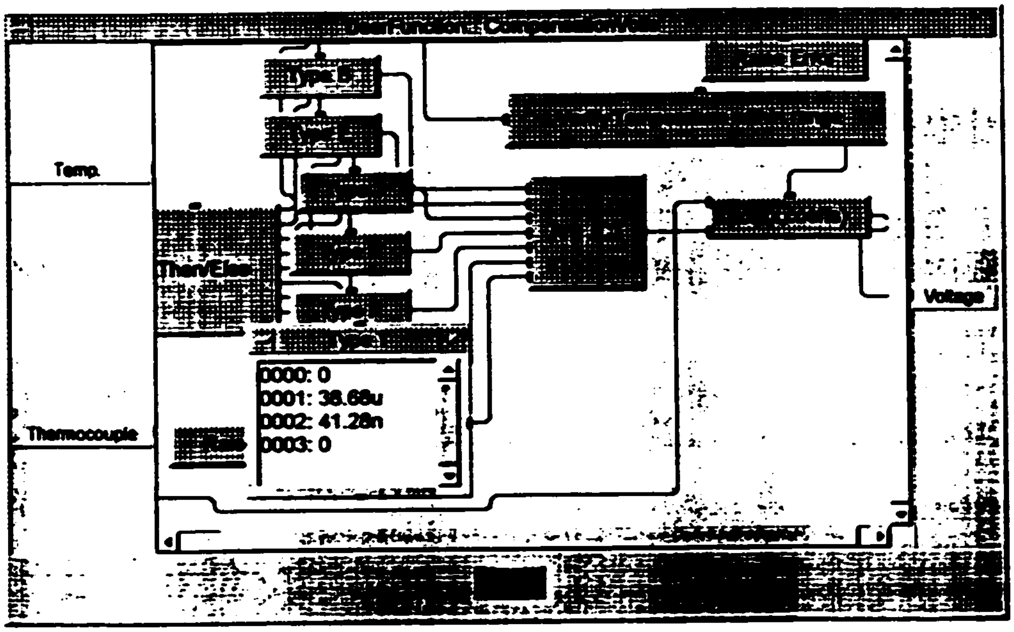

```
0000: 0
0001: 38.68u
0002: 41.28n
0003: 0
```

Untitled: CompensationVolts <Network>

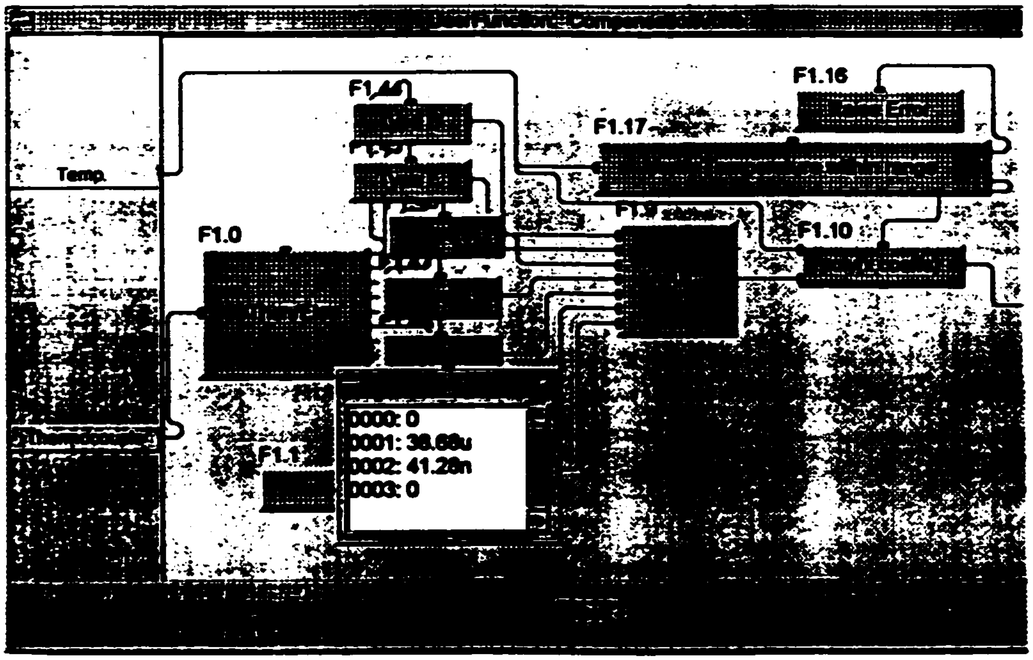

```
0000: 0
0001: 38.68u
0002: 41.28n
0003: 0
```

APPENDIX F. CONTRIBUTIONS TO KNOWLEDGE

The following list of publications was based on the results of this thesis, and are the contributions to knowledge in this field.

Refereed Publications

J.S. Chang, D.R. Novog, S. Li, S.T. Yin, "High Heat Flux Heat Transfer to a Cylinder in Thermal Plasma Cross Flow", Advances in Multiphase Flow, Elsevier of Science, New York, 1995, (A. Serizawa, T. Fukano, J. Bataille Ed.), pp. 529-538.

Articles for Submission to Refereed Journals

D.R. Novog, S.T. Yin and J.S. Chang, "High Heat Flux Heat Transfer and Pressure Drop Under Subcooled Boiling Smooth and Swirl Flow Conditions", To be Submitted to the ASME Journal of Thermal and Fluid Science, Nov. 2000.

D.R. Novog, K. Hori, J.S. Chang, "Real Time Neutron Radiography and High Speed X-Ray Computed Tomography of Flow Boiling in Smooth and Swirl Flow Geometries", To Be Submitted to the Journal of Nuclear Methods and Instruments in Physics Research A, March 2001.

Papers in Refereed Conferences

D.R. Novog, J.S. Chang, G.D. Harvel, and K. Hori, "Void Distribution Measurement of Swirl-Flow Boiling Freon by Real Time Neutron Radiography and High Speed X-Ray Computed Tomography, NURETH 9, CD-ROM Publication, San Francisco, Oct 3-8, 1999.

D.R. Novog, R.L. Judd and J.S. Chang, 'Subcooled Flow Boiling Hysteresis Characteristics for Freon 134a in a Tubular Channel", Procs. of the 17th Japanese Multiphase Flow Symposium, Tokyo, Japan, July 23-24, 1998.

D.R. Novog and J.S. Chang, "Real Time Neutron Radiography of Boiling Refrigerant 134a Under Smooth- and Swirl-Flow Conditions", 4th World Conference on Experimental Heat Transfer Fluid Mechanics and Thermodynamics, Brussels, Belgium, June 2-6, 1997.

D.R. Novog, S.T. Yin and J.S. Chang, "High Heat Flux Subcooled Boiling Heat Transfer and Pressure Drop Under Smooth and Swirl Flow Conditions", Proceedings of the 1995 U.S. National Heat Transfer Conference, ANS Publishing Inc., Illinois, HTC-Vol. 8, p.139 - 146.

J.S. Chang, D.R. Novog, S. Li, S.T. Yin, "Thermal Plasma Generated High Heat Flux Heat Transfer and Two-Phase Flow", Proceedings of the 2nd International Conference on Multiphase Flow, Serizawa Ed., Volume 3, pp. IA1-13, 1995.

D.R. Novog, S. Li, J.S. Chang, "High Heat Flux Heat Transfer and Pressure Drop for a Cylinder in Thermal Plasma Cross Flow", Bulletin of the American Physical Society, Volume 39, No. 6, p. 1459.

Other Publications

D.R. Novog, "Real Time Neutron Radiography of Swirl Flow Boiling Freon 134a in A Vertical Channel", Procs. of the 1999 CNA/CNS Student Conference, Peterborough, Ontario, pp. 28-35, 1999.

D.R. Novog, "Subcooled Flow Boiling Hysteresis of Freon 134a in a Tubular Channel", Procs. of the 1998 CNA/CNS Student Conference, Kingston, Ontario, pp. 155-161, 1998.

D.R. Novog, "Real Time Neutron Radiography of Freon134a Flow Boiling in a Horizontal Channel", Procs. of the 1997 CNA/CNS Student Conference, St. John, New Brunswick, 1997.

D.R. Novog, "High Heat Flux Subcooled Boiling Heat Transfer and Pressure Drop Under Smooth and Swirl-Flow Conditions", Proceedings of the 1995 CNA/CNS Student Conference, Winnipeg, Manitoba, pp. 135-139, 1995.

D.R. Novog, "Cooling of Plasma Facing Components for the International Thermonuclear Experimental Reactor; Experimental Simulation", Proceedings of the 1994 CNA/CNS Student Conference, Toronto, Ontario, pp. 67-72, 1994.

J.S. Chang, D.R. Novog, S. Li, P.C. Looy, G.D. Harvel, M. Niejadlik, W. He and S.T. Yin, "Development of a Thermalhydraulics Correlation Package for High Heat Flux Components of ITER Fusion Reactors", URIF Technical Report, Ref. No. MC22-005, March 1, 1995.

Publications Produced Unrelated to This Work Include

J.S. Chang, P.C. Looy, D. Novog, S. Jamal, "Thermal Pyrolysis of Used Tires: The Effect of Plasma Torch Power and Plasma Gases", Progress in Plasma Processing of Material, Begall House Inc., New York, 1997, (Pierre Fauchais Ed.), pp. 403-410.

J.S. Chang, D.R. Novog and S. Jamal, "Evaluation of Ash Toxicity Generated From The Thermal Plasma Pyrolysis of Used Automobile Tires ", 1996 Gaseous Electronics Conference, Oct. 20-24, 1996, Argonne, Illinois, Bulletin of the American Physical Society, 1996.

APPENDIX G. COPYRIGHT EXCEPTIONS

It is understood that the Copyrights for figures and content of this thesis is shared between the author and supervisor, J.S. Chang.